

UC Santa Cruz

UC Santa Cruz Electronic Theses and Dissertations

Title

Optofluidic Devices for Biomolecule Sensing and Multiplexing

Permalink

<https://escholarship.org/uc/item/1bw3g52s>

Author

Ozcelik, Damla

Publication Date

2016

Copyright Information

This work is made available under the terms of a Creative Commons Attribution-NonCommercial-ShareAlike License, available at <https://creativecommons.org/licenses/by-nc-sa/4.0/>

Peer reviewed|Thesis/dissertation

UNIVERSITY OF CALIFORNIA
SANTA CRUZ

**OPTOFLUIDIC DEVICES FOR BIOMOLECULE
SENSING AND MULTIPLEXING**

A dissertation submitted in partial satisfaction
of the requirements for the degree of

DOCTOR OF PHILOSOPHY

in

ELECTRICAL ENGINEERING

by

Damla Ozelik

December 2016

The Dissertation of Damla Ozelik is
approved:

Professor Holger Schmidt, Chair

Professor Joel Kubby

Professor Claire Gu

Tyrus Miller

Vice Provost and Dean of Graduate Studies

Copyright © by

Damla Ozcelik

2016

Table of Contents

1	Introduction.....	1
2	Background.....	9
2.1	Planar integrated optofluidic platform	9
2.2	Theory of ARROW	11
2.3	Fabrication of ARROWs.....	19
2.4	Fluorescence detection on ARROWs.....	22
2.4.1	Chip characterization	25
2.4.2	Post-fabrication improvements on devices	29
3	Tunable Spectral Filters based on ARROW	32
3.1	Spectral ARROW filter	38
3.2	Dual Liquid-Core Optofluidic Chip.....	47
3.2.1	Device Design.....	47
3.2.2	SNR Enhancement by Spectral Filtering	50
3.2.3	Multi-wavelength Tuning by Bulk Absorption.....	52
4	Signal to Noise Ratio (SNR) Enhancement by Multi-Spot Excitation.....	59
4.1	Signal processing algorithm.....	61
4.2	Multi-spot excitation based on Y-splitters	68
4.2.1	Y-Splitter design and optimization	70

4.2.2	Y-Splitter characterization with beads	78
4.2.3	SNR Enhancement for single virus detection	85
5	Multiplexed Bioparticle Detection based on Multi-Mode Interference (MMI)...	93
5.1	Multi-mode interference waveguide design for spectral multiplexing	97
5.1.1	MMI waveguide theory.....	97
5.1.2	MMI waveguide design and simulations	107
5.1.3	MMI characterization.....	122
5.2	Bioparticle detection and identification by spectral multiplexing	129
5.2.1	Single-color labeling multiplexed detection	130
5.2.2	Combinatorial labeling multiplexed detection.....	133
5.3	Bioparticle detection and identification by spatial and spectral multiplexing	136
5.3.1	Triple-core Channel Layout Design.....	137
5.3.2	Spatially Multiplexed Detection	146
5.3.3	Combination of spatial and spectral multiplexing	148
5.4	Cascade MMI Design & Results	150
5.5	Effect of Flow Properties on Particle Signal Intensity and Particle Velocities	158
5.5.1	Variation in Particle Intensity	158

5.5.2	Variation in Particle Velocity	160
5.5.3	Hydrodynamic Focusing	163
6	Conclusions.....	168
7	Appendices.....	172
7.1	Appendix A Setup Details.....	172
7.1.1	A.1 Single Molecule Detection Setup.....	172
7.1.2	A.2 Compound Microscope Setup.....	176
7.1.3	A.3 White Light Setup	178
7.2	Appendix B Filling and Cleaning Procedure of Liquid-Core Waveguides	182
7.3	Appendix C MMI Alignment Procedure.....	185
7.4	Appendix D Virus Labeling Procedure.....	187
7.5	Appendix E ARROW Waveguide Fabrication Parameters and Procedure.	189
7.5.1	E.1 Tunable Filter – TF11.....	190
7.5.2	E.2 Y-Splitters – SP2	191
7.5.3	E.3 Standard MMI – MA13	194
7.5.4	E.4 Triple Core MMI – TC7	195
7.6	Appendix F MMI Spot Pattern Analyzer Software.....	199
7.7	Appendix G Multiple-peak Identification Software.....	206
8	Bibliography	212

List of Figures

- Fig. 2.1 The cross section of ARROW structure, showing the core layer with thickness d_c , refractive index n_c ; cladding layers with thicknesses t_i and refractive indices n_i . Light propagates along the z direction with a propagation constant β 12
- Fig. 2.2 ARROW cross-section showing the field directions for x-polarized light. TE loss depends on the structure in vertical direction, and the TM loss depends on the structure in horizontal direction. 14
- Fig. 2.3 Calculated TE loss dependence on wavelength, for an x-polarized beam. The design wavelength is $\lambda_D=633\text{nm}$ 16
- Fig. 2.4 Schematic of a standard ARROW chip with single top oxide layer and the cross-section. The red dashed arrow shows the excitation path, and the blue one shows the collection path for a standard fluorescence experiment. Key points for the coupling efficiency are labeled. 16
- Fig. 2.5 Cross-section of three different types of ARROW structures. (a) Earlier version of ARROW with top cladding layers and no self-aligning pedestal (SAP). Tunable filter platforms are based on this design. (b) Improved ARROW with SAP and top cladding layers. [106] (c) Preferred version of ARROW design. It has a single-over coating (SOC) and SAP. MMI and Y-splitter platforms are based on this design. 18
- Fig. 2.6 Fabrication process of SOC-SAP ARROW. (a) 6 ARROW layers are deposited on silicon wafer. (b) Sacrificial core is created by using SU-8, on ARROW layers. (c) Thin nickel layer is created to protect the solid-core and hollow core

waveguides, by using lift-off process. (d) Self aligned pedestals are created by etching away the ARROW layers on the rest of the wafer, by reactive-ion etching (RIE).

Nickel layer is removed. (e) A thick (6 μm) SiO₂ layer is deposited on top of the entire wafer, to create the top ARROW layer, and the solid-core waveguides. (f) Solid-core waveguides are formed by etching the SiO₂ top layer, by RIE. (g) Sacrificial core is removed by using Piranha etching to form the hollow-core waveguide. 19

Fig. 2.7 (a) Schematic of basic fluorescent detection on a standard ARROW chip with an orthogonal layout. Red dotted line represents the excitation path, and the blue dotted line represents the collection path for the fluorescence signal. (b) Schematic of a simple experiment setup..... 23

Fig. 2.8 Defects found during visual inspection. (a) Broken liquid core (b) Broken solid core MMI (c) Broken facet 25

Fig. 2.9 The mode profiles of solid-core excitation waveguides. (a) Fundamental mode guiding on the center of the ridge waveguide. (b) Fundamental mode guiding on the upper region of the ridge waveguide..... 27

Fig. 2.10 (a) The fluorescence signal collected from 22nM Cy[®]5 dye at the 633nm excitation wavelength. (b) The fluorescence signal collected from 200nm Invitrogen[®] Crimson Fluospheres. 28

Fig. 3.1 The absorption and emission spectra of Alexa Fluor[®] 633. (data retrieved from: [119])..... 33

Fig. 3.2 The three generations of integrated ARROW filters. (a) Collection solid-core waveguide with ARROW filter layers. [133] (b) Single liquid-core ARROW filter. [45] (c) Dual liquid-core ARROW filter. [44]..... 38

Fig. 3.3 (a) Schematics of the cross-sections of liquid- and solid-core waveguides, showing the ARROW layers. The filter layer (t_4) is indicated in the zoomed in section. (b) SEM images of the cross sections of fabricated structures for both liquid- and solid-core waveguides (TF11 wafer). The filter layer is marked. 39

Fig. 3.4 Calculated spectral response of the liquid- (black) and solid-core (red) waveguides with a filter layer ($t_4=230\text{nm}$), filled with water. Blue curve represents the spectral response of the liquid-core with the anti-resonant layer, for comparison. ($t_4=115\text{nm}$) (a) Absorption spectra. (b) Transmission spectra..... 41

Fig. 3.5 The spectral response of the fabricated device with water as a core fluid for $L=0.7\text{cm}$ (red). Calculated spectral response is also shown (black). 43

Fig. 3.6 The dependence of the peak rejection ratio of the ARROW notch filter on the length of the liquid-core waveguide filter. Measured data (black markers), as well as linear fit (blue line) with an equation Rejection Ratio [dB] $\approx 29+2$ [dB/mm] \times Filter Length [mm] are shown. 44

Fig. 3.7 (a) Transmission spectra of the liquid-core ARROW filter for different concentrations of Ethylene Glycol. Normalized transmission spectra for four EG:water mixtures show that the minimum-transmission wavelength decreases as the EG concentration and n_c increase. (b) Dependence of the tunable filter dip wavelength, λ_F , on the fractional ethylene glycol concentration C_{EG} . Symbols

represent the data and the solid line represents the calculation. The dashed line is the HeNe laser excitation (632.8 nm) line, which corresponds to an EG:water ratio of 72% : 28%..... 46

Fig. 3.8 (a) Schematic of an integrated optofluidic dual-channel chip with two different liquid-core sections (blue) for detection and tunable filtering, optically coupled by a solid-core waveguide section (orange). (b) Photograph of a complete chip on a U.S. quarter coin. (c) SEM cross-section of the liquid-core waveguide, showing the ARROW layers..... 49

Fig. 3.9 (a) Single particle detection with optofluidic integrated filter chip. A maximum signal-to-baseline ratio of 35 was achieved for detection through the optofluidic filter. (b) Signal collected from the other end of the chip which has no filter in the path..... 51

Fig. 3.10 (a) Normalized transmission curves of different concentrations of absorber dye (Sudan II) in isopropanol. Dashed lines are the measured data and the solid lines are the Gaussian lineshape fits. Non-zero absorption for Sudan II between 550 and 565 nm is observed. (b) Concentration dependence of the extracted maximum absorbance of absorber dye (Sudan II) in isopropanol. Symbols: experimental data; line: fit with linear absorption dependence..... 53

Fig. 3.11 Normalized transmission absorbance spectra of universal indicator for two different pH values measured using a NanoDrop spectrophotometer. 55

Fig. 3.12 (a) Normalized transmission spectra of universal indicator with different pH values taken on chip. Dashed lines are the off-chip spectra, normalized to match the

concentration. The blue line indicates the activated filter and the red line indicates the deactivated filter; (b) Independent multi-wavelength tuning function. For the blue and cyan curves, the absorption filter is active and the ARROW filter is independently shifted to another wavelength. For the red and orange curves, the absorption filter is deactivated and the LC-ARROW filter is tuned independently. 56

Fig. 4.1 Symbolic data showing the signal parameters with $N=4$ 62

Fig. 4.2(a) Theoretical analysis of *SNR* enhancement varying the noise and mean values for $P=5$ and $N=8$. Color bar shows the *SNR* enhancement in a logarithmic scale. (b) Theoretical analysis of the limits of the *SNR* enhancement. The yellow region shows the values at which the *SNR* enhancement is above one, and the green region represents values at which the *SNR* enhancement is below one. 65

Fig. 4.3 Simulated data for *SNR* enhancement depicting signal (red) and noise (blue) levels for different N values. (a) Original data. (b) *SNR* enhancement with $N=2$ (c) $N=4$ (d) $N=8$ 67

Fig. 4.4 (a) *SNR* Enhancement dependence on number of peaks (N). Blue dots represent the simulated data and the red line is an exponential fit. (b) *SNR* enhancement cut-off dependence on N 67

Fig. 4.5 The probability of finding a zero for $N-1$ multiplications, for different initial p_0 values (i.e. y -intercepts), from 0.1 to 0.9. 68

Fig. 4.6 Schematic of Y-splitter ARROW waveguide platform for $N=8$ 69

Fig. 4.7 (a) Schematic of a 1×2 Y-splitter with an S-shaped taper. (b) Dependence of the total transmission in 1×2 Y-splitter waveguide on the fan-out angle of the Y-junction, for $\Delta x = 25 \mu\text{m}$, and $w = 4 \mu\text{m}$ 72

Fig. 4.8 Simulations of Y-splitters for a wider waveguide (here: $w = 6 \mu\text{m}$) supporting multiple lateral modes. (a) Beating of the waveguide mode (b) Unequal splitting of the power when there is asymmetrical mode at the intersection. (c) 1×8 Y-splitter waveguide showing the unequal distribution of the total power, due to the beating modes. (d) The output intensity profile of the 1×8 Y-splitter device in (c). 73

Fig. 4.9 Simulations of Y-splitters for a narrow single-mode waveguide (here: $w = 4 \mu\text{m}$). (a) Single mode propagation. (b) Balanced splitting of the power. (c) 1×8 Y-splitter waveguide showing a more balanced distribution of the total power. (d) The output intensity profile of the 1×8 Y-splitter device in (c). 74

Fig. 4.10 The characterization of the excitation patterns for all three designs by using quantum dot solution in the liquid-core waveguide. The top images are the actual images taken from top, and the plots show the excitation patterns obtained from the actual images. (a) 1×2 Y-splitter (b) 1×4 Y-splitter (c) 1×8 Y-splitter 77

Fig. 4.11 (a) SEM image of the multiple excitation spots created by 1×8 Y-splitter waveguides. (b) Experiment setup used for particle detection. 78

Fig. 4.12 (a) Particle trace of the raw data, $F(t)$ (b) $F(t)$ for an individual particle showing the $N=8$ fluorescence peaks from the data trace in (a). (c) $F(t)$ for an individual particle from separate experiments showing the $N=4$ and 2 fluorescence peaks. 80

Fig. 4.13 (a) Autocorrelation curve for the single particle in Fig. 4.12b, which exhibits peaks at multiples of $\Delta T=0.8\text{ms}$. (b) $S(t)$ for the particle shown in Fig. 4.12b, after the signal processing algorithm is applied..... 81

Fig. 4.14 (a) Original data trace collected from the ARROW platform with $N=8$ with added noise. (b) Data trace $S(t)$, after the *SNR* enhancement algorithm is applied. 82

Fig. 4.15 *SNR* enhancement exponential dependence the number of spots (N) in these three experiments (symbols), providing a good match between the calculation (line) based on average μ and σ values..... 84

Fig. 4.16 (a) Red-dye labeled H1N1 virus detected by APD. (b) Single virus fluorescence signal demonstrating 8 clear peaks. (c) Autocorrelation curve of the single peak in 2(b), showing that the ΔT is around 0.8 ms. (d) Virus signal from 2(b) after signal processing for $N=8$ 86

Fig. 4.17 Probability of finding zero values in noise for N multiplication. The marked spot shows where above experiment corresponds, with the probability of 0.14. 87

Fig. 4.18 Histogram of the particle velocities showing the variation due to the position of the virus in the channel. 88

Fig. 4.19 (a) Theoretical analysis of *SNR* enhancement varying the noise and mean values using the signal average from the experiment. The marked spot corresponds to the experimental values of μ and σ with an *SNR* enhancement is 2×10^5 . (b) Theoretical analysis of the limits of the *SNR* enhancement. The light region shows the values at which the *SNR* enhancement is above one, and the dark region represents

values at which the <i>SNR</i> enhancement is below one. The marked spot is the experimental values of μ and σ	89
Fig. 4.20 Dependence of <i>SNR</i> on the number of excitation spots (<i>N</i>). Good match between the experiments (symbols), and calculations (lines) based on the μ and σ values of each experiment.....	91
Fig. 5.1 The schematic for a MMI waveguide, depicting the device parameters and the propagation constants.....	98
Fig. 5.2 Illustration of first 10 lateral modes in a MMI waveguide. Modes with even <i>v</i> numbers are symmetrical, odd <i>v</i> numbers are asymmetrical.....	99
Fig. 5.3 The simulated MMI waveguide pattern for a symmetrical single-mode input, showing the self-image and multiple image formations at different positions along <i>z</i> axis.....	105
Fig. 5.4 Sketch of MMI waveguide with liquid-core waveguide, showing the design parameters.....	109
Fig. 5.5 The simulated MMI waveguide patterns on the same device by using a beam propagation method. The relationship between <i>N</i> and λ is shown for the design wavelengths. The total output mode field is demonstrated on the right hand side, for the corresponding wavelengths.....	113
Fig. 5.6 The simulated output pattern of the MMI waveguide at $L=3400\mu\text{m}$ is demonstrated for $w=100\mu\text{m}$, $\lambda=633\text{nm}$ with $N=7$. The important parameters of the excitation pattern are shown where <i>P</i> is the intensity of excitation spot.....	113

Fig. 5.7 (a) Cross section of the input waveguide pattern for single-mode excitation.
(b) The total output mode field shown at the cross section of the MMI at $z=3400\mu\text{m}$.
..... 115

Fig. 5.8 (a) The 3D simulation of input and MMI waveguide pattern for multi-mode
input excitation in horizontal direction. (b) The total output mode field shown at the
cross section of the MMI at $z=3400\mu\text{m}$ 116

Fig. 5.9 (a) The side view of 3D simulation of input waveguide pattern for multi-
mode input excitation in vertical direction. The beat pattern in vertical direction is
observed. (b) Cross section of the input waveguide pattern for vertical multi-mode
excitation. (c) The total output mode field shown at the cross section of the MMI at
 $z=3400\mu\text{m}$. The plot shows the intensity profile in the middle of the waveguide
vertically. 117

Fig. 5.10 The schematic of ARROW fluorescence detection platform based on MMI
waveguides..... 119

Fig. 5.11 The simplified version of optical setup used for the experiments. 120

Fig. 5.12 (a) SEM image of an ARROW optofluidic platform with an MMI
waveguide. (b) The photograph of 1cm by 1cm chip, showing two fluidic reservoirs
holding microliters of sample volume. 122

Fig. 5.13 (a) The schematic of the device where MMI waveguide pattern intersects
with the liquid-core waveguide for $N=6$. (b) Photographs of multi-spot excitation
patterns created in fluidic channel filled with fluorescent liquid. The entire visible
spectrum is covered by independent channels (405 nm/11 spots, 453/10, 488/9, 553/8,

633/7, 745/6). (The original black and white color scale was rendered in the actual excitation colors.).....	124
Fig. 5.14 (a) Fluorescence image of the liquid-core waveguide, filled with quantum dot solution, and excited at $\lambda=633\text{nm}$. (b) The intensity profile of the excitation pattern extracted from (a), showing the important parameters for characterization.	125
Fig. 5.15 The photograph and the intensity profile of a sample taken from a low quality wafer (MA34), showing the low quality MMI pattern for $\lambda=633\text{nm}$.	127
Fig. 5.16 The schematic of MMI waveguide and liquid-core waveguide intersection, showing how target particles get excited while passing through the liquid-core channel. [212]	127
Fig. 5.17 (a) The particle trace of the raw data, directly obtained by the detector with excitation wavelengths of $\lambda=633\text{nm}$ & $\lambda=488\text{nm}$ (b) Zoomed in data trace for an individual particle showing the $N=7$ and $N=9$ fluorescence peaks from the data trace in (a).	129
Fig. 5.18 Three-color multiplex virus detection. (a) representative fluorescence signal emitted by single H1N1 virus excited at 488nm showing 9 distinct peaks spaced by Δt_B ; (b) Corresponding single-particle autocorrelation signal. Multiple peaks are observed at multiples of Δt_B ; dashed line: fit to underlying flow-limited correlations. (c) Single-particle autocorrelation for 3 virus types after subtraction of flow-based contribution. The peak positions depend strongly on excitation spot number (arrows mark the 5 th peak for each virus type). (d) Segment of fluorescence from virus mixture excited at all three colors. Events are identified using single-particle	

autocorrelations. All but one identified signals (99.2%) agree with manual inspection of events. (after [212])	132
Fig. 5.19 Analysis of single virus fluorescence signals. (a) sketch of fluorescently labeled H3N2 virus, responding to excitation at 745 nm; (b) fluorescence signal from single H3N2 virus showing six peaks with average spacing Δt_{DR} ; (c) corresponding processed signal using shift-multiply algorithm with Δt_{DR} showing dramatically increased SNR. (after [212]).....	134
Fig. 5.20 Two-color combinatorial detection of single viruses. (a) schematic view of labeling scheme for the three influenza types and their resulting single-virus fluorescence signals; the H2N2 virus shows a mixture of six and nine peaks upon blue and dark red excitation; (b) bar histograms of signals after shift-multiply processing at Δt_B and Δt_{DR} . Singly labeled viruses appear in only one Δt channel, while the double labeled virus creates signal in both color channels. (after [212])	135
Fig. 5.21 Schematic view of the optofluidic platform with MMI waveguide intersecting three separate liquid-core waveguides, and a Y-coupler to combine the signals from three channels.....	138
Fig. 5.22 (a) SEM image of the MMI waveguide crossing three liquid-core waveguide channels. (b) The photograph of the full optofluidic platform with reservoirs attached.	139
Fig. 5.23 The simulated MMI waveguide patterns for both wavelengths, (a) $\lambda=633\text{nm}$ and (b) $\lambda=520\text{nm}$. The channel locations are marked to show six excitation patterns with distinct N generated by using two wavelengths and three channels.	141

Fig. 5.24 Alternative spatial multiplexing design using three liquid core waveguides and three MMI waveguides. This device is not functional, due to the high losses at the excitation Y-splitter waveguides.....	143
Fig. 5.25 the fluorescence images of the three channels excited with two different wavelengths, $\lambda=633\text{nm}$ and $\lambda=520\text{nm}$, showing six separate excitation patterns with a distinct N . The corresponding intensity plots are also shown, and the excitation spot peaks are marked.....	144
Fig. 5.26 Simplified experiment setup showing the excitation and collection paths.	145
Fig. 5.27 Spatial multiplexing of three different samples with H2N2 human influenza viruses (a) Data trace of the fluorescence signal collected from the viruses, excited with $\lambda=633\text{nm}$. The signals are marked according to the channel they belong. (b) The zoomed-in particle signals shown in (a), demonstrating the single virus detection with three different N (8,6, and 4) coming from three separate channels.....	147
Fig. 5.28 . (a) Fluorescence signal collected from viruses in three channels, excited with both wavelengths $\lambda=520\text{nm}$ and $\lambda=633\text{nm}$. They are labeled based on the number of peaks they emitted. (b) The zoomed-in particle signals shown in (a), demonstrating the three different signals of H1N1 viruses with $N =10,7,$ and 5 coming from three separate channels.....	149
Fig. 5.29 The schematic of an asymmetrical MMI waveguide, showing the bar- and cross- coupling routes, for two different wavelengths.....	151

Fig. 5.30 The simulated MMI waveguide patterns on the same device by using a beam propagation method, for two design wavelengths: (a) $\lambda_B=488\text{nm}$ (bar-coupler) and (b) $\lambda_C=745\text{nm}$ (cross-coupler)	152
Fig. 5.31 The schematic of the cascade MMI design, showing the regions for asymmetrical and symmetrical MMI waveguides, and S-shaped waveguides.....	154
Fig. 5.32 Predicted example signal for a combinatorial multiplexing, using the cascade MMI waveguides. (adapted from: [212])	155
Fig. 5.33 The layout image of the cascade MMI design, with five different designs for characterization. The differences among these designs are shown in the table.....	156
Fig. 5.34 The intensity profiles and the power ratios of the asymmetrical MMI waveguide output for excitation wavelengths of $\lambda_B=488\text{nm}$ and $\lambda_C=743\text{nm}$	157
Fig. 5.35 The excitation patterns obtained by using the first design, for excitation wavelengths of $\lambda_B=488\text{nm}$ and $\lambda_C=743\text{nm}$	158
Fig. 5.36 Excitation and Collection mode profiles for a liquid-core waveguide channel. x is the excitation direction and z is the collection direction. The color represents the relative intensities in arbitrary units. (a) Excitation mode profile, and cross-section. (b) Collection mode profile.....	159
Fig. 5.37 (a) Uniform particle distribution among the cross-section of the liquid-core waveguide channel. (b) Histogram plot of the calculated intensities for particles shown in (a).....	160
Fig. 5.38 Simulation for the velocity variation among the channel due to the Poiseuille flow.	161

Fig. 5.39 The ΔT distribution of the two different colored target molecules. The variation in the velocity results in high FWHM in ΔT , hindering the differentiation capacity.	162
Fig. 5.40 The particle trajectories for a 2D hydrodynamic focusing with $V_S=V_M=3\text{cm/s}$ channel flow velocities.	163
Fig. 5.41 Particle distribution at the liquid-core waveguide cross-section excitation area, for different side channel flow velocities, 0-3cm/s.	164
Fig. 5.42 Histogram plot of the calculated intensities for particles shown in Fig. 5.40. It is evident that there are more particles with higher intensities compared to non-focused particle distribution.	165
Fig. 5.43 (a) SEM image of MMI ARROW platform with hydrodynamic focusing section, showing the three arms of the inlet. (b) Zoomed in image of the hydrodynamic focusing section. (c) PDMS control layer for precise pressure control of the inlets.	166
Fig. 5.44 The autocorrelation curves for the data traces with and without the hydrodynamic focusing, showing the slight improvement in the ΔT variation.	167

List of Tables

Table 4.1 The design angles for the three separate Y-splitter waveguide designs, where $N=2, 4,$ and $8.$	75
Table 4.2 Analysis on the excitation patterns shown in Fig. 4.10. Average and standard deviation values are shown for spot spacing (Δx), peak (P) and valley (V) values.	77
Table 4.3 The initial noise values, and the SNR enhancement for $N=2,4$ and 8 with added noise. The theoretical SNR enhancement based on the initial noise values is also shown for comparison.	83
Table 4.4 Table showing the noise, mean, and SNR values of the original data and the enhancement values after the signal processing.	90
Table 5. The multiple channels designed for spectral multiplexing with MMI waveguides.....	108
Table 6. Analysis on the excitation patterns shown in Fig. 5.14. Average and standard deviation values are shown for spot spacing (Δx), peak (P) and valley (V) values. ...	125

Abstract

Damla Ozcelik

Optofluidic devices for biomolecule sensing and multiplexing

Optofluidics which integrates photonics and microfluidics, has led to highly compact, sensitive and adaptable biomedical sensors. Optofluidic biosensors based on liquid-core anti-resonant reflecting optical waveguides (LC-ARROWs), have proven to be a highly sensitive, portable, and reconfigurable platform for fluorescence spectroscopy and detection of single biomolecules such as proteins, nucleic acids, and virus particles. However, continued improvements in sensitivity remain a major goal as we approach the ultimate limit of detecting individual bio-particles labeled by single or few fluorophores. Additionally, the ability to simultaneously detect and identify multiple biological particles or biomarkers is one of the key requirements for molecular diagnostic tests. The compactness and adaptability of these platforms can further be advanced by introducing tunability, integrating off-chip components, designing reconfigurable and customizable devices, which makes these platforms very good candidates for many different applications. The goal of this thesis was to introduce new elements in these LC-ARROW optofluidics platforms that provide major enhancements in their functionality, making them more sensitive, compact, customizable and multiplexed.

First, a novel integrated tunable spectral filter that achieves effective elimination of background noise on the ARROW platform was demonstrated. A unique dual liquid-core design enabled the independent multi-wavelength tuning of the spectral filter by adjusting the refractive index and chemical properties of the liquid. In order to enhance the detection sensitivity of the platform, Y-splitter waveguides were integrated to create multiple excitation spots for each target molecule. A powerful signal processing algorithm was used to analyze the data to improve the signal-to-noise ratio (SNR) of the collected data. Next, the design, optimization and characterization of the Y-splitter waveguides are presented; and single influenza virus detection with an improved SNR was demonstrated using this platform. Finally, multiplexing capacity is introduced to the ARROW detection platform by integrating multi-mode interference (MMI) waveguides. MMI waveguides create wavelength dependent multiple excitation spots at the excitation region, allowing the spectral multiplexed detection of multiple different target molecules based on the excitation pattern, without the need for additional spectral filters. Successful spectral multiplexed detection of three different types of influenza viruses is achieved by using separate wavelengths and combination of wavelengths. This multiplexing capacity is further enhanced by taking advantage of the spatial properties of the MMI pattern, designing triple liquid-core waveguides that intersect the MMI waveguide in different locations. Furthermore, the spectral and spatial multiplexing capacities are combined in these triple liquid-core MMI platforms, allowing these devices to distinguish multiple different targets and samples simultaneously.

To my grandparents: Suzan, Kemalettin, Sevim and İsmet

Acknowledgements

The journey through my doctoral studies was one of the most challenging and transformational experiences of my life. In addition to the isolating nature of doctoral study, as an international student, there were a lot of lonely times and difficulties. For this very reason, this work would not have been possible without the support of numerous people, for whom I am extremely grateful.

Foremost, I would like to express my sincere gratitude to my advisor Prof. Holger Schmidt for the continuous support of my Ph.D. study and research, for his patient guidance, motivation, and teaching. I am very thankful for his assurance and encouragement when I was ready to give up, his skillful feedback to helped me push past my learning edges. His immense knowledge and exciting ideas encouraged me in my research.

Gratefully I acknowledge my committee members, Prof. Joel Kubby and Prof. Claire Gu, for their advice, teaching and critical suggestions which were very instrumental in finishing my Ph.D. I am also very grateful for the experiences I had as a teaching assistant with Prof. Nobby Kobayashi, who supported me fully. I also would like to thank our collaborators in BYU for their extremely valuable and important contributions. I thank Professor Aaron Hawkins for his leadership on the fabrication of optofluidic devices, which made my research possible.

I would like to thank my colleagues Dr. Rebekah Brandt, Dr. Kaelyn Leake, Dr. Philip Measor, Dr. Yu Yahagi, Dr. Shuo Liu, Dr. Cathy Hong Cai, Josh Parks, Jennifer Black, Cassidy Berk, Mike Jaris, Gopikrishnan Gopalakrishnana Meena, Alexandra

Stambaugh, Md. Mahmudur Rahman, Dr. Tom Yuzvinsky, Anik Duttaroy, Armando Oviedo and Dr. Aadhar Jain not only for providing suggestions and collaboration on projects, but also for making the frustrating hours spent in the lab a lot easier by sharing the struggle, and for being precious companions throughout my whole study.

I also feel very grateful for the resources UCSC and Santa Cruz provided. I would like to thank CAPS and Sharon Nash for their tremendous support on my well-being; Audrey Kim and the Graduate Women's Group for holding a caring and compassionate space for me as a female student; Dennis and Lonna for providing a home at the Byrne Haus, along with wonderful housemates who fed me, encouraged me, and laughed with me; Sephardic/Balkan music jams and musician friends who made me feel at home; the Santa Cruz dance community for helping me decompress and explore; the Pomodoro technique for helping me when I was stuck looking at a blank page and imagining a completed dissertation; and the redwoods for nourishing me during lunch breaks, and inspiring with their resilience.

Last and most importantly, I would like to thank my parents, İnci, Lütfi, and my extended family, who provided endless support and love for me, even while in Turkey.

I am also very thankful to my friends, here and far, for their support, sense of humor, and encouragement to finish my degree.

1 Introduction

On December 29, 1959, Richard Feynman gave his famous talk “There is Plenty of Room at the Bottom”, introducing his insights on manipulating and controlling things on a small scale, and planting the seeds for miniaturization for variety of technical applications, such as, information storage, small-scale machines, computers and mechanical surgeons [1]. The fascination of inventing small-scale technology influenced the direction of technological research and transformed our relationship with technology. In 1940s, the world’s first general-purpose computer ENIAC (Electronic Numerical Integrator and Computer) was built. Its size was 1800ft², consuming more than 150kW of electricity and it cost more than \$6 million if the inflation is taken into account [2]. Today, easily available phones that fit into the palm of our hands, can provide more than a million times higher computing power, with dramatically lower power consumption and cost. Developments towards miniaturization enabled us to create cheaper, highly functional, simple to use devices which are also portable, making them available for a higher percentage of the population. The same drive for miniaturization has been taking place for many different research fields, and applications, by continuing to provide low-cost, simple-to-use and reconfigurable technology to address a variety of problems. All of these were initially enabled by the rapid advances in semiconductor fabrication technologies, creating smaller, cheaper ways to build integrated circuits (ICs). The capability of fabricating small-scale devices quickly spread to different fields, using semiconductor technology as a building block. One of the earliest fields to take advantage of this microfabrication

technology was photonics, integrating more optical components onto a compact chip with high degrees of functionality, giving rise to the field of optoelectronics, originally for communication purposes [3]. In the 1970s, the benefits of silicon microfabrication technology were also applied to micro-scale mechanics, initially creating pressure sensors and ink jet nozzles [4]. In the 1990s, the new field micro-electro-mechanical systems (MEMS) emerged by combining the mechanical and electrical components, such as micro-motors [5], actuators [6], sensors [7], and optical switches [8]. MEMS had a major impact on many disciplines including biology, chemistry, medicine, optics, aerospace, mechanical and electrical engineering [9]. Especially for biological and chemical applications, the integration of the fluidics onto the planar systems was also necessary to achieve compact devices, which gave rise to microfluidics. By solving the challenges of new physical phenomena caused by operating on a small scale, microfluidics not only created a new paradigm of system control: micropumps [10], [11], microfilters [12], transport and mixing [13]; but also facilitated the integrated biochemical analysis systems which mostly involves liquid specimens and reagents: molecular characterization [14], flow cytometry [15], [16], DNA sequencing [17], electrochemical sensors [18]. The idea of bringing room size equipment into a small compact device to perform the macro-scale laboratory processes at small-scales, was implemented by integrating the fluidic channels into miniature monolithic platforms, creating the systems called lab-on-a-chip (LOC) and micro total analysis systems (μ TAS) [19]–[22]. These miniature systems offer advanced devices, by integrating many different tools and processes, creating multi-functional platforms.

Inevitably, optofluidics, the combination of optics and microfluidics, emerged to create highly versatile systems, by taking advantage of the interaction of light and liquid on a micro-scale [23]–[25]. This synthesis of the two very advanced fields transcended their original capabilities, and created a new realm of photonic functionalities that were not possible before. First of all, optofluidics enabled the manipulation of optical properties by manipulating the fluids, providing highly functional and reconfigurable devices. One of the main advantages of introduction of fluidics onto photonic systems is the ability to manipulate the fluids easily within the structure to provide many different aspects for optical tuning. For example, the refractive index of the optofluidic system can be tuned by simply replacing the liquid with another liquid. Highly reconfigurable and tunable photonic components and systems were invented by incorporating the fluidics in the photonics systems. Optofluidic light sources are built with various approaches, for example, by using organic dyes in microchannels as the gain medium [26], [27] or the dynamic tuning of the laser emission wavelength by using mechanical deformation of the microfluidic chip [28], [29]. Various other components based on optofluidics were built, including fluidic waveguides [30]–[32], tunable fluidic lenses [33]–[38], optical switches [39], [40], interferometers [41], ring resonators [42], [43] and filters [44], [45]. As the individual optofluidic elements and devices have reached higher performance levels and maturity, reconfigurability on the system level has recently become more desirable. Optofluidic platforms can further be functionalized by the hybrid integration of other microfluidic control platforms, which are capable of multiple functions such as mixing, size filtering and fluidic distribution [46]–[48].

The other advantage optofluidic platforms provide is using the fluidics to carry the substances to be analyzed in the LOC systems, while using the optics to enable non-invasive and highly precise analysis methods. One of the main applications of optofluidics in life sciences is the ability to manipulate the particles by using optical forces. This requires seamless incorporation of the sample fluids into the photonic structures to create very elaborate interactions of the light and target particles in the fluid. Optofluidic particle manipulation and trapping were achieved based on different methods with various applications: off-chip trapping beam [49], [50], evanescent field for trapping [51]–[53], sorting [54]–[57], photonic crystal based trapping [58]–[61], micro-disk resonator based trapping [42], [62]–[64]. One attractive approach for particle manipulation is using liquid-core waveguides to guide both light and liquid in the same channel, to create high levels of reconfigurability and particle-light interaction [65]–[70].

In terms of bioanalysis, there has been a rising interest in point-of-care (POC) devices, where optofluidics have provided successful devices, especially highly functional biosensors. Optofluidics offers advanced miniature diagnostic platforms by combining the compact and rapid processing of fluidic samples while achieving high detection sensitivity of target specimen. For decades, conventional biosensor instrumentation has been relying on bulky components. Relying on bulky components for diagnosis limits the availability of them in remote and resource-limited locations. Specifically, infectious diseases cause a lot of fatalities all around the world, leading to more than 8% of all deaths worldwide [71]. Unfortunately, infectious diseases are intimately

connected to poverty where the lack of treatment and nutrition making the recovery very difficult, even though most of these diseases are treatable. The countries with low income and the higher number of infectious disease cases coincide almost perfectly, where the availability of medical diagnosis and care is limited [72]. This vicious circle is not limited to the low-income countries, it is also affecting the groups all over the world who have a limited access to health-care, such as immigrants and refugees especially in refugee camps [73]. Survival is dependent on rapid diagnosis and early treatment, both of which are difficult to achieve when laboratory support and clinics are scarce [74]. However, it is a challenge to accurately diagnose infectious diseases due to their similar early symptoms, and low natural concentration levels of the pathogens. Current diagnostic tools such as real-time polymerase chain reaction (RT-PCR), amplify the small amounts of target nucleic acids of the pathogens to be able to detect them [75]–[77]. Even though this technique is highly sensitive and specific, it is not ideal for rapid point-of-care detection because they are bulky, expensive and they also require long processing times, advanced clinics and highly trained personnel for operation which makes them further unavailable for resource-limited settings.

Portable, low-cost, simple-to-use rapid diagnosis systems need to be built in order to reach these populations who are in need. Optofluidics addresses all these problems, by providing miniaturized portable devices. Integrating, automating and calibrating multiple functions from sample preparation to detection and interpretation, eliminates the need for advanced laboratories and trained personnel. Using common fabrication procedures, low power consumption, low material and reagent use due to its small size

make them available at a low-cost. Since they have a very high sensitivity, the detection can be done at clinical concentrations without amplification. Depending on the application and the need, versatile approaches have been implemented to create highly sensitive platforms. Biosensors based on the idea of specific binding of a target analyte to a surface are developed by using surface-enhanced Raman scattering (SERS) [78]–[81] and surface plasmon resonance (SPR) [82]–[85]. These methods are sensitive however it is challenging to reach the single biomolecule detection limit due to ineffective transport of target particles to the binding sites, non-specific binding, limited dynamic range. On the other hand, flow based optofluidic biosensors allow for the detection of single biomolecules by light scattering, fluorescence and absorption as they move along a channel. Liquid-core waveguides, by using the same channel for both fluidic transport and optical waveguide, enable high interaction of light and the target biomolecules in a very small volume, which creates very high sensitivity. The single particle fluorescence detection was reached by using liquid-core anti-resonant reflecting optical waveguide (ARROW) platforms to create optical excitation/detection volumes on the order of femtoliters, which will be discussed later in chapter 2 [86], [87]. This approach also allows for the incorporation of very effective detection mechanisms such as fluorescence spectroscopy [88]–[90], Förster resonance energy transfer (FRET) [45], and SERS [78].

Optofluidic biosensors are moving even further toward improved sensitivity, adaptability and compactness, creating innovative tools in rapid diagnosis systems [91]. However, continued improvements in sensitivity remain a major goal as we approach

the ultimate limit of detecting individual bio-particles labeled by single or few fluorophores. Improving the sensitivity of these sensors increases the accuracy of the diagnostic tests, allowing it to be applied to a wide dynamic range of target biomolecules. Integrating off-chip components into these platforms makes them more compact and portable, while reducing their cost. Taking advantage of optofluidics, innovative approaches have been developed to integrate tuning capacity making these platforms more adaptable and customizable for different applications. Furthermore, multiplexing is a key element for a competitive diagnostic test, allowing for extensive screenings and parallel processing. A standard influenza test, for example, simultaneously screens for 8 pathogen types, enabling differential diagnosis of diseases with similar early symptoms [92]. Being able to identify multiple target molecules with high sensitivity improves the capability and function of these optofluidic devices. Exploring even further within the enormous capacity of “the room in the bottom”, tuning functionality is merged with the multiplexing power to provide very competitive optofluidic diagnostic platforms that are highly sensitive, compact, multi-functional and adaptable. In this work, the theory, design, characterization and application of these novel miniature platforms are presented.

This thesis is organized as follows. Chapter 2 presents the background on optofluidic platforms based on liquid-core ARROW; including ARROW theory, fabrication, single molecule detection, device characterization and platform improvements. Chapter 3 introduces an integrated tunable spectral filter based on ARROWs, and the results to show the signal to noise ratio (SNR) enhancement by activating these spectral filters.

Multi-wavelength tuning of the filter is shown by combining different filtering mechanisms. In Chapter 4, the SNR enhancement technique by multi-spot excitation based on Y-splitter waveguides is shown. Signal processing algorithm, platform design, optimization and characterization are discussed. SNR enhancement for detection of influenza viruses is shown and the results are analyzed. Chapter 5 introduces two different platforms with integrated multi-mode interference (MMI) waveguides, introducing high multiplexing capacity into these platforms. Design parameters, characterization and multiplexed detection of influenza viruses are shown with discussion of data analysis methods. Finally, this work will end with conclusions (chapter 6), appendices (chapter 7) and bibliography.

2 Background

2.1 Planar integrated optofluidic platform

Detection of biological particles is very challenging because of their small size. In the case of disease diagnosis, enabling early diagnosis is especially difficult due to the very low concentration levels of the pathogens as well as their small size. There is an immense need for highly sensitive, time and cost effective and easy-to-use detection platform for diagnosis of the bioparticles. Lab-on-a-chip platforms proved to be one of the most effective approaches for bio-sensing by improving the analysis throughput and sensitivity through miniaturization and advanced instrumentation [3]. Integration of multiple functions required for bio-analysis into a single platform, allowed for a cost-effective and easy-to-use tools. Specifically, in terms of analyte detection for clinical diagnostics, these platforms dramatically enhanced the accessibility of diagnostics tools, especially in resource-limited settings. Single-molecule methods are powerful tools to detect bioparticles with low concentrations, probe the complex behavior of biological molecules, and understand dynamics and function of proteins, nucleic acids and their complexes [93]–[100]. These methods require high sensitivity and speed in order to be utilized for disease diagnosis.

Optofluidics is a relatively new field that combines optics and microfluidics, allowing more sensitive, compact devices. These platforms enable the detection of molecules in very small sample volumes [32]. Liquid-core waveguides create high interaction between the liquid and light, by allowing both light and the analyte guide through the micron-scale hollow channels, simultaneously. The majority of waveguides are based

on the principle of total internal reflection (TIR). In order to achieve index guiding, the light inside the waveguide should be reflected from the walls of the cladding layers, confining the power mostly in the waveguide core. TIR can be achieved only if the incident light angle between core and cladding layers, is above the critical angle defined as; $\theta_c = \arcsin(n_{clad} / n_{core})$. To make this possible, the core refractive index should be higher than the cladding refractive index. However, due to the condition, $n_{core} > n_{clad}$, making liquid-core waveguides based on TIR is tricky. Most solid materials have higher refractive index than most of the liquids. There are few different ways to make liquid-core waveguides based on TIR, such as using low index material (Teflon AF), nano-porous cladding material, liquid-liquid core waveguide and slot waveguides. However, all these methods are limited in terms of sensitivity, fabrication challenges and integration [32].

Another approach to make liquid-core waveguiding possible is using interference. Creating periodic structures to reflect the light back into the core from the boundaries, allows us to make liquid-core waveguides possible. Bragg waveguides and photonic crystal waveguides based on periodic cladding structures guide the light based on this interference principle. Antiresonant reflecting optical waveguides (ARROWs) also work based on the interference principle however they do not require the cladding layers to be periodic [32].

Since the ARROWs are fabricated by using common silicon fabrication techniques, and have planar layout, they serve as a highly configurable and integrable fully planar optofluidic structure. To start with, the standard design provides a highly sensitive

single-molecule sensing platform. Later, this platform is improved by reconfiguring the layout and integrating additional optical devices (such as Y-splitters, MMIs, on-chip tunable filters) in order to increase the functionality and sensitivity.

It is important to first understand the basic principles of the standard ARROW platforms, and their fabrication procedure, before moving to the broad capabilities and functionalities that are achieved by modifying this platform.

2.2 Theory of ARROW

ARROWs make guiding possible in a low-index material creating anti-resonance in the cladding layers. In order to trap the light inside of the core, the phases of the reflected light should constructively interfere with each other, inside of the core. Also, to prevent the light to be guiding through the cladding layers, the anti-resonant condition should be satisfied in these layers. In order to understand the basics, Fig. 2.1 represents a simple ARROW structure cross-section in vertical direction, with a core layer with thickness d_c , refractive index n_c ; cladding layers with thicknesses t_i and refractive indices n_i . Light propagates along the z direction with a propagation constant β .

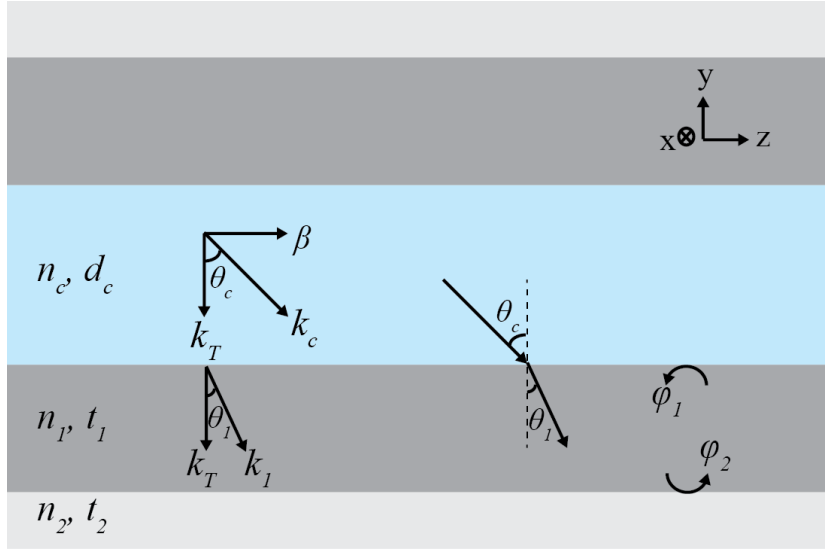


Fig. 2.1 The cross section of ARROW structure, showing the core layer with thickness d_c , refractive index n_c ; cladding layers with thicknesses t_i and refractive indices n_i . Light propagates along the z direction with a propagation constant β .

In order to prevent the transmission to the first cladding layer with a refractive index n_1 and a thickness t_1 , the light waves in this layer should destructively interfere with each other. This means that the total phase shift in this layer should be odd multiples of π . Thus, the anti-resonant condition for this layer in the ARROWs can be written as [101]–[103]:

$$\phi_1 + \phi_2 + 2t_1 k_T = M\pi; M = 1, 3, 5... \quad (2.1)$$

where, ϕ_1, ϕ_2 are the phase shifts due to the reflection from the adjacent layers, t is the thickness of the cladding layer, k_T is the transverse component of the wave vector in y direction and M is an odd integer. Since $n_1 > n_2, n_c$, the total phase shift due to the

reflection from the adjacent layers becomes $\phi_1 + \phi_2 = 2\pi$. The thickness for the i^{th} ARROW layer can be derived as follows:

$$t_i = \frac{M\pi}{2k_T} \quad (2.2)$$

Additionally, the mode condition for the fundamental mode in the core is as follows:

$$k_T d_c = \pi \quad (2.3)$$

Snell's law, and geometrical equations from the structure are as follows:

$$\begin{aligned} k_T &= k_i \cos \theta_i = k_c \cos \theta_c \\ n_i \sin \theta_i &= n_c \sin \theta_c \end{aligned} \quad (2.4)$$

Combining equations (2.2), (2.3) and (2.4) the thickness of the ARROW cladding layer with a design wavelength of λ_D can be rewritten as [101], [102]:

$$t_i = \frac{M\lambda_D}{4n_i \sqrt{1 - \frac{n_c^2}{n_i^2} + \frac{\lambda_D^2}{4n_i^2 d_c^2}}} \quad (2.5)$$

When each cladding layer is designed to meet the anti-resonant condition, the transmission into these layers would be prevented, ensuring the high confinement of the light in the core.

In the actual structures we built, the values are; $d_c=5\mu\text{m}$, $n_c=1.33$ (H_2O), $n_i=1.47$ (SiO_2) or $n_i=2.107$ (Ta_2O_5) and design wavelength $\lambda_D=633\text{nm}$. Using the equation (2.5), we can find that $t_i=251\text{nm}$ for SiO_2 and $t_i=97\text{nm}$ for Ta_2O_5 , and all the ARROW layers in our structures are designed based on this equation. In these structures, since the core

thickness is bigger and the index contrast high, $n_1^2 - n_c^2 \gg \lambda^2 / 4d_c$, equation (2.5) can be simplified to;

$$t_i \approx \frac{M \lambda_D}{4\sqrt{n_i^2 - n_c^2}} \quad (2.6)$$

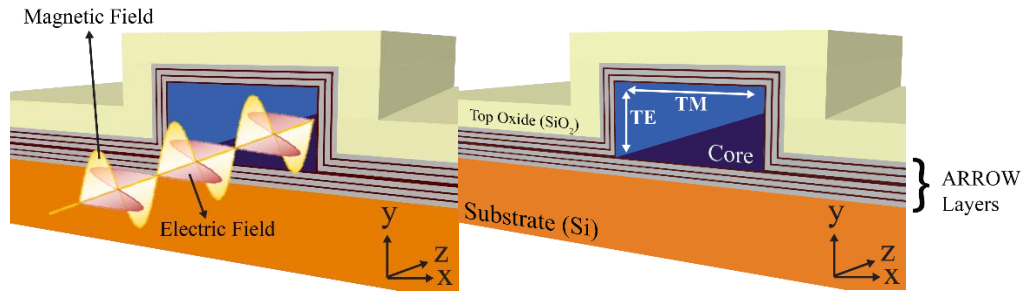


Fig. 2.2 ARROW cross-section showing the field directions for x-polarized light. TE loss depends on the structure in vertical direction, and the TM loss depends on the structure in horizontal direction.

Due to its leaky nature, it is important to understand the loss characteristics of ARROW structures. In order to decrease the propagation losses, the number of ARROW layers, N_L , can be increased. However, the effect of layers on the waveguide loss decreases as we increase N_L , so they need to be optimized. ARROWs have 2 dimensions that affect the loss profile, vertical and horizontal. For x-polarized light where the electric field vector is on the x axis, the transverse electric (TE) component of the loss is affected by the vertical structure and transverse magnetic (TM) component is affected by the horizontal structure, where both components are added to find the total loss. (Fig. 2.2)

For y-polarized light, the opposite scheme holds true. The minimum loss coefficients for N_L number of anti-resonant layers, for TE and TM modes are given as follows [101], [102]:

$$\alpha_{TE,\min} = \left(\frac{n_2^2 - n_c^2}{n_1^2 - n_c^2} \right)^{N_L/2} \alpha_0$$

$$\alpha_{TM,\min} = \left(\frac{n_1}{n_2} \right)^{2N_L} \frac{n_1^2}{n_c^2} \alpha_{TE,\min} \quad (2.7)$$

$$\alpha_0 = \frac{\lambda_D^2 (m+1)^2}{n_c d_c^3 \sqrt{n_1^2 - n_c^2}}, m = 0, 1, 2, \dots$$

where, m is the mode order and $n_1 > n_2 > n_c$. If we calculate the losses for the fabricated structure with $d_c=5\mu\text{m}$, $n_c=1.33$ (H_2O), $n_1=2.1$ (Ta_2O_5), $n_2=1.47$ (SiO_2), $\lambda_D=633\text{nm}$, $N_L=6$ and $m=0$, then the losses would be $\alpha_{TE,\min} = 0.048\text{cm}^{-1}$ and $\alpha_{TM,\min} = 8.7\text{cm}^{-1}$ which shows that TM loss is a lot more dramatic. The lowest loss measured experimentally for a rectangular ARROW with the top layers is $\alpha \approx 0.3\text{cm}^{-1}$ [104].

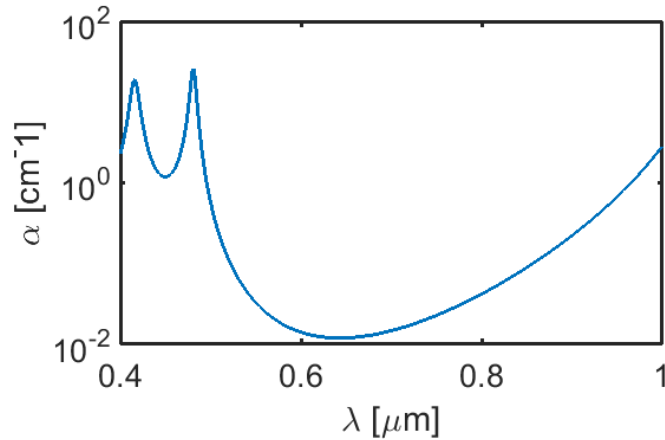


Fig. 2.3 Calculated TE loss dependence on wavelength, for an x-polarized beam. The design wavelength is $\lambda_D=633\text{nm}$.

ARROW waveguides can be designed and optimized for different wavelengths. For our experiments, wavelengths ranging from 488nm to 750nm are used. Because 633nm is the main characterization wavelength and it is in the middle of the range we are using, it is chosen as the design wavelength for our ARROW devices. Fig. 2.3 shows the dependence of ARROW TE loss on wavelength, for x-polarized beam for $\lambda_D=633\text{nm}$.

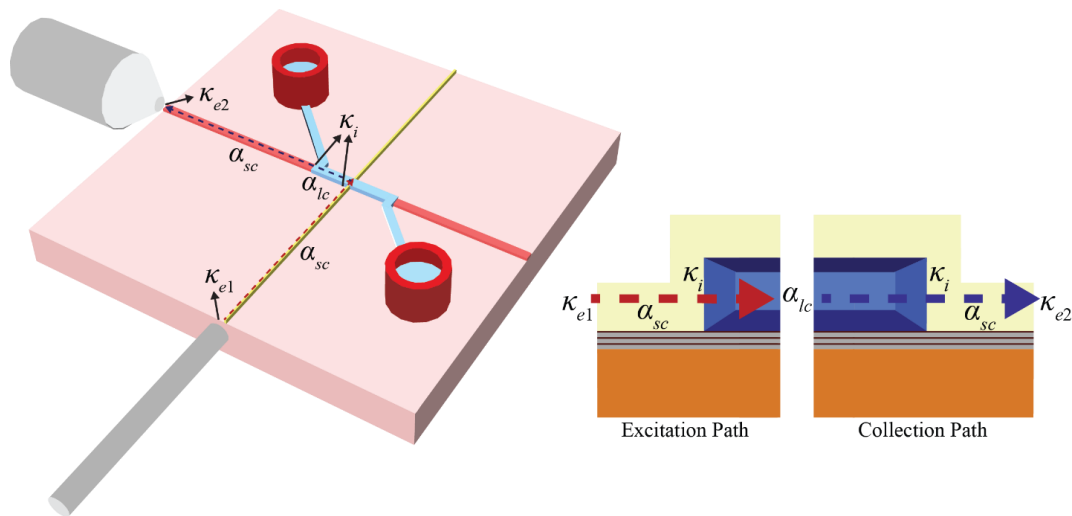


Fig. 2.4 Schematic of a standard ARROW chip with single top oxide layer and the cross-section. The red dashed arrow shows the excitation path, and the blue one shows the collection path for a standard fluorescence experiment. Key points for the coupling efficiency are labeled.

In the optofluidic platform we developed, in addition to the propagation loss, there are other losses contributing to the functionality of the device. These are mainly interface

losses and coupling losses. Fig. 2.4 shows a schematic of a standard ARROW chip with a single top oxide layer. Excitation light is coupled from fiber to the solid-core input waveguide (yellow) which then goes through the solid-core (SC)-liquid core (LC) waveguide (blue) interface to reach the excitation region (red path). The signal generated inside the liquid-core waveguide is collected through another SC-LC interface, collection solid-core waveguide (red) and an objective, perpendicular to the excitation (blue path). The transmission efficiency from the interfaces in between SC-LC waveguides (κ_i), coupling efficiency from fiber to SC waveguide (κ_{e1}), and coupling efficiency from SC waveguide to collection objective (κ_{e2}) should all be considered to optimize the sensing. The overall throughput can be represented as follows [105]:

$$T = \kappa_{e1} e^{-\alpha_{sc} l_{sc}} \kappa_i^2 e^{-\alpha_{lc} l_{lc}} \kappa_{e2} \quad (2.8)$$

where α_{sc} is the solid core waveguide loss, l_{sc} is the path length, α_{lc} is the liquid core waveguide loss, and l_{lc} is the path length. Edge coupling efficiencies κ_{e1} depend on the mode match of the fiber to the input solid-core waveguide. The dimensions of the solid-core waveguide are designed to achieve maximum transmission of light from fiber (Newport F-SV) to the device, however the loss here is quite dominant due to the mode mismatch, and facet defects. The collection efficiency, κ_{e2} is very good as we are able to capture almost all of the light through an objective. Typical numbers for the total edge coupling efficiency is $\kappa_{e1} \times \kappa_{e2} \approx 0.55$ [105].

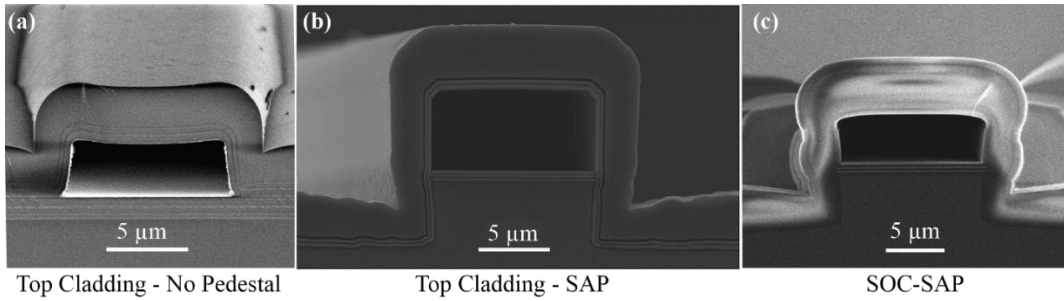


Fig. 2.5 Cross-section of three different types of ARROW structures. (a) Earlier version of ARROW with top cladding layers and no self-aligning pedestal (SAP). Tunable filter platforms are based on this design. (b) Improved ARROW with SAP and top cladding layers. [106] (c) Preferred version of ARROW design. It has a single-over coating (SOC) and SAP. MMI and Y-splitter platforms are based on this design.

The other important parameter for the overall chip quality is the interface between the solid-core waveguide and the liquid-core waveguide. When light travels from SC to LC, going through the ARROW layers, fabrication imperfections such as the crevice formed at the intersection [10] and the roughness of the walls decrease the interface coupling efficiency dramatically. Significant optimizations have been made to the ARROW layout in order to maximize κ_i . First of all, the top layers are replaced with single over-coating (SOC) of oxide to prevent the losses coming from the fluctuations of the ARROW layers on the sides. (Fig. 2.5c) Even though the ARROW loss increased to $\alpha_{lc} \approx 2\text{-}5\text{cm}^{-1}$ [107] due to the lack of top layers, this improved the κ_i from 0.35 to 0.79, and overall throughput by 1.7 times [105]. Another improvement has been made by creating a self-aligned pedestal (SAP) under the core (Fig. 2.5b-c), to create air layer

termination on the sides, improving α_{lc} . [106], [108] Top-oxide thickness also plays a crucial role on the mode-matching at this interface, and it is optimized by making it thicker to compensate the fabrication non-idealities that contributes to the loss. This also resulted in significant improvements of the interface and overall coupling efficiencies [107].

Except for the Tunable Filter design in Chapter 3, all the optofluidic platforms in this research have a self-aligning pedestal, single layer of top oxide and its thickness is optimized to achieve maximum transmission.

2.3 Fabrication of ARROWs

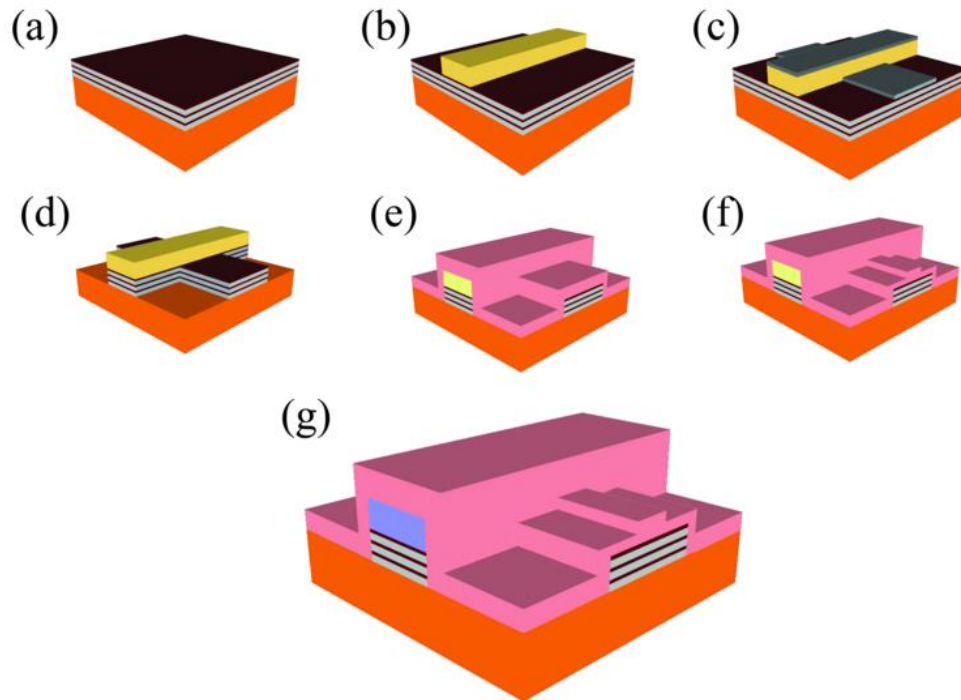


Fig. 2.6 Fabrication process of SOC-SAP ARROW. (a) 6 ARROW layers are deposited on silicon wafer. (b) Sacrificial core is created by using SU-8, on ARROW

layers. (c) Thin nickel layer is created to protect the solid-core and hollow core waveguides, by using lift-off process. (d) Self aligned pedestals are created by etching away the ARROW layers on the rest of the wafer, by reactive-ion etching (RIE). Nickel layer is removed. (e) A thick (6 μm) SiO₂ layer is deposited on top of the entire wafer, to create the top ARROW layer, and the solid-core waveguides. (f) Solid-core waveguides are formed by etching the SiO₂ top layer, by RIE. (g) Sacrificial core is removed by using Piranha etching to form the hollow-core waveguide.

ARROW fabrication is based on standard micro-fabrication techniques, which allows cost-effective and planar construction of the platform. The liquid-core formation is achieved by creating a sacrificial core, which is surrounded by the ARROW layers. As mentioned in the previous section, a lot of improvements have been made on ARROW structure to achieve best transmission properties. In addition to single-over coating (SOC) top oxide layer [105], creating the liquid-core on top of the self-aligning pedestal (SAP) [106], [108]; optimizations have been made on the materials used for the layers as well. SiN, which was originally used for ARROW layers is replaced with Ta₂O₅ which reduced the photoluminescence background, leading to higher signal-to-noise ratio in the detected signal [109]. Additionally, silicate spin-on-glass is used to coat PECVD SiO₂ waveguides in order to smooth out surface topology [110] and buried channel waveguides are implemented to protect the waveguide from water absorption [111].

The fabrication procedure for the SOC-SAP optofluidic chip is shown in Fig. 2.6. First of all, 6 ARROW layers were deposited on a silicon wafer. SiO₂ (refractive index \approx

1.46) and Ta₂O₅ refractive index ≈ 2.045) are grown in an alternating fashion with the thicknesses 265/102 nm respectively, starting with SiO₂. ~5 μ m thick layer of SU-8 is deposited and patterned to create sacrificial core with a 12 μ m width. In order to create a self-aligning pedestal for all the waveguide structures, waveguides are protected by nickel over coating, using standard lift-off step. The unprotected area surrounding the waveguides is etched anisotropically by using deep reactive-ion etching technique down to the silicon substrate, and then the Ni layer is removed. A 6 μ m thick SiO₂ layer is deposited on the entire wafer, using plasma enhanced chemical vapor deposition (PECVD). Then the solid-core ridge waveguides are patterned with different widths based on the function, by using reactive-ion etching [112]. The width of the excitation waveguide is designed as 4 μ m to create single-mode waveguide, and varies among different wafers due to the fabrication intolerances. The collection solid-core is designed to have 12 μ m width to achieve best collection efficiency from liquid-core waveguide to the collection objective. The multi-mode interference solid-core is fabricated with widths of 50 μ m, 75 μ m and 100 μ m, which is discussed in Chapter 5 in more detail. Finally, the SU-8 sacrificial core is removed by using piranha etching, forming the hollow-core waveguide [113].

Recently, it has been also shown that, applying thermal annealing process on these platforms improves the transmission qualities of the chip, by eliminating the effects of the defects and refractive index change by water absorption during fabrication [114].

The height of the solid-core ridge waveguides also plays an important role in the mode profiles, where a through-etched waveguides are fabricated to achieve better

performance. Through-etched waveguides are obtained by etching the solid-cores down to the ARROW layers, leaving no SiO₂ on the sides of the core.

On the other hand, tunable filter waveguides discussed in Chapter 3, are fabricated using previous approach, with top cladding layers (TC), without the self-aligning pedestal and using SiN instead of the Ta₂O₅ [44].

2.4 Fluorescence detection on ARROWs

In the early stages of fluorescence detection on ARROW chips, efficient detection of Alexa 647 dye in ethylene glycol solution was achieved with as few as 490 molecules. [115] This was done by using only a liquid-core channel, and excitation and collection were done on the same axis. In the next stage of the fluorescence detection, the orthogonal layout, where excitation waveguides are perpendicular to the collection waveguides, was used. This allowed for more efficient and sensitive single molecule detection by decreasing the excitation volume down to sub-picoliter level. (see Fig. 2.7a) On this detection scheme, dye with a 500pM concentration, which corresponds to 40 molecules per excitation volume was successfully detected [86], [104]. Shortly after these results, detection of single liposomes on a fully planar standard ARROW chip was successfully achieved [87].

ARROW chips are powerful devices also by allowing high sensitivity fluorescence correlation spectroscopy (FCS) and surface enhanced Raman scattering (SERS) measurements. FCS is a powerful method by enabling high sensitivity measurements by detecting the fluctuations in the fluorescence signal. Advances on the ARROW

design and incorporating FCS into the integrated optical and fluidic setting led to successful detection of Q β bacteriophages, with single virus sensitivity [88], [89]. Furthermore, additional analysis methods such as fluorescence cross correlation spectroscopy (FCCS) in combination with fluorescence resonance energy transfer (FRET), allowed us to detect the denaturation process of double-stranded DNA at nanomolar concentration [116]. Additionally, the ARROW platform was utilized for SERS detection, allowing for high mode intensities along microfluidic channels containing molecules optimized for SERS. This enabled detection of Rhodamine 6G molecules with down to 30nM concentration [78].

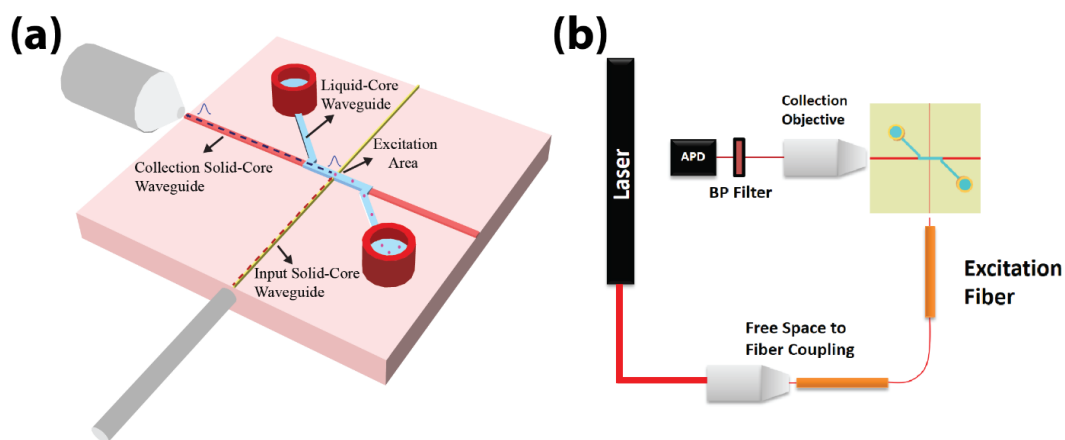


Fig. 2.7 (a) Schematic of basic fluorescent detection on a standard ARROW chip with an orthogonal layout. Red dotted line represents the excitation path, and the blue dotted line represents the collection path for the fluorescence signal. (b) Schematic of a simple experiment setup.

The basic experimental setup implemented for single molecule fluorescence detection can be seen in Fig. 2.7b. Free space laser light is coupled into a single-mode fiber

through an objective. Depending on the experiment, different laser sources, and combination of them are used. More information on the detailed setup and how they are combined can be found in Appendix A.1. Single-mode fiber is then butt-coupled into the single-mode excitation input waveguide. The optimum coupling is achieved by using precision translation stages. This alignment step is very crucial in terms of introducing the optimum mode into the excitation region, increasing the detection sensitivity and improving the functionality. Fluorescently labeled target molecules passing through the excitation volume are subjected to the excitation light and thus each target produces fluorescent signals. (see Fig. 2.7a) These signals are captured by the liquid-core waveguide orthogonal to the excitation axis, transmitted into the collection solid-core waveguides. The signals are collected from the collection waveguide by an objective lens (NA:0.85, 60X) and pass through a spectral filter (band pass/notch). This filter is chosen such that it blocks the excitation wavelength and lets the fluorescent signal pass through.

After being coupled into a multi-mode fiber, fluorescent signals are delivered into avalanche photodiode single photon counting module (SPCM-AQR-14-FC, Excelitas). The photons are recorded using a time-correlated single photon counting PCI-board (Time Harp 200, PRT 400 router; Picoquant, Germany) and commercial software (Timeharp, Picoquant, Germany) in time-tagged time-resolved (TTTR) collection mode.

2.4.1 Chip characterization

The first step for characterization of a new wafer is doing visual inspection. This step involves checking the chip under the microscope, and looking for defects that could be detectable from top view. This step is very crucial especially determining broken liquid-cores, facets and broken devices. Fig. 2.8 shows some of the common defects that can be determined under the microscope. It is important to note that, regardless of some of the defects, a chip can still be functioning depending on where the defect is located and the severity of the defect.

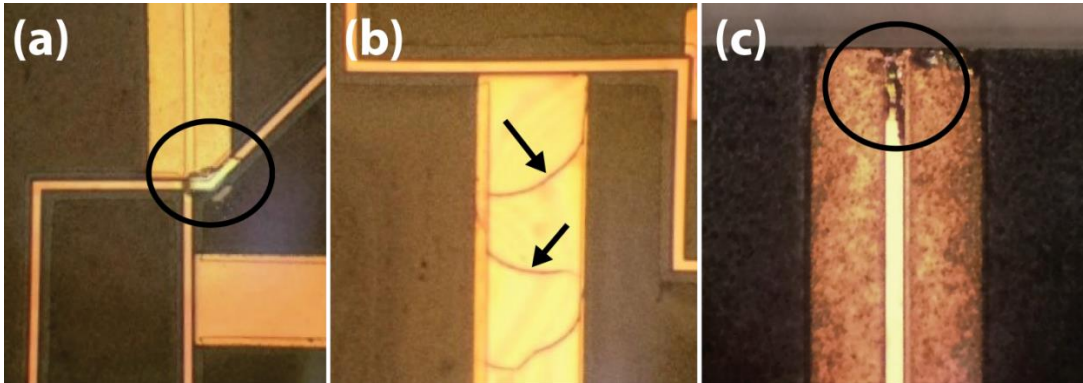


Fig. 2.8 Defects found during visual inspection. (a) Broken liquid core (b) Broken solid core MMI (c) Broken facet

Another important parameter for the chip quality is the fluidic properties of the channels. If the final etching process of the channel creates a hydrophilic surface, and the channel surface is free of defects, then the analyte could be delivered with no complications. This is also important to provide sufficient flow for the analyte and prevents clogging of the channels. Determining if the liquid-core waveguides are filled

can be challenging, and the visual cues vary among the wafers. Refer to the Appendix B for further details.

One of the most important steps of characterization of the chips is determining transmission efficiencies and mode profiles. Transmission efficiency on the excitation path and collection path directly affects the signal to noise ratio of the detected fluorescence from the targets. The sensitivity of the device increases as the transmission increases, which enables the detection of very small molecules generating very few photons. The transmission efficiency in solid core is measured by using an excitation fiber, and the transmitted light is measured with a power-meter after the scattered light is removed by an iris.

The location of the mode also affects the signal to noise ratio and the transmission efficiency directly. Fig. 2.9a shows the fundamental mode in an excitation solid-core waveguide, which is located at the center of the ridge waveguide. If the mode profile in the excitation waveguide is not in the center of the channel, the excitation energy is not being delivered to the liquid-core channel efficiently which reduces the fluorescent signal that is generated. One of the main issues with mode profiles is that the location of the center of the mode can be towards the upper part of the solid-core ridge waveguide, which only excites the upper part of the liquid-core waveguide (Fig. 2.9b). This is due to the altered index profile of the ridge waveguide, during the fabrication process [114]. Another important aspect of the mode profile is the single mode property. The excitation waveguides are designed such that it only supports fundamental mode in horizontal axis. However, due to fabrication abnormalities of the

waveguide dimensions, (eg. higher width of the waveguide), the excitation mode profile could become multi-mode. This especially becomes a problem for the MMI excitation patterns.

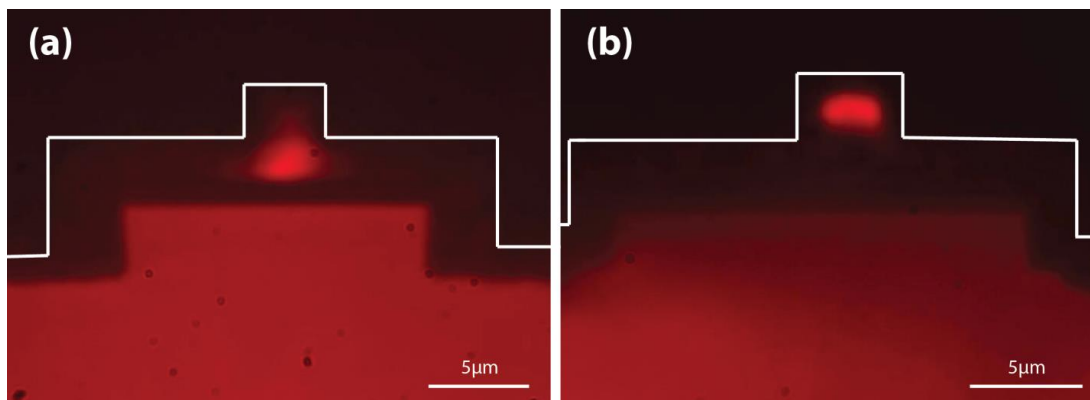


Fig. 2.9 The mode profiles of solid-core excitation waveguides. (a) Fundamental mode guiding on the center of the ridge waveguide. (b) Fundamental mode guiding on the upper region of the ridge waveguide.

The most effective and accurate method for characterization is running the experiment with test analytes. A standard characterization test had to be created for an accurate analysis of the wafers. 22nM Cy@5 dye is one of the standard test analytes used to measure the fluorescence signal to noise ratio. By using the same analyte and same wavelength (633nm) for testing all the chips and different wafers, accurate comparison among them is achieved. Additionally, characterization for single molecule detection is carried out by using fluorescent polystyrene microspheres. Since the actual target molecules are in the order of 100nm, similar size fluorescent polystyrene microspheres with similar concentrations are used for the tests. The microspheres are obtained from Invitrogen™, and diluted down to the relevant concentrations for single molecule

detection (10^6 particles/ml). The 2 main colors of fluorescent microspheres (Yellow-green (505/515), Crimson (625/645)) are used to characterize the transmission properties in 2 different wavelengths (488nm, 633nm).

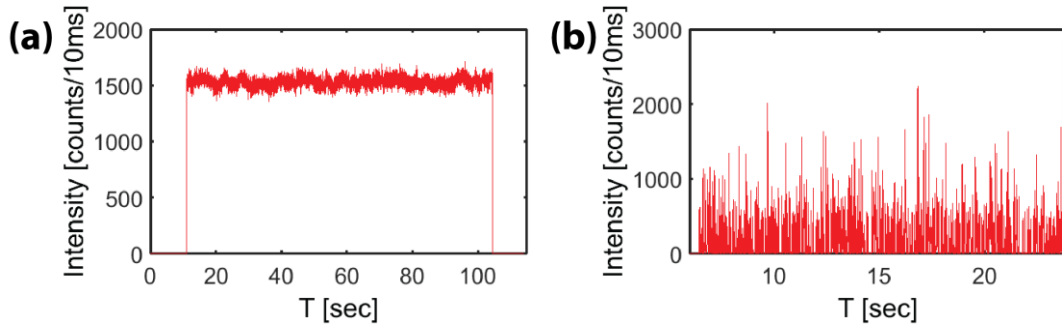


Fig. 2.10 (a) The fluorescence signal collected from 22nM Cy@5 dye at the 633nm excitation wavelength. (b) The fluorescence signal collected from 200nm Invitrogen@ Crimson Fluospheres.

Fig. 2.10 shows the characterization with fluorescent dye and fluorescent polystyrene microspheres for one of the chips from high quality wafers (MA36). Fig. 2.10a shows the fluorescent signal collected from the 22nM Cy@5 dye at the 633nm excitation wavelength. The average signal to noise ratio is calculated by the ratio of average signal (S) to background standard deviation (σ), S/σ . For example, the calculated value for signal to noise ratio in this specific measurement is 2185, with $S \sim 1540$ and $\sigma = 0.68$ counts/10ms. The plot is also normalized based on the input power level and collection efficiency which ensures the direct comparison with the other samples and wafers. Fig. 2.10b shows the fluorescent signals generated by the 200nm Invitrogen@ Crimson Fluospheres at a 10^6 particles/ml concentration. The average signal to noise ratio is calculated as 240 for the fluorescent microsphere test. Each spike represents an

individual microsphere. In addition to the power normalization, the comparison needs to be made at the same binning time and with same conditions in terms of the velocity of the particles.

2.4.2 Post-fabrication improvements on devices

It was shown that the improvements in the chip design, and fabrication process created devices with higher transmission and sensitivity. As discussed in the previous section, self-aligned pedestals [106], single-over-coating SiO₂ layer [105] and adjustments in the thicknesses of this layer [107] dramatically increased the sensing capabilities of these devices. Another very important aspect to improve the transmission and the functionality of the device is achieved through post-fabrication steps, and troubleshooting the problems that occurs during the experiments.

One of the most important factors that changes transmission dramatically is the shift in the refractive index of the SiO₂ layer during the core-etching process of fabrication. In order to etch the sacrificial SU-8 layer, the wafer is kept in the piranha solution (H₂SO₄:H₂O₂) approximately 120h in 90°C. During this process, semi-porous SiO₂ layer absorbs some of the liquid which shifts up the refractive index of this layer [114]. Due to the higher refractive index on top of the waveguide, the mode profile shifts at the edge of the waveguide, creating lower transmission through the solid-core liquid-core interface, and delivers a reduced excitation power to the targets. This problem can be addressed after the fabrication by using a low temperature annealing step. The thermal annealing step is carried out by using an annealing furnace which ramps up to 300°C in 4h, maintain it for 8h, and ramps down in 4h to a room temperature [114]. This step

ensures the release of the absorbed liquid from the SiO₂ layer, and shifts the mode down to the center of the ridge waveguide while increasing the transmission. It is important to note that any contact with water or etching liquid reverses the process by leading the SiO₂ layer to absorb the liquid. The thermal annealing step has to be repeated to increase the transmission level if such contact occurs.

Although the thermal annealing step is a great way to increase the sensitivity of the device, one important drawback, specifically for the MMI waveguides is observed. Most of the time, the MMI patterns significantly worsen after the thermal annealing step, most likely due to the non-uniformities in the refractive index of the waveguide formed during the process. This unfortunately limits the use of this method for MMI based designs.

During the experiments, one of the main problems is the clogging of the liquid-core channels. This occurs due to the particles binding to the walls of the channel, and aggregating which prevents the analyte from flowing. This can be prevented to a certain extent by using Bovine Serum Albumin or Tween® 20 in the solution. Using a lower concentration of target molecules also decreases the chance for clogging. However, if it occurs, the particles need to be removed using certain procedures. The main procedure for cleaning the channel would be washing the channel with water and IPA, and then acetone if those do not solve the problem. Another solution is to submerge the chip into hot water while applying negative pressure on one of the inlets. Although this method can be effective, it is important to note that the submerging into hot water reverses the thermal annealing step and may change the refractive index and the transmission properties of the waveguides [114]. On the other hand, using a Nano-

Strip® (stabilized H₂SO₄:H₂O₂) solution is the most effective method to remove the bound particles from the walls of the liquid-core waveguide. For this procedure, the chip needs to be submerged into 50°C Nano-Strip® solution for couple hours which also reverses the effects of thermal annealing.

The regular procedure for cleaning the surface of the chips is to gently wash them with acetone-IPA-water-IPA by squirt bottles, in this order. The washing cycle needs to be completed with IPA in order to prevent water absorption of SiO₂ layer and the excess liquid is blow-dried.

After fluorescence experiments, even if the channel is not clogged, the excess dye needs to be cleaned to prevent the next measurements to have higher background. In the cases where the channel is not completely clean, bleaching the channel by using a sodium hypochlorite (household bleach) solution solves the problem. However, this process needs to be done carefully to prevent clogging of the channel by salt crystals formed by the solution.

3 Tunable Spectral Filters based on ARROW

Fluorescence is one of the most powerful methods used for biomedical analysis and molecular sensing, allowing for very specific and sensitive labeling technology [117]. Fluorescence detection systems require high signal to noise ratio, especially when the target is small particles, which is the case for bio-particles such as nucleic acids. There are many parameters that affect the signal to noise ratio in a fluorescence detection system: quantum yield of fluorophores, labeling efficiency, excitation and collection efficiency of the setup, efficient filtering and the sensitivity of the photon counting module. A major problem that affects the sensitivity in fluorescence measurements is interference due to scattered light, photoluminescence, or sample impurities [118]. One of the key points for addressing these problems is developing efficient and tailorable filtering systems to eliminate the effects of these factors. In this chapter, an integrated tailorable filtering device based on ARROW technology is presented creating a high precision, customizable, and low-cost on chip filtering for fluorescence detection.

The fluorescence emission spectrum typically occurs at a higher wavelength/lower energy than the absorption spectrum of the material, a phenomenon known as Stokes shift [118]. Fig. 3.1 shows typical fluorescence absorption and emission spectra of a commonly used fluorescent dye, Alexa Fluor® 633. The emission spectrum of fluorescent dyes is also typically independent from the excitation wavelength, which allows for a wide selection of excitation wavelengths within the absorption spectrum. Ideally, the excitation wavelength should be close to the peak of the absorption spectrum to create higher emitted signal. For a basic fluorescence measurement, in

order to increase the signal to noise ratio, the excitation wavelength has to be sufficiently eliminated from the signal while most of the emission spectrum has to be efficiently collected. Some of the applications such as detection methods based on Förster resonance energy transfer (FRET), require more complex selective transmission spectra, by demanding the elimination of multiple spectral bands while transmitting other bands [45]. There are many different methods to achieve selective transmission.

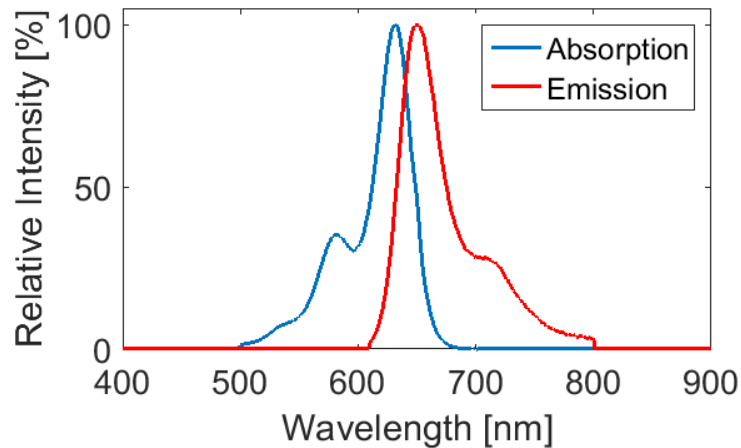


Fig. 3.1 The absorption and emission spectra of Alexa Fluor® 633. (data retrieved from: [119])

One of the most common methods is to use off-chip optical thin-film filters [120]. However, this adds extra costs and bulky components to the system, compromising the lab-on-a-chip approach of the device. This method is also limited in terms of tailorability, requiring different filter sets for new applications and new fluorescent dyes. Towards highly sensitive and fully self-contained lab-on-chip systems, integration of spectral filters is essential.

There are few different integrated filtering methods for fluorescence spectroscopy and detection. Some of the most common integrated filters are based on interference, such as quarter wavelength filters, DBRs [121]. These filters work on the principle of rejection of certain wavelengths from periodically structured layers with a certain thickness. Based on the refractive index and the thickness of these layers, any spectral absorption can be achieved [122]–[124]. However, since the quality of the layers determines the spectrum, they need to be fabricated very precisely, which is expensive and hard to achieve. Additionally, these structures cannot be tuned to different wavelengths and they do not allow for rejection of multiple spectral bands, making them only useful for limited amount of applications. There are a few tunable interference based integrated filters created by using tunable porous silicon, but they are not very feasible for planar integrated devices [125], [126].

Another very common approach for integrated optical filtering for fluorescence detection is using the absorption properties of materials [127]–[129]. Absorption filters are based on the materials with wavelength dependent absorption coefficients. The efficiency of the filter is determined by the Beer-Lambert Law, $I = I_0 e^{-\alpha x}$, where I is the intensity of the light after the filter, I_0 the intensity of the incident light, α the absorption coefficient, and x the filter length [121]. Based on their working principle, there are two types of absorption filters: semiconductors [130], [131] and chromophores [132]. Semiconductor materials have bandgaps which absorb higher energy photons but pass lower energy photons, acting as a long-pass spectral filter. On the other hand, chromophores are molecules which absorbs certain visible frequencies,

acting as spectral filter as well. The main disadvantage of these methods is that the applications are limited by the material availability, by requiring specific materials for specific spectral bands [121]. Since they are material specific, once the device is fabricated, it does not allow for any tuning of the spectral response.

On the other hand, on-chip spectral filtering based on ARROW technology allows for high precision, customizable, and low-cost filtering [32]. They only require a few dielectric layers to implement the filter on planar optofluidic platforms. The basic working principle is based on the interference that is created by the ARROW layers as it was discussed in Chapter 2. In order to create a spectral filter, the inherent spectral property of ARROW layers is tailored to achieve high loss propagation for the wavelengths that need to be rejected. The idea is to create a resonant condition for the excitation wavelength, and an anti-resonant condition for emission wavelength, which will be discussed in detail in the next section. There are multiple approaches that have been used to achieve on-chip ARROW fluorescence filtering.

The first approach was to create the ARROW filter layers only at the collection solid-core waveguide (see Fig. 2.7a) [133]. This way, the excitation laser would reach the detection area, and both fluorescent emission and scattered excitation light would be delivered to the collection solid-core waveguide. Since the layers of the collection solid-core waveguide are designed to create high loss guiding for excitation wavelength but low-loss guiding for the fluorescent emission wavelength, the excitation light is successfully filtered out before it reaches to the detector. However, since this layout requires deposition of different ARROW layers on different parts of the platform, a

more complex fabrication procedure is necessary. Creation of selectively defined regions is achieved by a lift-off method using a combination of SU-8 and PMGI (Polymethylglutarimide) [133]. With this method, a notch filter with a rejection of ~2 dB/mm is achieved over long section of solid-core filter ARROW at 632.8nm [133]. Although this was a great approach to add the on-chip filter capability to the ARROW detection platforms, the fabrication complexity and the need for long collection waveguides to achieve higher rejection ratios make it less desirable for our applications. Alternatively, a liquid-core notch filter is designed and implemented on the ARROW platform [45]. (see Fig. 3.2b) Instead of creating different layers in the solid-core collection waveguide, the ARROW layers are designed to reject the excitation light at the liquid-core part of the device, while still transmitting the excitation and emission lights at the solid-core waveguide sections. Eliminating the need for creating different ARROW layers for different parts of the platform simplifies the fabrication process dramatically. The ARROW layer thicknesses are designed to filter out the excitation light, while transmitting the emitted fluorescent light, this time by using the liquid-core index profile. This design allowed for an extinction of 37 dB, a narrow rejection band of 2.5 nm and a free spectral range of 76 nm using specifically designed dielectric layers [45].

FRET is one of the most common methods to monitor molecular interactions by detecting the energy transfer between FRET pairs (donors and acceptors) [118]. In order to achieve higher sensitivity, the FRET filters need to be designed to reject the excitation wavelength, and transmit both the donor and the acceptor wavelengths.

Because of the high design capacity, the liquid-core ARROW filter is successfully tailored as a FRET filter, filtering out $\lambda_{\text{ex}} = 532$ nm, and passing $\lambda_{\text{d}} = 570$ nm and $\lambda_{\text{a}} = 690$ nm, and demonstrated the FRET detection using doubly labeled oligonucleotides [45].

ARROWs have been shown to have a very sensitive spectral dependence as a function of the layer thicknesses. One of the main challenges of implementing these devices is to be able to precisely fabricate the designed thicknesses. Even a very small deviation in the thickness of the fabricated layer would shift the notch filter wavelength dramatically. As an example, taking the same device dimensions presented in Chapter 2.2, $d_c=5\mu\text{m}$, $n_c=1.33$ (H_2O), $n_i=1.47$ (SiO_2) and $t_i=251\text{nm}$, and using the equation (2.6), 1% ($\sim 2.5\text{nm}$) deviation in single ARROW layer thickness would cause 6nm shift in the wavelength. This clearly presents a big disadvantage for using this approach, making it very unreliable for applications with definite wavelengths.

On the other hand, ARROWs also have a very sensitive spectral dependence as a function of the core index. This in fact can be used for our advantage and the spectral response of the notch filter can be tuned by modifying the index of the liquid that is used in the liquid-core channel. Even though this can be used to compensate the fabrication deviations, it introduces new complications to the platform. The functionality of the device remains limited because the analyte liquid dictates the core index and thus fixes the spectral transmission of the channel, thereby eliminating one of the key benefits of optofluidics-dynamic reconfiguration. In order to overcome these limitations, a dual-core optofluidic chip is designed and implemented for independent

particle detection and fluidically tunable spectral filtering. (see Fig. 3.2c) In this chapter, first, the theory and calculations of the ARROW filter design is explained. Then, device characterization, length dependence and index tuning of ARROW filter are presented. The design and the strength of the dual-core layout is presented and finally, using this chip geometry, improved fluorescence particle detection as well as novel approaches to reconfigurable spectral filtering are demonstrated.

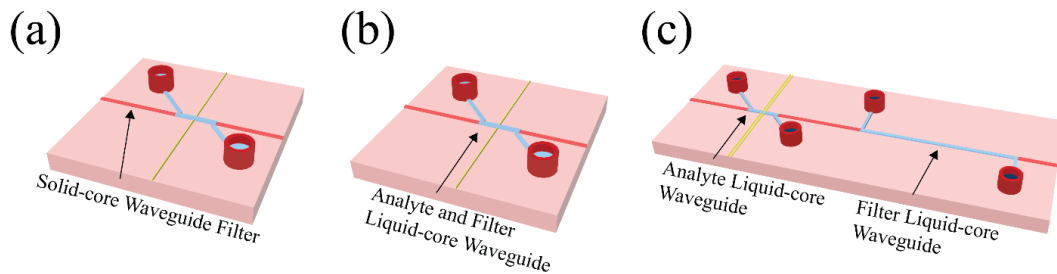


Fig. 3.2 The three generations of integrated ARROW filters. (a) Collection solid-core waveguide with ARROW filter layers. [133] (b) Single liquid-core ARROW filter. [45] (c) Dual liquid-core ARROW filter. [44]

3.1 Spectral ARROW filter

The working principle of the ARROW filter is based on the fundamentals of the anti-resonant and resonant ARROW thickness condition. As discussed in Chapter 2, the spectral response of an ARROW can be determined by choosing specific dielectric layers. The thickness of these cladding layers is chosen to result in high reflection (anti-resonance; guiding) or high transmission (resonance; loss) at a desired wavelength. This can be expressed mathematically by the ARROW thickness condition; where the thickness of the i^{th} cladding layer is defined as:

$$t_i \approx \frac{M \lambda_D}{4\sqrt{n_i^2 - n_c^2}} \quad (3.1)$$

where n_i is the cladding layer refractive index, λ_D is a design wavelength, n_c is the liquid-core refractive index, and M is the order of the interference effect. Even values of M result in high loss, while odd M values produce efficient guiding. In order to create a high-loss for a certain wavelength, i.e. introducing a notch filter in the liquid-core waveguide, an even M for one of the cladding layers is chosen. This ensures the high-loss profile for the design wavelength in the liquid-core waveguide.

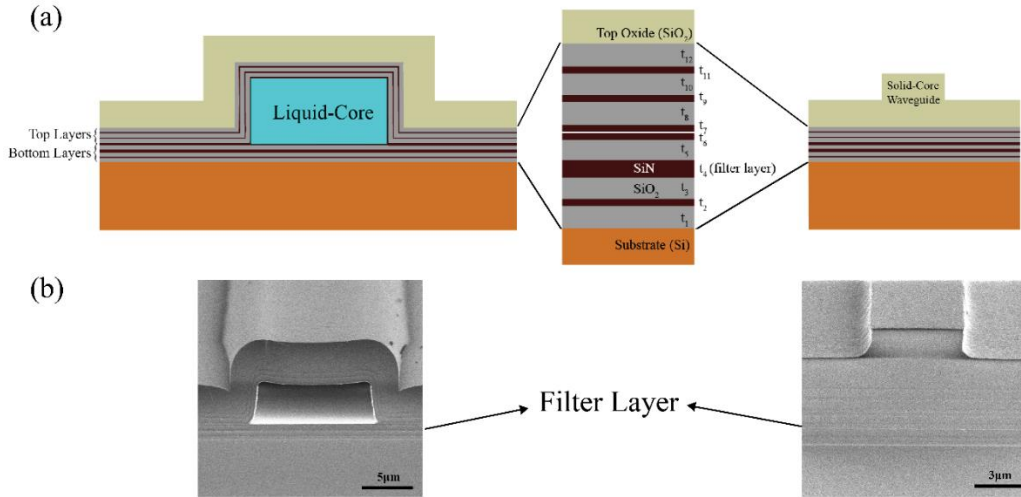


Fig. 3.3 (a) Schematics of the cross-sections of liquid- and solid-core waveguides, showing the ARROW layers. The filter layer (t_4) is indicated in the zoomed in section. (b) SEM images of the cross sections of fabricated structures for both liquid- and solid-core waveguides (TF11 wafer). The filter layer is marked.

In a fabricated device, the thicknesses of the bottom ARROW layers are designed to create high loss for the design wavelength in the liquid core waveguide. The design

wavelength is chosen to be $\lambda_D=714\text{nm}$, for a liquid-core notch filter. Taking the $n_c=1.33$ (water), $n_i=2.045$ (SiN), and $M=2$ (resonant condition), using the equation (3.1), the thickness of the filter layer would be $t=230\text{nm}$. The rest of the bottom layers are designed to have the anti-resonant condition, to ensure high transmission for other wavelengths. Using the same parameters, and setting $M=1$, one can find that the rest of the SiN layers should have a thickness of $t=115\text{nm}$, and SiO_2 ($n = 1.46$) should have $t=296\text{nm}$. Thus, the bottom layers are designed and fabricated with the following thicknesses: $t_1=t_3=t_5=296\text{ nm}$ (SiO_2 , anti-resonant), $t_2=t_6= 115\text{ nm}$ (SiN, anti-resonant) and $t_4=230\text{ nm}$ (SiN, resonant, filter layer). (see Fig. 3.3)

On the other hand, high transmission through the solid-core waveguide has to be achieved to deliver the excitation wavelength to the liquid-core waveguide, and collect the fluorescence signals from the liquid-core waveguide. The neat fabrication procedure allows us to deposit the top layers before we create the solid-core ridge waveguides with the oxide deposition. (see Fig. 3.3) In order to have high transmission in the solid-core waveguide, thus the top ARROW layers are chosen to create broadband transmission. The resonant high-loss condition for these layers are picked to be around 400nm , which is out of the operation spectrum of the device. Thus, the top layers are chosen as $t_7=t_9=t_{11}=128\text{ nm}$ (SiN, anti-resonant) and $t_8=t_{10}=t_{12}=368\text{ nm}$ (SiO_2 , anti-resonant). (see Fig. 3.3)

The calculations of the optical transmission spectrum along the liquid and solid-core waveguides are done by using 2×2 transfer matrix formalism [134], [135] and the approximate expressions for loss coefficients [101]. Fig. 3.4 shows the calculated

transmission and the absorption spectra of the designed device with the resonant filter layer ($t_4=230\text{nm}$), filled with water, demonstrating the high loss and high transmission regions of the spectral response for the liquid-core and solid-core waveguides. The calculated spectrum for the liquid-core waveguide with the anti-resonant layer ($t_4=115\text{nm}$) is also shown as a comparison, demonstrating the lack of notch filter response. These spectra clearly show how a single resonant layer can create a notch filter at the design wavelength, while broadband spectrum can be achieved for solid-core waveguides. The rejection ratio of the filter is dependent on the length of the liquid-core section. In this case, the length of the liquid-core waveguide is taken as $L=7\text{mm}$, which creates more than 900dB rejection ratio and 40nm 3dB bandwidth.

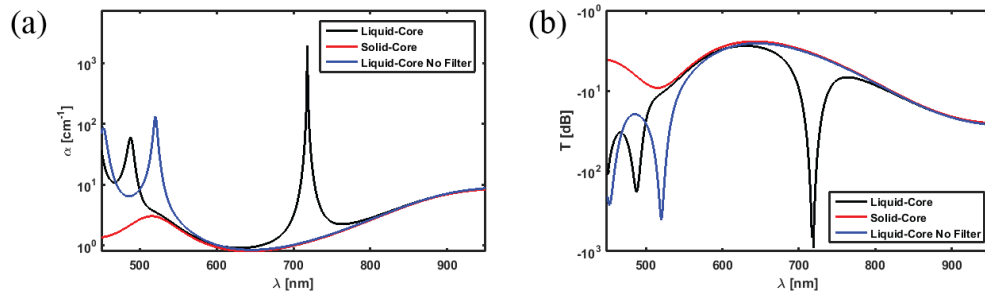


Fig. 3.4 Calculated spectral response of the liquid- (black) and solid-core (red) waveguides with a filter layer ($t_4=230\text{nm}$), filled with water. Blue curve represents the spectral response of the liquid-core with the anti-resonant layer, for comparison.

($t_4=115\text{nm}$) (a) Absorption spectra. (b) Transmission spectra.

Fig. 3.5 shows the actual spectrum measured through a 7mm long liquid-core waveguide filled with pure water. It is fabricated with the design specifications mentioned earlier. The measured filter wavelength deviates approximately $\sim 20\text{nm}$ from

the design wavelength, due to the fabrication imperfections. The theory curve is adjusted based on the center filter wavelength of the measured spectrum, by changing the filter thickness to 220nm, which showed 4% deviation in the filter thickness during the fabrication. It can be seen from the data in Fig. 3.5 that the rejection ratio of the actual measurement is ~43dB, with a 3dB bandwidth of 52nm, which is very sufficient for fluorescence detection, and has a higher rejection ratio than the other existing on-chip filters [121].

For optical measurements of the spectral response of the liquid-core filter sections, a white light source was used to generate transmission spectra. (see Appendix A.3 for details.) In order to create the white light source, femtosecond laser pulses at 850 nm were coupled via an optical isolator and an objective lens into a nonlinear photonic crystal fiber, creating a broad continuum of wavelengths covering the visible and near-IR ranges. The white light is then coupled into a single mode fiber (SMF) and directed into the ARROW to be analyzed. The transmitted light was collected by an objective and sampled in an optical spectrum analyzer (OSA) to determine the spectral response. Transmission spectra were obtained by subtraction from a reference spectrum without the optofluidic chip.

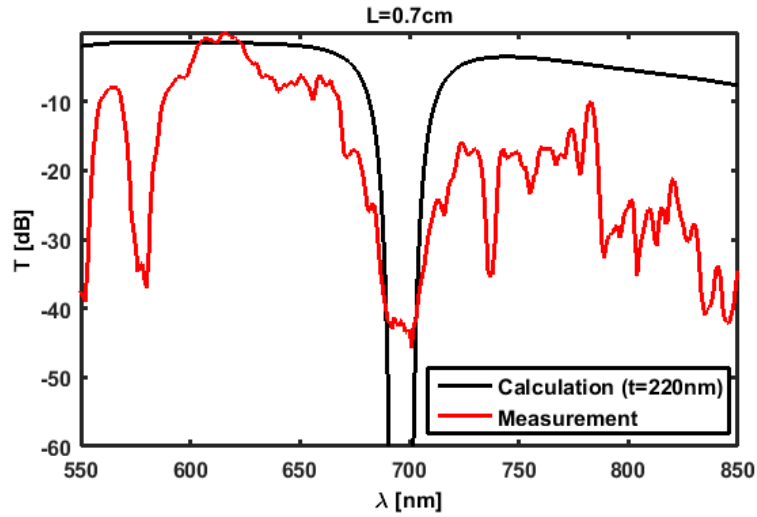


Fig. 3.5 The spectral response of the fabricated device with water as a core fluid for $L=0.7\text{cm}$ (red). Calculated spectral response is also shown (black).

Filter length dependence

The length of the liquid-core filter plays an important role for the rejection ratio. Longer interaction between the light and the ARROW filter layer would result in higher losses for that resonant wavelength, creating higher rejection ratio. In order to observe this phenomenon, 4 different lengths (4,5,6, and 7mm) of ARROW filter liquid-core waveguides are fabricated. All of them are filled with pure water and the transmission spectra are taken as in Fig. 3.5. The rejection ratio of the notch filter in each device is calculated by taking the difference between the peak of the notch filter and the base line. Fig. 3.6 shows the linear dependence of the peak rejection ratio on the filter length for devices with 4 different lengths. This shows that ARROW filters with higher rejection ratios can be fabricated by simply increasing the length of the liquid-core waveguide, as needed [136].

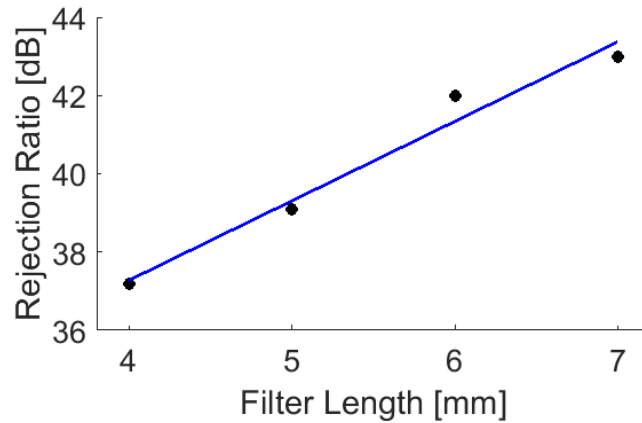


Fig. 3.6 The dependence of the peak rejection ratio of the ARROW notch filter on the length of the liquid-core waveguide filter. Measured data (black markers), as well as linear fit (blue line) with an equation $\text{Rejection Ratio [dB]} \approx 29 + 2 \text{ [dB/mm]} \times \text{Filter Length [mm]}$ are shown.

Spectral tuning of the ARROW filter

One of the advantages of optofluidics is the ability to have dynamic control over the light by using different properties of fluids, e.g. refractive index [137]. In this case, different fluids and their mixtures are used to achieve the tuning of the refractive index of the core, thus the spectral tuning of the ARROW filter response. Based on the ARROW filter theory in equation (3.1), one can see that once the device is fabricated, the only remaining variable would be the refractive index of the core. ARROW devices provide the freedom to tune this variable by simply using different liquids and mixtures with various refractive indices.

The equation (3.1) is rearranged to display the dependence of the filter wavelength, λ_F , on the device parameters:

$$\lambda_F \approx \frac{4t_i \sqrt{n_i^2 - n_c^2}}{M} \quad (3.2)$$

Equation (3.2) shows that the filter wavelength can be varied by changing the refractive index of the core n_c in the liquid-core channel. This can simply be accomplished by filling the liquid-core channel with different liquids or solutions with different refractive indices. In order to explore this potential for spectral tuning by core index, the liquid-core ARROW filter was filled with different mixtures of Ethylene Glycol (EG) (refractive index 1.43) and water (refractive index 1.33). Different ratios of the EG and water created different refractive indices, which allowed the device to be dynamically tunable for the desired specific wavelength. Fig. 3.7 shows the transmission spectra of the liquid-core ARROW filter for mixtures of EG and water with different ratios, covering the entire tuning range of 0.1 refractive index units (RIU). Highly efficient notch filter operation was achieved for all core liquids, and the minimum-transmission wavelength decreases as the EG concentration, and thus n_c , increases. It can be seen from the data in Fig. 3.7a that a rejection ratio of at least 43 dB was achieved for pure water (black curve). It is important to note that the transmission dip bottoms out for pure water, due to the detection limits of the OSA. As the EG concentration is increased, the transmission at the bottom of the dip increases as well. This is due to the higher core index of the liquid-core waveguide which decreases the loss of the waveguide [44], [138].

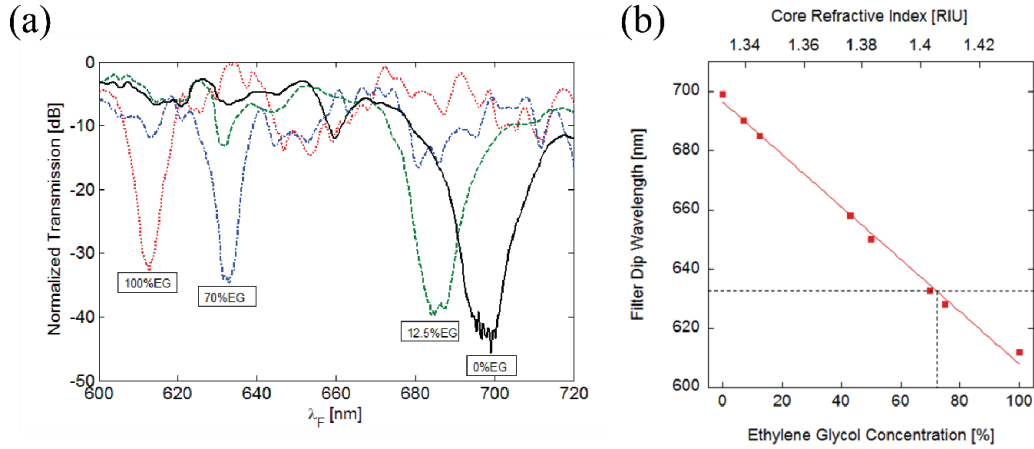


Fig. 3.7 (a) Transmission spectra of the liquid-core ARROW filter for different concentrations of Ethylene Glycol. Normalized transmission spectra for four EG:water mixtures show that the minimum-transmission wavelength decreases as the EG concentration and n_c increase. (b) Dependence of the tunable filter dip wavelength, λ_F , on the fractional ethylene glycol concentration C_{EG} . Symbols represent the data and the solid line represents the calculation. The dashed line is the HeNe laser excitation (632.8 nm) line, which corresponds to an EG:water ratio of 72% : 28%.

Fig. 3.7b shows the dependence of the tunable filter dip wavelength, λ_F , on the fractional ethylene glycol concentration C_{EG} . The dependence is nearly linear and agrees extremely well with the response predicted by an analytical 2×2 transmission matrix calculation and the equation (3.2), denoted by a solid line. The data indicates a concentration dependence of the filter response of $\Delta\lambda_F/\Delta C_{EG} = -0.883$ [nm %⁻¹] and fluidic tunability of $\Delta\lambda_F/\Delta n = -875.36$ [nm RIU⁻¹] which, to our knowledge, is the

largest observed with an optofluidic waveguide structure. The filter wavelength was tuned by ~ 90 nm by changing the EG concentration from 0% to 100%. This allows for adaptation of the filter for a large number of experimental configurations and target wavelengths [44]. For example, the dashed line in Fig. 3.7b corresponds to the HeNe laser excitation (632.8 nm), which is a commonly used wavelength. In order to tune the filter to the desired wavelength, the required concentration of EG can be obtained from the calculations and the plot that is derived from the measurements. In this case, the EG:water ratio needs to be 72% : 28% to tune the filter wavelength to 632.8nm.

The core index tuning is also largely temperature insensitive. Given the temperature dependence of the refractive indices (H_2O : $8 \times 10^{-5} \text{ K}^{-1}$, EG: $2.6 \times 10^{-4} \text{ K}^{-1}$) and assuming a very moderate temperature stability of 1 K, the thermal fluctuation in the filter response is only 0.23 nm, well below the spectral width of the dip [44].

3.2 Dual Liquid-Core Optofluidic Chip

3.2.1 Device Design

The spectral tuning of integrated ARROW filters allows for many different applications of fluorescence detection by establishing dynamic control over the spectral response. Having the capability of tuning also compensates for the fabrication deviations, creating a filter at the desired wavelength. The improvements on fluorescent particle detection with ARROW filters have already been demonstrated previously [45]. However, as discussed, a single optofluidic channel which is used for both analyte

detection and optical filtering (Fig. 3.2b) limits the flexibility and capacity of these devices, by restricting the types of fluids that can be used for fluidic tuning.

Here, a dual liquid-core optofluidic platform is introduced, which separates spectral filter and particle detection channels on a single optofluidic chip. (see Fig. 3.8) These channels are optically connected by a solid-core waveguide section, while remaining fluidically independent. The spectral response of the filter channel can now be separately controlled by changing the liquid inside the channel without concern for the analyte channel solution. In addition, different chemicals such as selective absorbers and different chemical conditions can be introduced in the filter section which further increases the flexibility of this optofluidic device.

The perpendicular detection scheme of ARROW optofluidic platforms has been preserved as it acts as a spatial filter to dramatically reduce the coupling of the excitation light into the collection waveguides. Incorporating a separate liquid-core waveguide with ARROW filter at the collection side of the channel eliminates the scattered excitation light at the solid to liquid-core waveguide interface. The analyte section is also desired to have a shorter length to reduce losses while the filter section is preferred to be longer to create higher rejection ratios to fulfill the desired extinction. Combining all these features, this design is a very powerful compact platform by integrating off-chip components onto the device, while allowing for versatile functioning of the device.

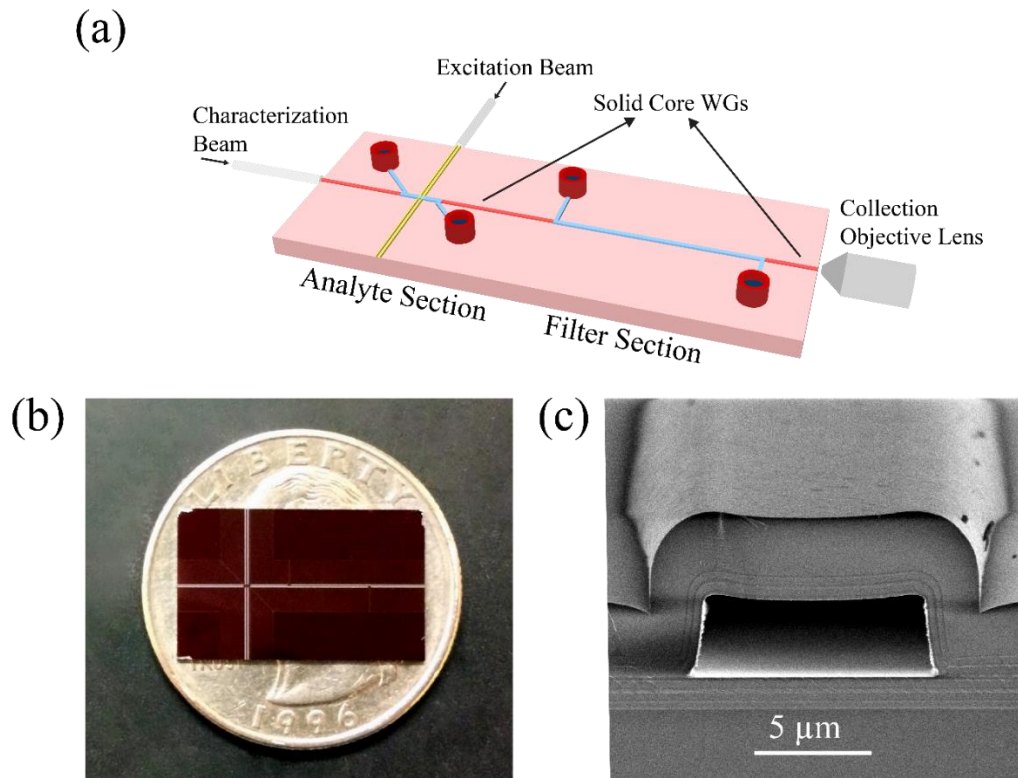


Fig. 3.8 (a) Schematic of an integrated optofluidic dual-channel chip with two different liquid-core sections (blue) for detection and tunable filtering, optically coupled by a solid-core waveguide section (orange). (b) Photograph of a complete chip on a U.S. quarter coin. (c) SEM cross-section of the liquid-core waveguide, showing the ARROW layers.

Dual liquid-core ARROWs were fabricated based on the standard fabrication procedure explained in Chapter 2. They are fabricated with top cladding layers, and they do not have any self-aligning pedestal. (see Fig. 2.5a) Bottom layer thicknesses are 296/115/296/230/296/115 nm starting with a SiO₂ layer ($n = 1.46$) and top layers are 128/368/128/368/128/2516 nm starting with a SiN layer ($n = 2.045$). The liquid-core

dimensions are $3.75\ \mu\text{m} \times 12\ \mu\text{m}$, and the topmost thick oxide layer is deposited for structural integrity as well as to create the solid-core waveguides that lead to and from the liquid channel. In order to prevent slow roughening of the SiN cladding layers by the sacrificial core etchant during the fabrication of the longest channels, an ultrathin SiO₂ layer (50 nm) was added directly around the hollow core. The length of the analyte section is 300 μm , while filter sections are created with various lengths (4–7 mm). For fluorescence particle experiments, devices with 7mm filter length is used to achieve maximum rejection [44]. The details of the fabrication procedure can be found in Appendix E.1.

3.2.2 SNR Enhancement by Spectral Filtering

Signal-to-noise ratio improvement with ARROW spectral filter has been demonstrated with 100nm nanoparticles with a 4.7-fold improvement over a 2mm long ARROW channel. This was achieved by using the single liquid-core ARROW filter platform [45]. Here, the advantage of using the independently adjustable spectral response on a dual liquid-core ARROW filter platform is illustrated by demonstrating single particle fluorescence detection. For fluorescence detection, 100 nm diameter fluorescent particles (Invitrogen TetraSpeck) were introduced to the liquid-core analyte channel. The nanoparticles were diluted with water to a final concentration of 2.6×10^{10} particles per mL which corresponds to 0.3 particles in the optical excitation volume defined by the waveguide intersection. Particles were ultrasonicated to prevent coagulation and bovine serum albumin (BSA) protein was added to prevent sticking on the walls. Since

a HeNe laser is used to excite fluorescent particles, the ARROW filter was tuned to 632.8 nm by using a 70%:30% EG:water mixture in the filter channel in order to eliminate the excitation signal from the fluorescence signal. The correct mixing ratio of EG and water is obtained from the plot in Fig. 3.7b (dashed line). The fluorescence signal is collected through the solid-core collection waveguide after passing through the liquid-core filter section, collected by an objective lens (NA:0.85, 60X) and detected by the avalanche photodiode single photon counting module (see Appendix A.1). Fig. 3.9a shows the sample sequence of detected single particles through the ARROW filter section [44].

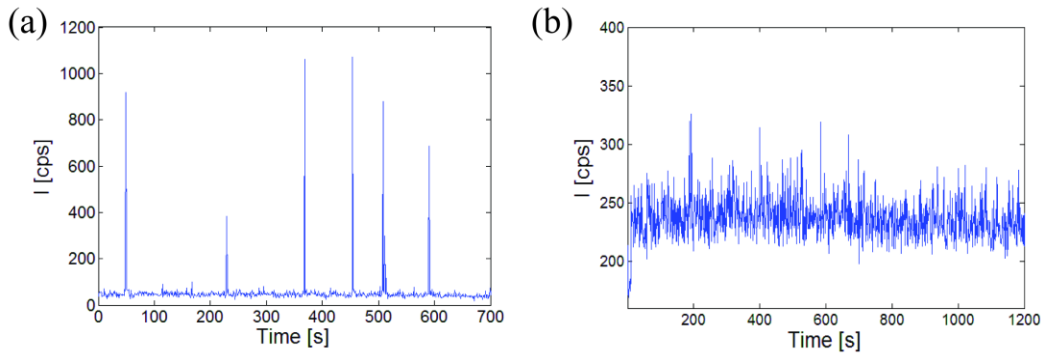


Fig. 3.9 (a) Single particle detection with optofluidic integrated filter chip. A maximum signal-to-baseline ratio of 35 was achieved for detection through the optofluidic filter. (b) Signal collected from the other end of the chip which has no filter in the path.

The fluctuation in peak levels is due to variations in the particle brightness and specific location within the excitation volume [139]. Clear single particle resolution with excellent signal-to-noise ratio (average: 18, maximum: 35) was achieved. In contrast,

when particle detection was attempted from the other end of the device where there is no ARROW filter, no particles could be detected (see Fig. 3.9b). Since on-chip filtering was absent in this case, the excitation power had to be reduced to keep the background level lower. The remaining power was insufficient to generate enough fluorescence to rise above the higher background level. This experiment shows that highly sensitive particle detection is possible through multiple liquid-core waveguides, and the dedicated filter section can be easily tuned away from its design wavelength by tens of nm (here 67 nm) to accommodate a specific fluorescence assay [44].

3.2.3 Multi-wavelength Tuning by Bulk Absorption

In addition to eliciting a desired spectral response via the core refractive index, a liquid-core waveguide filter can also be adjusted using the intrinsic bulk optical properties of the core liquid. Here, we demonstrate two conceptually different approaches: addition of selectively absorbing molecules and pH dependent absorption. Most importantly, these features can be controlled independently from the core index, and thus allow for independent control over the spectral device response in different wavelength regions. This is particularly attractive for multi-wavelength spectroscopic applications such as FRET [118].

The first approach to spectral filtering using bulk liquid properties is adding absorber dyes in the liquid-core channel, here fat soluble dye Sudan II (Sigma Aldrich - 199656-25G). Different concentrations of Sudan II dye dissolved in isopropanol (IPA, index $n_c = 1.377$) were used for characterization measurements. Transmission spectra for four

different concentrations were obtained by using the white light source as described above. Fig. 3.10a shows the normalized transmission curves for each concentration, which were obtained after subtraction of the IPA-only transmission spectrum. The spectra show an absorption for Sudan II between 550 and 565 nm [44]. The spectrum is limited by the white light excitation source, which is why the plot starts at 550 nm.

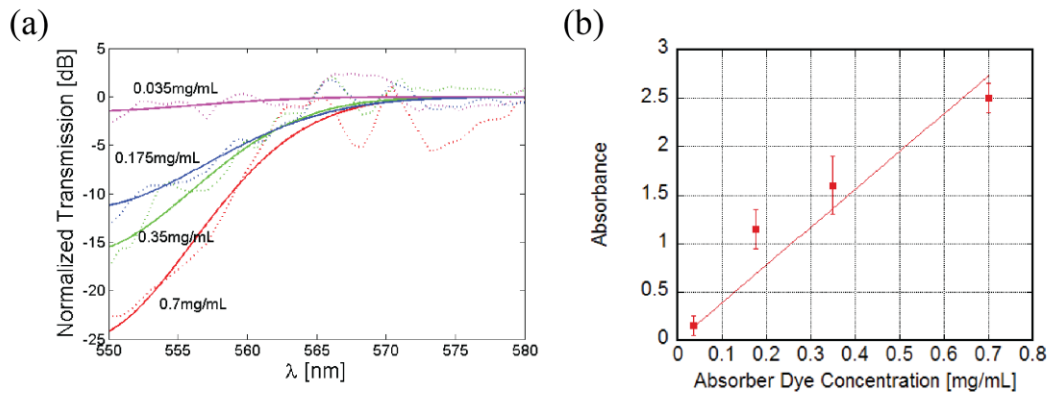


Fig. 3.10 (a) Normalized transmission curves of different concentrations of absorber dye (Sudan II) in isopropanol. Dashed lines are the measured data and the solid lines are the Gaussian lineshape fits. Non-zero absorption for Sudan II between 550 and 565 nm is observed. (b) Concentration dependence of the extracted maximum absorbance of absorber dye (Sudan II) in isopropanol. Symbols: experimental data; line: fit with linear absorption dependence.

As expected, the filter transmission decreases with increasing dye concentration. For quantitative analysis, a Gaussian absorption lineshape was fitted to the curves to analyze the maximum absorption around 550 nm. Fig. 3.10b shows the concentration dependence of the extracted maximum absorbance which is defined by the ratio of

measured input and output powers as $A = \log(P_{in}/P_{out})$. The solid line represents a linear fit to the data with reasonable agreement. A linear dependence is expected since absorbance scales linearly with absorber concentration [118]. Clearly, the addition of an absorbing dye allows for additional filtering, either by increasing the rejection ratio at the same wavelength determined by the core index, or by adding a second transmission notch whose position and depth can be tuned by dye type and concentration, respectively.

The second technique for tuning the liquid-core filter response is to control the chemical properties of the liquid. We demonstrate this capability by taking advantage of the pH dependence of the transmission of certain molecules. Universal indicator (UI) is a combination of different absorbing dyes that absorb different parts of the spectra for different pH values [140]. Specifically, for a pH of 10.0, the UI transmission is lowest around 600 nm which makes the solution blue; when the pH equals 4.1, the transmission dip shifts to 450 nm and the solution appears red; while the solution is virtually transparent above 600 nm. The bulk transmission spectra of the UI taken with a NanoDrop spectrophotometer at these pH values are shown in Fig. 3.11. This duality can be used to create a switchable filter for wavelengths above 600 nm.

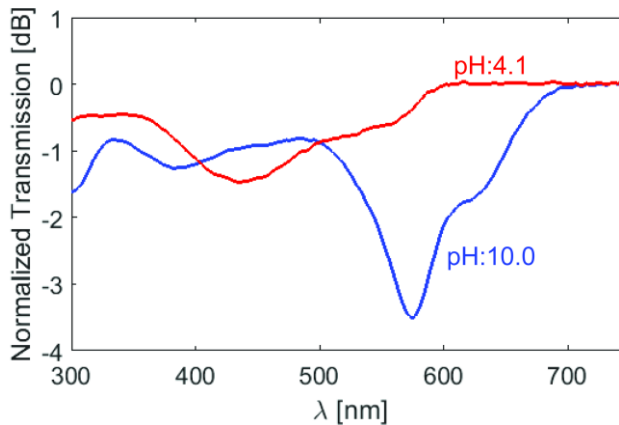


Fig. 3.11 Normalized transmission absorbance spectra of universal indicator for two different pH values measured using a NanoDrop spectrophotometer.

To demonstrate this effect, two solutions with different pH values were prepared by using a 40%:60% EG:water mixture. The 7 mm long liquid-core filter section was filled with these solutions and then the transmission spectra were taken. The pH-dependent dye response was then obtained by subtracting the UI transmission spectra from the pure 40%:60% EG:water mixture.

Fig. 3.12a shows the transmission response of the dye for pH = 10.0 and pH = 4.1, respectively. It is observed that, changing only the pH of the solution, the filter can be activated and deactivated for the wavelength range of interest. This function could be dynamically turned off and on by simply adding a drop of acid or base to the filter section reservoir during the measurement.

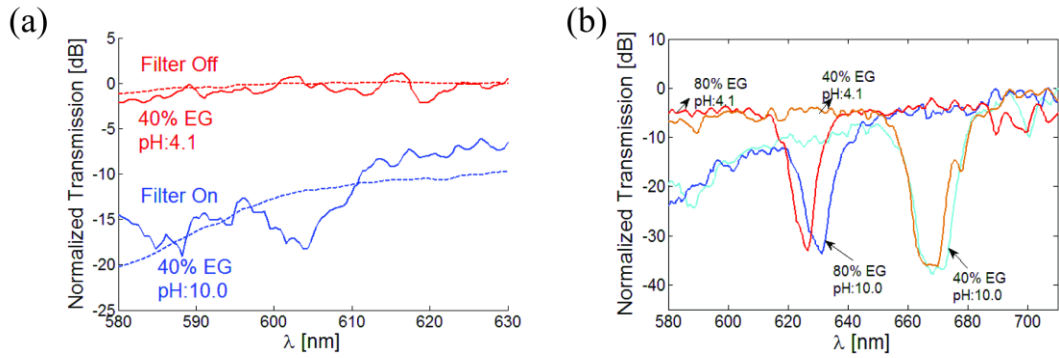


Fig. 3.12 (a) Normalized transmission spectra of universal indicator with different pH values taken on chip. Dashed lines are the off-chip spectra, normalized to match the concentration. The blue line indicates the activated filter and the red line indicates the deactivated filter; (b) Independent multi-wavelength tuning function. For the blue and cyan curves, the absorption filter is active and the ARROW filter is independently shifted to another wavelength. For the red and orange curves, the absorption filter is deactivated and the LC-ARROW filter is tuned independently.

One of the biggest advantages of using this optofluidic integrated filter design is to be able to combine different tunable filtering methods dynamically. We demonstrate this capability using the combination of core index and pH tuning. Independently changing the EG concentration and the pH of the solution allows separate control over the two different filter dips. Fig. 3.12b presents this independent tuning function. When the pH is tuned to 10.0, the UI filter is activated and the corresponding filter dip is observed around 580 nm. While keeping the UI filter active, the ARROW filter can then be shifted to a different wavelength of interest by changing the EG concentration of the solution. Fig. 3.12b shows the example of a 40 nm shift using core index control while

leaving the UI response unchanged (blue and cyan curves). Finally, the UI filter can be deactivated by simply changing the pH value to 4.1 by adding acid, while keeping the core-index filter around the desired wavelength (red and orange curves). The acid solution should be prepared to match the refractive index of the solution in the channel, which corresponds to the filter dip at 580nm. The small shift in the short wavelength dip could be eliminated by more careful control over the index of the added acid solution.

In conclusion, successful on chip tunable ARROW filter design and implementation is demonstrated. The fabrication of the ARROW filter is achieved with a very simple modification to the standard ARROW fabrication, resulting in very high rejection ratios $\sim 43\text{dB}$, for on-chip notch filters rivalling those of standard off-chip components. The length dependence of the absorption is shown by fabricating liquid-core ARROW filters with 4 different lengths, and the linear relationship between the absorption and the length is observed, in agreement with the theoretical expectations. The spectral tuning based on fluidic core refractive index tuning of the ARROW filter is demonstrated with up to $\sim 90\text{ nm}$ tuning range, with an extremely large tuning of the filter response by 875 nm RIU^{-1} . Finally, we have introduced a powerful, new on-chip sensor architecture based on the serial arrangement of liquid-core ARROW analyte and filter sections. By decoupling the spectral filter segment from a dedicated analysis region, full advantage of the dynamic reconfiguration possibilities of the liquid filter channel can be taken. The dual-core chips were used to demonstrate highly efficient detection of single fluorescent nanoparticles aided by on-chip elimination of the

excitation signal. In addition to the core index tuning approach we demonstrated spectral tunability of the filter transmission using intrinsic bulk optical properties of the core liquid, with two different approaches: using selectively absorbing molecules (Sudan II) and pH dependent absorption (Universal Indicator). Combining this approach with the core index tuning, the simultaneous and independent control over two independent spectral absorption features was demonstrated for the first time. This could be exploited in multi-wavelength techniques such as FRET. For example, the device could be further expanded by adding filter sections on each side of the analyte channel. These filters could be independently tuned to transmit donor and acceptor signals, respectively, without the need for additional off-chip filtering. Incorporation of spectral filtering is another important step towards full optofluidic integration that includes additional back-end optical processing such as photodetector integration.

4 Signal to Noise Ratio (SNR) Enhancement by Multi-Spot Excitation

The fluorescence detection of single bioparticles requires high sensitivity. As we have reached the ultimate limit of detecting individual bio-particles labeled by single or few fluorophores as is the case for antibody-labeled proteins or nucleic acid detection with molecular beacons, high sensitivity measurements are challenging, and required [141]. The recent advancements of new fluorophores, novel designs and more powerful instruments make fluorescence detection even more interesting by increasing the sensitivity reaching the single-molecule detection levels [142]. The main problems that could hamper high sensitivity fluorescence measurements are quenching and interference of the background noise. If the background noise is relatively high, then the detected signal may not be analyzed confidently.

There are many different approaches to increase the signal-to-noise-ratio (SNR) of fluorescence detections. First of all, the quantum yield of fluorophores and the number of fluorophores on each target can be improved to create more signal. Higher excitation energy would also improve the emitted signal, but it is limited by the quenching and it also may increase the background noise. High power lasers and more sensitive detectors are also expensive, making the whole detection platform less implementable [142]. Additionally, increasing the detection efficiency [143], combining on-chip and off-chip spectral filters [44], implementing lock-in amplifiers [144], metal or plasmonic enhancement [145]–[148] and Surface-Enhanced-Raman-Scattering (SERS) [149], [150] have been successful methods to achieve higher SNR fluorescence detection.

Although these methods are very effective for increasing the sensitivity of the device, they either depend on complex instrumentation or complex experimental procedures.

One of the most effective approach to improve the SNR in flow-based fluorescence detection, without adding expensive instruments or complex chemical procedures is using spatial modulation to create temporal coding of the fluorescence signal. SNR enhancement by spatial modulation has been successfully shown by using chopper wheels [151], integrated patterned masks [152]–[158] and arrayed waveguides [159], [160]. The SNR enhancement is achieved by correlating the spatially modulated signal with the known pattern that is created either in the excitation region or the collection region. For example, Lien et. al implemented an optofluidic detection platform, where each sample by passed eight equally-spaced sets of interrogation and collection waveguides, yielding eight detected signals. Using the known time delay between expected signals, cross-correlation was performed, yielding great improvement of the signal-to-noise ratio of the data. Microbead signals invisible to the eye were readily extracted with excellent clarity [159].

Liquid-core antiresonant reflecting optical waveguide (LC-ARROW) platforms have shown an excellent performance for single molecule fluorescence detection, thus incorporating SNR enhancement with temporal coding onto these devices would further increase the sensitivity. LC-ARROW platforms are easily customizable and allow for integration of many different functionalities. Here, we took advantage of this benefit, and implemented multi-spot excitation by using Y-splitter waveguides in order to achieve SNR enhancement. Instead of creating multiple detection channels, we have

incorporated multi-spot excitation to create temporally encoded signals. As only the targets produce a time-dependent signal that reflects this multi-spot excitation pattern, detection can be enhanced by a simple signal processing step to drastically increase *SNRs*.

In this chapter, we systematically investigate multi-spot based *SNR* enhancement on a LC-ARROW platform for single virus detection. First of all, the theory of signal processing algorithm for *SNR* enhancement is introduced. Then, the design and fabrication of the Y-splitter waveguides and their limitations are presented. Finally, three different Y-splitter waveguides creating $N=2, 4,$ and 8 spots were fabricated and tested using fluorescently labeled beads and H1N1 viruses as analytes. A comparison of these devices elucidates the dependence of *SNR* enhancement on spot number. High *SNR* enhancement with different analysis methods is demonstrated and challenges to the method are analyzed.

4.1 Signal processing algorithm

The *SNR* enhancement by spatial modulation method relies on the idea of correlation. The contrast between the random behavior of the noise and pre-defined signal response forms the basis of this enhancement. The modulation methods based on using pre-defined masks cross-correlate the collected data with this defined pattern to eliminate the randomly generated noise [152], [155], [156]. In a similar manner, when a target molecule is excited multiple times as it moves along the excitation region, multiple fluorescence emissions generated at different times from the target are collected. It is

important to realize that all of these fluorescence signals are time-correlated. In our device, instead of a random pattern for cross-correlation, equal spatial distribution of the multiple excitation spots creates equal temporal distribution of the collected signals. Thus, the signal processing algorithm relies on this equal temporal distance between each signal.

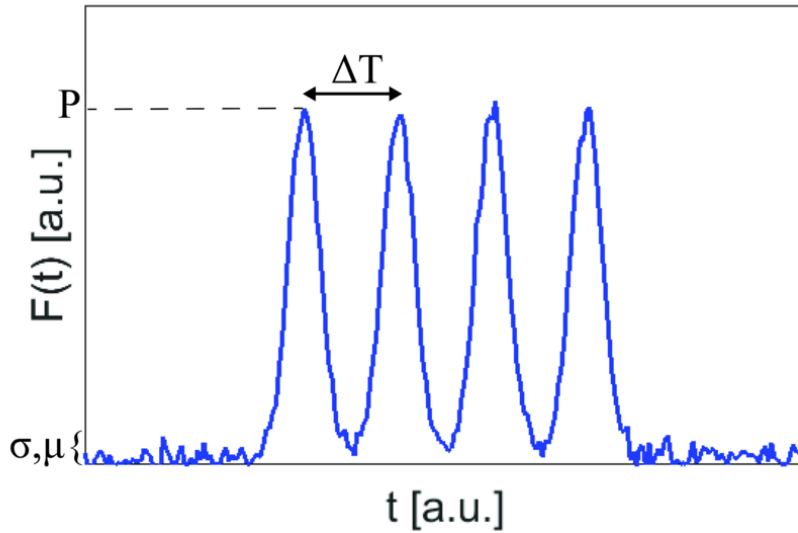


Fig. 4.1 Symbolic data showing the signal parameters with $N=4$.

The signal processing algorithm that is used to increase the SNR of the particle fluorescence by correlating these temporally encoded signals is as follows: [159]

$$S(t, \Delta T) = \prod_{i=0}^{N-1} F(t - i \cdot \Delta T) \quad (4.1)$$

where ΔT is the time difference between any two of the N signals coming from each excitation spot. Signals that are correlated by ΔT are enhanced while the random noise, which is not correlated, is filtered out efficiently. The noise background is characterized by its mean value μ and standard deviation σ . SNR is defined as the ratio of P , the

average peak value of the particle's signal to the standard deviation of the background signal [161]. (see Fig. 4.1)

The *SNR* of the original data before processing is then defined as:

$$SNR_o = \frac{P}{\sigma} \quad (4.2)$$

Since the noise is random, mean value and standard deviation for products of the data should be treated as the products of multiple independent random variables, defined as [162]:

$$\begin{aligned} \mu_s &= \mu^N \\ \sigma_s &= \sqrt{\langle S(t)^2 \rangle - \langle S(t) \rangle^2} \end{aligned} \quad (4.3)$$

Combining equations (4.1) and (4.3), the standard deviation after the signal processing can be derived as follows:

$$\begin{aligned} \sigma_s &= \sqrt{\langle F(t)^2 \rangle \cdot \langle F(t-\Delta T)^2 \rangle \dots \langle F(t-(N-1)\cdot\Delta T)^2 \rangle} \\ &= \sqrt{-\langle F(t) \rangle^2 \cdot \langle F(t-\Delta T) \rangle^2 \dots \langle F(t-(N-1)\cdot\Delta T) \rangle^2} \\ &= \sqrt{(\sigma_{F(t)}^2 + \langle F(t) \rangle^2) \cdot (\sigma_{F(t-\Delta T)}^2 + \langle F(t-\Delta T) \rangle^2) \dots (\sigma_{F(t-(N-1)\cdot\Delta T)}^2 + \langle F(t-(N-1)\cdot\Delta T) \rangle^2)} \\ &= \sqrt{-\langle F(t) \rangle^2 \cdot \langle F(t-\Delta T) \rangle^2 \dots \langle F(t-(N-1)\cdot\Delta T) \rangle^2} \\ &= \sqrt{\prod_{i=0}^{N-1} (\sigma_{F(t-i\cdot\Delta T)}^2 + \langle F(t-i\cdot\Delta T) \rangle^2) - \prod_{i=1}^N \langle F(t-i\cdot\Delta T) \rangle^2} \end{aligned} \quad (4.4)$$

The standard deviation and the mean of the shifted data stay the same, since it is only a temporal shift:

$$\begin{aligned} \sigma_{F(t)} &= \sigma_{F(t-(N-1)\cdot\Delta T)} = \sigma \\ \langle F(t) \rangle &= \langle F(t-(N-1)\cdot\Delta T) \rangle = \mu \end{aligned} \quad (4.5)$$

Combining equations (4.4) and (4.5), the standard deviation of the data after the signal processing becomes;

$$\sigma_s = \sqrt{(\sigma^2 + \mu^2)^N - (\mu^2)^N} \quad (4.6)$$

The average peak value of the particle signal is enhanced by N times after the signal processing algorithm:

$$P_s = P^N \quad (4.7)$$

It is important to note that this is an approximation with the assumption of all peaks having the equal peak intensity, with equal temporal spacing. The variation in the peak intensities decreases this value which will be discussed later.

The dependence of SNR enhancement on original mean and noise values is derived by combining equations (4.2), (4.6) and (4.7) to yield:

$$\frac{SNR_s}{SNR_o} = \frac{P^{N-1}\sigma}{\sqrt{(\sigma^2 + \mu^2)^N - \mu^{2N}}} \quad (4.8)$$

This formula reveals the dependence of the SNR change on the properties of the original signal and the spot number. Note that if the original signal P is higher and σ and μ values are lower, i.e. high SNR_o , better SNR enhancement can be achieved. It is also clear that the method works best for large N . However, an SNR enhancement can still be achieved for higher of σ and μ values.

In order to understand the true power of SNR enhancement based on this algorithm, a detailed analysis of this equation has been done. The calculation of SNR enhancement based on the equation (4.8) is done, assuming hypothetical original data trace values where $P=5$ and $N=8$. Fig. 4.2a shows the SNR enhancement for different values of σ

and μ of the original data. The logarithmic scale data shows that the SNR enhancement is highest ($\sim 10^{10}$) when σ and μ are lowest. However, the true power of this algorithm can be seen when the noise levels are higher. For example, for an original data with $\sigma=3$ and $\mu=3$ where the SNR_O is very low with $P=5$, after the signal processing SNR can be enhanced by ~ 2.3 times. (see Fig. 4.3) This allows us not only to increase the SNR but also recover the particles that are buried in the noise in the original data. Even though this algorithm is very powerful, there are still some limitations to it. When the noise levels get very high, the recovery or SNR enhancement may not be achieved. Fig. 4.2b shows the boundary for initial σ and μ values to be able to achieve SNR enhancement. With σ and μ values in the yellow region, SNR enhancement can be achieved, however for higher values of σ and μ , SNR enhancement cannot be achieved, which is denoted by the green region.

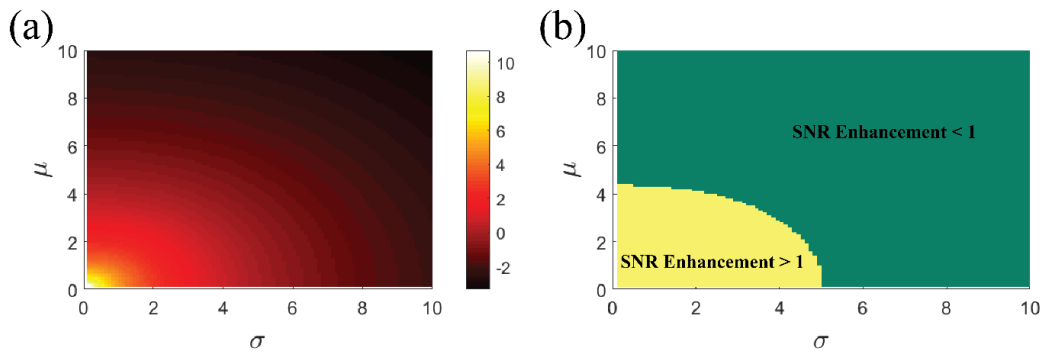


Fig. 4.2(a) Theoretical analysis of SNR enhancement varying the noise and mean values for $P=5$ and $N=8$. Color bar shows the SNR enhancement in a logarithmic scale. (b) Theoretical analysis of the limits of the SNR enhancement. The yellow region shows the values at which the SNR enhancement is above one, and the green region represents values at which the SNR enhancement is below one.

Furthermore, SNR enhancement is simulated with randomly created noise ($\sigma=3$ and $\mu=3$) and a signal ($P=5$). Fig. 4.3 shows the intermediate steps during of the SNR recovery algorithm with different number of shifts ($N-1$). In Fig. 4.3a, it is clear that the original data (red) is buried in the noise (blue) with an $SNR=1.7$, where the signal technically cannot be detected. However, as we shift and multiply the data multiple ($N-1$) times, the noise suppression and the enhancement in the signal level can be observed. Fig. 4.3d shows the signal and noise levels after applying the algorithm for $N=8$, shift and multiply the signal 7 times. This also clearly shows that higher SNR enhancement and better signal recovery can be achieved with higher N . It is important to note that, the red curve is a representation of a peak signal, and (4.7) is applied on the simulated data to show the theoretical peak value.

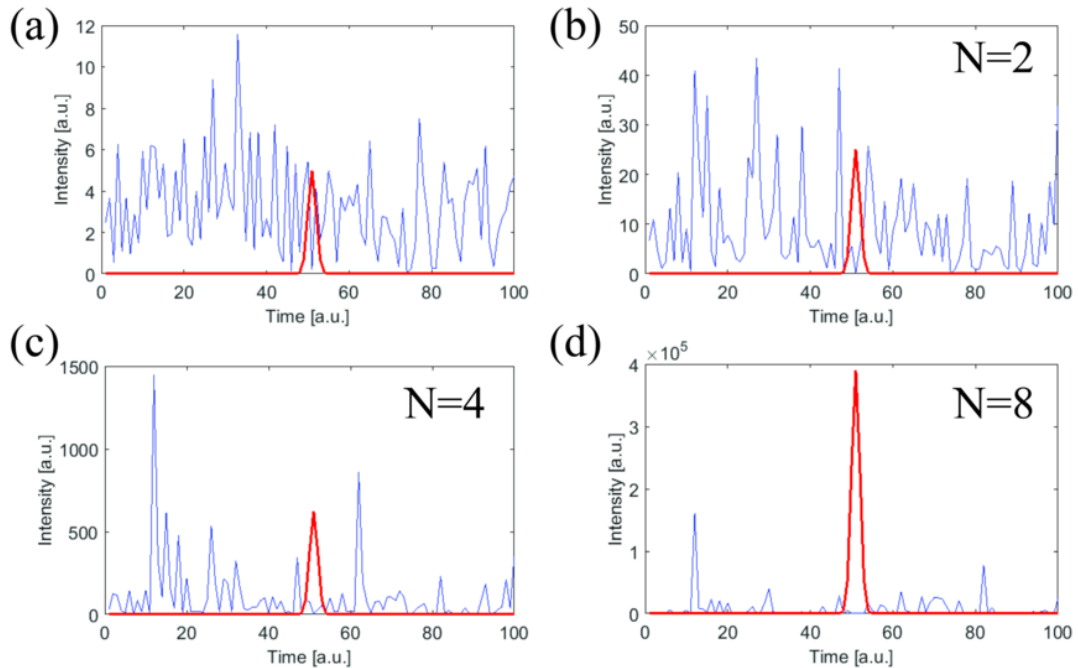


Fig. 4.3 Simulated data for SNR enhancement depicting signal (red) and noise (blue) levels for different N values. (a) Original data. (b) SNR enhancement with $N=2$ (c) $N=4$ (d) $N=8$

Fig. 4.4a shows how SNR Enhancement increases with the number of peaks (N). The data is obtained by creating random noise as seen in Fig. 4.3, and calculating the SNR for each N . The noise and signal values are taken as ($\sigma=3$ and $\mu=3$) and $P=5$. The blue dots are the simulated data points where the red line is an exponential fit. Fig. 4.4b demonstrates how cut-off for SNR enhancement changes for different N values as explained in Fig. 4.2b. It's clear that SNR enhancement can be achieved for higher noise values, if N is higher. This also helps to optimize the N for the actual device, as the increasing the N further than 8 does not dramatically improve the cut-off for SNR enhancement.

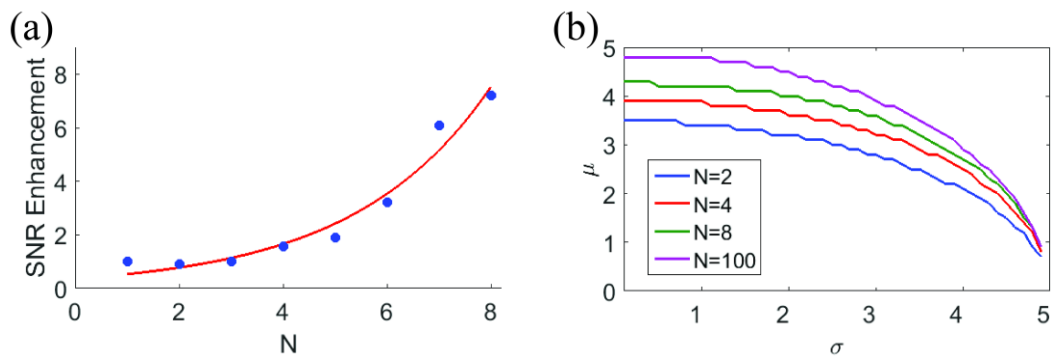


Fig. 4.4 (a) SNR Enhancement dependence on number of peaks (N). Blue dots represent the simulated data and the red line is an exponential fit. (b) SNR enhancement cut-off dependence on N .

In Fig. 4.4a, it is also important to note that the simulated SNR enhancement (~ 7.2) is higher than the calculated value (~ 2.3). This is due to the background noise which contains occasional time points with zero value, which further increases the SNR enhancement. A single zero value is sufficient to render the entire product equation (4.1) to zero. Given a probability p_0 of finding a zero in the original signal $F(t)$, the probability of $S(t)=0$ is easily shown to be:

$$p_{S=0} = 1 - (1 - p_0)^N \quad (4.9)$$

Fig. 4.5 shows the probability of finding zero for $N-1$ multiplications, for different initial p_0 values (i.e. y-intercepts), from 0.1 to 0.9. Consequently, the SNR enhancement further increases and can reach extremely large values.

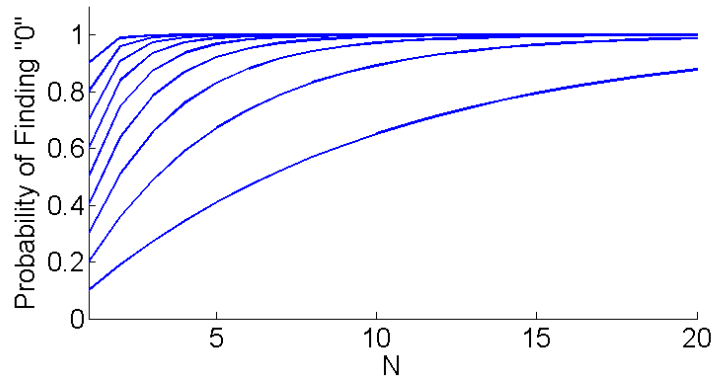


Fig. 4.5 The probability of finding a zero for $N-1$ multiplications, for different initial p_0 values (i.e. y-intercepts), from 0.1 to 0.9.

4.2 Multi-spot excitation based on Y-splitters

Y-splitter waveguides are very suitable for multi-spot excitation as they have no spectral dependence, create high quality excitation profiles, and are ideal for systematically varying the number of excitation spots. The new optofluidic analysis

chip with Y-splitters is based on LC-ARROW devices which can be filled with low-index fluids, and used for fluorescence detection. These liquid-core waveguides are combined with solid-core waveguides for orthogonal fluorescence excitation and collection with high coupling efficiency. Y-splitters are introduced to the LC-ARROW platform replacing single solid-core excitation waveguide, to create multiple excitation spots at the liquid core-solid core intersection. (see Fig. 4.6) This way, signal processing algorithm presented in the previous section can be applied to the collected fluorescence signal to achieve high SNR enhancement. Since ARROW platform is very easy to customize, the introduction of Y-splitters into the optofluidic detection platform is very straightforward. However, the design of the Y-splitters requires comprehensive optimization to achieve smaller devices with low-loss, due to the losses caused by the curves.

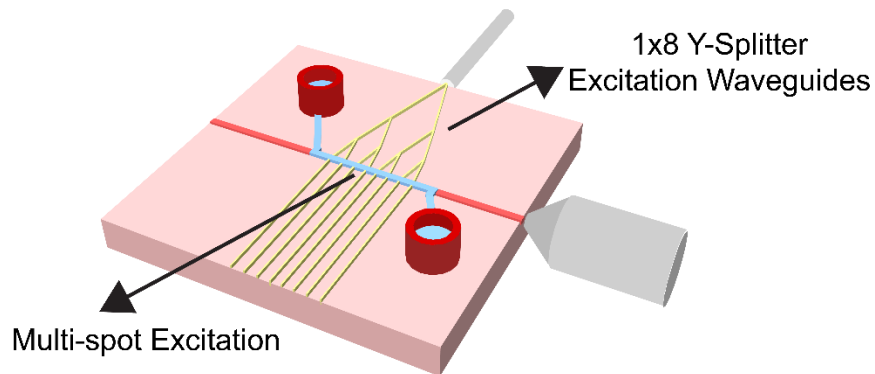


Fig. 4.6 Schematic of Y-splitter ARROW waveguide platform for $N=8$.

4.2.1 Y-Splitter design and optimization

In order for the SNR enhancement algorithm to work with better enhancement, there are few different parameters to consider for the excitation pattern. First of all, the spacing between the excitation spots, Δx , should be the same, as the correlation algorithm depends on this. Secondly, high peak-to-valley ratio of the excitation pattern should be achieved, by creating higher intensity peak values while keeping the areas in between the excitation spots minimized. In addition to this, the SNR algorithm works better if the excitation spots have a narrow bandwidth, by eliminating the enhancement at different time stamps. Another important requirement is to have minimum variation among the peak values of the excitation intensity, requiring fairly equal splitting of the input power into the multiple excitation spots. All of these parameters should be considered while designing the Y-splitter waveguides.

First of all, equal spacing of the multiple excitation spots should be achieved. Since Y-splitter waveguides are physically separated, this is easily achieved by creating the waveguides equally spaced from each other. In order to create more distinct separation between the peaks, while not creating wider bends for the Y-splitter waveguide curves, Δx is taken as $25\mu\text{m}$. As the particle passes through these excitation spots, the equal spatial separation creates equal temporal separation in the collected fluorescence signal. The most challenging optimization problem was to create high peak to valley ratio for the excitation patterns. This is a very important parameter as this ratio directly translates to the SNR_O value in the collected fluorescence signal. In order for the algorithm to work better, this value should be maximized, as it was discussed in the

previous section. First of all, the intensity of each spot should be maximized, which means the overall loss of the waveguide should be minimized. The main trade-off of minimizing the loss is between the Y-splitter waveguide curvature and the device length. If the Y-splitter waveguides have a higher angle of curvature, then the losses introduced by the curves are going to be dominating [163]. If the Y-splitter waveguides have lower angle of curvature, it will increase the length of the Y-splitter waveguides and the whole device, causing more propagation loss. This trade-off is analyzed by using a beam propagation software (FimmWAVE, Photon Design), and optimum angles for each of the splits are found. The fundamental mode was launched into the Y-junction and the output power from the two ends of the Y-junction were simulated as a function of Y-junction fan-out angle, θ . One important finding was that the fan-out angle of each splitter should be kept below 2° . Fig. 4.7b shows the dependence of the total transmission in S-shaped 1×2 splitter on the fan-out angle (θ) of the splitter, for $\Delta x = 25 \mu\text{m}$, and waveguide width (w) = $4 \mu\text{m}$, while varying the length of the device at $\lambda = 633 \text{nm}$. While keeping the angle below 2° ensured the high transmission from the curvature of the Y-splitter waveguides, at lower angles, the device size gets bigger and the propagation losses start to dominate. Taking both losses into account, the maximum total transmission is achieved for the fan-out angle values of 1.3 - 1.8° . This ensured maximum transmission for each Y-junction, increasing the excitation intensity for each spot. Another important part of the Y-splitter design is the shape of the bends. S-shaped Y-splitter waveguides create smoother bends, reducing the losses at the bending

regions. [163] The design of the Y-splitter taper is made based on a sine function, resulting in higher transmissions compared to the linear tapered Y-junctions.

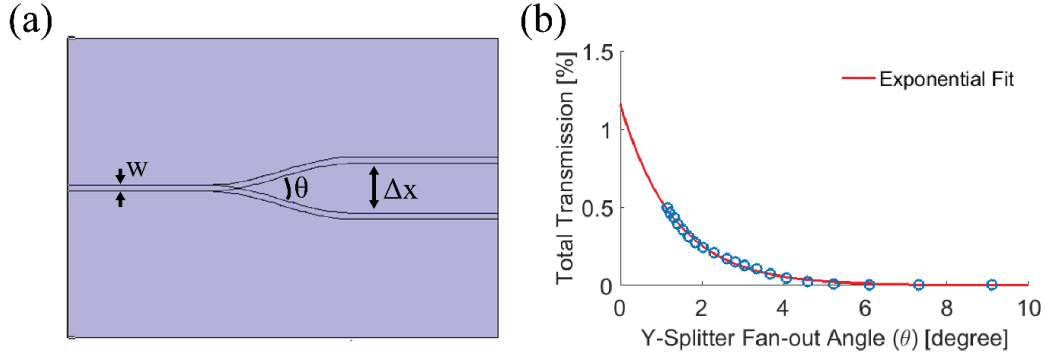


Fig. 4.7 (a) Schematic of a 1×2 Y-splitter with an S-shaped taper. (b) Dependence of the total transmission in 1×2 Y-splitter waveguide on the fan-out angle of the Y-junction, for $\Delta x=25\mu\text{m}$, and $w=4\mu\text{m}$.

Even though the Y-splitter waveguides are physically separated from each other, there are still some spurious peaks observed in between the excitation spots. This is mainly due to the scattered light coming from the Y-splitter waveguides and increases the background and noise in the actual signal. However, compared to the other methods such as MMIs, which will be discussed in the next chapter, Y-splitter waveguides create very low valley intensity. This is one of the main advantages of using Y-splitters for SNR enhancement.

In order to achieve maximum intensity in each excitation spot, the distribution of the total power should be equal. This is achieved by a careful design of the Y-splitter waveguides, preventing the unequal splitting of the power. According to the V-number,

$V = \frac{\pi}{\lambda} w \sqrt{n_1^2 - n_2^2}$, when the waveguide width (w) increases, the waveguide can

support multiple modes [164]. When these multiple modes interfere with each other, they create beating waveguide mode. (see Fig. 4.8a) When the waveguide starts to split into two separate arms, depending on where the mode center is, unequal split occurs. (see Fig. 4.8b) This creates unequal distribution of the total power at the output waveguides. (see Fig. 4.8c-d)

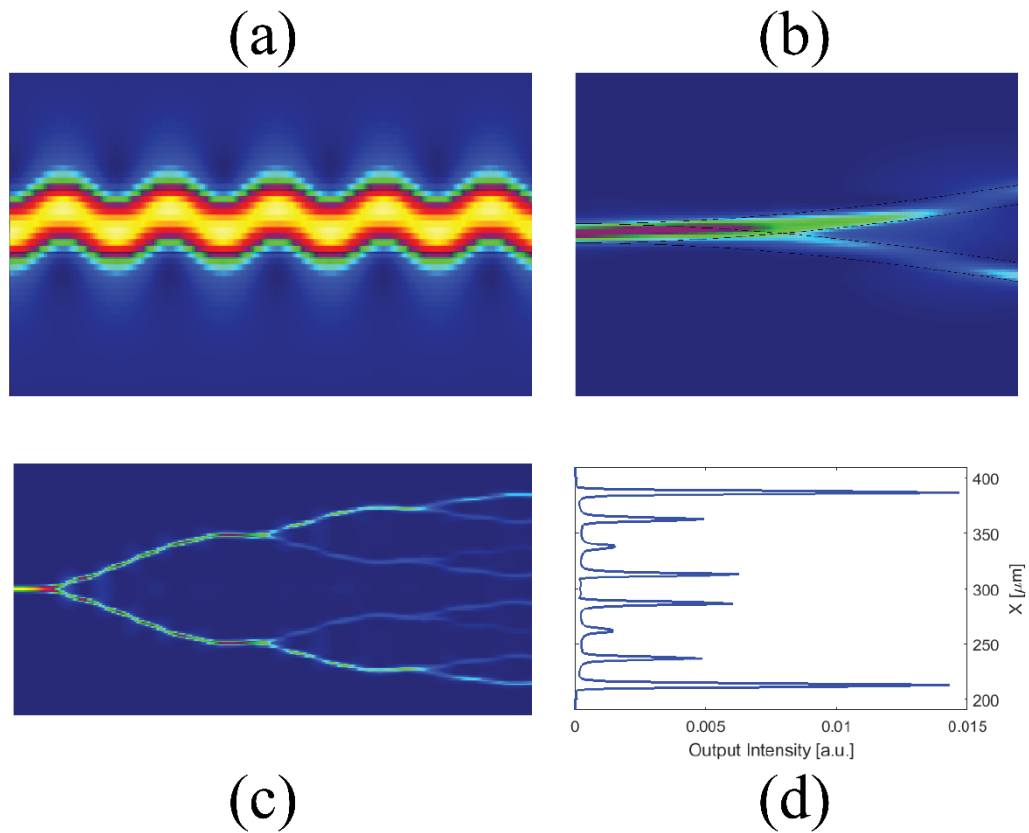


Fig. 4.8 Simulations of Y-splitters for a wider waveguide (here: $w=6\mu\text{m}$) supporting multiple lateral modes. (a) Beating of the waveguide mode (b) Unequal splitting of the power when there is asymmetrical mode at the intersection. (c) 1×8 Y-splitter waveguide showing the unequal distribution of the total power, due to the beating modes. (d) The output intensity profile of the 1×8 Y-splitter device in (c).

In order to prevent unequal distribution caused by asymmetrical mode profile, the waveguide width is picked as $w=4\mu$, to achieve single-mode guiding. Fig. 4.9 shows the simulations demonstrating how balanced distribution is achieved by creating single-mode waveguides.

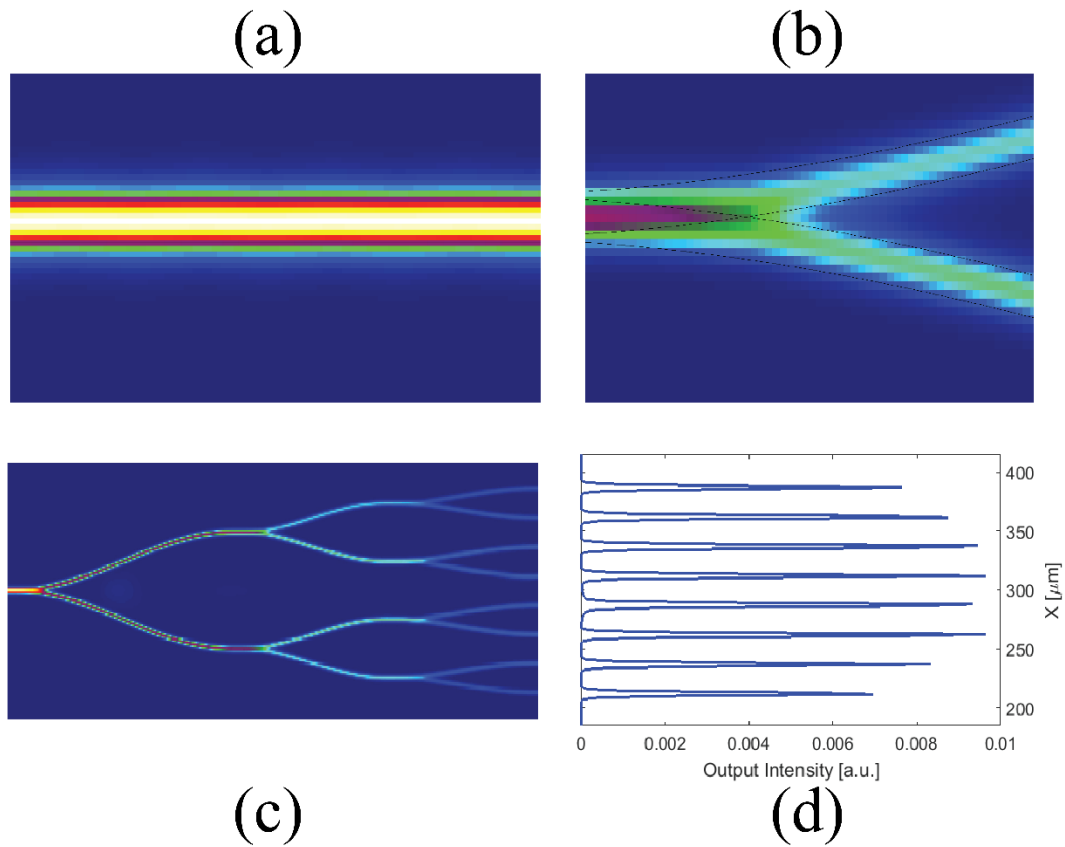


Fig. 4.9 Simulations of Y-splitters for a narrow single-mode waveguide (here: $w=4\mu\text{m}$). (a) Single mode propagation. (b) Balanced splitting of the power. (c) 1×8 Y-splitter waveguide showing a more balanced distribution of the total power. (d)

The output intensity profile of the 1×8 Y-splitter device in (c).

Another advantage of using Y-splitter waveguides is the narrow full width half maximum (FWHM) of the excitation spots. This is another important parameter to increase the SNR enhancement in the device, by allowing better suppression of the background. If the FWHM of the excitation spot is wider, the noise that is multiplied with the higher value at the sides of the peak does not get suppressed. This also creates higher values in the multiplied data for different ΔT values, creating deviations while determining ΔT values.

Taking all of these parameters and simulations into account, three different Y-splitter waveguides creating $N=2, 4$ and 8 spots were designed. The width of the waveguide is set to $w=4\mu\text{m}$ to ensure single-mode guiding. The fan-out angle of each splitter is kept below 2° , while the total lengths of the Y-splitter waveguide sections are kept below 6mm . Specifically, the Table 4.1 shows the design angles for the three separate designs, where $N=2, 4$, and 8 . The difference between each spot is kept at $25\mu\text{m}$ in order to create distinct spot patterns.

	1×2	1×4	1×8
<i>1st Split</i>	1.43°	1.727°	1.727°
<i>2nd Split</i>	-	1.400°	1.727°
<i>3rd Split</i>	-	-	1.400°

Table 4.1 The design angles for the three separate Y-splitter waveguide designs, where $N=2, 4$, and 8 .

Y-splitter devices were created using an optimized fabrication procedure discussed in Chapter 2. They have a single-over coating (SOC) and self-aligning pedestal (SAP) shown in Fig. 2.5c. Dielectric layers, SiO₂ (refractive index $n=1.47$) and Ta₂O₅ ($n=2.107$), with the thicknesses of 265/102/265/102/265/102 nm starting with SiO₂ in order of deposition, were deposited on Si wafers. A hollow channel, with the dimensions of $5.5 \mu\text{m} \times 12 \mu\text{m}$ was defined lithographically using SU-8. A $6\mu\text{m}$ thick SiO₂ layer was deposited in order to create the solid core layers including Y-splitters and the top sides of the liquid core channel. The SU-8 was then removed using a mixture of H₂O₂ and sulfuric acid, creating the hollow-core waveguide [165]. The details of the fabrication procedure can be found in Appendix E.2.

The spot patterns created by the Y-splitting devices were characterized by filling the liquid-core channel with quantum dots (Crystalplex) and introducing 633nm laser light into a single waveguide at the edge of the chip. The emitted light from quantum dots is imaged using a custom compound microscope. (see Appendix A.2 for details.) Fig. 4.10 shows the emission collected from the quantum dots at the excitation spots in the liquid-core waveguide, for all 3 designs. The plots are the excitation profiles obtained from the images on the top. It is clear that the Y-splitter waveguides created multiple, equally separated spots for all three designs. Table 4.2 shows more detailed analysis for the excitation patterns, showing the important characteristics of the spots. This analysis confirms the equal spacing between the spots ($\Delta x \approx 25\mu\text{m}$), with a very low deviation. It also shows the high peak (P) to valley (V) ratio for excitation spots, with a slight deviation in the peak values. Since there is very little scattering between the

output waveguides, the Y-splitters have a 4 times larger peak to valley ratio in the excitation region (~ 13), compared to MMIs (~ 4), which will be discussed in the Chapter 5.

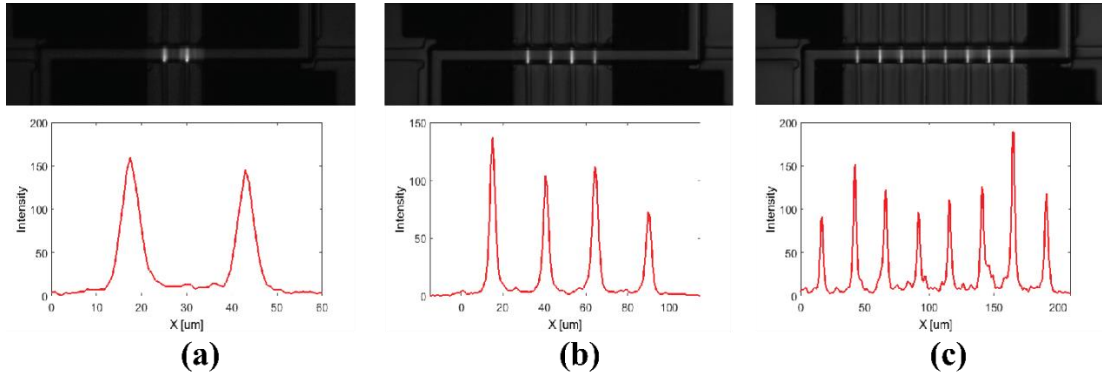


Fig. 4.10 The characterization of the excitation patterns for all three designs by using quantum dot solution in the liquid-core waveguide. The top images are the actual images taken from top, and the plots show the excitation patterns obtained from the actual images. (a) 1×2 Y-splitter (b) 1×4 Y-splitter (c) 1×8 Y-splitter

N	<i>Average</i> Δx	$\sigma (\Delta x)$	<i>Average P</i>	$\sigma (P)$	<i>Average</i> V	$\sigma (V)$
2	25.45	N/A	153	10	11.5	1.75
4	24.93	0.92	106	26.3	4.75	1.18
8	24.88	0.99	126	31.7	10.9	3.05

Table 4.2 Analysis on the excitation patterns shown in Fig. 4.10. Average and standard deviation values are shown for spot spacing (Δx), peak (P) and valley (V) values.

Fig. 4.11a shows the SEM image of the fabricated Y-splitter ARROW platform, showing the Y-splitter waveguides and liquid-core waveguide interface creating multiple excitation spots. Fig. 4.11b shows the experiment setup used for optical particle detection with multi-spot excitation. A 633nm HeNe laser is coupled into a single-mode fiber, which then butt-coupled into the Y-splitter section of the chip. The fluorescence signals emitted by the fluorescent particles or labeled viruses are collected orthogonal to the excitation through the liquid- and solid-core waveguides. An avalanche photo diode (Excelitas) is used to detect the fluorescence signal after removing the 633nm excitation wavelength with a band pass filter. The details of the setup can be found in Chapter 2, also in Appendix A.1.

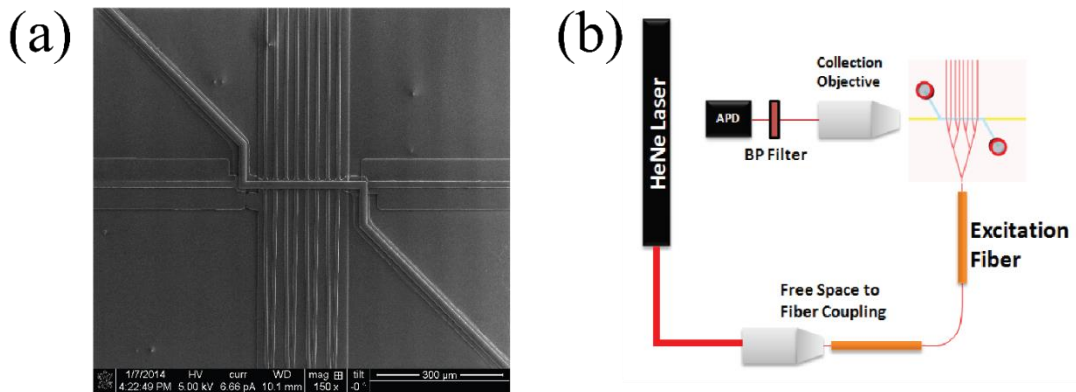


Fig. 4.11 (a) SEM image of the multiple excitation spots created by 1×8 Y-splitter waveguides. (b) Experiment setup used for particle detection.

4.2.2 Y-Splitter characterization with beads

In addition to the characterization of the multiple excitation spots done by using quantum dot solution and top imaging, the quality and the SNR enhancement properties

of the device is characterized by detecting fluorescent polystyrene microspheres. Fluorescent particles with a diameter of $0.2\mu\text{m}$ (Invitrogen Crimson Fluospheres 625/645) were introduced to the liquid-core analyte channel via inlet reservoir with a concentration of $\sim 10^7$ per mL, i.e. 0.1 particles per excitation volume. The concentration is kept low enough to avoid multiple particles in the excitation area at the same time. A HeNe ($\lambda=633\text{nm}$) laser was used to excite the fluorescent particles and a negative pressure is applied to a second reservoir to induce particle flow, and pull the particles through the channel and past the excitation area. As the particles travel down the liquid core, each particle passes these multiple optical excitation spots, which creates signals whose peaks are correlated in time and space. These signals are collected and detected, resulting in N sequential temporally encoded individual fluorescence peaks. Fig. 4.12a shows the particle trace of the raw data, $F(t)$, directly obtained by the detector, collected from the ARROW platform with 1×8 Y-splitter waveguides. Fig. 4.12b shows $F(t)$ for an individual particle detected in the same trace, showing the $N=8$ fluorescence peaks that is the result of an exposure to the multiple excitation spots. This clearly shows how the spatial encoding of the excitation pattern is translated into temporal encoding in the detected signal. Fig. 4.12c shows the individual particle signal collected from other devices with $N=4$ and $N=2$, showing the corresponding number of peaks in the detected fluorescence signal.

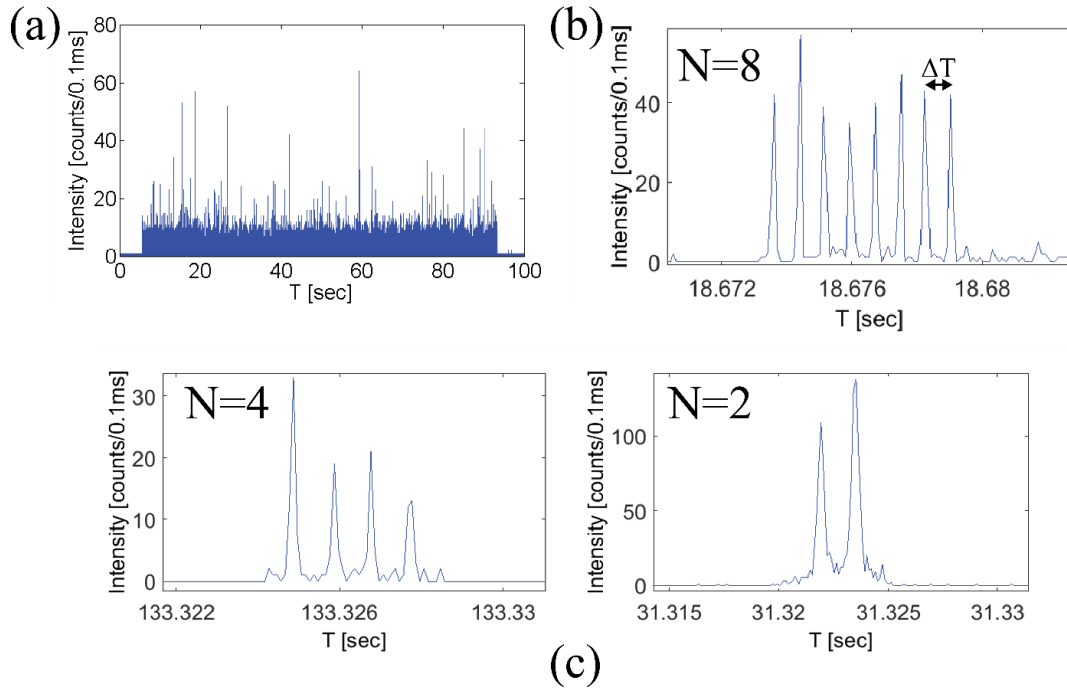


Fig. 4.12 (a) Particle trace of the raw data, $F(t)$ (b) $F(t)$ for an individual particle showing the $N=8$ fluorescence peaks from the data trace in (a). (c) $F(t)$ for an individual particle from separate experiments showing the $N=4$ and 2 fluorescence peaks.

The raw data trace $F(t)$ shown in Fig. 4.12a, shows $P=17$ counts per 0.1ms binning time per particle on average, with $\sigma=1.2$ and $\mu=0.57$ counts/0.1ms, leading to average particle signal to noise ratio of $SNR_o=29.8$. The peak intensities vary between particles due to the variation in dye amounts per particle, location in the channel, and speed in the excitation area which will be discussed later in this section. In order to show the enhancement by the algorithm in (4.1), the correct temporal spacing ΔT should be determined. A very effective method to find the average ΔT value is doing the autocorrelation analysis on the original signal. Fig. 4.13a shows the autocorrelation

curve for the single particle in Fig. 4.12b, which exhibits peaks at multiples of ΔT ; here 0.8 ms. The autocorrelation of the complete signal $F(t)$ allows us to determine the average ΔT value which is used to run the signal processing algorithm. Fig. 4.13b shows the $S(t)$ for the particle seen in Fig. 4.12b, after the signal processing algorithm is applied. For this experiment, we achieved an infinite SNR enhancement, due to the background noise reaching to zero, which is due to the zero points in the original signal. As explained with the equation (4.9), a single zero renders the entire product equation to zero, leading to further suppression of the background noise. When there are enough zeros, as in this case, the entire background noise can reach to zero, leading to infinite SNR enhancement, during the finite observation time. This phenomenon is more likely to happen if there are more number of multiplications (N), as shown in Fig. 4.5.

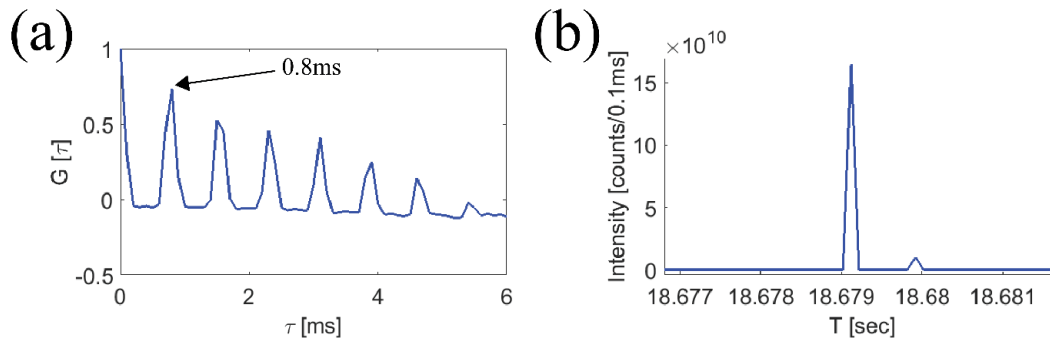


Fig. 4.13 (a) Autocorrelation curve for the single particle in Fig. 4.12b, which exhibits peaks at multiples of $\Delta T=0.8$ ms. (b) $S(t)$ for the particle shown in Fig. 4.12b, after the signal processing algorithm is applied.

Moreover, in order to demonstrate the SNR enhancement limits for the three designs with $N=2,4$, and 8, the characterization with lower SNR_0 should be carried out. In order to decrease the SNR_0 , background noise is added by introducing white light in the

detection environment. Fig. 4.14a shows the raw data trace collected from the ARROW platform with $N=8$ Y-splitter waveguides, with $P=16$ counts per 0.1ms binning time per particle on average, with $\sigma=1.66$ and $\mu=2.27$ counts/0.1ms. After the signal processing algorithm is applied, we achieved an SNR enhancement of 10^4 , where the $S(t)$ can be seen in Fig. 4.14b. It is important to note that few peaks with higher intensities could not be fit into the plot in order to show the smaller peaks that are enhanced. The contrast between the two figures shows the effectiveness of this method, by demonstrating the enhancement visually as well.

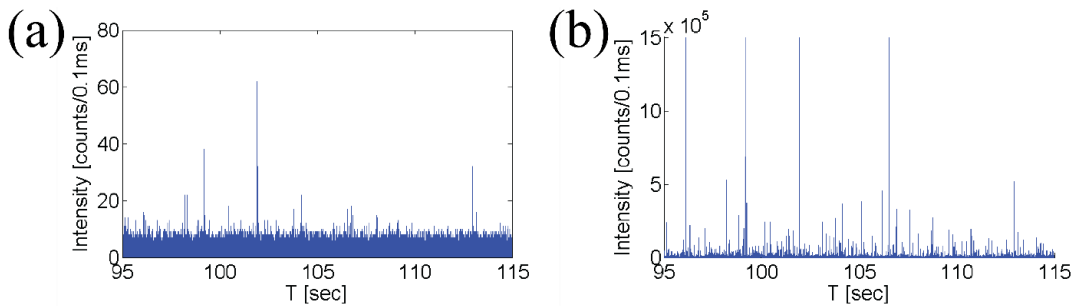


Fig. 4.14 (a) Original data trace collected from the ARROW platform with $N=8$ with added noise. (b) Data trace $S(t)$, after the SNR enhancement algorithm is applied.

In order to show the effect of N , experiments with white light noise were carried out for $N=2$ and $N=4$ devices as well. The same analytes are introduced, and the particles are detected under identical experimental conditions. The excitation power of the laser was adjusted to get similar average signal value P for the three experiments.

Table 4.3 shows the initial signal and noise values for all three experiments, and the SNR enhancement. The experimentally achieved SNR enhancement demonstrates a good match with theoretical calculations done based on the initial noise values,

although they have slightly lower values than the theory due to the imperfections in the spot patterns. Fig. 4.15 shows how the *SNR* enhancement increases exponentially with the number of spots (N) in these three experiments (symbols), providing a good match between the calculation (line) based on average μ and σ values. Due to the different properties of each individual chip, there is a slight variation in the noise (σ), mean (μ) and the average peak (P) values of the experiments, which results in the difference from the theoretical curves. It is evident that using 1×8 Y-splitters creates much higher *SNR* enhancement compared to 1×4 and 1×2 Y-splitters.

N	μ (initial mean)	σ (initial standard deviation)	<i>SNR Enh.</i> (Experiment)	<i>SNR Enh.</i> (Theory)
8	2.27	1.66	10^4	1.15×10^5
4	1.35	1.16	327	550
2	3.57	1.9	1.08	3.7

Table 4.3 The initial noise values, and the *SNR* enhancement for $N=2,4$ and 8 with added noise. The theoretical *SNR* enhancement based on the initial noise values is

also shown for comparison.

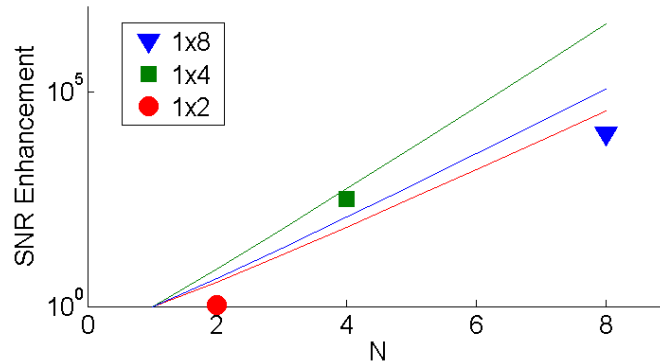


Fig. 4.15 *SNR* enhancement exponential dependence the number of spots (N) in these three experiments (symbols), providing a good match between the calculation (line) based on average μ and σ values

One of the main challenges of this process is caused by the variation of particle speeds when they move along the channel. This causes a variation in the ΔT value, making the algorithm less efficient. For this reason, it is important to make sure the particles are moving with a uniform speed. Increasing the velocity of the particles decreases the variation coming from the Brownian motion. However, at very high speeds, the fluorescence emission would decrease, causing the particle signal to be weaker. The velocity of the particles is also limited due to the flow characteristics of the liquid-core channel. Even if the particles move fast enough to overcome the variation due to the Brownian motion, there is still a variation in velocities depending on where the particle is located in the channel due to the Hagen–Poiseuille flow profile. This limits the efficiency of the algorithm [166]. (See Section 5.5 for more details.)

4.2.3 SNR Enhancement for single virus detection

In order to show the capacity and versatility of this device, it is crucial to demonstrate the high sensitivity detection and *SNR* enhancement by using real bio-particles. For this purpose, H1N1 Human Influenza virus is fluorescently labeled and the experiments are carried out in a similar manner as in the previous section. The fluorescence detection experiments are run on three different Y-splitter waveguide devices with $N=2, 4$ and 8 spots to show the advantage of the multiple-spot excitation with higher N .

Biological analyte is prepared by taking purified, inactivated H1N1 Human Influenza A/PR/8/34 Virus (Advanced Biotechnology Inc.) and labeling with Dylight 633 NHS ester-activated dye according to manufacturer specifications (Thermo Scientific). Unbound dye was removed by column chromatography using a PD MiniTrap G-25 column and $1 \times$ PBS elution buffer (GE Healthcare Life Sciences), and efficient labeling was verified by TIRF microscopy. (see Appendix D for details.)

First of all, the 1×8 Y-splitter device is used to show the high *SNR* enhancement of the method, proving this platform to be highly sensitive for bio-particle detection. The labeled H1N1 viruses were introduced to the inlet reservoir with a concentration of 10^7 per mL, i.e. 0.1 particles per excitation volume. Negative pressure was applied on the outlet in order to pull the particles through the channel and past the excitation area. Because viruses are exposed to 8 different excitation spots, they emit fluorescence signal in these multiple spots. This creates an 8-peak pattern per virus in the detected fluorescence signal. The particle trace of the raw data, directly obtained by the detector, can be seen in Fig. 4.16a, demonstrating that single viruses can be detected in flow on

this chip. $F(t)$ shows $P=30$ counts per 0.1ms binning time per particle on average, with $\sigma=2.2$ and $\mu=4.2$ counts/0.1ms, leading to average particle signal to noise ratio of $SNR_0=13$. Fig. 4.16b shows $F(t)$ for one of the detected viruses revealing 8 clear peaks, separated by ΔT . Fig. 4.16c demonstrates the autocorrelation curve for the single particle in 2b, which exhibits peaks at multiples of ΔT ; here 0.8 ms. The autocorrelation of the complete signal $F(t)$ allows us to determine the average ΔT value which is used to run the signal processing algorithm (4.1). Fig. 4.16d shows the processed $S(t)$ for the particle seen in Fig. 4.16b. On average, we achieve an SNR enhancement of 5×10^4 over the course of this experiment.

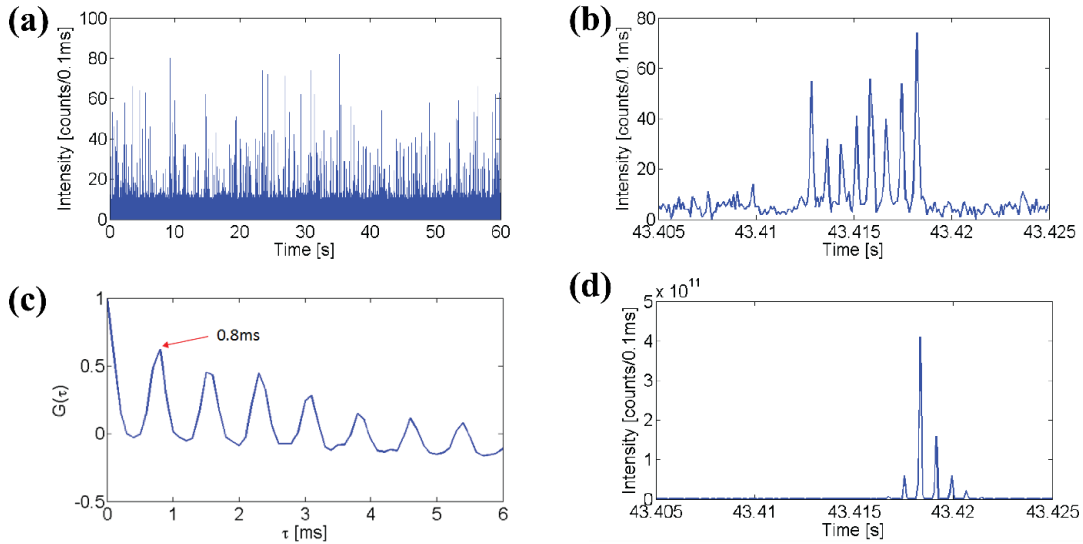


Fig. 4.16 (a) Red-dye labeled H1N1 virus detected by APD. (b) Single virus fluorescence signal demonstrating 8 clear peaks. (c) Autocorrelation curve of the single peak in 2(b), showing that the ΔT is around 0.8 ms. (d) Virus signal from 2(b) after signal processing for $N=8$.

On the other hand, the zero points of the original data affect the *SNR* enhancement as well. The initial probability of finding a zero, p_0 for this experiment is 0.019, the ratio of the number of bins with zero counts to total number of bins in the background data. Fig. 4.17 shows the probability of finding a zero in $S(t)$ according to (9) as a function of spot number for this experiment. For the present sample, $N=8$, and $p_{S=0}$ becomes 0.14, in excellent match with the theory (line).

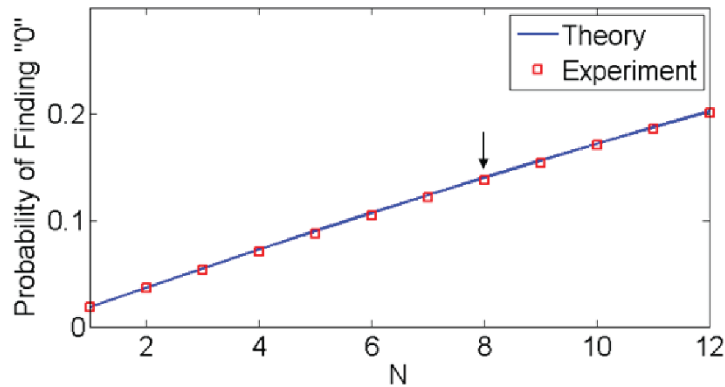


Fig. 4.17 Probability of finding zero values in noise for N multiplication. The marked spot shows where above experiment corresponds, with the probability of 0.14.

High variation of the ΔT values decreases the performance of the algorithm, since it is the key part of the algorithm to use the correct value for the time shift. It is important to observe the statistical distribution of this variation which is directly related to the particle velocities. Computing the autocorrelation on all individual virus signals allows us to determine the statistical distribution of ΔT and thus the particle velocities. Fig. 4.18 shows the histogram for the velocities of the detected particles, showing a relative

wide variation due to fluctuations in applied pressure and different locations within the Hagen-Poiseuille flow profile of the rectangular channel.

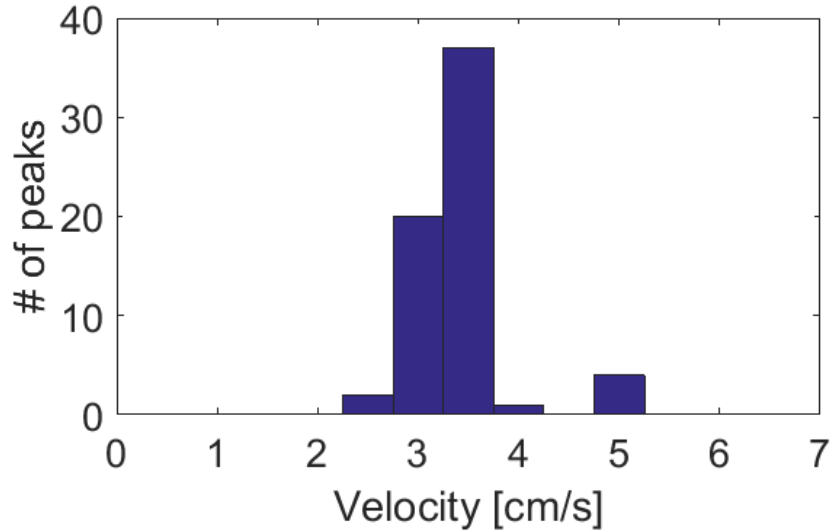


Fig. 4.18 Histogram of the particle velocities showing the variation due to the position of the virus in the channel.

More detailed analysis can be shown on Fig. 4.19a, demonstrating the theoretical calculation on how the properties of the background affect the SNR enhancement as discussed in the first section and where this particular experiment corresponds on them. In this curve, the variations in SNR_s / SNR_o according to (4.8) are depicted by varying the σ and μ , and taking the signal average value ($P=30$) from the experiment. The marked spot represents the experimental (σ, μ) values. An SNR enhancement of 2×10^5 is predicted, which is slightly higher than the experimental result due to variation in peak signal values for each detected particle and the ΔT variation coming from the different particle velocities. Fig. 4.19b shows the limits of the SNR enhancement, for

this experiment. The light region indicates where the *SNR* enhancement is above 1, and the dark region is below 1. The marked spot shows the value for our experiment.

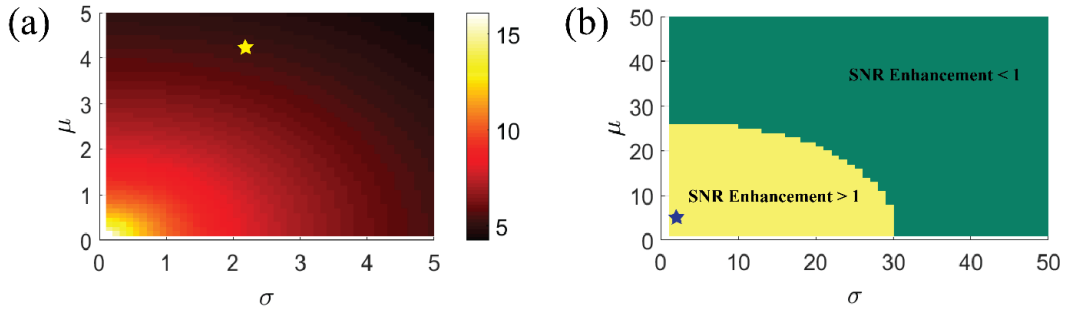


Fig. 4.19 (a) Theoretical analysis of *SNR* enhancement varying the noise and mean values using the signal average from the experiment. The marked spot corresponds to the experimental values of μ and σ with an *SNR* enhancement is 2×10^5 . (b) Theoretical analysis of the limits of the *SNR* enhancement. The light region shows the values at which the *SNR* enhancement is above one, and the dark region represents values at which the *SNR* enhancement is below one. The marked spot is the experimental values of μ and σ .

We have also shown the dependence of the *SNR* enhancement on the number of spots, by detecting fluorescently labeled viruses. The same analytes, labeled H1N1 viruses, are introduced to all three devices, with the concentration of 10^7 per mL. Viruses were then detected under identical experimental conditions. The excitation power of the laser was adjusted to get the similar average signal value P for the three experiments. The *SNR* parameters of these three experiments are shown in the Table 4.4. The experimentally achieved *SNR* enhancement demonstrates a good match with theoretical calculations. Fig. 4.20 shows how the *SNR* enhancement increases exponentially with

the number of spots (N) in these three experiments (symbols), providing a good match between the calculation (line) based on average μ and σ values. It is evident that using 1×8 Y-splitters creates much higher SNR enhancement compared to 1×4 and 1×2 Y-splitters for fluorescently labeled viruses as well. The 1×8 Y-splitter is also optimal for ARROW device dimensions because increasing the number of spots further would make the chip larger, and hence, the propagation loss higher. However, this problem can be addressed by replacing the Y-splitters with MMIs which makes it possible to get higher number of spots with significantly smaller dimensions.

N	μ [cnts/0.1ms]	σ [cnts/0.1ms]	P [cnts/0.1ms]	SNR_o	SNR Enh. (Experiment)	SNR Enh. (Theory)
8	4.22	2.2	30	13.6	52,794	198,000
4	5.84	2.47	37	15	62	111
2	4.49	2.17	43	19.8	4.72	6.4

Table 4.4 Table showing the noise, mean, and SNR values of the original data and the enhancement values after the signal processing.

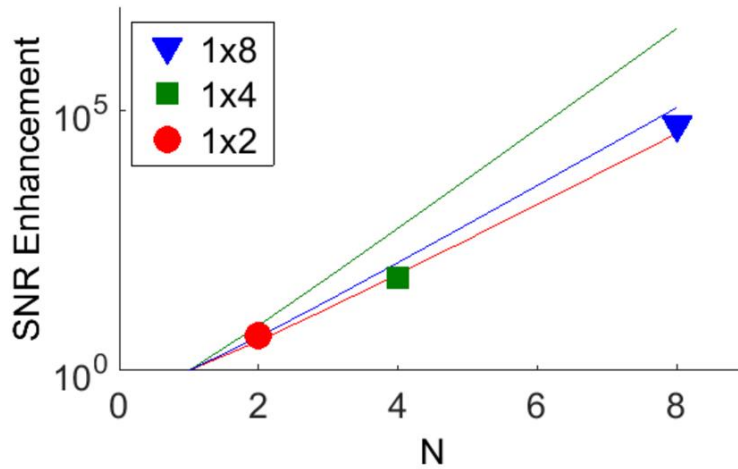


Fig. 4.20 Dependence of *SNR* on the number of excitation spots (*N*). Good match between the experiments (symbols), and calculations (lines) based on the μ and σ values of each experiment.

In conclusion, we have demonstrated large *SNR* enhancement for single virus detection on LC-ARROW chips that use Y-splitter waveguides to create temporally encoded fluorescence signals. First, the derivation and the theoretical analysis of the signal processing algorithm was introduced. The design and optimization of Y-splitter waveguides were presented and the challenges of the method were discussed. Y-splitter waveguides were successfully integrated to a LC-ARROW fluorescence spectroscopy platform, by creating multiple excitation spots at the detection area. Three different Y-splitter waveguides creating $N=2, 4$ and 8 spots were fabricated, characterized and tested using polystyrene beads and fluorescently labeled viruses as analytes. The temporally encoded fluorescence signal from single polystyrene beads and single H1N1 viruses were successfully collected and processed with a signal processing

algorithm. For virus experiments, 50,000 fold SNR enhancement was achieved in good agreement with theoretical analysis. The effect of number of spots in the signal enhancement process has been analyzed. It was shown that, with higher number of excitation spots, the *SNR* enhancement increases exponentially. Thus, the LC-ARROW platform with integrated Y-splitter solid-core waveguide array provides the best performance if maximizing the signal-to-noise ratio is critical. MMI-based multi-spot excitation is an alternative when using multiple wavelengths or minimizing chip dimensions is the goal.

5 *Multiplexed Bioparticle Detection based on Multi-Mode Interference (MMI)*

Early diagnosis and treatment have an important role in preventing the development of long-term complications and transmission of infectious agents [74]. Developing rapid diagnostics systems is crucial; however, it is a challenge to accurately diagnose infectious diseases due to their similar early symptoms, and low natural concentration levels of the pathogens [167]. Simultaneous detection of multiple pathogens and samples (multiplexing) is one of the key requirements for diagnostic tests in order to enable fast, accurate and differentiated diagnoses. In addition, a suitable multiplexing principle needs to be compatible with other desirable test features such as high sensitivity, low complexity, and high speed. A standard influenza test, for example, simultaneously screens for 8 pathogen types, enabling differential diagnosis of diseases with similar early symptoms [92]. For many types of cancers, it will not be sufficient to study a single protein marker, but rather a suite of markers that allow one to diagnose and follow the disease as a function of treatment [168].

Recently, many different biosensors have been developed to provide multiplexed sensing system for a large number of molecular species from a single solution with a small amount of sample. The current multiplexing detection methods for nucleic acids and proteins utilize mainly two different approaches, chip based (planar arrays) and particle based (suspended), both of which have application-specific advantages [169]. Planar arrays, such as DNA and protein microarrays, are best for applications requiring ultra-high-density analysis. Microarray immunoassays have been a successful multiplexing method where a large number of different probes for proteins or nucleic

acids are immobilized on a planar solid support that the identities of the probes are labeled as a specific positional address on the planar array [170]–[174]. On the other hand, particle based approach are more advantageous to use detecting a modest number of targets over large populations, by providing higher sample throughput, ease of assay modification and better quality control [169]. They allow for various different approaches for encoding, such as: spectrometric, electrochemical, magnetic, graphical and physical (size-based) [175]. Graphical encoding involves creating probes with functionalized areas in order to create visual pattern to identify the target molecules. The most common examples are test strips [176]–[178] and, bio-barcodes [168], [169], [179]–[182]. Multiplexing techniques based on electrochemical processes depend on the voltammetric signature of the probe with distinct electrical hybridization signals for the corresponding nucleic acid targets [183]–[186]. Magnetic methods utilize the distinct magnetic resonances of different magnetic nano-particles to distinguish among the target nucleic acids [187], [188].

One of the most common methods that is used for multiplexed biosensors is to use the distinct spectroscopic responses of the probes. In order to distinguish between the spectral responses, use of multiple different spectral channels that are dedicated to different target molecules is necessary. The ability to overlay multiple electromagnetic waves in the same physical space by virtue of linear superposition is arguably at the root of modern communication as we know it. Originally implemented in the radio frequency regime, this wavelength division multiplexing (WDM) principle was transferred to optical wavelengths in the visible and near infrared range which can be

carried by a single, low-loss silica fiber [189]. Here, the WDM principle from data communications is transferred into a different realm, that of chip-based biomedical analysis where multiple colors are superimposed to create multiplexed biosensors. Utilizing multiple channels within a single detection scheme allows for more compact devices with a simpler detection interface. This principle is used to create various multiplexing approaches using different optical components and their properties. Raman spectroscopy utilizes multiple nanoparticles as probes to distinguish multiple target molecules with multiple spectral channels [190], [191]. A similar idea of using multiple spectral channels was also adapted to refractometric sensors which spectrally respond to the refractive index change at the surface of the device. This approach is useful for implementing label-free detection. Multiplexed surface plasmon resonance sensors use different areas of sensing surface or different geometries to create different spectral channels [192]–[198]. Ring resonator arrays are also powerful multiplexing platforms, where the multiple spectral channels are created by using different sizes of ring resonators [199]–[201]. However, the main challenge of these platforms are the low efficiency of fluidic delivery to the device.

Fluorescence spectroscopy has been a very efficient method to implement multiple color detection of bio-molecules. Fluorescent dyes are commonly used to tag the target molecules. However, due to their overlapping spectra, they are limited to form only a few number of spectral channels. Quantum dots address this problem to some extent by allowing for fine tuning of the spectral response by simply adjusting the size [202],

[202]–[205]. This method still suffers from the need for spectral filters, and they depend on the successful de-multiplexing of the multiple channels based on the wavelength.

To address these problems, we implemented WDM on an optofluidic platform for on-chip analysis of bio-molecules. In place of silica fiber as the physical carrier, we created a single waveguide structure that combines multiple spectral channels for fluorescence excitation of biological targets. Instead of temporally modulating each channel to transport information, we use this waveguide to produce wavelength-dependent spatial patterns in an intersecting fluidic channel. The spatial encoding of spectral information then allows for direct identification of multiple labeled targets with extremely high sensitivity and fidelity without the need for a spectral de-multiplexing. The idea of transferring the spectral encoding into spatial or time encoding has been implemented on different platforms [155], [206]. This allows the spectral information to be obtained directly from the collected signal, based on the spatially encoded pattern.

We achieved spectral multiplexing on an optofluidic ARROW platform by using multi-mode interference (MMI) waveguides to create wavelength-dependent multiple excitation spots. Optofluidic devices based on MMI waveguides have been implemented for fluorescence detection, however they were only used for splitting purposes. Here, for the first time, we designed, characterized and implemented a novel optofluidic platform based on MMI waveguides for multiplexed fluorescence spectroscopy, by taking advantage of spectral and spatial capabilities of MMI devices. In this section, we first discuss the theory and the design of MMI waveguides, and integration on the ARROW optofluidic detection platform. Then, the characterization

procedures and important parameters for device qualities are discussed. Signal-to-noise ratio improvement on these platforms is shown by using the fluorescently labeled influenza viruses. The spectral multiplexing capabilities of these platforms are demonstrated by using two different approaches for direct counting and identification of individual virus particles from three different influenza A subtypes – H1N1, H2N2, and H3N2 – at clinically relevant concentrations. To further increase the multiplexing capability of these platforms, three different liquid-core waveguides are integrated onto these optofluidic MMI waveguides. This method utilizes the spatial multiplexing capacity of the MMI waveguides, and improved further by incorporating the spectral multiplexing approach. Finally, cascade MMI waveguides designed to direct different colors to different locations by using the asymmetrical properties of these devices are discussed.

5.1 Multi-mode interference waveguide design for spectral multiplexing

5.1.1 MMI waveguide theory

Multi-mode interference (MMI) devices are widely used in various optical platforms mainly for power splitting purposes. In addition to spatial characteristics of these devices, in our platform, we have also utilized their wavelength dependent response. Before demonstrating the novel optofluidic device based on MMI waveguides, it is essential to discuss its basic working principle and how it is adapted to our scenario. An MMI waveguide is basically a wide solid-core optical waveguide which can support numerous waveguide modes with different propagation constants that interfere as they

propagate along the structure. At propagation distances where the relative phases of these modes match up correctly, well-defined images (spot patterns), including self-images of the original input mode, are created [207]. Here, in this section, the theoretical background will be explained, closely following the work of Soldano and Pennings in 1995 [207].

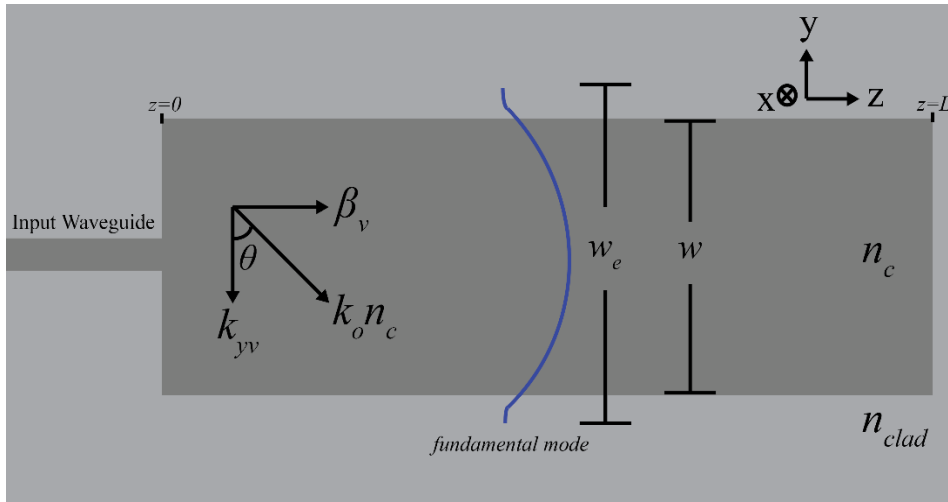


Fig. 5.1 The schematic for a MMI waveguide, depicting the device parameters and the propagation constants.

First of all, for the initial analysis of self-imaging properties of MMI waveguides, it is assumed that it is single-moded in the vertical direction, effectively simplifying the structure as 2D. A waveguide that can support multiple lateral modes is defined with a certain width (w), and length (L), refractive indices for core (n_c) and cladding ($n_{cladding}$) shown in Fig. 5.1. According to the V-number, $V = \frac{\pi}{\lambda} w \sqrt{n_c^2 - n_{cladding}^2}$, when the waveguide width (w) increases, the waveguide can support multiple modes. Based on the V-number, the waveguide supports m number of modes, labeled from $\nu=0, 1, \dots$

$(m-1)$ for a free space wavelength, λ . Representative shapes for these modes are illustrated in Fig. 5.2, showing the symmetrical and asymmetrical higher order modes.

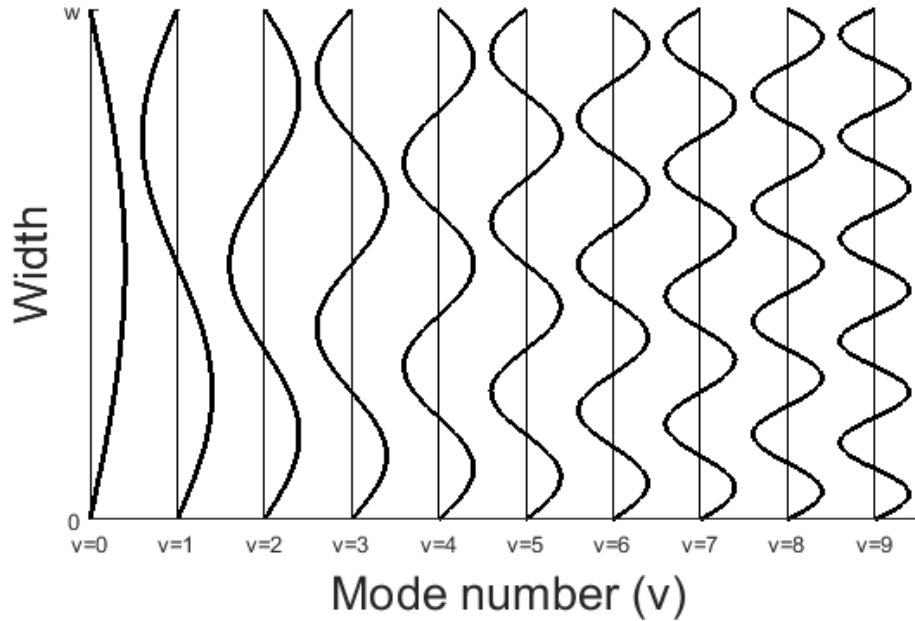


Fig. 5.2 Illustration of first 10 lateral modes in a MMI waveguide. Modes with even v numbers are symmetrical, odd v numbers are asymmetrical.

Fig. 5.1 shows the lateral wavenumber in y direction k_{yv} and the propagation constant β_v for the mode number v . They are related to the core index by the following equation:

$$k_{yv}^2 + \beta_v^2 = k_o^2 n_c^2 \quad (5.1)$$

with,

$$k_o = \frac{2\pi}{\lambda} \quad (5.2)$$

$$k_{yv} = \frac{(v+1)\pi}{w_{ev}} \quad (5.3)$$

where w_{ev} is the effective width of the MMI waveguide for the mode number v , which takes the mode penetration depth into account. The effective width of each mode can be approximated by the effective width of the fundamental mode, $w_{ev} \approx w_{e0} \approx w_e$, defined as:

$$w_e = w + \left(\frac{\lambda}{\pi}\right) \left(\frac{n_{clad}}{n_c}\right)^{2\sigma} (n_c^2 - n_{clad}^2)^{-1/2} \quad (5.4)$$

where $\sigma=0$ for TE, $\sigma=1$ for TM. For devices with a higher index contrast, penetration depth is small, so the effective width can be approximated to the width of the MMI waveguide, $w_e \approx w$. For example, for the devices we fabricated, it can be calculated that the penetration depth is $0.85\mu\text{m}$, very small compared to the MMI waveguide width $w=100\mu\text{m}$ (For $\lambda=0.633\mu\text{m}$, $n_{clad}=1.452$, $n_c=1.47$). Therefore, the effective width is taken as the MMI waveguide width for our calculations and however it was taken into consideration for the simulations and device design.

Starting from the equation (5.1), assuming that $k_{yv}^2 \ll k_o^2 n_c^2$, the propagation constants can be derived as follows:

$$\begin{aligned} \beta_v^2 &= k_o^2 n_c^2 - k_{yv}^2 \\ \beta_v &= [k_o^2 n_c^2 (1 - \frac{k_{yv}^2}{k_o^2 n_c^2})]^{1/2} \\ \beta_v &= k_o n_c [(1 - \frac{k_{yv}^2}{k_o^2 n_c^2})]^{1/2} \end{aligned} \quad (5.5)$$

Adapting first order binomial approximation $(1-x)^\alpha \approx (1-\alpha x)$ for $x \ll 1$, β_v can be rewritten as:

$$\beta_v = k_o n_c \left[1 - \frac{k_{yv}^2}{2k_o^2 n_c^2} \right] \quad (5.6)$$

$$\beta_v = k_o n_c - \frac{k_{yv}^2}{2k_o n_c}$$

Substituting equations (5.2) and (5.3), propagation constants for different modes are rewritten as follows:

$$\beta_v = k_o n_c - \frac{(v+1)^2 \pi \lambda}{4w_{ev}^2 n_c} \quad (5.7)$$

The coupling/beat length of the two lowest order modes, where the two modes are out of phase, is defined as follows:

$$L_\pi = \frac{\pi}{\beta_0 - \beta_1} \approx \frac{4n_c w^2}{3\lambda} \quad (5.8)$$

Combining the equations (5.7) and (5.8), the propagation constant spacing can be written as:

$$\beta_0 - \beta_v \approx \frac{v(v+2)\pi}{3L_\pi} \quad (5.9)$$

At position $z=0$, at the input of the MMI waveguide, input field profile $\Psi(y,0)$ can be written as the composition of the modal field distributions $\psi_v(y)$ of all guided modes. c_v is the field excitation coefficient which can be derived from the overlap integrals of the input field with the mode field distributions.

$$\Psi(y, 0) = \sum_{v=0}^{m-1} c_v \psi_v(y)$$

$$c_v = \frac{\int \Psi(y, 0) \psi_v(y) dy}{\sqrt{\int \psi_v^2(y) dy}} \quad (5.10)$$

The field profile at position z is simply the superposition of the all guided mode field distributions:

$$\Psi(y, z) = \sum_{v=0}^{m-1} c_v \psi_v(y) e^{j(\omega t - \beta_v z)} \quad (5.11)$$

The phase of each guided mode can be rewritten in relation to the phase of the fundamental mode, the equation (5.11) can be transformed into:

$$\Psi(y, z) = e^{j\omega t - j\beta_0 z} \sum_{v=0}^{m-1} c_v \psi_v(y) e^{j(\beta_0 - \beta_v)z} \quad (5.12)$$

where the time dependent part of the phase, $e^{j\omega t}$, is implicit for the rest of the analysis.

Combining the equations (5.9) and (5.12), the total field at the distance $z=L$ can be written as:

$$\Psi(y, L) = \sum_{v=0}^{m-1} c_v \psi_v(y) e^{j\left(\frac{v+2}{3L\pi}\right)L} \quad (5.13)$$

This shows that the mode phase factor will determine how the modes interfere with each other, for certain conditions, the self-image of the input mode profile will be produced, $\Psi(y, L) = \Psi(y, 0)$. The condition to obtain single-image mode profile can

be derived by making the mode phase factor equal to 1 for direct replica, -1 for mirrored replica of the input mode field.

$$e^{j\left(\frac{v(v+2)\pi}{3L_\pi}\right)L} = (-1)^v \quad (5.14)$$

It is clear that, the condition in equation (5.14) can be fulfilled by the following condition:

$$L = p(3L_\pi) \text{ with } p = 0, 1, 2, \dots \quad (5.15)$$

which result in direct self-images when p is even ($\psi_v(y)$), and mirrored images when p is odd ($-\psi_v(y)$). This property of MMI waveguides is commonly used to build bar and cross couplers [208]. In section 5.4, this property of MMI will be discussed to create cascade MMI waveguides.

At certain lengths, an MMI waveguide produces multiple images of the input mode field. If we consider the position in between the direct and mirrored images, the total guided mode profiles can be derived as follows:

$$\begin{aligned} &\text{for } L = \frac{P}{2}(3L_\pi) \text{ with } p = 1, 3, 5, \dots, \\ \Psi\left(y, \frac{P}{2}(3L_\pi)\right) &= \sum_{v=0}^{m-1} c_v \psi_v(y) e^{j(v(v+2)\pi\frac{P}{2})} \end{aligned} \quad (5.16)$$

By taking into account the mode field symmetry properties, this condition can be rewritten as:

$$\begin{aligned}\Psi(y, \frac{p}{2}(3L_\pi)) &= \sum_{v=even} c_v \psi_v(y) + \sum_{v=odd} -j^p c_v \psi_v(y) \\ &= \frac{1+(-j)^p}{2} \psi(y, 0) + \frac{1-(-j)^p}{2} \psi(-y, 0)\end{aligned}\quad (5.17)$$

This equation shows that, at the positions of $z = \frac{1}{2}(3L_\pi), \frac{3}{2}(3L_\pi), \frac{5}{2}(3L_\pi), \dots$, the total mode field is the combination of direct and mirrored images of the input mode field, with the amplitudes of $1/\sqrt{2}$. This property of MMI waveguides is commonly used for equal power splitting purposes. The equation (5.16) can easily be translated into multiple images more than two:

$$L = \frac{p}{N}(3L_\pi) \text{ with } p \geq 0 \quad (5.18)$$

where N is the number of images produced at distance L , where the amplitudes of these profiles are derived as $1/\sqrt{N}$.

Furthermore, in certain MMI devices, only some portion of the waveguides can be excited, which is called restricted interference, which can be realized in couple different ways. In our basic MMI waveguide detection platform design, we used the symmetric input mode profile, which couples into only the symmetric modes in the waveguide. This allows the self-images of the input mode profile to form at the distances four times shorter than the unrestricted modes [209]. Thus, the single images of the input mode field are obtained at the distances:

$$L = p\left(\frac{3L_\pi}{4}\right) \text{ with } p = 0, 1, 2, \dots \quad (5.19)$$

where the N -fold images of the input mode field will be obtained at distances of:

$$L = \frac{p}{N}\left(\frac{3L_\pi}{4}\right) \text{ with } p = 0, 1, 2, \dots \quad (5.20)$$

Fig. 5.3 shows the simulation for an MMI waveguide pattern with a symmetrical single-mode input. The self-image ($N=1$) and the multiple images ($N>1$) are depicted at the distances where the equation (5.20) suggests.

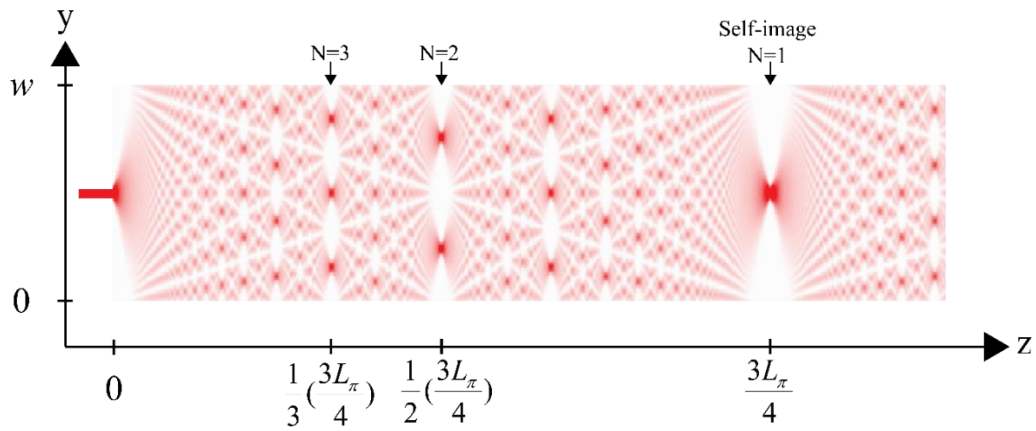


Fig. 5.3 The simulated MMI waveguide pattern for a symmetrical single-mode input, showing the self-image and multiple image formations at different positions along z axis.

Substituting the equation (5.8) into equation (5.20) gives the relationship between the number of images (N) obtained at the distance L for a MMI device with a certain width (w) and refractive index (n_c) at an input wavelength of λ , as following:

$$N = \frac{n_c w^2}{\lambda L} \quad (5.21)$$

The equation (5.21) will form a basis to understand the dependence of the number of excitation spots (N) on excitation wavelength (λ) and MMI device length (L). There are two important conclusions derived from this equation:

The first one applies to the case when the length (L), width (w), and the refractive index (n_c) of MMI device are constant, which is the case for a fabricated structure. Then the product of N and λ is constant. This allows us to implement on-chip WDM *spectral* multiplexing by creating physically different excitation patterns for different wavelengths, simultaneously from a single MMI waveguide, which is discussed in section 5.2.

The second conclusion is that for fixed width (w), and the refractive index (n_c), and a single wavelength (λ), the product of N and L is constant. This dictates that for different positions along the MMI device, we could obtain different number of excitation spots, which allows the *spatial* multiplexing optofluidic platform, which is discussed in section 5.3.

The high multiplexing capacity is also achieved by combining these two approaches, *spectral* and *spatial* multiplexing, by creating physically different excitation patterns, with different N .

5.1.2 MMI waveguide design and simulations

In order to create a highly functional MMI waveguide structure for multiplexing purposes, the design of the waveguide has to be done considering different parameters. The goal of this device is to be able to create multiple excitation spots in order to excite a particle moving along the liquid-core channel with this excitation pattern, where the number of spots (N) is dependent on the excitation wavelength, discussed in the previous section. First of all, the excitation spots need to be highly resolved to achieve successful distinction among different wavelengths and high signal to noise ratio enhancement by using the time spacing between the peaks. Another consideration is to be able to design a device that is compatible with the most common fluorescent dyes that are in the visible range. The size of the device should also be optimized to the space and fabrication requirements.

Device Design

1. Compatibility with the available fluorescent dyes:

For fluorescence spectroscopy, to detect the target molecules, they need to be labeled with fluorescent dye. Since the excitation pattern depends on the excitation wavelength, the spectral multiplexing channels should be chosen to prevent overlap and cross-talk between the absorption spectra of the corresponding fluorescent dyes. Minimizing the overlaps between the absorption spectra and using the wavelength of a widely available HeNe laser as a center design wavelength, six different multiplexing channels are designed. The product of $N \cdot \lambda$ is constant for fixed length, width and refractive index

(refer equation (5.21)). Therefore, the spectral channels are designed as shown in Table 5, with the corresponding available fluorescent dyes.

N (Number of Excitation Spots)	λ [nm] (Excitation Wavelength)	Fluorescent Dye
6	738	DyLight [®] 755, Alexa Fluor [®] 750
7	633	DyLight [®] 633, Alexa Fluor [®] 633
8	553	DyLight [®] 550, Alexa Fluor [®] 555
9	492	DyLight [®] 488, Alexa Fluor [®] 488
10	442	Alexa Fluor [®] 430
11	402	DyLight [®] 405, Alexa Fluor [®] 405

Table 5. The multiple channels designed for spectral multiplexing with MMI waveguides.

This shows that, the number and spectral positions of these six channels are a perfect match to the absorption spectra of commercially available fluorescent dyes [210]. Six different channels can be used for multiplexing, each dedicated to a different target, for the single-color MMI optofluidic detection procedure which is described in section 5.2.1. This multiplexing capability is ultimately limited by the finite absorption and emission bandwidths of the dye labels which can lead to channel cross-talk if the absorption spectra overlap.

2. Resolution of the excitation spots:

First of all, the resolution of the MMI waveguide spots is dictated by the condition that the number of modes supported (m) needs to be larger than the number of spots (N).

This condition can be written as follows:

	$m = \frac{w\sqrt{n_c^2 - n_{clad}^2}}{\lambda} > N$ $w > \frac{N\lambda}{\sqrt{n_c^2 - n_{clad}^2}}$	(5.22)
--	---	--------

In our design, the maximum number of spots is $N=9$ at $\lambda=492\text{nm}$. We have used the effective refractive index values from the ARROW device fabrication, which are $n_c=1.47$ and $n_{clad}=1.452$. This calculation shows that the width of the MMI waveguide should be at least $w_{min}=21\mu\text{m}$ where $m=10$.

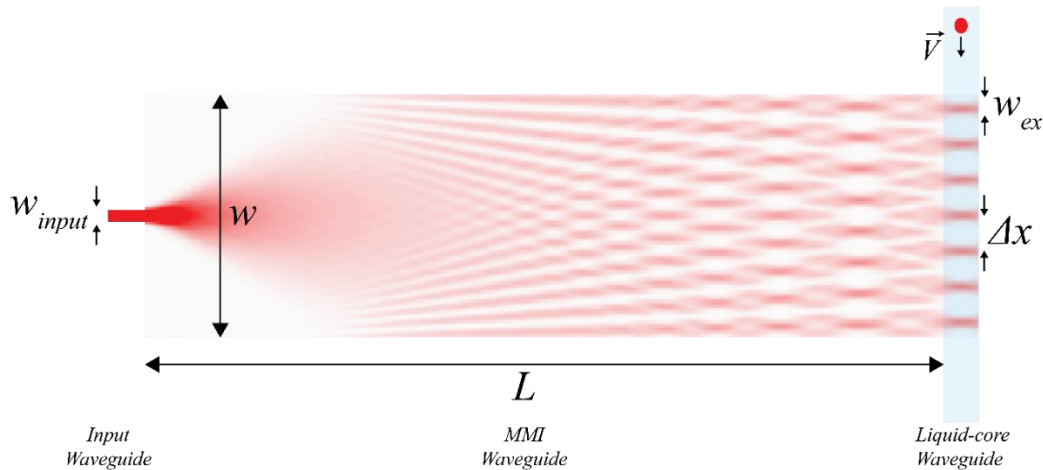


Fig. 5.4 Sketch of MMI waveguide with liquid-core waveguide, showing the design parameters.

The second parameter to create highly resolved spots for the actual detection is to make sure that the spacing between the excitation spots Δx is bigger than the excitation spot

width, w_{ex} . w_{ex} eventually translates into the temporal width of the collected signal, as the particle traveling with a speed of V along the channel, it is exposed to the excitation signal (see Fig. 5.4). The relationship between them is directly derived by the $\tau = \Delta x / V$ where τ is the temporal width of the signal pulse. Since the excitation spots are the images of the input mode field, as explained in the previous section, the excitation spot width w_{ex} is equal to the input mode width. For fabricated ARROW structures, the input solid-core waveguide width is typically $w_{input}=4\mu\text{m}$ in order to satisfy single-mode condition. The input mode width is taken as the FWHM value of the mode profile, which is approximately, $w_{ex}\approx 2.8\mu\text{m}$. The spacing between the excitation spots is defined as, $\Delta x = w / N$. In order to satisfy the condition of $\Delta x > w_{ex}$, width of the MMI waveguide should be at least $w_{min}=25.2\mu\text{m}$ for $N=9$. This also sets the minimum length of the MMI from the equation (5.21) to $L_{min}=211\mu\text{m}$.

So far, all of these limits are compatible with the size limitations of the optofluidic platform. However, one last condition that affects the resolution of the excitation spots is the need to distinguish the individual wavelengths with different spot patterns based on Δx . This requires the difference between the Δx values for different wavelengths to be bigger than the excitation spot width: $\Delta x_1 - \Delta x_2 = w(1/N_1 - 1/N_2) > w_{ex}$. Taking the smallest wavelengths in the design into account as our limit, minimum width can be found as, $w_{min}=216\mu\text{m}$, which results in $L_{min}=15,489\mu\text{m}$. However, due to the limitations of the fabrication process, the space considerations, and to keep the device more compact, this condition cannot be satisfied.

Taking all of these into account, the width of the MMI waveguide is fabricated with three different width and length pairs, $w=50\mu\text{m}$, $L=875\mu\text{m}$; $w=75\mu\text{m}$, $L=1900\mu\text{m}$; and $w=100\mu\text{m}$, $L=3400\mu\text{m}$. Due to the higher resolution, the devices with $w=100\mu\text{m}$ were found to be the most suitable for our applications with the standard MMI waveguide platform.

Simulations

Beam propagation software (FimmPROP, Photon Design) was used to confirm the designs based on the calculations. The MMI device with dimensions of $w=100\mu\text{m}$, $L=3400\mu\text{m}$ is built and the effective refractive indices are obtained from the mode analysis in vertical direction. The simulation is run by using a single-mode solid-core waveguide to introduce the input mode field. Single-mode input field is then coupled into the wide MMI waveguide, where more than 55 modes are supported for the lowest wavelength ($\lambda=402\text{nm}$). 2D effective index method is used to propagate the multiple modes along the length of the MMI (z axis), and multiple images are formed at certain distances. The output total mode profile is obtained at $z=L=3400\mu\text{m}$, showing the number of spots (N) corresponding to that wavelength.

Fig. 5.5 shows the MMI waveguide patterns for different design wavelengths on the same device. The total mode profile at distances $z=L=3400\mu\text{m}$ is shown on the right hand side, demonstrating the different number of excitation spots (N) for different wavelengths. Note that the intensity of the excitation spots is determined by the

$1/\sqrt{N}$ of the total power. This relation is observed in

Fig. 5.5, as the number of spots get smaller, the intensity of the excitation spots increases.

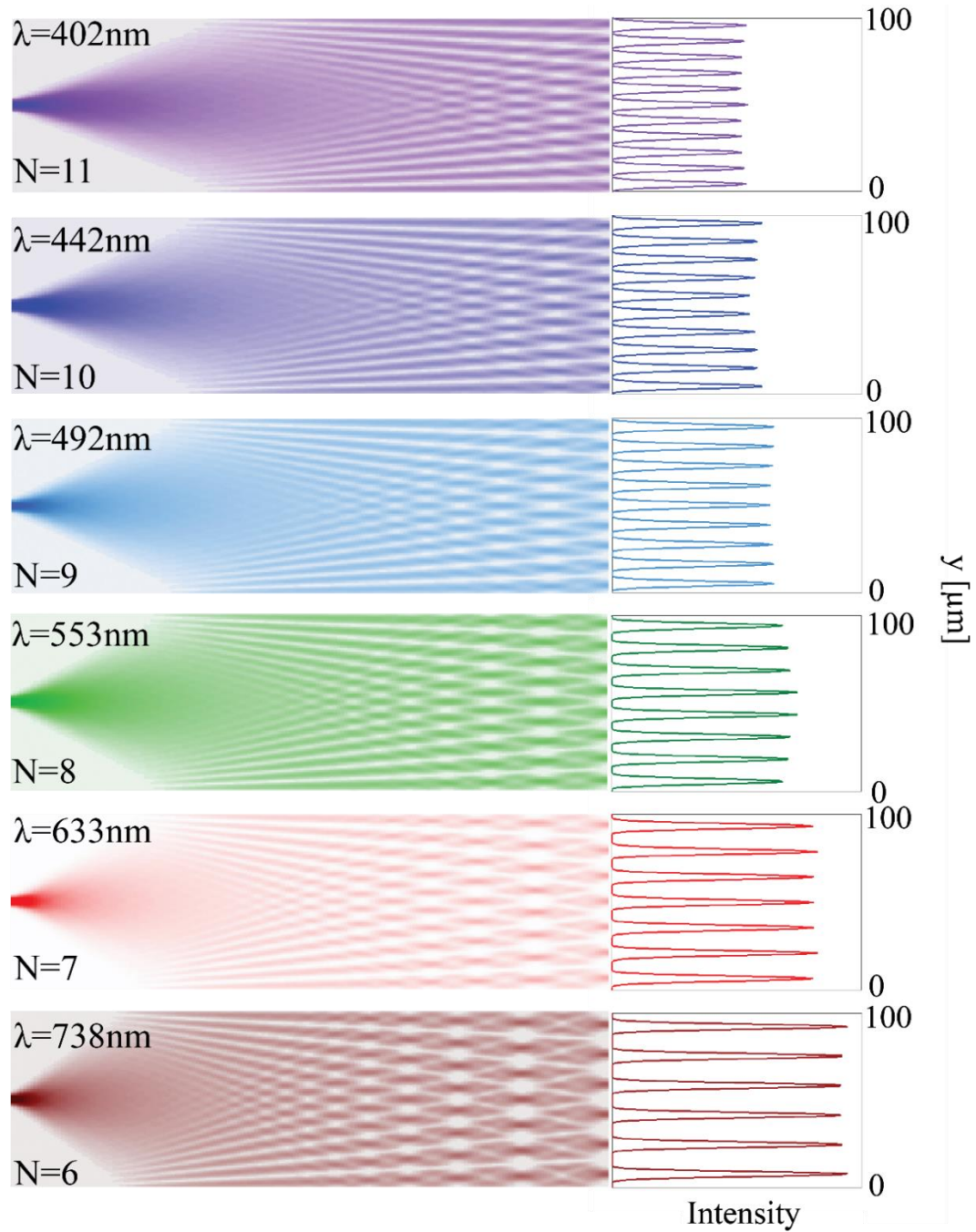


Fig. 5.5 The simulated MMI waveguide patterns on the same device by using a beam propagation method. The relationship between N and λ is shown for the design wavelengths. The total output mode field is demonstrated on the right hand side, for the corresponding wavelengths.

The simulated total output mode pattern at $z=L=3400\mu\text{m}$ is shown in Fig. 5.6, for $w=100\mu\text{m}$, $\lambda=633\text{nm}$ with $N=7$. For an ideal excitation pattern, the Δx value should be equal to w/N , for each pair of excitation spots. The width of the excitation spot, w_{ex} (here FWHM), should be narrow to prevent the cross-talk between the spectral channels. The intensity of the excitation spots, P , should also be uniform among all of them, splitting the power equally. The background value in between the excitation spots should ideally be zero as well.

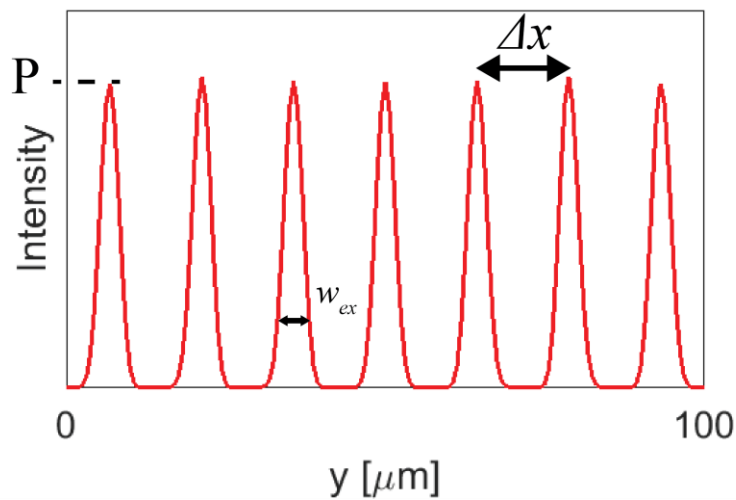


Fig. 5.6 The simulated output pattern of the MMI waveguide at $L=3400\mu\text{m}$ is demonstrated for $w=100\mu\text{m}$, $\lambda=633\text{nm}$ with $N=7$. The important parameters of the excitation pattern are shown where P is the intensity of excitation spot.

Effect of Input Waveguide Dimensions on the Output Pattern

Since the excitation spots are the direct replicas of the input mode, the design of the input mode waveguide has a huge effect on the excitation pattern. In our design, we have assumed that a single-mode input waveguide located at the center along the y axis ($y=w/2$) is used to couple light into the MMI waveguide. This allowed for applying the symmetrical restricted condition, which we based our design on. The single-mode condition should be satisfied not only for y-direction (lateral), but also for x-direction (vertical). However, due to the limits of the fabrication process, the width and the height cannot always be precisely controlled, resulting in wider or higher input waveguides than the design ($w_{\text{input}}=4\mu\text{m}$, $h_{\text{input}}=6\mu\text{m}$), supporting higher order modes. Therefore, it is important to analyze and demonstrate the effect of input waveguide dimensions on the output MMI waveguide pattern.

The design of the input waveguide is based on the simulations, where only the fundamental mode is supported both lateral and vertical directions. The number of modes supported in a waveguide increases as the dimension increases, as well as the excitation wavelength decreases (see equation (5.22)). As the input waveguide gets wider or taller, it starts supporting higher order modes, which are then coupled into the MMI waveguide. All of the analysis is done on “through-etch” waveguide structures, where the cladding of the waveguide is etched down to the pedestal, creating air interface on both sides of the core.

First of all, Fig. 5.7 shows the 3D simulation of the MMI waveguide pattern when it is excited with a single-mode input waveguide, for both horizontal and vertical directions.

The input waveguide dimensions are taken as $w_{\text{input}}=4\mu\text{m}$ and $h_{\text{input}}=5.8\mu\text{m}$, based on a fabricated structure. Fundamental mode shown in Fig. 5.7a, propagates through the input waveguide and couples into the MMI waveguide, eventually creating the multiple images of the input mode field at the output. Fig. 5.7b shows the cross-section of the MMI waveguide at the output where $z=L=3400\mu\text{m}$, where the excitation spots are narrow and uniform among both directions. The average full width half maximum (FWHM) of the excitation spots is calculated as $3.7\mu\text{m}$.

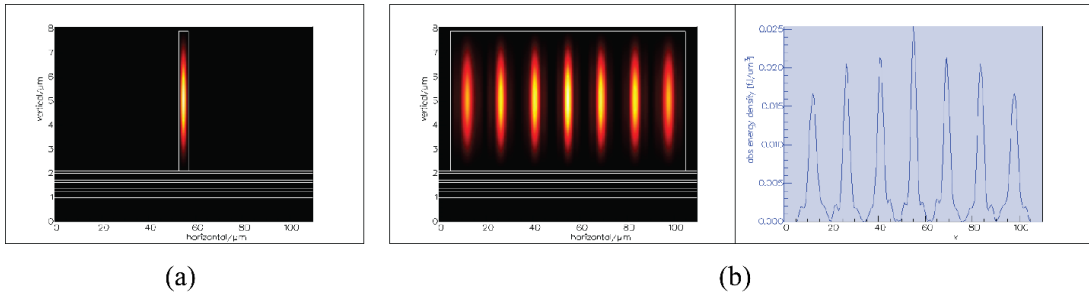


Fig. 5.7 (a) Cross section of the input waveguide pattern for single-mode excitation. (b) The total output mode field shown at the cross section of the MMI at $z=3400\mu\text{m}$.

When the input waveguide width is increased to $w_{\text{input}}=10\mu\text{m}$ and the height is kept the same ($h_{\text{input}}=5.8\mu\text{m}$), higher order modes in horizontal direction can be supported. While multiple modes propagate through the input waveguide, they interfere with each other and create a beat pattern, which switches back and forth between the multiple and single-mode pattern (Fig. 5.8a). If the beat pattern formed at the interface of the input and the MMI waveguides has the multi-mode phase, the MMI waveguide pattern will no longer be restricted. Therefore, the output pattern will reflect the multi-mode input mode profile, making it wider and distorted. Fig. 5.8b shows the cross section of the

MMI waveguide output, showing the distorted pattern, with wider excitation spots. The average FWHM of the excitation spots is calculated as $7.3\mu\text{m}$.

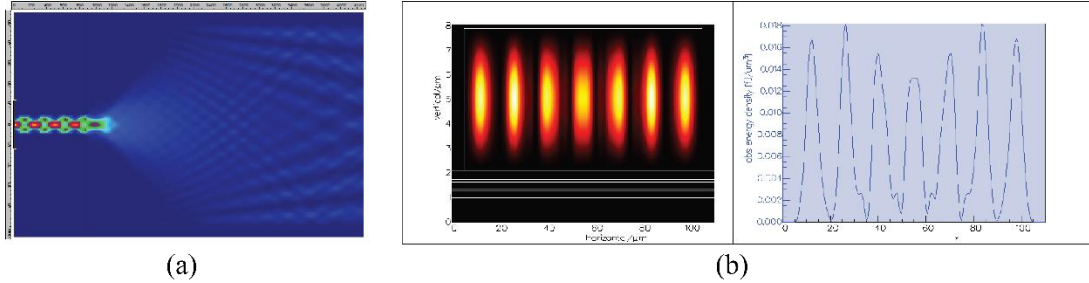


Fig. 5.8 (a) The 3D simulation of input and MMI waveguide pattern for multi-mode input excitation in horizontal direction. (b) The total output mode field shown at the cross section of the MMI at $z=3400\mu\text{m}$.

The same effect is observed when the height of the input waveguide is increased to $h_{\text{input}}=10\mu\text{m}$, while the width is kept at $w_{\text{input}}=4\mu\text{m}$. Higher order modes in vertical direction are supported, which then couple into the MMI waveguide. The beat pattern forms in vertical direction (see Fig. 5.9a), and the multi-mode input mode profile in vertical direction is introduced to the MMI waveguide (see Fig. 5.9b). This creates distortion in the vertical direction of the output mode profile (see Fig. 5.9c). It is important to note that, since the particles are moving along the y-axis (horizontal direction), vertical multi-mode behavior does not contribute to the increase in the width of the excitation spots (w_{ex}) as much as the horizontal multi-mode behavior. However, depending on where the particle is located on the vertical direction, it will be exposed to slightly different patterns, creating non-uniformity among the collected signal. The average FWHM of the excitation spots is calculated as $3.4\mu\text{m}$.

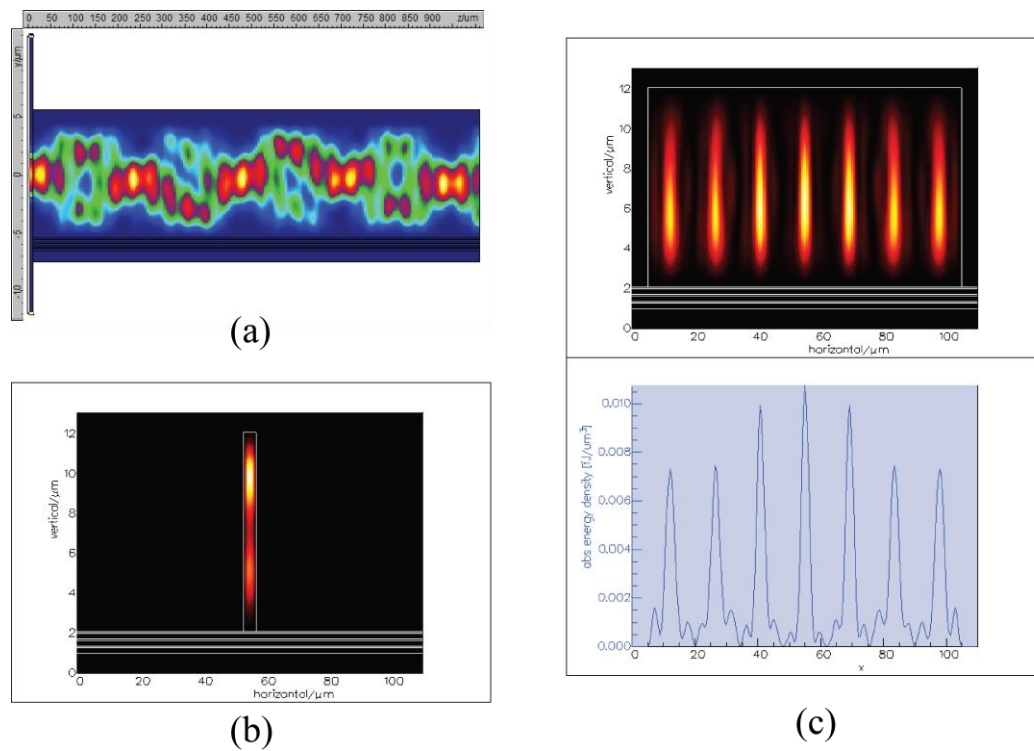


Fig. 5.9 (a) The side view of 3D simulation of input waveguide pattern for multi-mode input excitation in vertical direction. The beat pattern in vertical direction is observed. (b) Cross section of the input waveguide pattern for vertical multi-mode excitation. (c) The total output mode field shown at the cross section of the MMI at $z=3400\mu\text{m}$. The plot shows the intensity profile in the middle of the waveguide vertically.

To conclude, the input waveguide dimensions have a direct impact on the MMI waveguide output pattern and the excitation spot width (w_{ex}). In order to get excitation spots without distortions, the input waveguide dimensions should be kept small enough to support only fundamental mode. The simulations also showed that the multi-modal behavior in the horizontal dimension deteriorates the MMI waveguide output profile

more dramatically than the vertical dimension. Furthermore, keeping the input waveguide width narrower not only ensures the single-mode input profile, but also creates narrower excitation spots as the input mode width gets smaller with narrower input waveguide.

Integration of MMI waveguide on ARROW optofluidic platform

In order to create multiplexed detection scheme, MMI waveguides are integrated on the ARROW optofluidic platform discussed in Chapter 2. The solid-core excitation waveguide is simply replaced by the MMI waveguide, where the end of the waveguide is intersecting the liquid-core waveguide orthogonally. We designed the MMI based on the calculations and the simulations discussed in the previous section, so that a fluidic microchannel intersects the waveguide at a position that corresponds to a well-defined, integer number of spots for multiple wavelengths. Fig. 5.10 schematically shows the principle of WDM fluorescence detection on an optofluidic chip, demonstrating how the MMI waveguide is intersecting the liquid-core waveguide. On the other side of the liquid-core waveguide, an identical MMI waveguide is created with 7 output single-mode waveguides in order to observe the excitation pattern with $N=7$ through these waveguides. This side can also be used for excitation, by simply using the single-mode waveguide in the center. Furthermore, a single-mode excitation waveguide is built right next to the MMI waveguide for characterization purposes. In MMI waveguide, since the total power is split into N different excitation spots, the single-mode waveguide can deliver more power with its single excitation spot. This allows for the characterization of the target molecules.

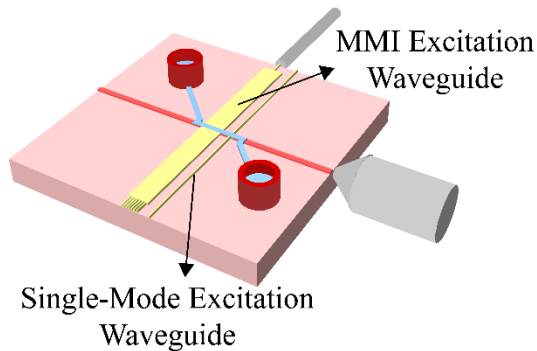


Fig. 5.10 The schematic of ARROW fluorescence detection platform based on MMI waveguides.

A simplified version of the optical setup used for the experiments is illustrated in Fig. 5.11. The full setup implements multiple lasers, a 488 nm Ar-Ion laser, a 556nm DPSS laser, a 633nm HeNe laser, and a Ti:Sapphire laser tuned to ~ 745 nm in CW mode. All of the laser lines were coupled into a single mode fiber (see Appendix A.1). Alternatively, a white light laser (NKT SuperK Extreme) passing through a multi-line tunable filter with a narrow bandwidth (NKT SuperK Select) can be coupled into the single-mode fiber. The single-mode fiber is then butt coupled into a narrow ($4 \mu\text{m}$) single mode excitation solid-core waveguide on the ARROW optofluidic chip. The single-mode waveguide ends in the center of the $100 \mu\text{m}$ wide and 3.4 mm long MMI waveguide. In the MMI waveguide, multiple modes interfere with each other, creating equally separated spots at the liquid-core waveguide section. Fluorescently labeled particles passing through the MMI waveguide excitation volume are subjected to the MMI waveguide pattern and thus produce multiple fluorescence signals per particle. These signals are captured by the liquid-core waveguide, transmitted into the collection

solid-core waveguide, and are collected at the chip facet by an objective. The signal is collimated, passed through a single penta-bandpass optical filter (FF01-440/521/607/694/809-25, Semrock) to eliminate the excitation wavelengths, and is finally detected by a single photon avalanche diode (Excelitas). No spectral filters to separate the emission colors are required. (see Chapter 2 for more details) This detection scheme requires only a single photodetector for multiple fluorescent targets, which minimizes the assay complexity and further reduces the footprint of the future portable chip-based analysis system.

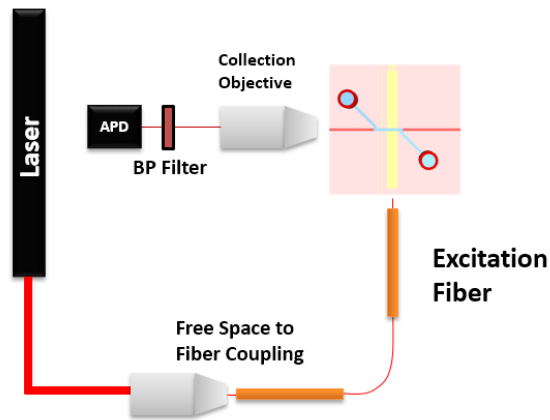


Fig. 5.11 The simplified version of optical setup used for the experiments.

Fabrication procedure

MMI waveguide devices were created using an optimized fabrication procedure discussed in Chapter 2. They have a single-over coating (SOC) and self-aligning pedestal (SAP) shown in Fig. 2.5c. The optofluidic chip used in this study was fabricated on a 100 mm silicon substrate on which a sequence of dielectric layers for optical guiding was sputter deposited. These cladding layers consisted of Ta₂O₅ and

SiO₂ (refractive index: 1.46 and 2.107) chosen to minimize background photoluminescence. Their thicknesses in nm starting from the substrate were 265/102/265/102/265/102, where the material sequence reads SiO₂/Ta₂O₅/SiO₂/Ta₂O₅/SiO₂/Ta₂O₅. SU8 photoresist (SU8-10, MicroChem) was spun on the wafer, patterned and developed to define the hollow waveguide channel with a rectangular cross section of 12μm wide by 5μm high. The SU8 and a thin nickel layer were used as a mask to etch a self-aligned pedestal into the wafer using an inductively-coupled-plasma reactive ion etcher (ICP-RIE). The pedestal serves to raise the SU8 and subsequent hollow core above the wafer surface so it is surrounded by air on its sides. A single SiO₂ overcoat layer of 6μm thickness was deposited over the SU8 by plasma-enhanced chemical vapor deposition. Three micron tall ridges were etched into the SiO₂ layer, again using the ICP-RIE, to form MMI and single mode ridge waveguides that intersect multiple points of the hollow waveguide as illustrated in Fig. 5.10. Fluid inlets into the hollow channel were exposed with a wet etch through the top SiO₂ layer and the SU8 was then removed with a H₂SO₄:H₂O₂ solution to form the hollow core. After rinsing and drying, the wafer was cleaved into individual chips of approximately 10x10 mm². The details of the fabrication procedure can be found in Appendix E.3.

The SEM image in Fig. 5.12a shows the physical implementation of this concept - an optofluidic platform that combines solid-core and liquid-core ARROWs with a solid-core MMI waveguide. The full chip, including fluidic reservoirs for introducing microliters of sample volume into the channel, is shown in Fig. 5.12b.

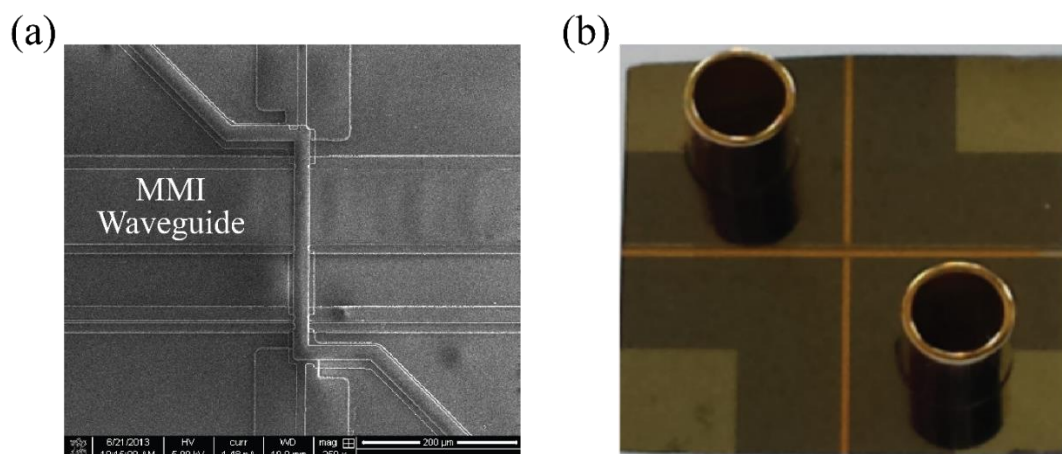


Fig. 5.12 (a) SEM image of an ARROW optofluidic platform with an MMI waveguide. (b) The photograph of 1cm by 1cm chip, showing two fluidic reservoirs holding microliters of sample volume.

5.1.3 MMI characterization

In addition to the characterization of the ARROW optofluidic platform, discussed in Chapter 2, it is crucial to characterize the MMI waveguide output pattern. This excitation pattern directly translates into the fluorescence signal collected from the target particle, directly affecting the sensitivity and multiplexing quality of the device. Due to the slight variations during the fabrication process, the wavelengths resulting in the multiple spot patterns can be shifted from the design wavelengths. For this reason, it is necessary to figure out the wavelengths that would result in the optimum excitation patterns.

The first step to characterize the output excitation pattern is to use a fluorescent solution for imaging the pattern from the top. The MMI waveguide is excited by tunable laser sources in the visible and dark red ranges. The liquid-core channel is filled with the

mixture of quantum dots (Crystalplex, Trilite™ Deep Red - Carboxyl CdSeS Core Nanocrystals) for the visible range, and Alexa Fluor®750 for the dark red range. The emitted light from the fluorescent solution is imaged using a custom compound microscope (see Appendix A.2). Fig. 5.13a illustrates the MMI waveguide pattern and its intersection with the liquid-core waveguide for $N=6$. Fig. 5.13b shows the emission collected from the fluorescent solution at the excitation spots in the liquid-core waveguide, for multiple different wavelengths (MA13 wafer). It is important to note that the wavelengths to generate the optimum excitation patterns vary slightly compared to the design wavelengths. The entire visible spectrum is covered by six independent channels (405 nm/11 spots, 453/10, 488/9, 553/8, 633/7, 745/6). The 7th channel at $\lambda=886\text{nm}$ with $N=5$ spots is also observed [69]. The emitted light from the quantum dots is around 660nm for all the excitation wavelengths at the visible range. However, the images are artificially tinted to the excitation wavelengths to make the multiplexing concept more clear.

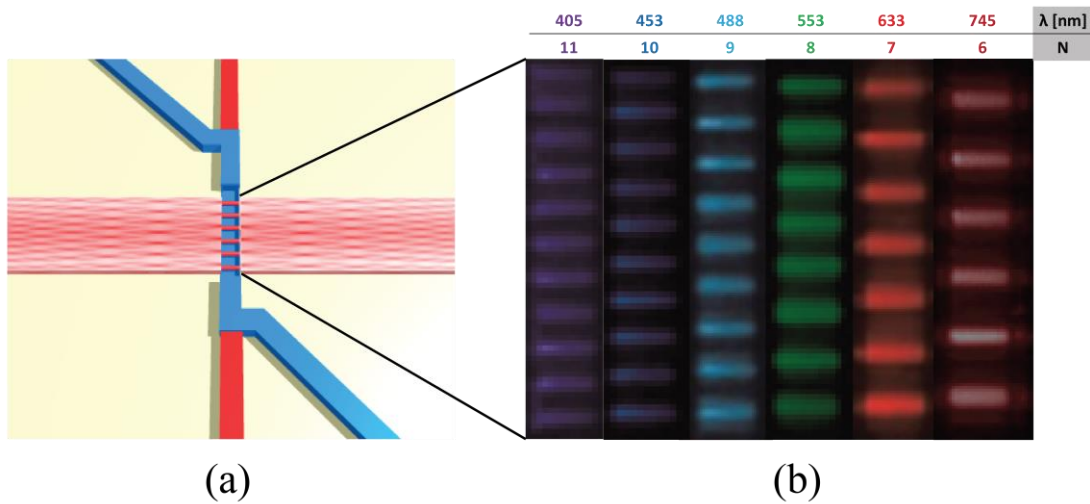


Fig. 5.13 (a) The schematic of the device where MMI waveguide pattern intersects with the liquid-core waveguide for $N=6$. (b) Photographs of multi-spot excitation patterns created in fluidic channel filled with fluorescent liquid. The entire visible spectrum is covered by independent channels (405 nm/11 spots, 453/10, 488/9, 553/8, 633/7, 745/6). (The original black and white color scale was rendered in the actual excitation colors.)

Based on the fluorescence images obtained from the liquid-core channel, initial characterization of the quality of the excitation patterns can be made. It is important to note that these images show the total emitted signal in vertical direction and do not reflect the variations of the pattern in vertical direction. However, based on the simulations in the previous section, the vertical distortion is not as critical as the horizontal distortion. As an initial characterization, this approximation is enough to get an idea of the expected fluorescence signal from the particles.

Fig. 5.14a shows the fluorescence image of the MMI waveguide pattern at the liquid-core channel, excited at $\lambda=633\text{nm}$, showing $N=7$ excitation spots. Fig. 5.14b shows the intensity profile of the excitation pattern shown in Fig. 5.14a. This intensity profile is generated by using the pattern analyzer applet based on MATLAB GUI interface, explained in detail in Appendix F. The important characterization parameters are shown on the plot. Based on this excitation pattern, the parameters in Table 6 are calculated. This analysis confirms the equal spacing between the spots $\Delta x \approx 14.35\mu\text{m}$, with a very low deviation from the expected value ($\Delta x = 100/7 = 14.28\mu\text{m}$), and ($\Delta x = 101.7/7 = 14.53\mu\text{m}$) including the penetration depth. It also shows the peak (P) to

valley (V) values for excitation spots. The deviation in the peak and valley values are also calculated which shows a small variation. The peak to valley ratio for this specific sample and wavelength is found to be around 8.6. This analysis also shows the average w_{ex} value, which translates into the temporal width of the peaks in the collected signal.

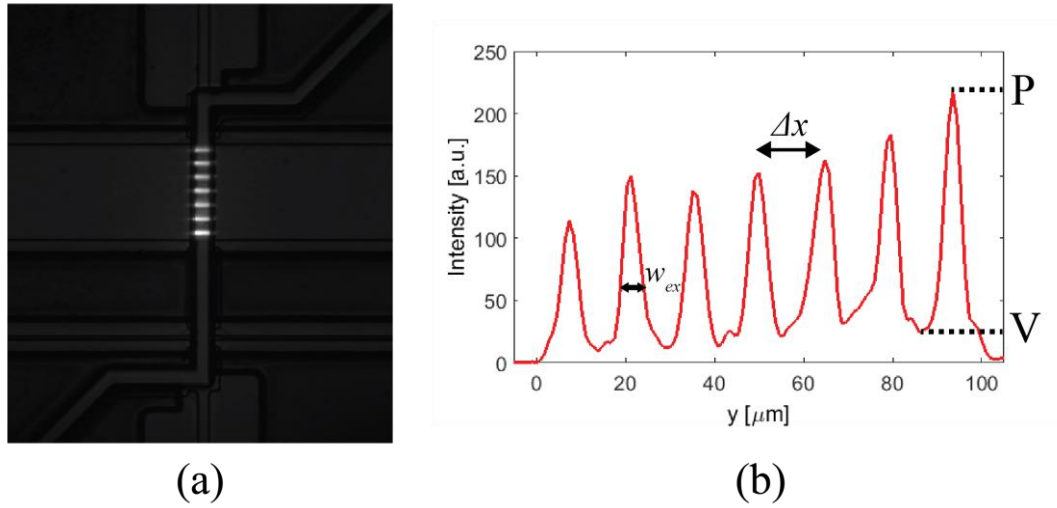


Fig. 5.14 (a) Fluorescence image of the liquid-core waveguide, filled with quantum dot solution, and excited at $\lambda=633\text{nm}$. (b) The intensity profile of the excitation pattern extracted from (a), showing the important parameters for characterization.

N	Average Δx	$\sigma(\Delta x)$	Average P	$\sigma(P)$	Average V	$\sigma(V)$	Average P/V	Average w_{ex}
7	14.35 μm	0.5 μm	160	33	18.6	8.8	8.6	5.1 μm

Table 6. Analysis on the excitation patterns shown in Fig. 5.14. Average and standard deviation values are shown for spot spacing (Δx), peak (P) and valley (V) values.

It is important to note that optimum excitation patterns can be obtained at different wavelengths than the design wavelengths, due to the distortions in fabrication process. The sample should be characterized by scanning through the whole visible spectrum and determining the best excitation spot patterns. However, for some samples, there may not be any resolved excitation spots, for the entire visible spectrum. Fig. 5.15 shows a pattern that was obtained from a low quality chip, where the excitation spots are not resolved. (MA34) There might be few different reasons causing the low resolution of the excitation spots. First of all, if the input waveguide introduces higher order modes into the MMI waveguide, the interference will not be among the restricted modes, which will distort the output excitation pattern, which was discussed in the previous section. Another possibility is the variations in composition and waveguide dimensions which results in fluctuations of the effective index. The fluctuations in the effective index deforms the MMI waveguide interference pattern, resulting in distorted excitation pattern. [211]

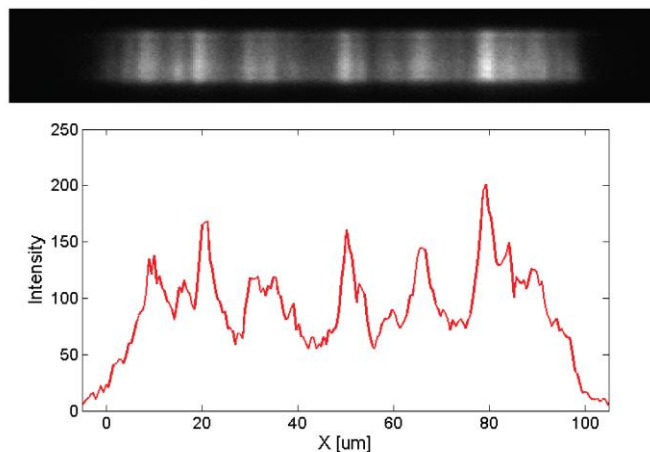


Fig. 5.15 The photograph and the intensity profile of a sample taken from a low quality wafer (MA34), showing the low quality MMI pattern for $\lambda=633\text{nm}$.

In order to show the limitations of the design, the tolerance of the device parameters to the fabrication variations is calculated. For the design, $w=100\mu\text{m}$, the length of the MMI waveguide excitation spots are $\sim 100\text{-}150\mu\text{m}$, depending on the wavelength, longer for shorter wavelengths, and shorter for longer wavelengths. This length determines the tolerance of the device, increasing the limits of where the liquid-core waveguide corresponds in the pattern. Using the equation (5.21), and setting $L= \pm 50\mu\text{m}$ (half of the minimum total spot length), the tolerance for the index and the width can be found as $\delta w=\pm 0.75\mu\text{m}$ and $\delta n=\pm 0.0216$. This means that, the device can tolerate the deviation up to these values, while still producing resolved excitation spot patterns at the design wavelength.

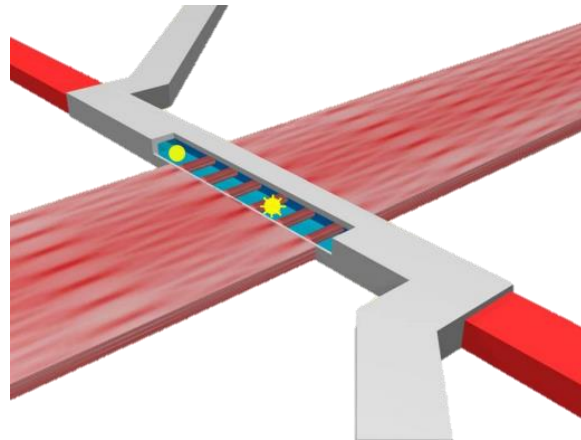


Fig. 5.16 The schematic of MMI waveguide and liquid-core waveguide intersection, showing how target particles get excited while passing through the liquid-core channel. [212]

In addition to the characterization of the multiple excitation spots done by using fluorescent solution and top imaging, the quality of the excitation spots is characterized by detecting fluorescent polystyrene microspheres. Fluorescent particles with a diameter of $0.2\mu\text{m}$ with different fluorescent dyes (here: Invitrogen Crimson Fluospheres 625/645 and Yellow-green Fluospheres (505/515)) were introduced to the liquid-core analyte channel via inlet reservoir with a concentration of $\sim 10^7$ per mL, i.e. 0.1 particles per excitation volume. The concentration is kept low enough to avoid multiple particles in the excitation area at the same time. Multiple wavelengths were used to excite the fluorescent particles and a negative pressure is applied to a second reservoir to induce particle flow, and pull the particles through the channel and past the excitation area. As the particles travel down the liquid core, each particle passes these multiple optical excitation spots, where N depends on the wavelength. They emit fluorescence signals depending on the fluorescent dye that they are tagged with (see Fig. 5.16). These signals are collected and detected, resulting in N sequential temporally encoded individual fluorescence peaks. Fig. 5.17a shows the particle trace of the raw data directly obtained by the detector, collected from the ARROW platform for $N=7, \lambda=633\text{nm}$ and $N=9, \lambda=488\text{nm}$. Fig. 5.17b shows an individual particle detected in the same trace, showing the particles with $N=7$ and $N=9$ fluorescence peaks that is the result of an exposure to the multiple excitation spots. This clearly shows how the spatial encoding of the excitation pattern is translated into temporal encoding in the detected signal, and how the particles with different fluorescent dyes fluoresce different number of times, demonstrating the multiplexing example with two channels. It is

important to note that some of the particles may produce distorted signals, even though the excitation spots are resolved. This may be because of the vertical position and the varying speed of the particle while moving in the channel.

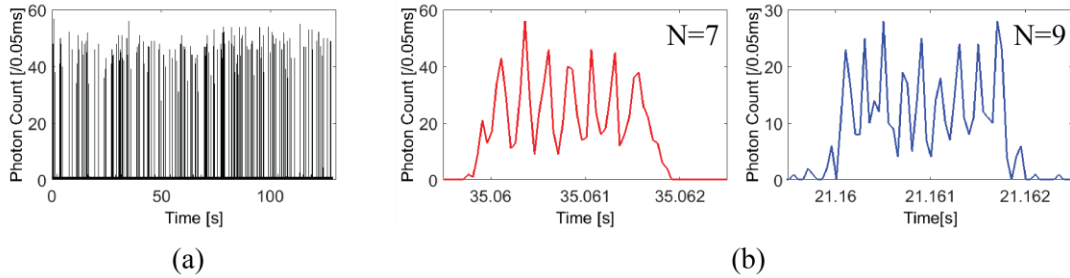


Fig. 5.17 (a) The particle trace of the raw data, directly obtained by the detector with excitation wavelengths of $\lambda=633\text{nm}$ & $\lambda=488\text{nm}$ (b) Zoomed in data trace for an individual particle showing the $N=7$ and $N=9$ fluorescence peaks from the data trace in (a).

5.2 Bioparticle detection and identification by spectral multiplexing

In this section, the spectral multiplexing technique of the ARROW optofluidic platform with MMI waveguide is demonstrated in two implementations for direct counting and identification of individual virus particles from three different influenza A subtypes – H1N1, H2N2, and H3N2 – at clinically relevant concentrations. The discussion follows closely the one in [212]. For the virus detection assays, three deactivated virus types were labeled with one or two of the selected fluorescent dyes (for details see Appendix D) and up to three of the channels shown in Fig. 5.13b were used. The viruses were mixed and a 5 μl aliquot was pipeted into one of the reservoirs covering the ends of the fluidic channel (see Fig. 5.12b). The solution was then pulled through the channel and

past the MMI excitation areas using negative pressure applied to the second reservoir. Light from up to three lasers was coupled into single mode optical fiber and into a single-mode solid-core waveguide connecting the MMI to the edge of the chip. The excitation wavelengths (488, 633, and 745 nm) were chosen to create 9, 7, and 6 spots, respectively (see Fig. 5.13b).

We implemented two multiplex assays and analyzed them with two different methods to demonstrate the capabilities of our approach: single-color labeling and combinatorial labeling.

5.2.1 Single-color labeling multiplexed detection

For the single-color labeling multiplexed detection, each of the three virus types was labeled with a different dye and all three excitation wavelengths were used. Fig. 5.18a shows a representative fluorescence signal $F(t)$ emitted from a single H1N1 virus at 488 nm excitation, collected along the liquid-core waveguide channel. Nine distinct peaks are clearly visible, illustrating both the high quality of the MMI pattern and the sensitivity of the optofluidic chip to single virus particles using only waveguides for excitation and collection. The virus type can be identified visually by the number of peaks (here: nine), but more sophisticated analysis algorithms can be applied that are compatible with rapid and automated signal processing of large numbers of particles in a clinical setting. For this assay, we used single-particle autocorrelations for demultiplexing. Once a particle has been detected, i.e. the fluorescence intensity exceeds the background level, an autocorrelation is performed on this single event. This

background is due to residual photoluminescence of the solid waveguide materials, which was minimized by the choice of cladding materials. The detection threshold was set to 10 cts/0.1ms to ensure high confidence identification without false positives. Fig. 5.18b shows the autocorrelation signal $G(\tau)$ corresponding to the event of Fig. 5.18a. As is typical for fluorescence correlation spectroscopy (FCS), a curve with an overall decay due to drift and diffusion is observed (dashed line) [213]. Superimposed on this, however, we observe a number of distinct peaks that arise at integer multiples of the lag time Δt_B that correspond to the time it takes the particle to travel between excitation spots. Fig. 5.18c shows close-ups of the autocorrelations for each virus type in the region of these cross-correlation peaks. The drift-induced overall decay seen in Fig. 5.18b was subtracted from each trace. Corresponding peaks are clearly separated (see arrows for 5th peak) and allow for correct assignment of the virus. By using the delay time for the fifth peaks, we analyzed the fluorescence trace from a particle mixture over 120 s as shown in Fig. 5.18d. It is important to note that neither spectral separation nor filtering of the emitted light was needed. All spectral information was extracted from the temporally encoded detector signal. The symbols in Fig. 5.18d indicate the virus type identified using single particle autocorrelations. All but one event (0.8% false positive rate) were correctly assigned as verified by manual inspection of each signal for peak number and spacing. 73 events were correctly detected as viruses above the background level, but could not be confidently identified by subtype. We note that the distribution of individual fluorescence signal intensities originates mainly from differences in the position of the particles within the waveguide cross section. (see

section 5.5 for further analysis) This produces variations in the excitation and collection efficiencies in accordance with the optical mode profiles in the solid-core excitation and liquid-core collection waveguide [139]. The virus concentrations were measured from the count rates and flow speed (H1N1: 3.2×10^6 /ml; H2N2: 2.0×10^6 /ml; H3N2: 8.9×10^5 /ml). This shows that we were able to carry out high-fidelity multiplex detection of single viruses at clinically relevant concentrations [77], [214]–[216]. For the MMI used here (illuminated volume: $5 \mu\text{m} \times 12 \mu\text{m} \times 100 \mu\text{m} = 6 \text{pL}$), limitations due to simultaneous presence of multiple targets in the excitation volume do not arise until concentrations exceed 1.67×10^8 /mL – well above the viral titer range of influenza and other diseases [77], [214]–[216].

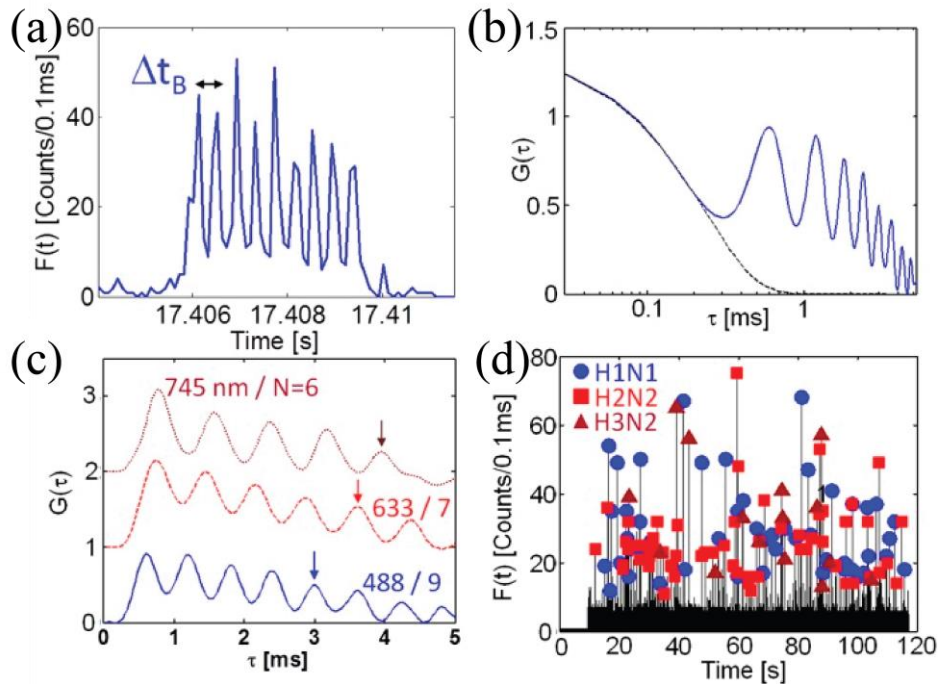


Fig. 5.18 Three-color multiplex virus detection. (a) representative fluorescence signal emitted by single H1N1 virus excited at 488nm showing 9 distinct peaks spaced by

Δt_B ; (b) Corresponding single-particle autocorrelation signal. Multiple peaks are observed at multiples of Δt_B ; dashed line: fit to underlying flow-limited correlations. (c) Single-particle autocorrelation for 3 virus types after subtraction of flow-based contribution. The peak positions depend strongly on excitation spot number (arrows mark the 5th peak for each virus type). (d) Segment of fluorescence from virus mixture excited at all three colors. Events are identified using single-particle autocorrelations. All but one identified signals (99.2%) agree with manual inspection of events. (after [212])

5.2.2 Combinatorial labeling multiplexed detection

3x multiplexing is already sufficient for some applications, but extended differentiation is often desired. Simply increasing the number of wavelengths quickly reaches a limit due to limited choice of fluorescent dyes and laser sources as well as overlapping emission spectra. A combinatorial approach, however, which assigns multiple labels to a target can be scaled up favorably. Here, we demonstrate combinatorial multiplexing by MMI excitation using two colors for identifying three virus types. To this end, the H2N2 virus was co-labeled with both blue and dark red dye, while H1N1 (blue) and H3N2 (dark red) (see Fig. 5.19a) remained singly labeled. Again, we analyzed a mixture of all three viruses, now simultaneously excited by two sources. We implemented a different signal processing algorithm to de-multiplex the virus types. Fig. 5.19b shows the fluorescence signal $F(t)$ from a single H3N2 virus. $F(t)$ is shifted and multiplied with itself $N-1$ times to create a processed signal as it was discussed in Chapter 4, equation (4.1). $S(t, \Delta t)$ will take on a large value only at the correct Δt

value(s) for a given signal, allowing us to define two color channels when equation (4.1) is applied with Δt_B and Δt_{DR} , respectively. This shift-multiply algorithm also increases the signal-to-noise ratio of the particle detection [165], [217], (see Chapter 4). This SNR improvement is evident in Fig. 5.19c which shows $S(t, \Delta t)$ for the mixed signal of Fig. 5.19b at $\Delta t_{DR}=0.63\text{ms}$ (dark red).

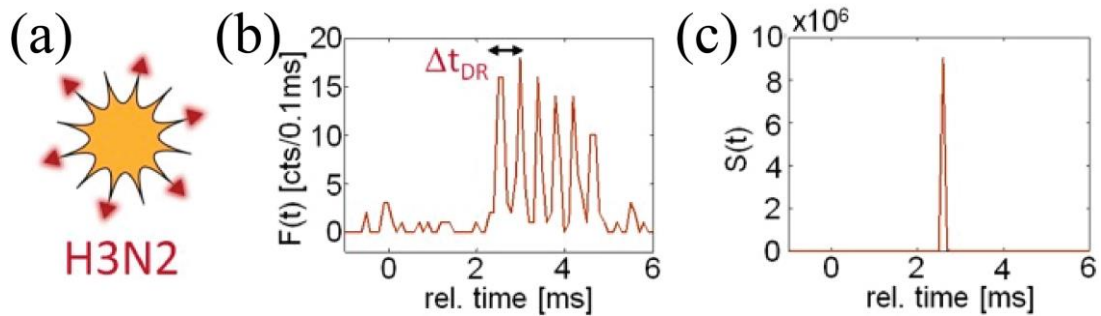


Fig. 5.19 Analysis of single virus fluorescence signals. (a) sketch of fluorescently labeled H3N2 virus, responding to excitation at 745 nm; (b) fluorescence signal from single H3N2 virus showing six peaks with average spacing Δt_{DR} ; (c) corresponding processed signal using shift-multiply algorithm with Δt_{DR} showing dramatically increased SNR. (after [212])

Fig. 5.20a shows the labeling and individual fluorescence signals from all three virus types under two-color excitation. Most notably, the signal for the double-labeled H2N2 changes and clearly shows a superposition of the 9-spot (488 nm) and 6 spot (745 nm) patterns. For further analysis, we first identified the average shift times Δt_B and Δt_{DR} for blue and dark red excitation using single color excitation. Then, each event of the mixed assay was analyzed using equation (4.1) at those Δt values. Fig. 5.20b shows

that a blue-labeled H1N1 virus only shows appreciable $S(t)$ at Δt_B . Likewise, an H3N2 virus shows strong signal in the Δt_{DR} channel. The double-labeled virus, however, shows large $S(t)$ in both channels, demonstrating that we can successfully identify three different viruses with two colors.

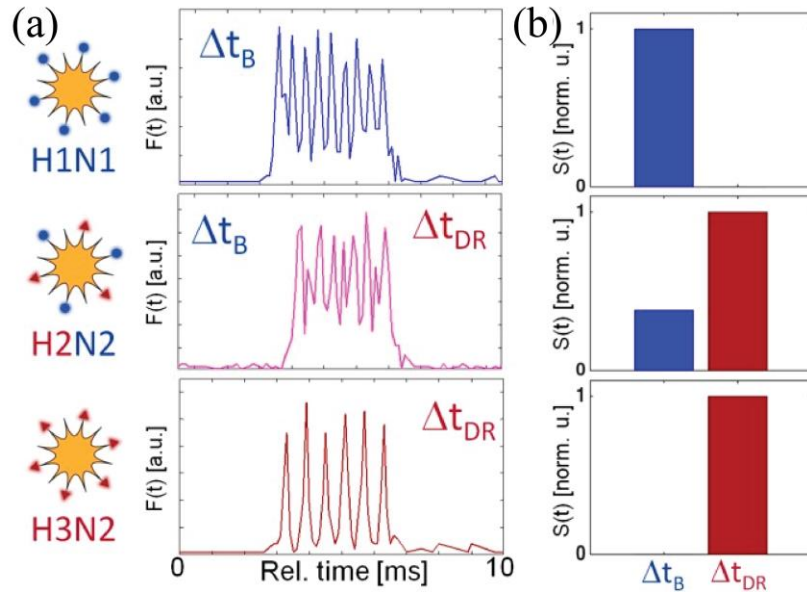


Fig. 5.20 Two-color combinatorial detection of single viruses. (a) schematic view of labeling scheme for the three influenza types and their resulting single-virus fluorescence signals; the H2N2 virus shows a mixture of six and nine peaks upon blue and dark red excitation; (b) bar histograms of signals after shift-multiply processing at Δt_B and Δt_{DR} . Singly labeled viruses appear in only one Δt channel, while the double labeled virus creates signal in both color channels. (after [212])

If we only rely on unique combinations of three colors, we can distinguish seven targets (2^3-1). With four colors, $15 \times (2^4-1)$ spectral multiplexing is possible, sufficient for the vast majority of diagnostic panels. The readout fidelity depends on the ratio of spot

spacing (determined by the MMI width w) and the individual spot width (determined by the width of the input single-mode waveguide w_{input}) and can be further improved by increasing w/w_{input} . Moreover, multiple fluidic channels addressed with MMIs of different dimensions can further increase the multiplexing power. The multi-color labeling strategy can readily be extended to fluorescently labeled nucleic acids and antibodies specific to target surface proteins.

MMI-based wavelength division multiplexing is clearly ideal for on-chip bioanalysis, providing the missing element to turn an optofluidic chip with single molecule detection sensitivity into the basis for a powerful and versatile diagnostic instrument for a variety of bioparticles and biomarkers. Beyond that, the ability to encode different wavelengths into unique spatial light patterns opens the door to new avenues for integrated photonic and optofluidic devices, for example spectrally reconfigurable optical particle traps or distribution of different colors to different areas on a chip [69].

5.3 Bioparticle detection and identification by spatial and spectral multiplexing

The spectral multiplexing capability discussed in the previous section is ultimately limited by the finite absorption bandwidth of the dye labels which can lead to channel cross-talk if the absorption and emission spectra overlap. We were able to increase the capacity of multiplexing by integrating a combinatorial labeling approach. However, we can further improve the multiplexing capacity by incorporating the spatial multiplexing feature of the MMI waveguide.

Here, we introduce a new multiple target sensing platform, based on the *spatial* multiplexing of multiple influenza strains, by using a *single* excitation wavelength along the MMI and creating channel dependent multi-spot patterns in *three* separate intersecting fluidic channels, a so-called triple liquid-core design. The number of spots for each fluorescence signal provides direct identification of multiple targets with high sensitivity. Additionally, we have combined the two approaches, *spectral* and *spatial*, on the same design to achieve high multiplexing capacity. This joint approach allows us to create spectrally and spatially unique multiple excitation patterns, where we could directly identify multiple different targets. Triple-core design also allows for parallel testing for different samples from different patients or increases the throughput for analysis of a single patient sample. [218]

5.3.1 Triple-core Channel Layout Design

A wide solid-core optical waveguide that acts as a multi-mode interference (MMI) waveguide is used to create location dependent multi-spot patterns for three orthogonally intersecting liquid-core waveguides (Fig. 5.21). This way, all three channels can be excited using a single MMI waveguide and a single solid-core input waveguide. As for the collection waveguides, Y-coupler waveguide is used to combine all the signals coming from three channels into a single waveguide. This creates a simple design by eliminating the need for complex off-chip optics, and requires only a single detector. The fluidics of the chip is designed to prevent contamination in between the channels. The inlets for the analyte are located on one side of the device, and these

three channels combine only after the detection, connecting to the outlet. Fluidic reservoirs are attached on the inlets and outlets, to create an interface for the fluidic delivery. Negative pressure is applied to the outlet reservoir to achieve one directional flow.

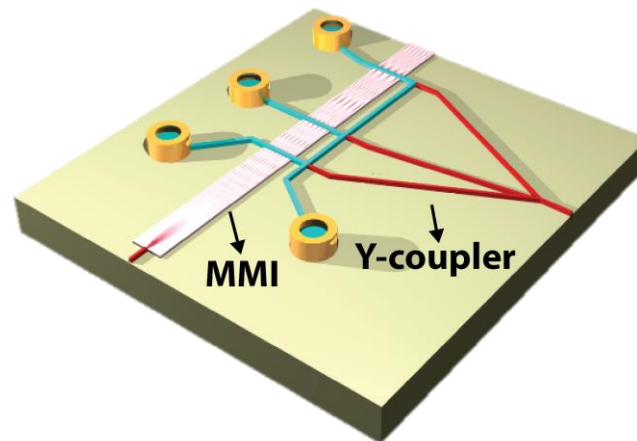


Fig. 5.21 Schematic view of the optofluidic platform with MMI waveguide intersecting three separate liquid-core waveguides, and a Y-coupler to combine the signals from three channels.

The SEM image in Fig. 5.22a shows the physical implementation of this concept - an optofluidic platform that combines three liquid-core ARROWs with a solid-core MMI waveguide and a Y-coupler. The full chip, including fluidic reservoirs for introducing microliters of sample volume into the channel, is shown in Fig. 5.22b.

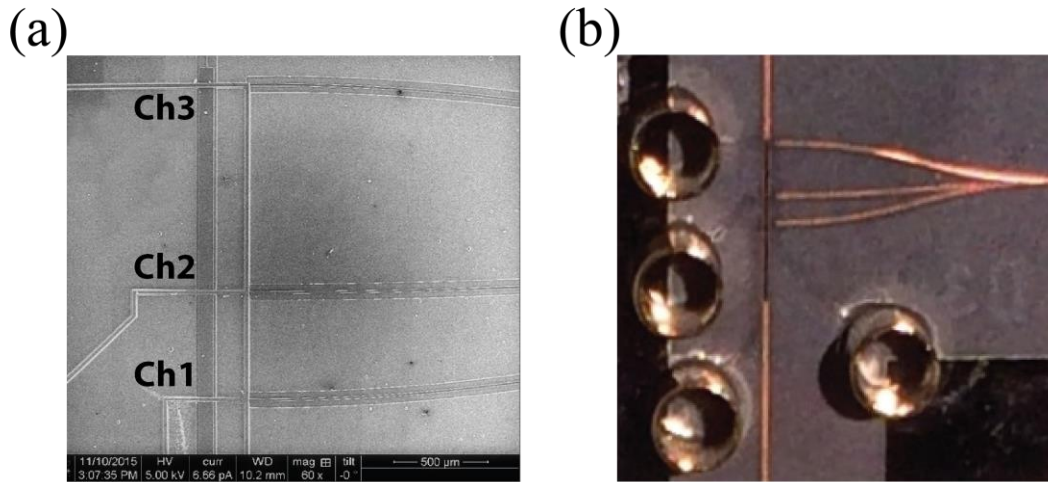


Fig. 5.22 (a) SEM image of the MMI waveguide crossing three liquid-core waveguide channels. (b) The photograph of the full optofluidic platform with reservoirs attached.

MMI Design Theory

In order to utilize the spatial multiplexing capability of MMI waveguides, discussed in Section 5.1.1, we designed an MMI waveguide such that three fluidic micro-channels intersect the waveguide at three different positions that corresponds to a well-defined, integer number of spots for a certain wavelength creating different numbers of spots in each channel. The product of spot number N and distance L from the beginning of the MMI waveguide and a wavelength λ , can be derived from the equation (5.21) and is given by:

$$NL = \frac{n_c w^2}{\lambda} \quad (5.23)$$

where w is the effective MMI waveguide width (here: 75 μm), n_c the effective refractive index of the MMI (here: 1.46), and λ is the excitation wavelength (here: 633 nm). This

allows us to produce $N=8$, 6 , and 4 well-defined spots at the MMI waveguide lengths of $L_1=1676\mu\text{m}$, $L_2=2243\mu\text{m}$, and $L_3=3350\mu\text{m}$ respectively. (see Fig. 5.23a) In order to combine the spectral property of the MMI waveguide, we have chosen a wavelength that would correspond to distinct number of spots in each channel, with respect to $\lambda=633\text{nm}$. For the exact same device, using the equation (5.23), one can see that $\lambda=520\text{nm}$ excitation wavelength creates $N=10$, 7 , and 5 well-defined spots at the same MMI waveguide lengths. (see Fig. 5.23b) The MMI waveguide simulations are carried out by using beam propagation software (FimmWAVE, Photon Design). Fig. 5.23 shows the simulated MMI waveguide patterns for both wavelengths, (a) $\lambda=633\text{nm}$ and (b) $\lambda=520\text{nm}$, where the locations of the three channels are marked to show six excitation patterns with distinct N generated by using two wavelengths and three channels.

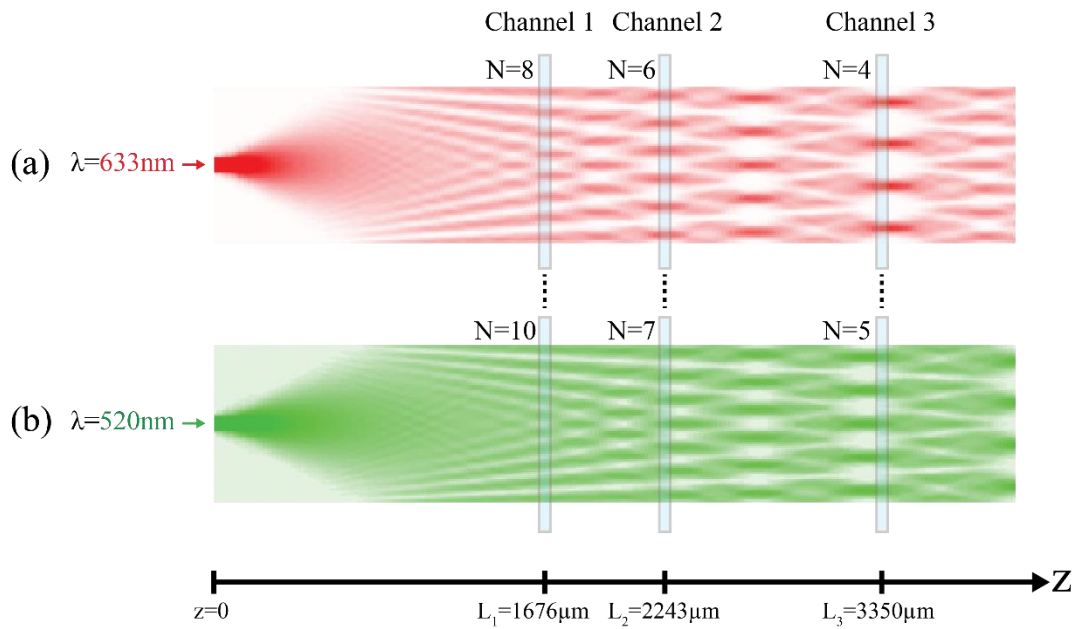


Fig. 5.23 The simulated MMI waveguide patterns for both wavelengths, (a) $\lambda=633\text{nm}$ and (b) $\lambda=520\text{nm}$. The channel locations are marked to show six excitation patterns with distinct N generated by using two wavelengths and three channels.

In this way, both spatial and spectral properties of MMI waveguide can be combined to create six distinct numbers of spots for multiplexing, from a single MMI waveguide, and only two excitation wavelengths. The differences in spot numbers are evident and constitute the basis for this new multiplex pathogen analysis technique. The width of the MMI is taken as $w=75\mu\text{m}$ in order to reduce the device dimensions and the curvature of the Y-coupler waveguides.

Another important part of the design is the collection of the signals from all three channels in an efficient manner. In order to do that, we have designed a Y-coupler to achieve maximum coupling efficiency. Beam propagation software (FimmWAVE, Photon Design) was used to design devices with minimized propagation loss in the curved waveguide sections. (see Chapter 4 for Y-waveguide simulations) Based on these simulations, the fan-out angle of the outmost collection arms is kept at minimum ($\sim 8^\circ$) while keeping the waveguide length small enough. On the other hand, it is important to balance the signal level from the first and the third channels, to increase our detection sensitivity. The MMI waveguide has a propagation loss which creates less excitation power in the third channel, compared to first and second channels. However, the signal intensity depends on the excitation power of each individual spot which is the total excitation power divided by N . Since, the total power is divided by smaller N in the third channel than the first channel, the signal intensity per peak is

higher. This property, in combination with the propagation loss, creates signal intensities within the same order of magnitude. For this reason, the angles of the Y-coupler are kept the same for the first and the third collection arms, to achieve equal collection efficiency for both first and third channels.

In addition, another triple liquid-core waveguide design based on MMI waveguides was fabricated. This design has three different MMI waveguides with the lengths L_1 , L_2 and L_3 , calculated for the first design. Three different liquid cores intersect three different MMI waveguides to achieve spatial multiplexing. (see Fig. 5.24) A Y-splitter waveguide is used to split the excitation into three arms to deliver the input light into three separate MMI waveguides. Another Y-coupler is used to collect the signal from the three different liquid-core waveguides and deliver it to the collection solid-core waveguide. Although this design implements the same idea as the other design, the losses in the input Y-splitter arms are very high, due to the very high curvatures. Unfortunately, this loss made this design not functional.

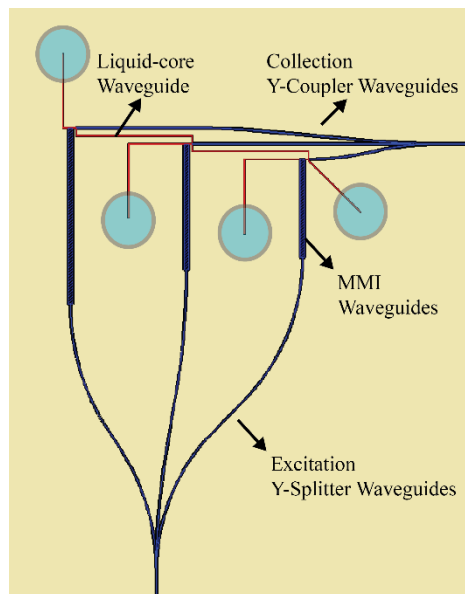


Fig. 5.24 Alternative spatial multiplexing design using three liquid core waveguides and three MMI waveguides. This device is not functional, due to the high losses at the excitation Y-splitter waveguides.

Characterization

The characterization of the excitation patterns is done in the same way, explained in the previous section. Quantum dot solution is introduced to the inlet reservoirs, and negative pressure is applied to fill all three channels. The laser light is coupled into the input waveguide, and scanning the whole spectral range to obtain the optimum patterns in all three channels. The images are taken by using a compound microscope (see Appendix A.2). Fig. 5.25 shows the fluorescence images of the three channels excited with two different wavelengths, $\lambda=633\text{nm}$ and $\lambda=520\text{nm}$, showing six separate excitation patterns with a distinct N .

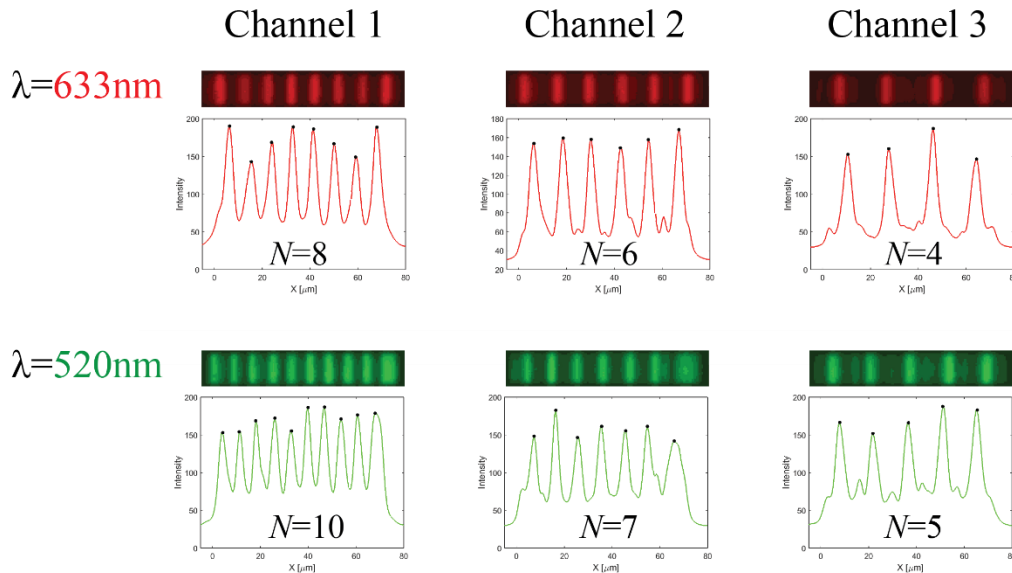


Fig. 5.25 the fluorescence images of the three channels excited with two different wavelengths, $\lambda=633\text{nm}$ and $\lambda=520\text{nm}$, showing six separate excitation patterns with a distinct N . The corresponding intensity plots are also shown, and the excitation spot peaks are marked.

Experimental Setup and Fabrication

The experimental setup implemented for optical virus detection with multi-spot excitation can be seen in Fig. 5.26. A white light laser (NKT SuperK Extreme) passing through a multi-line tunable filter with a narrow bandwidth (NKT SuperK Select) is coupled into a single-mode fiber. This way, we could precisely tune the source to a desired wavelength among a wide spectral range, and introduce multiple laser-lines at the same time into the fiber. Single-mode fiber is butt-coupled into the single-mode excitation waveguide which then couples into the center of the MMI section. Fluorescently labeled viruses passing through the MMI excitation volume are subjected to the MMI pattern and thus produce multiple fluorescent signals per virus. These signals are captured by the liquid-core waveguide orthogonal to the excitation, transmitted into the collection solid-core waveguides which then combined into a single solid core waveguide by the Y-coupler. An avalanche photo diode (Excelitas) is used to detect the fluorescence signal after removing the excitation wavelengths with a set of filters (Edmund Optics 633nm Notch Filter and Semrock 532nm Long Pass). No spectral filters or dichroic mirrors to separate the emission colors are required. (see Appendix A.1 for details.)

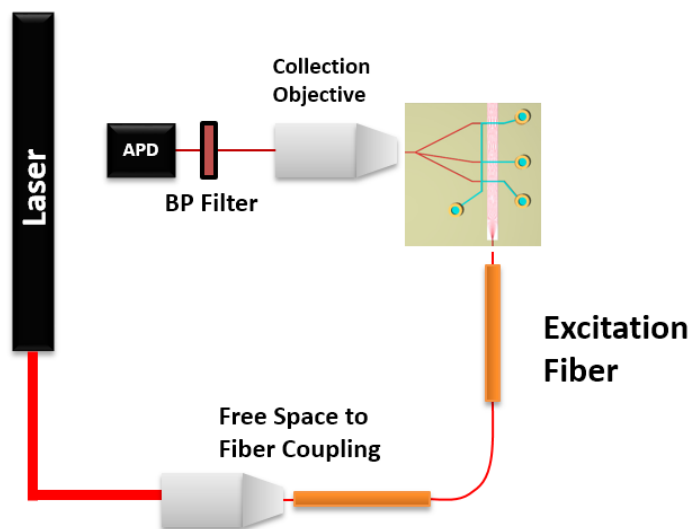


Fig. 5.26 Simplified experiment setup showing the excitation and collection paths.

Triple liquid-core detection platforms based on MMI waveguides were created using an optimized fabrication procedure discussed in Chapter 2. They have a single-over coating (SOC) and self-aligning pedestal (SAP) shown in Fig. 2.5c. The details of the fabrication procedure can be found in Appendix E.4.

For single molecule experiments, purified, H2N2 Human Influenza Virus (Advanced Biotechnology Inc., UV-inactivated A/2/Japan/305/57) was labeled with Dylight 633 and H1N1 Human Influenza Virus (Advanced Biotechnology Inc., β -Propiolactone-inactivated A/PR/8/34) was labeled with Dylight 550 NHS ester-activated dyes according to manufacturer specifications (Thermo Scientific). Unbound dye was removed by column chromatography using a PD MiniTrap G-25 column and 1 x PBS elution buffer (GE Healthcare Life Sciences), and efficient labeling was verified by TIRF microscopy. (see Appendix D for details.)

5.3.2 Spatially Multiplexed Detection

For the demonstration of spatially multiplexed biosensing, virus detection assay, H2N2 deactivated virus type was labeled with red (Dylight 633) fluorescent dye and they were pipetted into three input reservoirs covering the ends of the fluidic channels. Negative pressure to the outlet reservoir was applied to pull the solutions through three different liquid-core analyte channels and past the MMI waveguide excitation areas. NKT laser tuned to 633nm was used to excite the labeled viruses. When the labeled viruses were traveling down the liquid core waveguides, they passed through 4, 6, or 8 different excitation spots, depending on the channel they were in (see Fig. 5.25). These signals were captured by the liquid-core waveguide, collected by solid-core collection waveguides and combined into a single output waveguide by using a 3x1 Y-coupler (see Fig. 5.21). The excitation wavelength is eliminated by a 633nm notch filter (Edmund Optics), before the signal is finally detected by a single-photon-counting detector.

Fig. 5.27a shows fluorescence signals with different number of peaks, each emitted from a single labeled H2N2 virus collected from three different channels. In each particle, distinct peaks are clearly visible, illustrating both the high quality of the MMI pattern and the sensitivity of the optofluidic chip to single-virus particle detection (see Fig. 5.27b). By counting the number of peaks of each particle signal, we could identify which channel the virus was passing through while emitting fluorescence signals. For the details of the peak counting program, refer to Appendix G. The detection threshold was set to 10 cts/0.1ms to ensure high confidence identification without false positives.

Thirty-six events were correctly detected as viruses above the background level. All of the signals are correctly identified by using the peak counting algorithm as verified by manual inspection of each signal for peak number. This shows that we could run a simultaneous test for three different samples, and determine which ones contain the target virus. We could also use different types of viruses placed in the three different reservoirs in order to do simultaneous identification of different targets. Additionally, sophisticated analysis algorithms can be applied that are compatible with rapid and automated signal processing of large numbers of particles in a clinical setting, which were discussed in previous section.

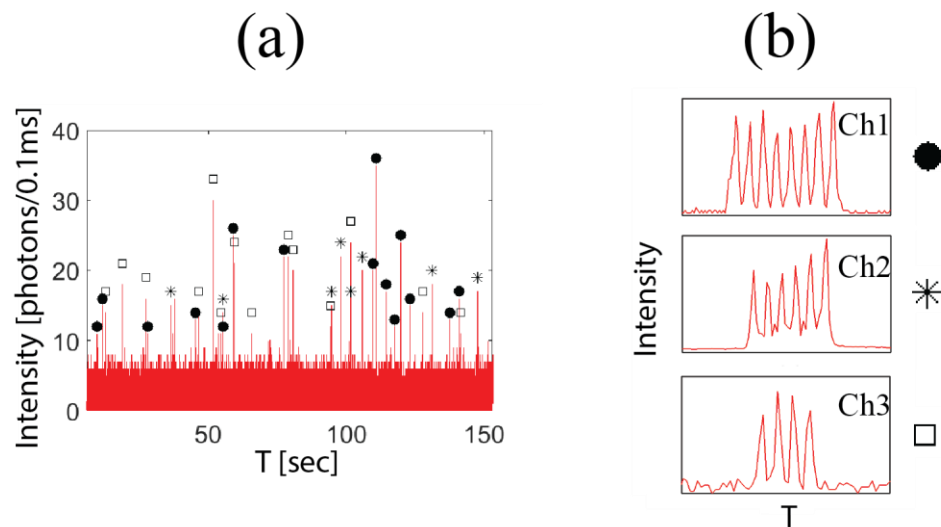


Fig. 5.27 Spatial multiplexing of three different samples with H2N2 human influenza viruses (a) Data trace of the fluorescence signal collected from the viruses, excited with $\lambda=633\text{nm}$. The signals are marked according to the channel they belong. (b) The

zoomed-in particle signals shown in (a), demonstrating the single virus detection with three different N (8,6, and 4) coming from three separate channels.

5.3.3 Combination of spatial and spectral multiplexing

Furthermore, we demonstrated the joint (spectral and spatial) multiplexing method, and showed how it increases the multiplexing capacity of the device. For the joint multiplexed biosensing of single viruses, H2N2 deactivated virus type was labeled with red (Dylight 633) fluorescent dye and H1N1 deactivated virus type was labeled with green (Dylight 550) fluorescent dye. They were mixed and pipetted into three input reservoirs covering the ends of the fluidic channels. The solutions are pulled through the channels by applying a negative pressure to the outlet reservoir.

Fig. 5.28a shows the data trace of the fluorescence signals, each emitted from a labeled single H1N1 or H2N2 virus generated in three different channels, and collected all together from a single collection waveguide. By counting the number of peaks, we were able to distinguish among six separate multiplexing routes, and identify both the channel and the type of virus for each signal. Automatically generated results when compared to the manual inspection gave 3% error during the identification, due to the distorted signal caused by the flow variations. Fig. 5.28b shows the individual virus signals that were generated from H1N1 viruses in three separate channels.

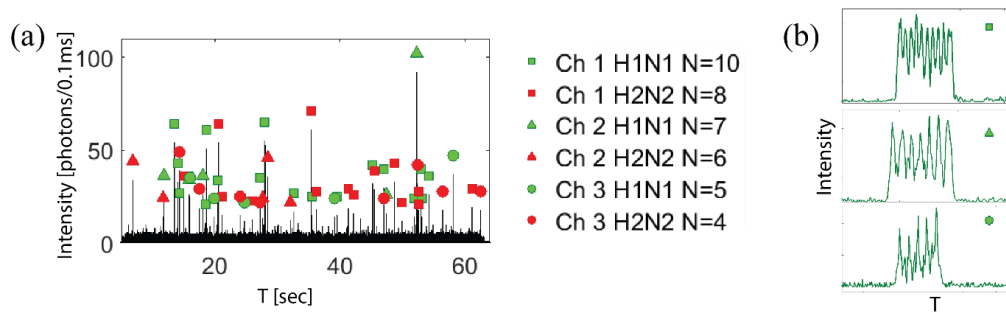


Fig. 5.28 . (a) Fluorescence signal collected from viruses in three channels, excited with both wavelengths $\lambda=520\text{nm}$ and $\lambda=633\text{nm}$. They are labeled based on the number of peaks they emitted. (b) The zoomed-in particle signals shown in (a), demonstrating the three different signals of H1N1 viruses with $N=10,7$, and 5 coming from three separate channels.

Furthermore, the velocities and the concentrations of the sample can be extracted by using the time difference between the peaks, $\Delta x/\Delta t$. The average velocity is found to be 0.87cm/s and the concentration is estimated to be 6×10^5 particles/mL, which is in a good agreement with previous findings that is at clinically relevant concentration. Combining multiple wavelengths with multiple channels, enabled us to detect and differentiate many different target samples based on the number of spots, in the same experiment, without the need for a spectral filter to separate signals.

In summary, joint (spatial and spectral) multiplexed detection of influenza viruses was achieved on an optofluidic platform consisting of triple liquid-core waveguides intersecting a single solid-core MMI waveguide. We successfully detected influenza viruses from each channel for two different strains, with single molecule detection

sensitivity, and distinguished among them based on the number of spots they generated. We further improved the ability of MMI waveguide based multiplexing which can take full advantage of established fluorescence technologies, therefore, it allows for simultaneous analysis of multiple bioparticles, even of different type, on a single, fully integrated platform. This platform can be used to incorporate the combinatorial multi-color labeling approach as well, further increasing the capacity of multiplexing. This platform serves as a powerful diagnostic tool by allowing the single-molecule detection and identification for variety of pathogens and biomarkers.

5.4 Cascade MMI Design & Results

The combinatorial multiplexing by labeling the target molecules with multiple colors was successfully shown in Section 5.2.2 [212]. This method requires balanced intensity for fluorescence emissions from both colors, to be able to distinguish the multiple-labeled viruses. However, the intensity of the emission may vary among targets, due to the stochastic nature of the labeling procedure. It also relies on complex analysis techniques for de-multiplexing which reduces the accuracy of the identification. In order to solve these problems, cascade MMI waveguides are proposed which relies on the asymmetrical properties of the MMI waveguides.



Fig. 5.29 The schematic of an asymmetrical MMI waveguide, showing the bar- and cross- coupling routes, for two different wavelengths.

The main idea is to create an MMI waveguide switch which acts as a bar and cross coupler depending on the wavelength (see Fig. 5.29). The two outputs of this asymmetrical MMI waveguide is then connected to two separate standard MMI waveguides discussed in Section 5.1.2, to create multiple excitation patterns at the liquid-core waveguide. In order to design the MMI waveguide switch, the dependence of asymmetric self-imaging properties on wavelength is used. Recalling equation (5.15) in order to create a single replica of the output, we can derive the following:

$$\begin{aligned} L &= p(3L_\pi) && \text{with } p = 0, 2, 4... \text{ (self-image)} \\ L &= q(3L_\pi) && \text{with } q = 1, 3, 5... \text{ (mirror-image)} \end{aligned} \quad (5.24)$$

In order to find the minimum L to create a bar coupler (self-image) and cross-coupler (mirror-image) on the same device with two separate wavelengths, these two equations are set equal to each other. Substituting the L_π from the equation (5.8) into (5.24), the following relationship can be derived:

$$\begin{aligned} p\left(\frac{4n_c w^2}{\lambda_B}\right) &= q\left(\frac{4n_c w^2}{\lambda_C}\right) \\ p(\lambda_C) &= q(\lambda_B) \end{aligned} \quad (5.25)$$

where, the λ_B is the wavelength for bar-coupler, and λ_C is the wavelength for cross-coupler. The smallest L is achieved when $p=2$ and $q=1$, resulting in the ratio of the wavelengths $\lambda_B/\lambda_C=2$ which cannot be achieved by taking both wavelengths in the visible range. The next smallest L would be achieved by taking $p=2$ and $q=3$, resulting in the ratio of the wavelengths $\lambda_B/\lambda_C=2/3$ which can be realized for both wavelengths

in the visible range. In order to be compatible with the previous MMI waveguide design, and the available lasers and fluorescent dyes, we set the wavelengths to $\lambda_B=488\text{nm}$ and $\lambda_C=745\text{nm}$, which has a ratio of $\lambda_B/\lambda_C=0.655$.

The device parameters are designed for a polydimethylsiloxane (PDMS) waveguide platform [219]. Thus, the refractive indices for this design are taken as $n_c=1.422$ for $\lambda_B=488\text{nm}$ and $n_c=1.412$ for $\lambda_C=745\text{nm}$, taking the dispersion into account. In order to decrease the device length, the width of the MMI waveguide is set to $w=30\mu\text{m}$, limited by the fabrication procedure. Using the equations in (5.24), the lengths of the designs are found to be $L_B=20,980\mu\text{m}$ and $L_C=20,614\mu\text{m}$. The final length is taken as $L=20,857\mu\text{m}$, optimizing the maximum output for both wavelengths. The simulations are carried out by using a beam propagation software (FimmPROP, Photon Design), and the results are shown in Fig. 5.30 for (a) $\lambda_B=488\text{nm}$ and (b) $\lambda_C=745\text{nm}$, showing the bar and cross coupling respectively.



Fig. 5.30 The simulated MMI waveguide patterns on the same device by using a beam propagation method, for two design wavelengths: (a) $\lambda_B=488\text{nm}$ (bar-coupler) and (b) $\lambda_C=745\text{nm}$ (cross-coupler)

Two output waveguides are connected to the end of this asymmetrical MMI waveguide, directing the two wavelengths into two separate symmetrical MMI waveguides, through S-shaped waveguides (see Fig. 5.31). These two MMI waveguides are

designed to generate multiple excitation spots at the liquid-core waveguide, $N=9$ for $\lambda_C=488\text{nm}$ and $N=6$ for $\lambda_C=745\text{nm}$. Fig. 5.32 shows the idea for the combinatorial multiplexing, three different viruses labeled with, blue, dark red and combination of both colors. As the single-colored viruses travel through the liquid-core waveguide, they would generate fluorescence signal at only one of the MMI waveguides, whereas co-labeled viruses would emit fluorescence for both of the MMI waveguides. This allows for the identification of all three colors, based on the number of peaks. The analysis method discussed in Section 5.2.2, using the time difference between the peaks, would work with more accuracy as well. In order to improve the use of this method, the time differences between the two MMI waveguide patterns can be increased by creating a wider MMI waveguide for the cross-coupler side. This would further increase the spatial difference between the $N=6$ spots generated at the $\lambda_C=745\text{nm}$, which directly translates into the time domain in the collected fluorescence signal. N number of output single-mode waveguides are created in between the secondary symmetrical MMI waveguides and the liquid core waveguide, to create cleaner excitation pattern.

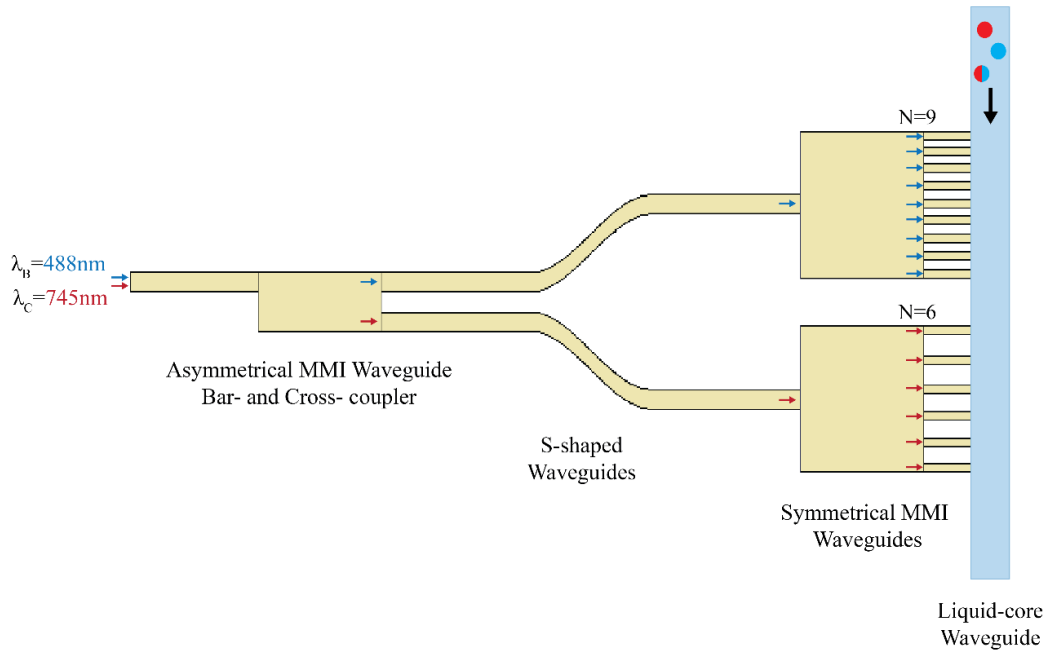


Fig. 5.31 The schematic of the cascade MMI design, showing the regions for asymmetrical and symmetrical MMI waveguides, and S-shaped waveguides.

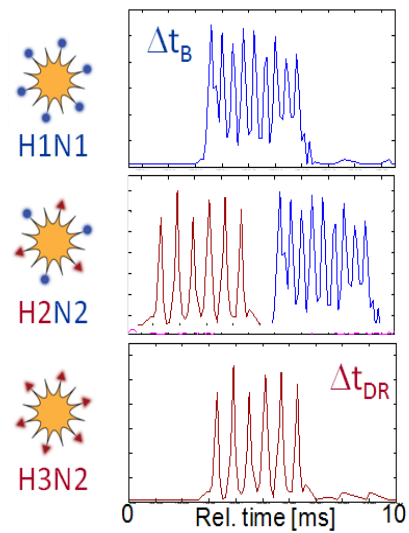


Fig. 5.32 Predicted example signal for a combinatorial multiplexing, using the cascade MMI waveguides. (adapted from: [212])

The fabrication of these devices was done using soft lithography, explained in detail by Parks et al. (2016) [219]. Briefly, the solid-core optical waveguides are fabricated by spinning 5:1 (base:curing agent) PDMS (Sylgard) onto a SU-8 master (Microchem). A 2-hour cure at 60 °C ensures full polymerization of the waveguide core material. A subsequent spin of 10:1 PDMS then creates a continuous membrane across the waveguide valve layer. This layer structure preserves the optical waveguide properties as the polymer is transparent throughout the optical spectrum [219].

Characterization

In order to characterize the asymmetrical MMI waveguide separately, 5 different devices fabricated right next to each other, intersecting the same liquid-core waveguide. Fig. 5.33 shows the layout of the fabricated device, showing five different versions for characterization. The table on the right side shows the differences among these devices. The first two devices include output coupling waveguides right before the liquid-core waveguide. The second and the fourth devices have a wider secondary symmetrical MMI waveguide for the side with lower number of peaks ($N=6$). The third device only has the asymmetrical MMI waveguide, in order to characterize the bar- and cross-coupling directly on the liquid-core waveguide.

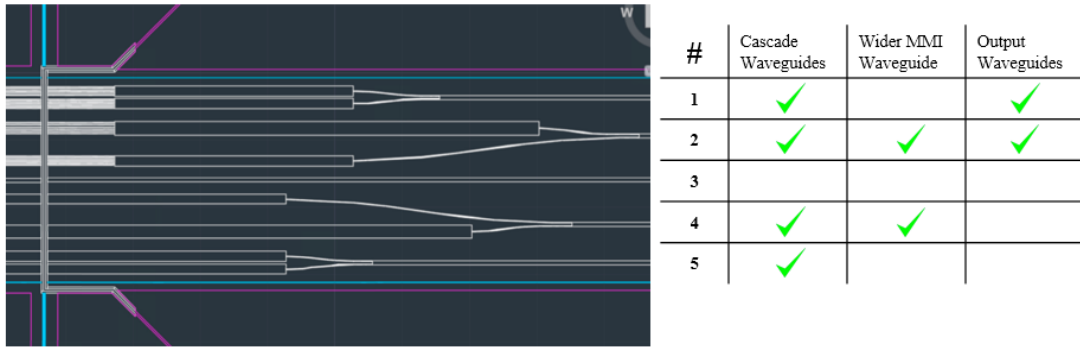


Fig. 5.33 The layout image of the cascade MMI design, with five different designs for characterization. The differences among these designs are shown in the table.

First of all, the characterization of the asymmetrical MMI waveguide is done by using the third design, where the output of the MMI waveguide directly intersects the liquid-core waveguide. Fig. 5.34 shows the intensity profiles and the power ratios of the outputs for excitation wavelengths of $\lambda_B=488\text{nm}$ and $\lambda_C=743\text{nm}$. Ideally, there should not be any power on one side of these intensity profiles, showing the perfect bar- and cross-coupling. According to the simulations (see Fig. 5.30), 99% of the light is bar-coupled into the output waveguide for $\lambda_B=488\text{nm}$ and 93.4% of the light is cross-coupled into the output waveguide for $\lambda_C=745\text{nm}$. This shows that there is a small leakage to the other channel, especially for cross-coupling. As expected, higher intensity is observed on the bar side for blue, and cross side for the dark red excitation, however, the excitation lights are leaking into the other channel as well.

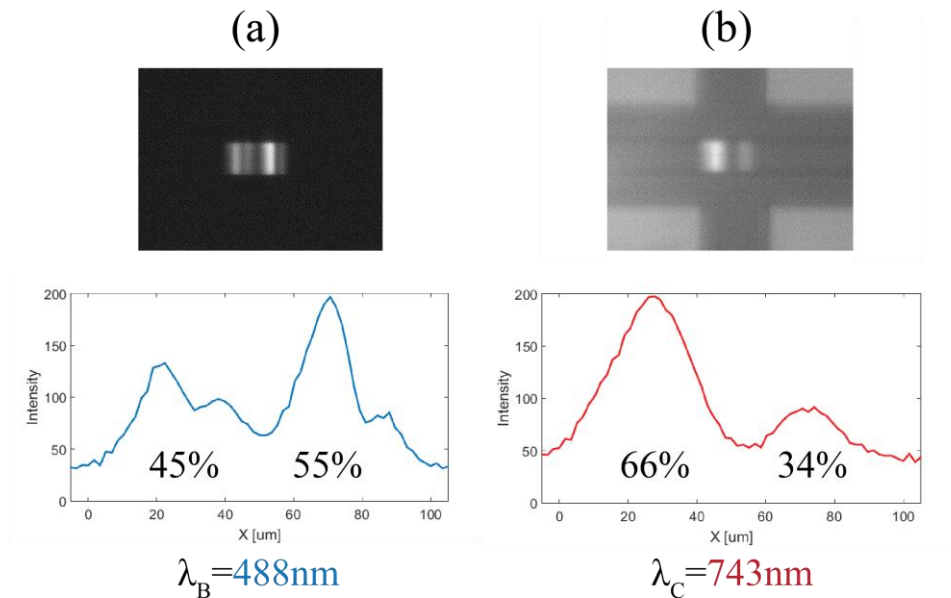


Fig. 5.34 The intensity profiles and the power ratios of the asymmetrical MMI waveguide output for excitation wavelengths of $\lambda_B=488\text{nm}$ and $\lambda_C=743\text{nm}$.

Fig. 5.35 shows the excitation patterns by using the first device with output coupling waveguides, for two wavelengths, (a) $\lambda_B=488\text{nm}$ and (b) $\lambda_C=743\text{nm}$. The correct number of spots are observed for both wavelengths, however the leaked power into the other channel is apparent as well. Since the output coupling waveguides are aligned with the correct pattern (i.e. $N=6$ on the cross-coupling side, for the dark red excitation), the patterns observed in the leaked channels do not have a resolved pattern, which shows the advantage of using the output coupling waveguides.

These are preliminary results of this device and improvements and optimizations are necessary. The imperfect bar- and cross-coupling is likely due to the imperfections and index variations in the very long solid-core PDMS waveguides. This could be

eliminated using liquid-core MMI waveguides, creating a more uniform interference medium [219].

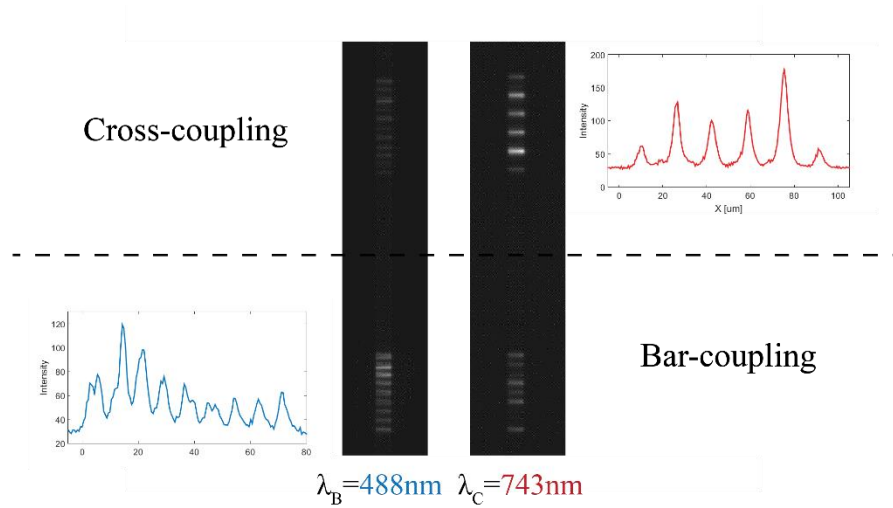


Fig. 5.35 The excitation patterns obtained by using the first design, for excitation wavelengths of $\lambda_B=488\text{nm}$ and $\lambda_C=743\text{nm}$.

5.5 Effect of Flow Properties on Particle Signal Intensity and Particle Velocities

5.5.1 Variation in Particle Intensity

As the particles pass through the excitation area in the channel, depending on their position, the detected fluorescence signal varies. This variation in the intensities is caused by couple different parameters. First of all, the excitation light does not excite the whole channel uniformly. Excitation mode profile of the solid-core waveguide can be seen on Fig. 5.36a. This shows that if the particle is away from the center in y direction, it will be exposed to less excitation light, which will create less fluorescence

emission. Another important parameter is the collection profile. Fig. 5.36b shows the mode profile of the liquid-core waveguide, showing the intensity distribution on x-y plane. This shows that, if the particle is away from the center in either direction, the collection efficiency of the emitted fluorescence will decrease. Combining these two parameters, intensity variation of the detected fluorescence signal can be calculated.

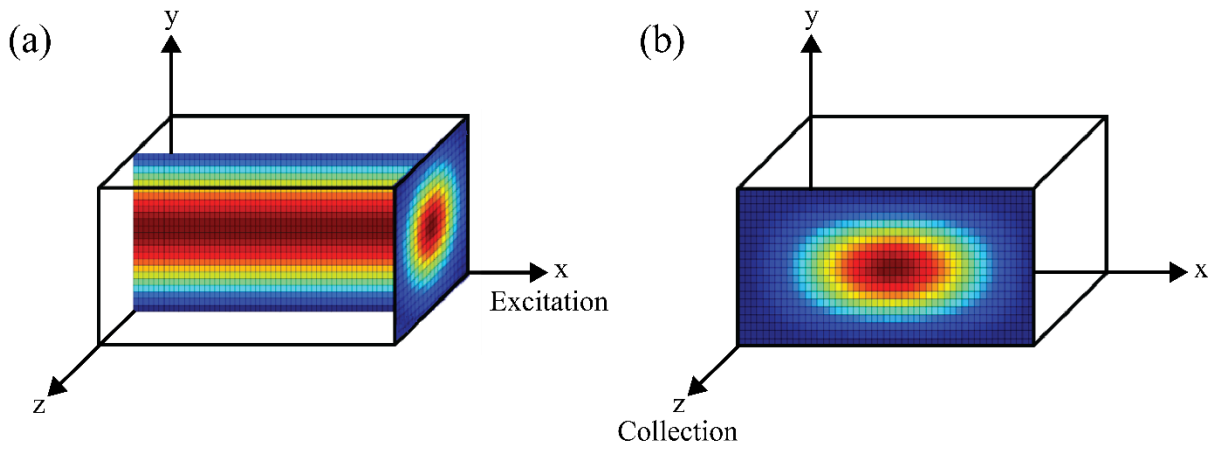


Fig. 5.36 Excitation and Collection mode profiles for a liquid-core waveguide channel. x is the excitation direction and z is the collection direction. The color represents the relative intensities in arbitrary units. (a) Excitation mode profile, and cross-section. (b) Collection mode profile.

In order to simulate the variation in the particle intensities, the particle locations should be determined. The particle distribution in the liquid-core waveguide is simulated by setting up a 3D model (COMSOL) consisting of a liquid-core channel and an inlet with the dimensions obtained from the fabricated devices. One hundred solid particles were introduced through the inlet and subjected to laminar Navier–Stokes flow in the channel. Particle trajectories were simulated using COMSOL's Particle Tracing

Module. The positions of the particles at the excitation area were obtained from the simulations and imported in MATLAB. This distribution across the $5 \times 12 \mu\text{m}$ liquid core is shown in Fig. 5.37a and shows a uniform distribution of particles among the channel.

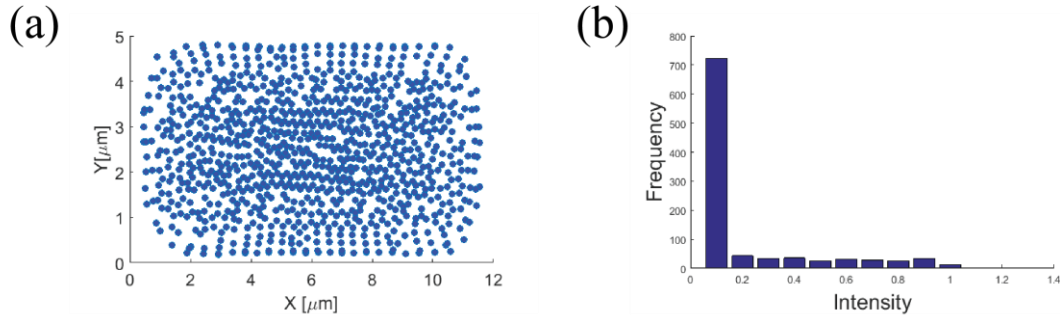


Fig. 5.37 (a) Uniform particle distribution among the cross-section of the liquid-core waveguide channel. (b) Histogram plot of the calculated intensities for particles shown in (a).

The particle locations obtained from this simulation are subjected to the corresponding excitation and collection mode profiles to derive the expected intensities for each of them. Fig. 5.37b shows the histogram of the intensities, demonstrating how most of the particles have lower intensities which results in lower signal to noise ratio.

5.5.2 Variation in Particle Velocity

In order to understand the characteristics of the particle velocities, the flow properties of the analyte in the channel should be analyzed. First of all, Reynold's number should be calculated to determine the flow type. For the liquid-core waveguides, the cross-

sectional dimensions are $5\mu\text{m} \times 12\mu\text{m}$, which results in hydraulic diameter of $D_H=7\mu\text{m}$.

Reynold's number can be calculated by using the formula: $Re = \frac{vD_H\rho}{\eta}$ [220], where

v is the velocity of the fluid, η is the dynamic viscosity, and ρ is the density of the fluid.

For water, the $Re \sim 0.21$, which shows that the flow is in the laminar flow regime. This

enables the simulations to be carried out by using Navier-Stokes equations. Since the

flow is steady with a constant pressure during the experiments, and there is no variation

in the channel dimensions, Poiseuille flow is observed in the simulations [221]. Fig.

5.38 shows the velocity distribution among the channel cross-section. As expected, the

liquid that is close to the center of the channel moves faster than the liquid closer to the

walls of the channel. As a result of this distribution, the particles located in different

parts of the channel also move with different velocities, which creates the velocity

distribution.

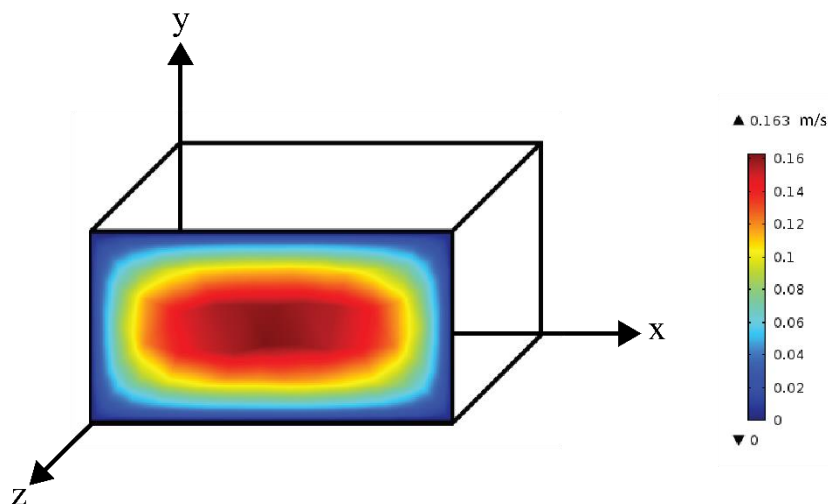


Fig. 5.38 Simulation for the velocity variation among the channel due to the Poiseuille flow.

This especially becomes a problem, where the uniform velocity of the particles is required, as in the case of Y-splitters and MMIs. Both in Y-splitter and MMI devices, the signal to noise ratio enhancement depends on the temporal distance between the peaks (ΔT), which directly depends on the velocity of the particle. Uniform velocity is also very crucial in MMI devices while differentiating among the different colored particles, based on the ΔT they have. If the variation in ΔT is high, the differentiation will not be as effective. Fig. 5.39 shows the ΔT variation in MMI experiment, caused by the variation in the velocities of the particles, for two different wavelengths. Overlapping regions in ΔT curves creates a problem for differentiation among different colored targets. In order to achieve more accurate differentiation, the bandwidth for each ΔT should be narrower, which means that the variation in the velocities should be minimized.

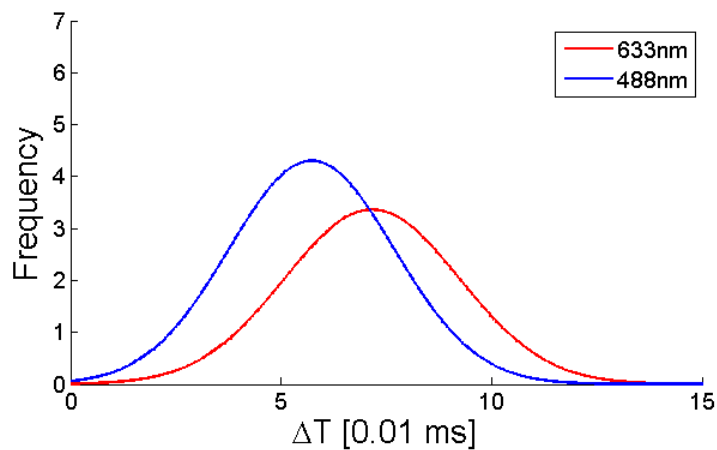


Fig. 5.39 The ΔT distribution of the two different colored target molecules. The variation in the velocity results in high FWHM in ΔT , hindering the differentiation capacity.

5.5.3 Hydrodynamic Focusing

In order to improve the aforementioned problems, particles need to be moved closer to the center, to create higher signals and also to move with more uniform velocities. One simple approach for achieving this is to hydrodynamically focus the particles towards the middle of the channel. Since the optofluidic device is planar, initially 2D focusing approach is implemented. In order to achieve 2D focusing on the horizontal (x) direction, two additional channels are created at the inlet to establish side flow channels to symmetrically apply pressure around the inlet [222].

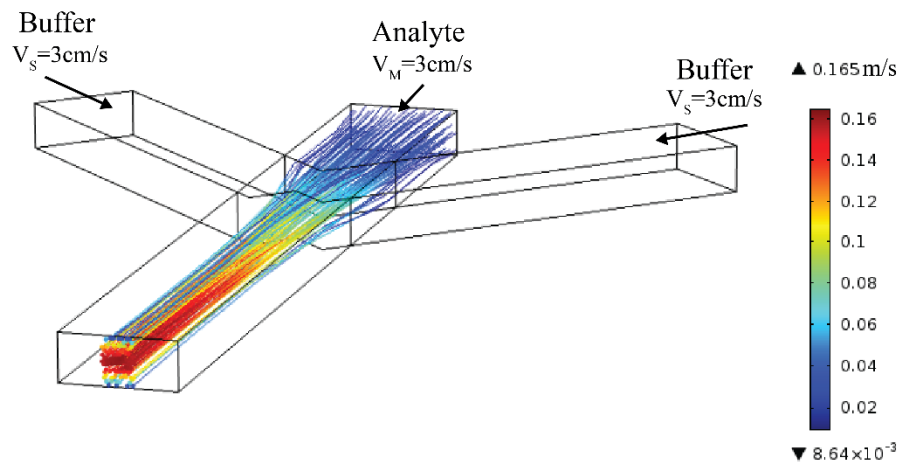


Fig. 5.40 The particle trajectories for a 2D hydrodynamic focusing with $V_S = V_M = 3\text{cm/s}$ channel flow velocities.

The simulations for the fluid flow, velocities and particle trajectories are carried out by setting up a 3D model (COMSOL) consisting of a liquid-core channel and an inlet with three arms. Fig. 5.40 shows the particle trajectories when the main inlet velocity

$V_M=3\text{cm/s}$, and the velocity of the side inlets $V_S=3\text{cm/s}$, showing the 2D hydrodynamic focusing. Fig. 5.41 shows the particle distributions when the side channels have different flow velocities, demonstrating how higher side velocities create more efficient focusing. The bottom right image refers to the scenario in Fig. 5.40.

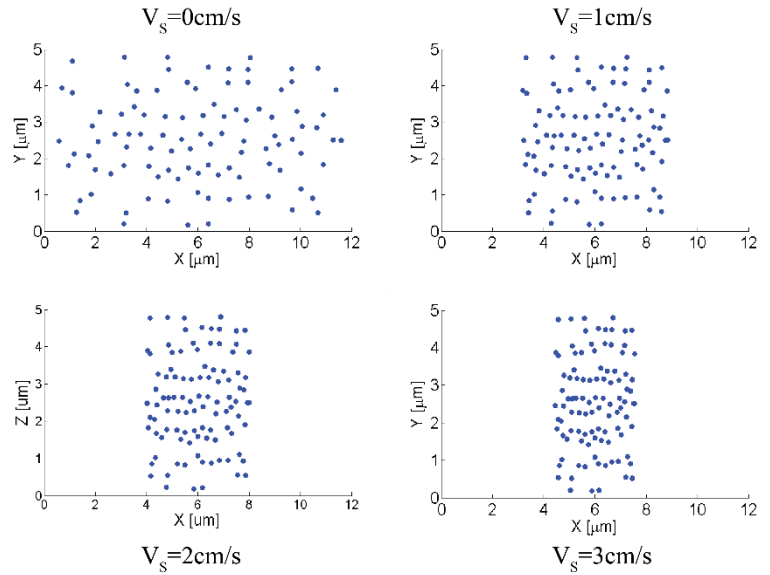


Fig. 5.41 Particle distribution at the liquid-core waveguide cross-section excitation area, for different side channel flow velocities, 0-3cm/s.

Based on the particle distributions obtained from the simulations, and the calculations presented in the Section 5.5.1, the intensity histogram for one hundred particles are generated for $V_S=V_M=3\text{cm/s}$. Fig. 5.42 shows the histogram plot, clearly proving how the 2D focusing improved the intensity distribution by creating more signals with higher intensities, compared to Fig. 5.37b.

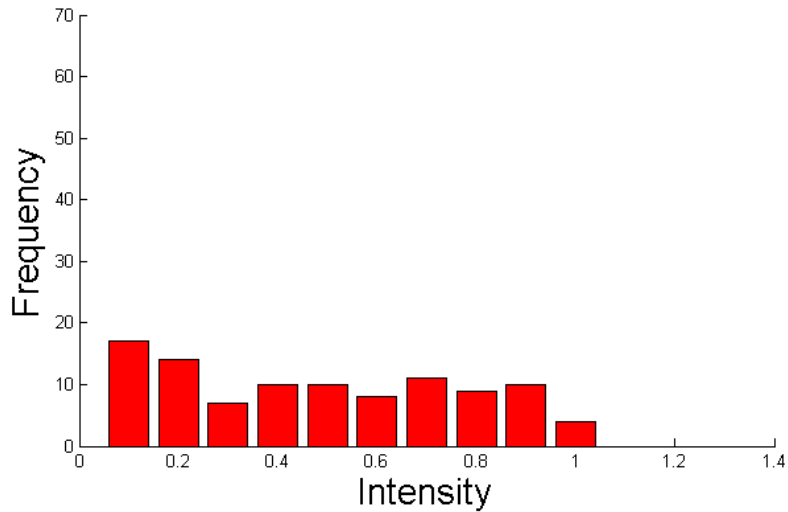


Fig. 5.42 Histogram plot of the calculated intensities for particles shown in Fig. 5.40.

It is evident that there are more particles with higher intensities compared to non-focused particle distribution.

The 2D hydrodynamic focusing is directly implemented on the existing MMI ARROW platform design, by simply adding two more side channels on the inlet of the liquid-core waveguide. Fig. 5.43 a-b shows the SEM image for the hydrodynamic focusing device implemented on an ARROW platform with an MMI waveguide. Additionally, a PDMS control layer is fabricated to control the fluidic pressure for all three channels. (see Fig. 5.43c) The particle experiments are carried out by using Invitrogen 0.2 μ m polystyrene beads, and the side channel flow speed is kept the same as the main inlet to achieve efficient focusing. (see Fig. 5.43b) Fig. 5.44 shows the autocorrelation curves for the data traces with and without the hydrodynamic focusing. It is observed that the particles are slightly faster, and ΔT is smaller for the experiment with hydrodynamic focusing. Even though it is slight, improvement in the FWHM of the

velocity variation is observed for experiment with hydrodynamic focusing. $FWHM_{\Delta T}$ for focused experiment is 0.343ms whereas, $FWHM_{\Delta T}$ for non-focused experiment is 0.367ms. Although this is not enough improvement to achieve significantly better differentiation, with more control over the flow and the process, this method helps to improve the velocity variation of the particles.

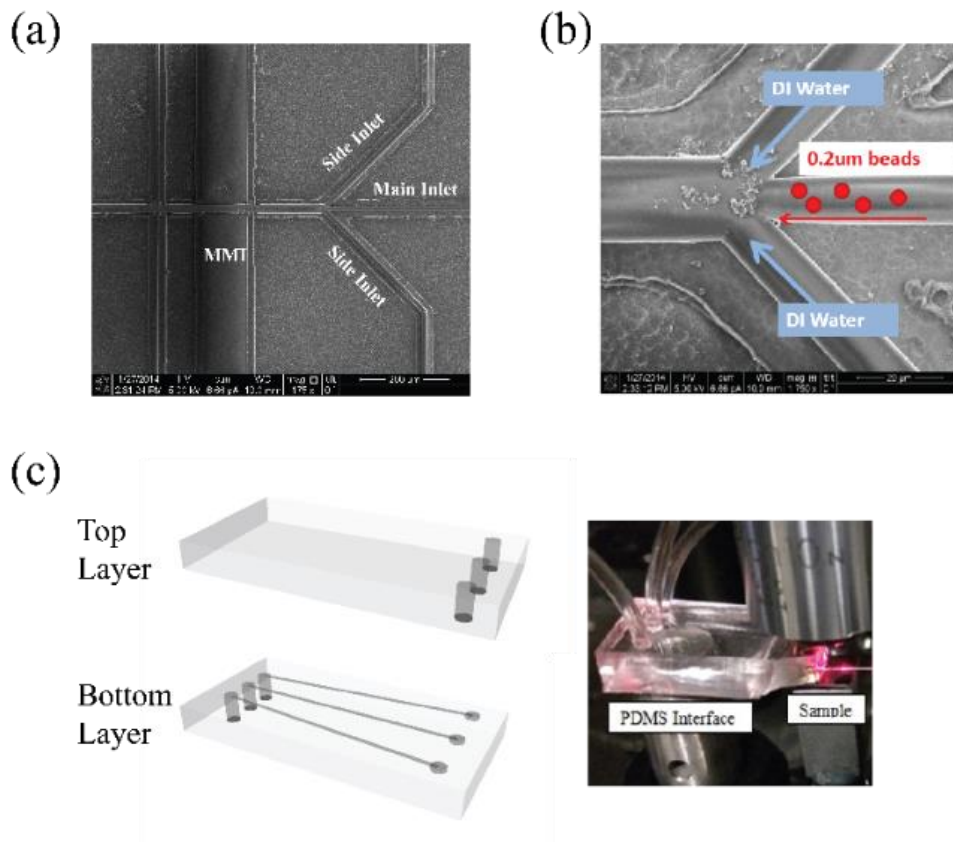


Fig. 5.43 (a) SEM image of MMI ARROW platform with hydrodynamic focusing section, showing the three arms of the inlet. (b) Zoomed in image of the hydrodynamic focusing section. (c) PDMS control layer for precise pressure control of the inlets.

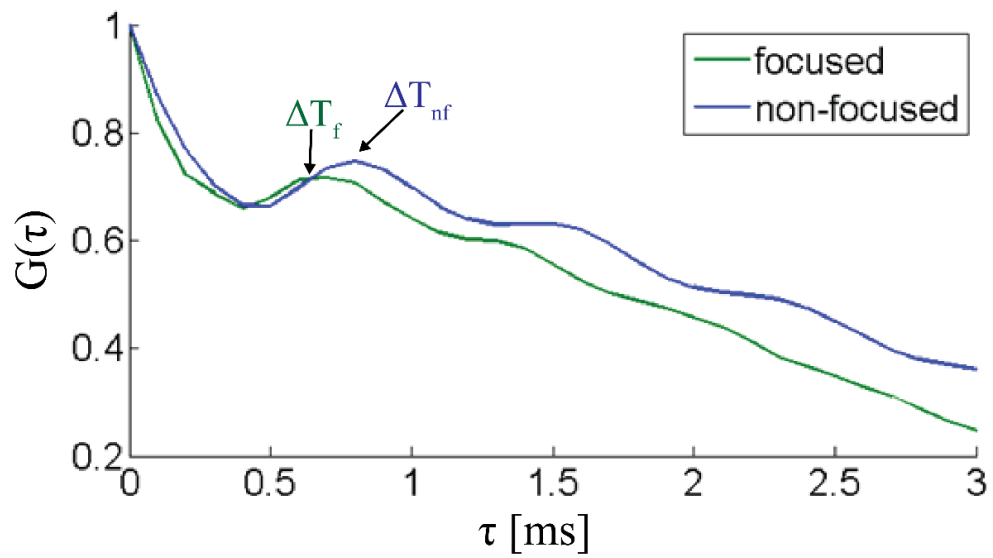


Fig. 5.44 The autocorrelation curves for the data traces with and without the hydrodynamic focusing, showing the slight improvement in the ΔT variation.

6 Conclusions

In conclusion, we have designed, characterized and demonstrated multiple novel optofluidic bio-sensing platforms. They dramatically improve the functionality and the sensitivity of the ARROW based biosensors, with multiple different aspects. First of all, an integrated tailorable filtering device based on ARROW technology is presented providing a high precision, customizable, and low-cost on chip filtering for fluorescence detection. A novel dual-core optofluidic chip is designed and implemented for independent particle detection and fluidically tunable spectral filtering. A separate fluidic channel for detection and filtering allowed for a room to incorporate multiple different tunable filtering approaches, while both channels remained optically connected. First approach was to modify the spectral response of the filter channel by changing the liquid inside the channel, resulting in very high rejection ratios $\sim 43\text{dB}$, for on-chip notch filters rivalling those of standard off-chip components. In addition to eliciting a desired spectral response via the core refractive index, a liquid-core waveguide filter was also adjusted using the intrinsic bulk optical properties of the core liquid, by using selectively absorbing molecules and pH dependent absorption. Combining this approach with the core index tuning, the simultaneous and independent control over two independent spectral absorption features was demonstrated for the first time. Incorporation of spectral filtering is an important step towards fully integrated optofluidic biosensors, reducing the cost and increasing the adaptability. [44], [138]

The fluorescence detection of single bioparticles requires high sensitivity. As we have reached the ultimate limit of detecting individual bio-particles labeled by single or few fluorophores, high sensitivity measurements are challenging, and required. We have addressed this problem by designing and implementing an optofluidic bio-sensing platform with integrated Y-splitter waveguides to achieve signal-to-noise ratio (SNR) enhancement. We have demonstrated SNR enhancement for single virus detection on LC-ARROW chips by multi-spot excitation to create temporally encoded fluorescence signals. Three different Y-splitter waveguides creating $N=2, 4$ and 8 excitation spots were fabricated, characterized and tested using polystyrene beads and fluorescently labeled viruses as analytes. The temporally encoded fluorescence signal from single H1N1 viruses were successfully collected and processed with a signal processing algorithm. 50,000 fold SNR enhancement was achieved in good agreement with theoretical analysis, further increasing the sensitivity of these optofluidic bio-sensors. [165], [217]

The ability to simultaneously detect and identify multiple biological particles or biomarkers is one of the key requirements for molecular diagnostic tests. Here, for the first time, we designed, characterized and implemented a novel optofluidic platform based on multi-mode interference (MMI) waveguides for multiplexed fluorescence spectroscopy, by taking advantage of spectral and spatial capabilities of MMI devices. First of all, we used a single multi-mode interference (MMI) waveguide to create wavelength dependent spot patterns across the entire visible spectrum and enable multiplexed single biomolecule detection on an optofluidic chip. Each target is

identified by its time-dependent fluorescence signal without the need for spectral demultiplexing upon detection. We demonstrated detection of individual fluorescently labeled virus particles of three influenza A subtypes, H1N1, H2N2 and H3N2, at clinically relevant concentrations, by using three wavelengths. Additionally, we demonstrated combinatorial multiplexing by MMI excitation using two colors for identifying three virus types. [212] To further increase the multiplexing capability of these platforms, three different liquid-core waveguides were integrated onto these optofluidic MMI waveguides. This method utilized the spatial multiplexing capacity of the MMI waveguides, and improved further by incorporating the spectral multiplexing approach. Combination of spectral and spatial multiplexing aspects of MMI waveguides improved the functionality of these platforms by enabling high capacity differential diagnosis. [218] Finally, cascade MMI waveguides are designed and implemented to improve the reliability of the combinatorial multiplexing approach by using the asymmetrical properties of these devices.

MMI-based wavelength division multiplexing is clearly ideal for on-chip bioanalysis, providing the missing element to turn an optofluidic chip with single molecule detection sensitivity into the basis for a powerful and versatile diagnostic instrument for a variety of bioparticles and biomarkers. Beyond that, the ability to encode different wavelengths into unique spatial light patterns opened the door to new avenues for integrated photonic and optofluidic devices, for example spectrally reconfigurable optical particle traps or distribution of different colors to different areas on a chip [69]. Furthermore, taking advantage of the flexible nature of PDMS, optofluidic platform

based on MMIs was created to provide multi-modal photonic reconfiguration and advanced fluidic sample handling [219]. The planar optical architecture also allowed for further integration of a dedicated microfluidic layer for upstream sample processing and distribution [46], [47], as well as techniques for focusing the particles in the center of the fluidic channel for optimized detection efficiency.

7 Appendices

7.1 Appendix A Setup Details

7.1.1 A.1 Single Molecule Detection Setup

The single molecule detection setup shown in Fig. A. 1, allows for high sensitivity measurement of the signals generated by the fluorescently labeled target molecules. Free space laser light from various sources {1,2,3,4} is coupled into a single-mode fiber {7} through an objective {6}. Depending on the experiment, different laser sources, and combination of them are used. This setup is also compatible to integrate any other source by simply replacing the excitation fiber. NKT White Light source is also used as an alternative source.

Single-mode fiber is butt-coupled into the single-mode excitation input waveguide. The optimum coupling is achieved by using precision translation stages {20}. Fluorescent signals generated in the channel are collected from the collection waveguide by an objective lens {13} and pass through a spectral filter {27} where the filter type depends on the application. This filter is chosen such that it blocks the excitation wavelength and lets the fluorescent signal pass through.

After being coupled into a multi-mode fiber {10}, fluorescent signals are delivered into the avalanche photodiode single photon counting module {5}. The photons are recorded using a time-correlated single photon counting PCI-board and commercial software in time-tagged time-resolved (TTTR) collection mode.

Simultaneously, during the experiment, the power in the liquid-core waveguide is monitored by collecting the throughput power from the excitation solid-core waveguide, and measuring the power with a powermeter. {14,21}

The alignment of the collection solid-core to the multi-mode collection fiber is achieved by illuminating the facet with an LED {18} and imaging the core with a CCD camera {17} and positioning the stage accordingly. The iris diaphragm {19} is close enough to block the scattered light, allowing the signal only from the waveguide core. After the alignment, the kinematic mirror {11} and the beam splitter {12} are removed to allow for collection of the signal.

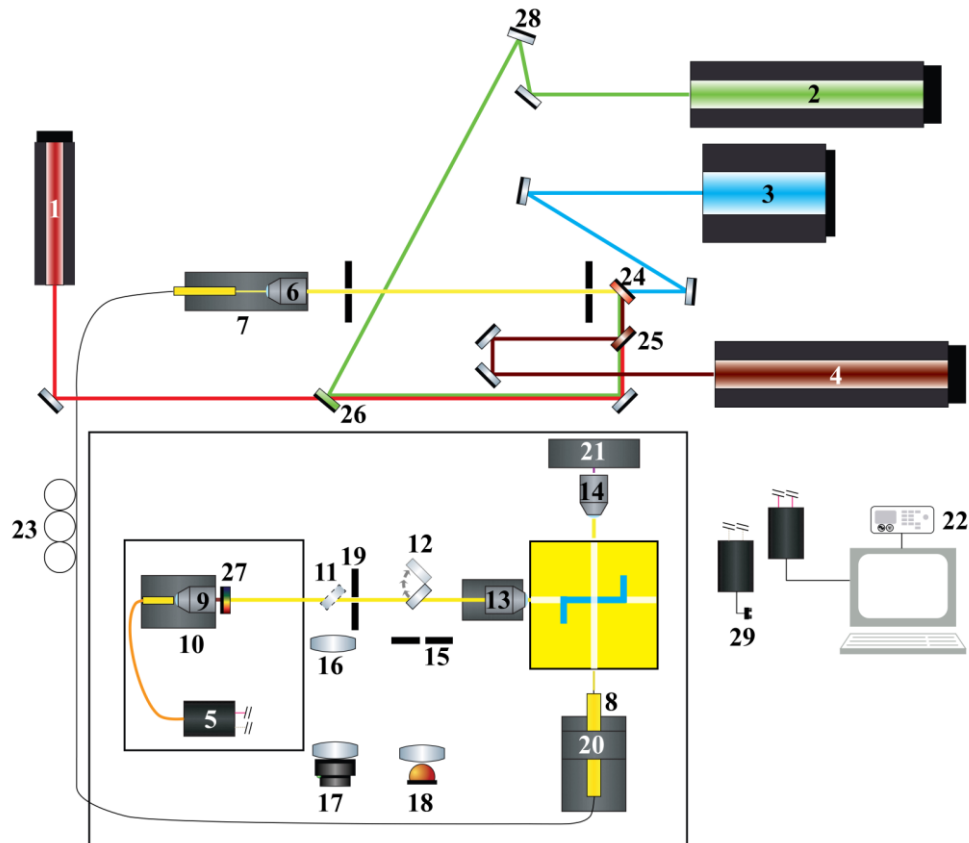


Fig. A. 1 Schematic for Single Molecule Detection Setup

REF	DESCRIPTION	DETAILS	#
1	HeNe Laser (633 nm)	Melles Griot, 12mW	x1
2	DPSS laser (556nm)	Shanghai Dream Lasers, 30mW	x1
3	Argon-Ion Laser (488nm)	Spectra Physics 361C	x1
4	Ti-Sapphire Laser (>745nm)	Del Mar Photonics-Trestles	x1
5	Single Photon Counting Module	Excelitas-SPCM-AQRH-14-FC	x1
6	Objective	Newport M-40x	x1
7	Single-Mode Fiber Coupler	Newport F-915T	x1
8	Fiber Chuck	FPH-S-2.5	x3
9	Objective	Newport M-40x	x1
10	Single-Mode Fiber Coupler	Newport F-915	x1
11	Mirror, kinematic mount	Thorlabs PF10-03-P01, KB1X1	x1
12	Beam splitter (pellicle), fork	Thorlabs BP145B1, BP107	x1
13	Objective	Newport M-60x	x1
14	Objective	Newport M-20x	x1
15	Iris Diaphragm	Newport ID1.0	x1
16	Plano-Convex Lens	Thorlabs LA1805	x1
17	CCD Board Camera	Allied Electronics CVC-50BC	x1
18	White LED	N/A	x1
19	Iris Diaphragm	Newport ID 0.5	x1
20	UltraAlign xyz stage	Newport 561D-XYZ, 561-FC	x1
21	Optical Multimeter	ILX Lightwave OMM-6810B	x1
22	Function Generator	Tabor Electronics WW5061	x1
23	Polarization controller	Thorlabs FPC030	x1
24	510 shortpass	Omega Optics 510SP	x1
25	Dichroic 700nm Shortpass Filter	Edmund Optics 69-194	x1
26	Dichroic 593nm Longpass Filter	Brightline FF01-593/LP-25	x1
27	Multiband Bandpass Filter	Brightline FF01-440/521/607/694/809	x1
28	Mirror	Thorlabs PF10-03-P01	x8
29	DC Power Supply	GW Instek GPS-2303	x1
Other	Time-correlated single photon counting PCI-board	(Time Harp 200, PRT 400 router; Picoquant, Germany)	x1

Table A. 1 Parts list for single molecule detection setup

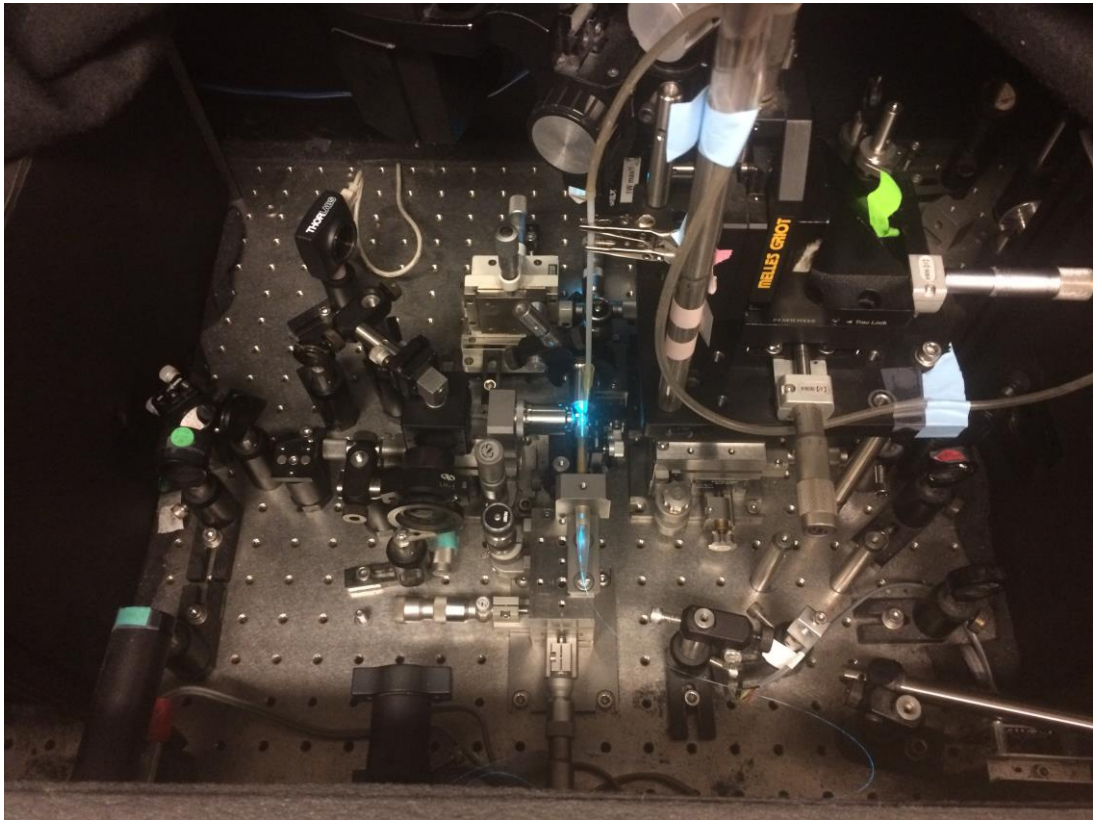


Fig. A. 2 Pictures of the Single Molecule Detection Setup - Excitation section inside the box.

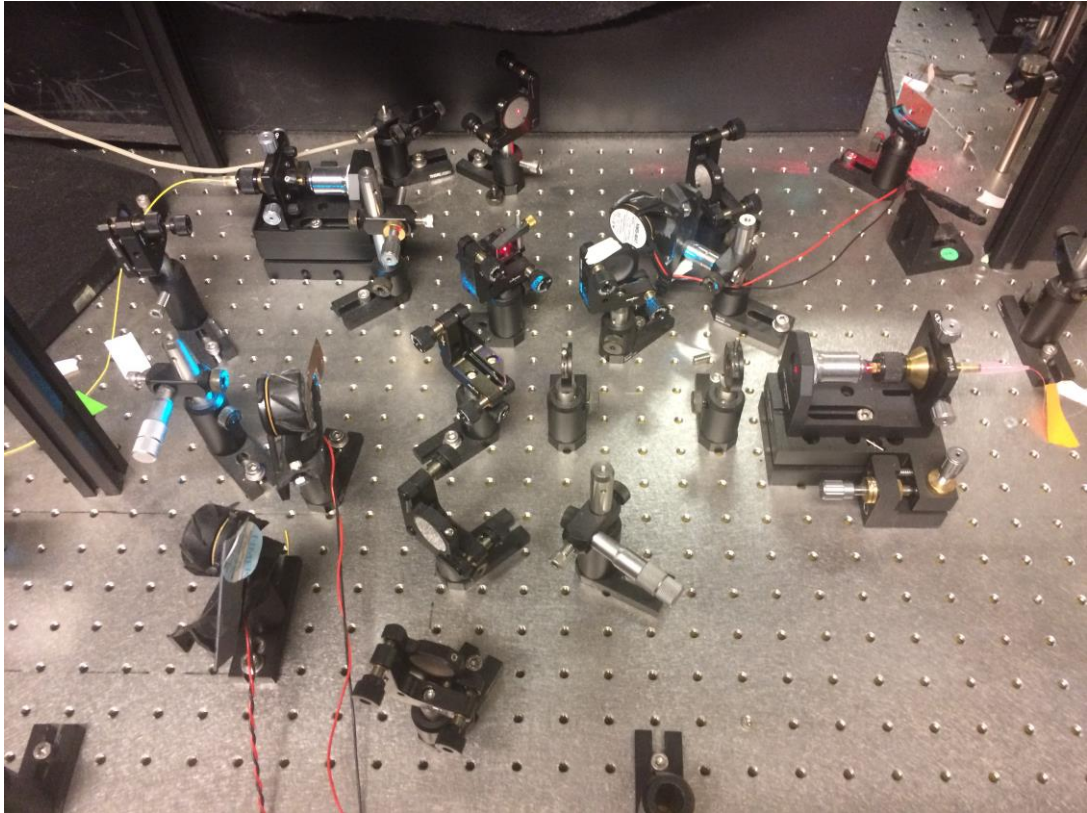


Fig. A. 3 Picture of the Single Molecule Detection Setup - Laser coupling section.

7.1.2 A.2 Compound Microscope Setup

The compound microscope setup allows for top down imaging of the sample, while being able to introduce laser light into it. For the projects discussed in this dissertation, it is mainly used to characterize the excitation spots in MMI and Y-splitter waveguides. Fig. A. 4 shows the schematic for the working principle of the infinity corrected compound microscope with a tube lens and the picture of the fabricated compound microscope. The infinity corrected optical system provides space (infinity space) to introduce optical components such as optical filters and beam splitters. The sample is illuminated by using LED light which is redirected onto the sample by a beam splitter.

It is important to make sure that the illumination is focused into the back aperture of the objective to prevent noise. The image from the sample is collected and passes through the spectral filters to eliminate the excitation light. The image is then focused into the camera by using an achromatic tube lens to prevent chromatic aberrations. The beam splitter platform is designed such that it can be removed during the imaging, when the illumination is not needed. The irises and diffusers on the illumination path allow for uniform illumination of the sample.

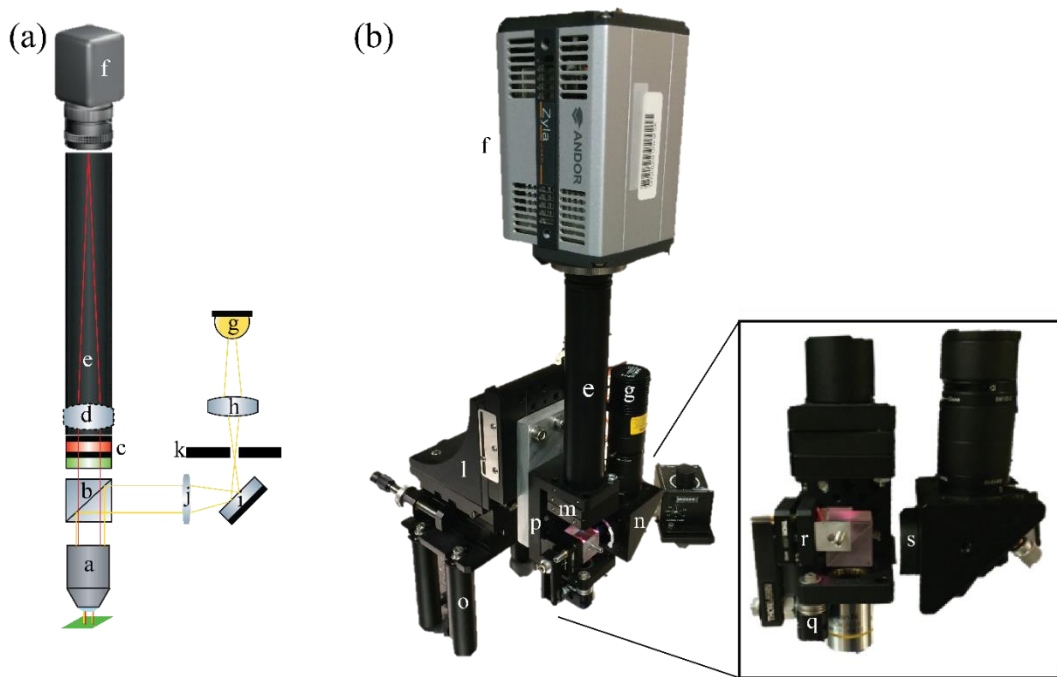


Fig. A. 4 (a) Schematic of the compound microscope. Yellow lines show the illumination path; red lines show the imaging path. (b) Picture of the compound microscope.

REF	DESCRIPTION	DETAILS	#
a	10X Olympus Plan Achromat Objective	Thorlabs RMS10X	x1
b	50:50 Non-Polarizing Beamsplitter Cube	Thorlabs BS016	x1
c	Spectral Filters	Omega 3RD640LP , 775ALP	x1
d	f=150.0 mm, Ø1" Achromatic Tube Lens	Thorlabs AC254-150-A	x1
e	Extension Tube, 6" Long	Thorlabs SM1E60	x1
f	sCMOS Camera	Andor's Zyla 5.5	x1
g	Cold White Mounted LED	Thorlabs MCWHL5	x1
h	Plano-Convex Lens	Thorlabs LA1805	x1
i	Mirror	Thorlabs PF10-03-P01	x1
j	Ground Glass Diffuser	Thorlabs DG10-600	x1
k	Lever-Actuated Iris Diaphragm	Thorlabs SM1D12	x1
l	XYZ Translation Stage, 2"	Thorlabs LT3	x1
m	Threaded 30 mm Cage Plate	Thorlabs CP02	x2
n	Kinematic Mirror Mount with Cage	Thorlabs KCB1	x1
o	Post Holder	Thorlabs PH4	x4
p	Cage System U-Bench	Thorlabs CB1	x1
q	Cage Mounting Bracket	Thorlabs CP02B	x1
r	Compact Kinematic Mirror Mount	Thorlabs KMS	x1
s	Lens Tube	Thorlabs SM1L05	x1
Other	Coupler Ring	Thorlabs SM1T2	x2
Other	Cage Assembly Rod	Thorlabs ER1	x2

Table A. 2 Parts list for compound microscope

7.1.3 A.3 White Light Setup

The white light source is a crucial part of spectral characterization measurements. In this research, it is mainly used to characterize the spectral responses of the liquid-core waveguides, especially the tunable filter waveguides. The white light is generated by using the non-linear response of the photonic crystal fiber (PCF). Fig. A. 5 shows the schematic for the white light generation setup.

A high intensity white light (~475 to 950 nm) is generated by coupling pulsed light (120 fs temporal width, 75 MHz repetition rate) at 850 nm {a}, into a highly nonlinear photonic crystal fiber {i}. The white light is then coupled through a water-filled optofluidic waveguide via the collection solid-core and collected by an optical spectrum analyzer at the opposite end.

Laser pulses (120fs, 75 MHz) at 850nm {a}, were coupled via an optical isolator and an objective lens (O1) into a nonlinear photonic crystal fiber {i}. As the high intensity laser pulse propagates through the PCF near the zero dispersion wavelength, a combination of various effects including self-phase modulation, cross-phase modulation, Raman scattering disperse the pulse into a broad continuum of wavelengths in the visible and near-IR ranges [223]. The white light is then coupled into a single mode fiber {k} and directed into the ARROW to be analyzed. The transmitted light is collected by an objective {o} and sampled in an optical spectrum analyzer {q} to determine the spectral response.

In order to get a stable spectrum, it is crucial to have a stable mode-locked source, and coupling stages. Since the coupling of laser into the photonic crystal fiber is very precise and sensitive, slight misalignments and fluctuations affect the output spectrum dramatically.

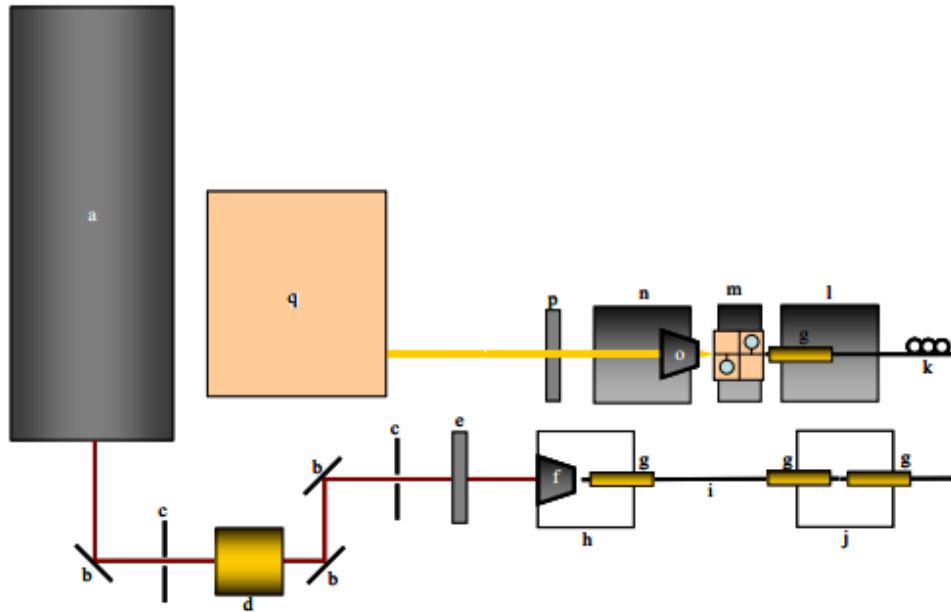


Fig. A. 5 The schematic for the white light setup.

REF	DESCRIPTION	DETAILS	#
a	Coherent Mira laser (850nm)	1W, (Mira 900F)	x1
b	Mirror, Mount	Thorlabs PF10-03-P01, KM100	x3
c	Iris Diaphragm	Thorlabs ID15	x1
d	Optical Isolator	OFR IO-3D-830-VLP	x1
e	Half-Wave Plate	Thorlabs WPH05M-830	x1
f	Objective	Newport M-60x	x1
g	Fiber Chuck	Newport FPH-S-2.5	x4
h	SMF coupling stage	Newport F-916	x1
i	Non-linear PCF	Thorlabs NL-2.3-790-02, 1m	x1
j	XYZ stage	Thorlabs MAX313	x1
k	Polarization Controller and Fiber	Thorlabs FPC030, F-SV	x1
l	UltraAlign xyz stage (Left handed)	Newport 561D-XYZ-LH, 561-FC	x1
m	UltraAlign yz stage	Newport 561D-YZ	x2
n	UltraAlign xyz stage	Newport 561D-XYZ, 561-FC	x1
o	Achromat 20x Objective	Thorlabs RMS20X	x4
p	Linear Polarizer	Thorlabs LPVIS050	x1
q	OSA	Ando AQ6370	x1

Table A. 3 Parts list for white light setup

Fig. A. 6 shows the spectrum of the generated white light ranging from ~470nm to 1000nm with a fairly uniform intensity in the visible range. The peak at ~850nm is coming from the input pulsed laser wavelength.

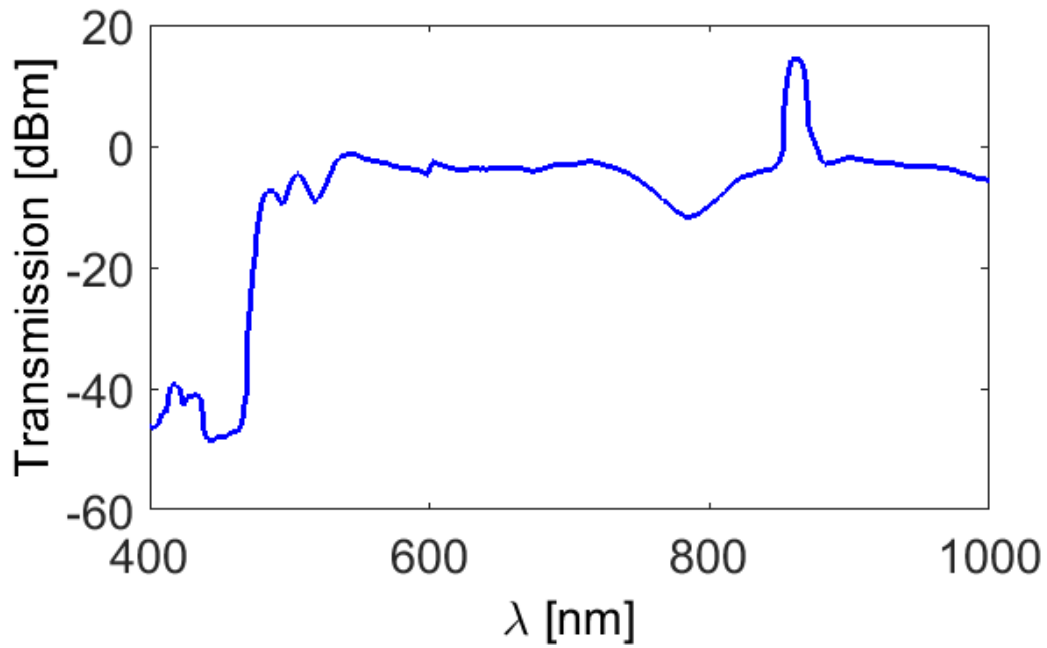


Fig. A. 6 Spectrum of the generated white light source.

7.2 Appendix B Filling and Cleaning Procedure of Liquid-Core

Waveguides

The main method for filling the liquid-core waveguide channels is done by creating a pressure difference between the channel inlets. The liquid is inserted in one of the reservoirs, and the positive pressure moves the liquid along the channel. The hydrophilic nature of the channel walls also create adhesion, and help the liquid move through the channel. In the cases where the channel walls are hydrophobic, or there is a clogging problem in the channel, negative pressure is applied to pull the liquid through the channel.

Fig. B. 1 shows a liquid core waveguide during the filling process, showing the concave meniscus of the liquid inside the channel. Although how the channel looks when filled depends on the wafer, this picture is a good representation of telling the difference between the filled and empty channels. There are couple different ways to identify if the channel is filled or not. One of the most effective way is the look for a bright line along the channel walls. This bright line would be dark for an empty channel. Another method is to check the color of the channel. The color of the channel tends to change after filled with a liquid, getting a similar tone to the solid core waveguides surrounding it. This color can also be compared to an empty channel in another sample to be able to tell the difference. When the channel is filled, it is important to make sure that there are no bubbles in the channel, and more negative pressure should be applied to move the bubble out.

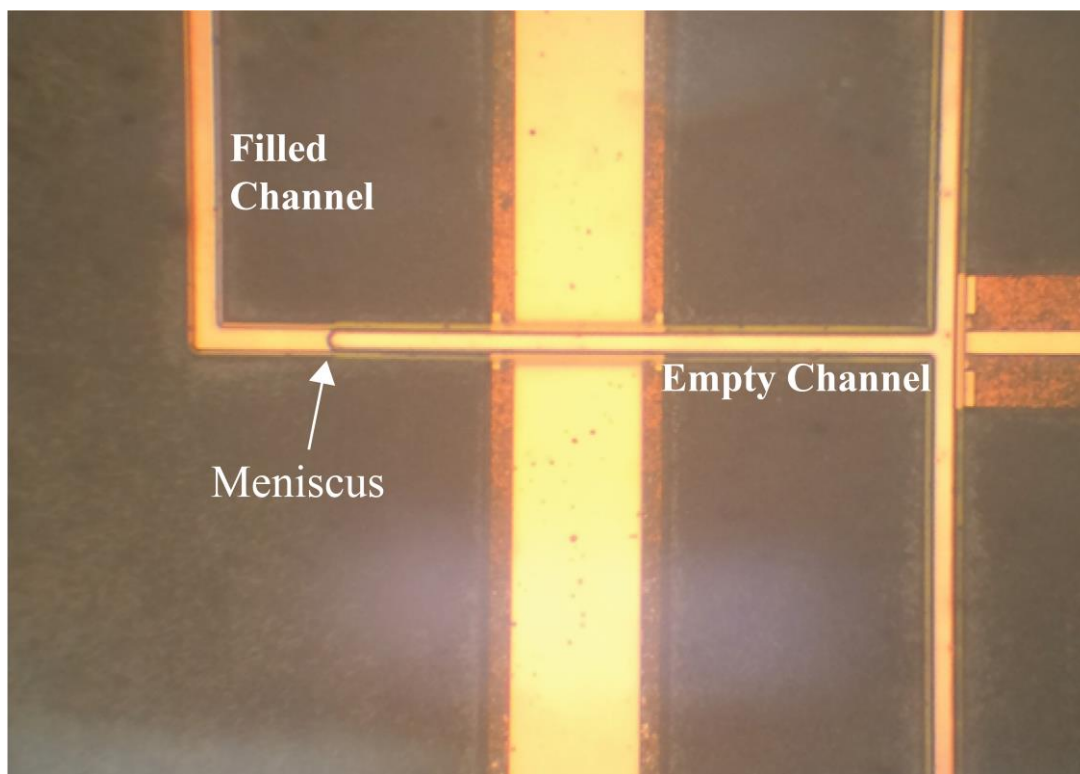


Fig. B. 1 The picture of a liquid-core waveguide channel during the filling procedure showing the filled and empty parts of the channel.

Due to the different procedures used during the fabrication, the channels can be hydrophobic which would make them harder to fill. If the water or the buffer used for the analyte is not filling the channel, isopropanol alcohol (IPA) can be used to fill the channel first and then the actual analyte can be introduced. Since IPA has a lower surface tension, it is easier to create adhesion and fill the channel initially.

In addition to these problems, after running the experiments, and introducing particles into the channel, clogging problems can occur. The channel should be cleaned by filling the reservoirs with water initially, and applying negative pressure on the other end, to rinse the channel. If the clogging persists, then IPA and acetone can be used to wash

the channel. It is important to note that acetone will dissolve the adhesive that is used to put on the reservoir. When using acetone to clean the sample, the reservoirs should be removed first, and all the adhesive should be cleaned to prevent it from getting it into the channel. Another very efficient method is to put the sample in 80°C water, while applying negative pressure to clean the channel. If the channel is not cleaned enough, and there is some residual fluorescent dye inside the channel, it will create a high background for the next experiment. In that case, sodium hypochlorite (household bleach) solution can be used to rinse the channel to bleach the dye. However, this process needs to be done not letting the solution dry in the reservoir to prevent clogging of the channel by salt crystals formed by the solution.

7.3 Appendix C MMI Alignment Procedure

In order to excite only the symmetrical modes, the input mode of the MMI waveguide should be located in the middle. Any slight offset creates deviation in the MMI pattern causing undesired spot pattern. For that reason, the alignment of the excitation fiber into the input waveguide is very crucial to get a proper spot pattern. It is also crucial for achieving maximum intensity inside the liquid-core waveguide.

Since MMI waveguides do not have a single output waveguide section, proper coupling is not straightforward. There are few different methods to achieve good coupling. The best way to establish a good spot pattern is to monitor the spot pattern with the compound microscope, while optimizing the coupling. Then, the scattered light at the output section can be recorded for future alignment without the microscope. Although there are slight variations among different wafers for this output scattered light, most of the time the scattered light pattern would be in a specific shape, when the fiber is properly aligned. Fig. C. 1a shows the scattered light imaged on a white surface when there is a proper alignment. Fig. C. 1b shows the scattered image when the fiber is misaligned in the horizontal direction. Based on these figures, the rough alignment can be achieved during the experiments, when the spot pattern is not monitored by the compound microscope. After this rough alignment, the spot patterns in the collected data need to be verified, and if the spot patterns are not good, more adjustments should be made until good patterns in the collected data is achieved.

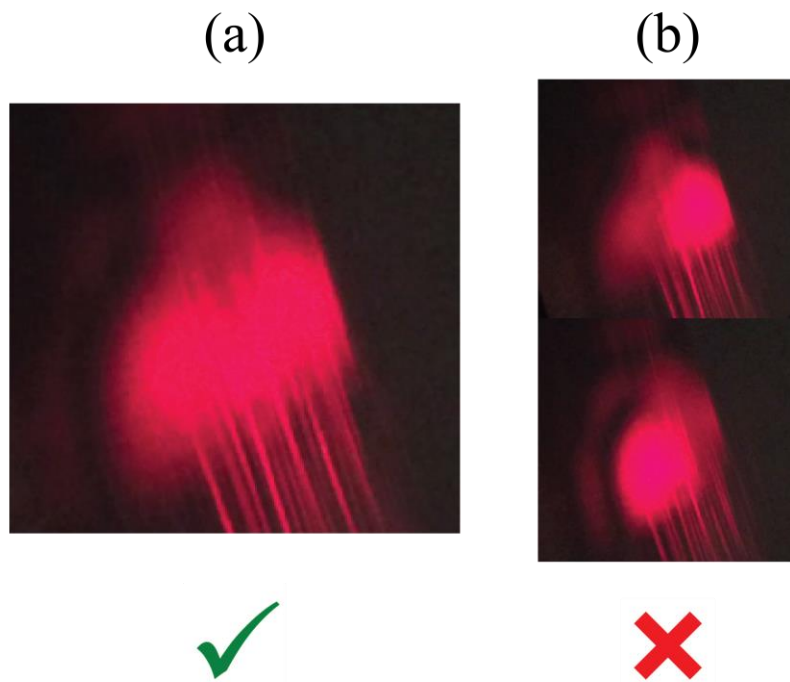


Fig. C. 1 Using the scattered light pattern for MMI alignment (a) Pattern when the fiber is aligned (b) Patterns when the fiber is horizontally misaligned

7.4 Appendix D Virus Labeling Procedure

Inactivated, whole influenza virus samples were purchased for testing.

- β -Propiolactone-inactivated A/PR/8/34 (H1N1) (Advanced Biotechnologies Inc.)
- UV-inactivated A/2/Japan/305/57 (H2N2) (Advanced Biotechnologies Inc.)
- Formalin-inactivated A/Aichi/68 (H3N2) (Charles River)

Viruses were dyed using NHS-activated Dylight fluorophores according to manufacturer instructions (Thermo Scientific). (see Table D.1 for details) Briefly, virus samples were added to aliquots of dried Dylight dyes and allowed to incubate at room temperature for 2 h. Samples were then separated from free dye using PD MiniTrap G-25 gel filtration columns (GE Healthcare). In gel filtration chromatography method, larger particles cannot enter the gel and they elute sooner because they have less volume to traverse compared to the smaller particles. Since the labeled viruses are bigger than the free dye, they elute sooner than the smaller free dye. While collecting the fractions during the gel filtration chromatography, the labeled viruses are collected first and then the concentration of free dye increases, creating a higher background for the detection. For that reason, it is important to pick the optimum fraction with high virus concentration with lower background. Fig. D. 1 shows the gel filtration chromatography process during the labeling procedure, showing the droplet with a high concentration of free dye. For characterization, the fractions are tested on a custom total internal reflection fluorescence (TIRF) microscope. Once identified, the viral fractions were aliquoted and flash-frozen via liquid nitrogen for later use. Although

manufacturer concentrations were reported, the variable dilution/fractionation process of gel filtration chromatography leads to an inability to directly account for virus concentration. However, TIRF-based measurements concluded that virus concentrations were on the order of femto-molar as observed by direct counting on the chip.

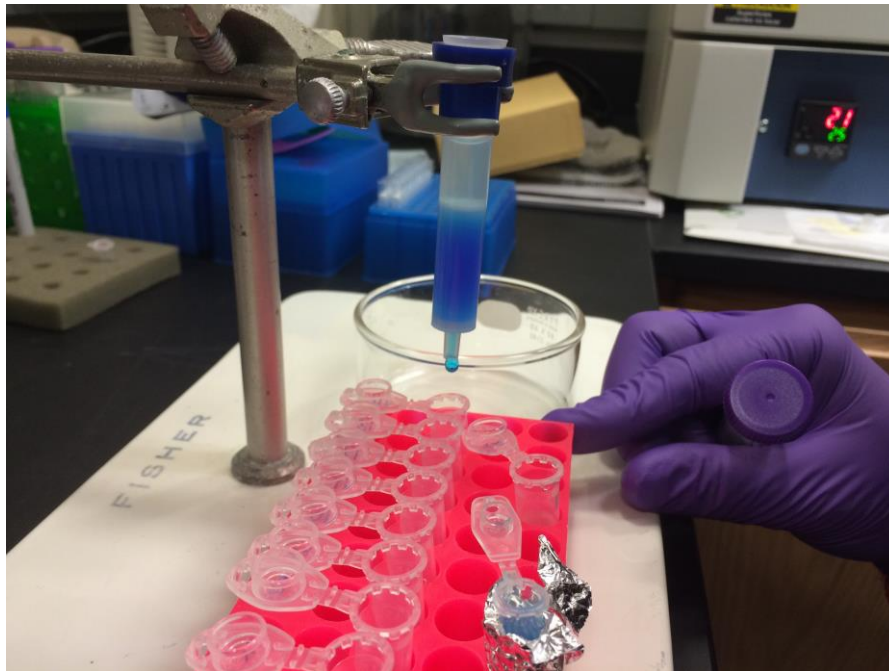


Fig. D. 1 Gel Filtration Chromatography Procedure

Labeling Procedure

- Aliquot stock virus sample into 75 μ L each and flash freeze them.
- Mix 1mg of stock NHS ester dye with 1mL DMSO and aliquot into 100 μ L.
- Keep the aliquots of dye in a vacuum centrifuge to dry off the DMSO.
- Each aliquot of dye has 0.1mg of dye.

- Mix 75 μ L of virus sample in 0.1mg of dye.
- Incubate in room temperature for 3-4 hours
- Take a PD MiniTrap G-25 gel filtration column and hold it in a stable stand. (see Fig. D. 1)

- Remove the top and the bottom cap.
- Empty the buffer drop by drop till the meniscus of the buffer reaches the cotton part of the column.
- Immediately fill the column with 1X PBS buffer. Never let the cotton dry!
- Do the same procedure 3 times to completely wash off the buffer in the column and substitute with PBS buffer.
- At the end of the third wash with PBS, when the meniscus touches the cotton part, pipet the incubated labeled virus sample at the center of the cotton surface.
- Start collecting the drops in vial #1
- Immediately pipet 100 μ L of PBS buffer on top of the pipetted virus.
- Wait for the meniscus formed to reach back the cotton (about 1-2 sec, one might collect 2-3 drops during this time).
- When meniscus reaches the cotton, fill the whole column with PBS buffer.
- Start collecting drops (2 drops each from vial #2 till vial #4 and 1 drop each from vial #5 onwards) (see Fig. D. 1)
- Collect the drops till they have concentrated dye in the drops, when they visibly change color. This will be around when drop collection reaches 20th-24th vial.
- Flash freeze the collected droplets for future characterization.
- Use a TIRF/confocal microscope to determine the vial with the higher concentration of the labeled viruses, with a low background.

Important:

- Never let the cotton dry.
- Let the pipetted virus and 100 μ L PBS buffer completely get absorbed by the cotton before filling the column with PBS buffer.

Table D.1 Virus Labeling procedure with gel filtration chromatography.

7.5 Appendix E ARROW Waveguide Fabrication Parameters and Procedure

Here, the fabrication procedure and the design details of ARROW wafers used in the experiments are explained.

7.5.1 E.1 Tunable Filter – TF11

TF11			
Bottom Layers			
Oxide 1	- 296 nm	43.76 nm/min	n=1.457
Nitride 1	- 115 nm	12.65 nm/min	n=2.068
Oxide 2	- 296 nm	41.40 nm/min	n=1.458
Nitride 2	- 230 nm	13.38 nm/min	n=2.044
Oxide 3	- 296 nm	42.80 nm/min	n=1.458
Nitride 3	- 115 nm	13.65 nm/min	n=2.044
Protective Oxide	35-40nm		
Nitride Recipe: 1000 mT, 70 W @ 250°C - 27% 96%			
Oxide Recipe: 600 mT, 3% RF @ 250°C - 9% 17%			
Chrome Stop Etch			
t= 120 nm			
Core (Z1 Core)			
Apply SU-8 10			
<ul style="list-style-type: none"> ○ pour small puddle (about quarter size) ○ 500 rpm @ 100/s, 6 s ○ 5700 rpm @ 1200/s, 60 s ○ 6000 rpm @ 6000/s, 2 s ○ soft bake - 65° 5 min, ramp to 95° 5 min ○ expose 7s ○ post exposure bake - 65° 5 min, ramp to 95° 5 min 			
2. Develop - 1 min			
Final core height: 3.750 um			

Top Layers

Protective Oxide	30-35 nm		
Nitride 4	- 128 nm	12.91 nm/min	n=2.046
Oxide 4	- 368 nm	35.44 nm/min	n=1.465
Nitride 5	- 128 nm	13.22 nm/min	n=2.035
Oxide 5	- 368 nm	37.48 nm/min	n=1.467
Nitride 6	- 128 nm	13.49 nm/min	n=2.020
Oxide 6	- 2516 nm	33.08 nm/min	n=1.472

Oxide 6 Overgrowth: **75%**

Nitride Recipe: 1000 mT, 70 W @ 250°C - 27% 96%

Oxide Recipe: 1100 mT, 3.5% RF @ 250°C - 9% 3%

Ridge Etch

Ridge etch completed:

- SU-8 3005 @ 900 rpm, 60 s
- PE2 O2 Descum @ 200 W, 20 s
- Trion RIE Etch, 229 s

Final ridge height: **1.305 um**

Core Expose Etch

7.5.2 E.2 Y-Splitters – SP2

SP2

Bottom Layers: 6 commercial layers

	SiO2	Ta2O5	SiO2	Ta2O5	SiO2	Ta2O5
n	1.47	2.107	1.47	2.107	1.47	2.107
t (nm)	265	102	265	102	265	102

Adhesion Promoter

- Grow 20nm SiO2 in PECVD2

Chrome Pre-core

- E-beam: Deposit 122nm Cr
- Pattern *ARROW Splitter PreCoremask* using AZ3330
- 5000 rpm, 60s
- Soft bake 90C, 60s
- Expose 8s, Aligner W/ Filter
- Develop 60s, AZ300 MIF
- Hard bake 110C, 2min
- Descum: 100W, 60s
- Etch Chrome
- Clean photoresist with Acetone & IPA
- Descum: 150W, 60s
- Dehybake

Core

- Pattern *ARROW Splitter Coremask* using SU8-10
- (1) 500 rpm, 6s (2) **4200 rpm**, 60s (3) 6000 rpm, 2s
- Soft bake 65C, 8min -> 95C, 8min -> 65C
- Expose 25s, With Filter
- PEB 65C, 6min -> 95C, 6min -> 65C
- Develop , SU8 Developer
- Hard bake 65C -> 200C, 10min (~12min) -> 65C
- Descum: 50W, 60s
- Hardbake 65C -> 250C, 5min(~8min) -> 65C
- Descum: 50W, 60s
- **Height:** Middle: 5.5um Edges: 5.4um

Pedestal Protection

- HMDS: 2800 @ 1100, 30s → 5000 @ 5000 2s
- AZ4620: 2800 @ 1100, 30s → 5000 @ 5000 2s
- Softbake: 70°C, 60sec; 90°C 60sec; 120°C 20s
- Expose: 55s + 7s Flood (without filter)
- Develop: 400K:H2O=1:4 ~3.5min
- **Height:** 2.8um
- Descum 50W, 30s
- HCL Dip: (HCL:H2O, 1:2) for a few seconds
- E-beam: 76nm, Ni
- Ni liftoff with acetone and IPA
- Descum 50W, 30s

Pedestal Etch

- SAPOxide, 710sec, um
- TC1 (H2O2:RS-6=1:10, 55C) 10min
- Dummy Step
- SAPbosch_Si, 2cycles + 6 steps
- Si_isotropic, 80s
- TC1 10min
- Nickel etchant, 3min
- TC1 10min
- Height 6.06um
- Descum 50W, 30s
- Dehydration bake

Top Oxide coat

- ~6um SiO2
- Test wafer Elipsometer before growth: Index: 1.460
- P1: 89.9 A1: 73.4 P2: 180.1 A2: 106.7
- Rate: 40 nm/min
- PECVD2 ran for 2hr and 31min
- Recipe: Temp 250C, RF:3.4, Pressure:1100mT, G1:9, G2:17 (The MFC on PECVD2 has changed since this was fabricated)
- Test wafer Elipsometer after growth: Index:1.466
- P1: 95.1 A1: 48.3 P2: 185.1 A2: 132.3

Ridge

- Pattern *Splitter New Ridgemask* using SU8-2025
- (1) 500 rpm, 6s (2) **3700 rpm**, 60s (3) 6000 rpm, 2s
- Soft bake 65C, 6min -> 95C, 8min -> 65C
- Expose **18s, North** (No Filter) (Align Gap of 10um) (Alignment marks on the new mask are way off check features to align.)
- PEB 65C, 7min -> 95C, **10min** -> 65C, 7min
- Let cool to room temp
- Develop, SU8 Developer: ~1.5min
- Hard bake 65 -> 180, 12 min, cool to 65 (about 15mins)
- Descum 100W, 90s
- Height: 17.4um

Ridge Etch

- Descum 100W, 15sec
- **SAPOxide** 1100sec

- Nanostrip 30min, 90C
- TC1 (H2O2:RS-6=1:10, 55C) 10min
- Descum: 100W, 60sec
- Dehybake
- **Height Etched:** ~2.8um

Core Expose

- Pattern *Splitter Core Expose* mask using AZP4620
- Spin 1500 rpm, 60s
- Soft bake 80C, 20min
- Rest 15min, room temperature
- Expose 30s, North Aligner (no Filter), Soft Contact
- Develop (AZ400K:H2O = 1:4) ~3min
- Hard bake 150C, 2hr
- Descum: 150W, 60sec
- BHF etch 490sec

SU-8 Core Etching

- 90mL H2O2 + 60mL Sulfuric Acid (Piranha)
- Placed in acid
- Changed daily

7.5.3 E.3 Standard MMI – MA13

MA13						
Bottom Layers : 6 commercial layers						
	SiO2	Ta2O5	SiO2	Ta2O5	SiO2	Ta2O5
n	1.47	2.107	1.47	2.107	1.47	2.107
t (nm)	265	102	265	102	265	102
Pedestal Protection						
Pattern <i>Arrow MMI Pedestal</i> mask using AZP4620						
<ul style="list-style-type: none"> • (1) 2800 rpm, 30s (2) 5000 rpm, 2s • Soft bake 70C, 60s; 90C, 60s; 120C, 20s • I accidentally Flood exposed before exposing with the mask • Flood expose 5s 						

- Expose 55s, North Aligner
- Develop 2 1/2 min (AZ400K:H2O = 1:4) measured 1.9 - 2.6um over core
- Redeveloped 20 sec (AZ400K:H2O = 1:4) 2.2-3.2um over core
- Descum 40W, 30s
- Hydrochloric dip
- Deposited 74nm Ni in E-beam
- Lift off Ni with Acetone 15 min
- Descum 50w, 30sec

SAP Oxide

1. 5 min (300s), .805um , rate .161um/min
 2. 3 min more, 1.33um
- TC1 10min, @ 55C
 - Trion Clean
 - **Bosch**
 1. After 2 cycles, 4.6um, rate .2357 um/step
 2. Ran 6 more steps, 6 um
 - **Si_isotropic** 60s, 6.75um
 - TC1 1 min @ 55C
 1. no bubbles needed change TC1
 2. new TC1 10min @ 55C
 - Ni Etchant, 3 min
 1. Left Ni Residue, Etched 2 more min, removed residue
 - TC1 10min @ 55C
 - Descum 50w, 30s
 - Dehydration bake overnight

7.5.4 E.4 Triple Core MMI – TC7

TC7						
Bottom Layers : 6 commercial layers						
	SiO2	Ta2O5	SiO2	Ta2O5	SiO2	Ta2O5
n	1.47	2.107	1.47	2.107	1.47	2.107
t (nm)	265	102	265	102	265	102
Adhesion Promoter						

- Grow 20nm SiO₂ in PECVD2 (Erik)

Chrome Pre-core

- Deposit **121 nm** Cr in E-beam
- Pattern *Triple Core V2 PreCore* mask using AZ3330
- 5000 rpm, 60s
- Soft bake 90C, 60s
- Expose 8s, Aligner W/out Filter
- Develop 60s, AZ300 MIF
- Hard bake 110C, 2min
- Descum: 100W, 60s
- Etch Chrome
- Clean photoresist with Acetone & IPA
- Descum: 150W, 60 sec
- Dehybake

Core

- Pattern *Tripple Core V2 Core* mask using SU8-10
- (1) 500 rpm, 6s (2) **4200 rpm**, 60s (3) 6000 rpm, 2s
- Soft bake 65C, 8min -> 95C, 8min -> 65C
- Expose **9.5s**, With Filter
- PEB 65C, 6min -> 95C, 6min -> 65C
- Develop , SU8 Developer
- Hard bake 65C -> 200C, 10min (~12min) -> 65C
- Descum: 50W, 60s
- Hard bake 65C -> 250C, 5min (~8min) -> 65C
- Descum: 50W, 60s
- **Height:** 5.9um - 6um

Pedestal Protection

- Pattern *Tripple Core V2 Pedestal*mask
- HMDS: 2800 @ 1100, 30s → 5000 @ 5000 2s
- AZ4620: 2800 @ 1100, 30s → 5000 @ 5000 2s
- Softbake: 70°C, 60sec; 90°C 60sec; 120°C 20s
- Expose: 55s + 7s Flood (without filter)
- Develop: 400K:H₂O=1:4 ~3min
- **Height:** ~2.7um
- Descum 50W, 30s
- HCL Dip: (HCL:H₂O, 1:2) for a few seconds
- E-beam: 90nm Ni
- Ni liftoff with acetone and IPA

- Descum 50W, 30s

Pedestal Etch

- SAPoxide, 1200sec
- TC1 (H2O2:RS-6=1:10, 55C) 10min
- Dummy Step
- SAPbosch_Si, 3 cycles 4 steps
- Si_isotropic, 30s
- TC1 10min
- Nickel etchant, 3min
- TC1 10min
- Descum 50W, 30s
- Height measured 6.2um
- Dehydration bake

Top Oxide coat

- ~6um SiO2
- Test wafer Elipsometer before growth: Index: 1.466
- P1: 82.6 A1: 128.8 P2: 172.7 A2: 51.3
- Rate: 69.75 nm/min
- PECVD3 ran for 1hr and 26min
- Recipe: 18W 10LF G1:164 G2:88 Temp 250C, Pressure:1900mT
- Placed in Dehybake

Ridge

- Pattern Triple Core V2 Ridge mask
- AZ3330: 1000 @ 1200, 60s → 6000 @ 6000 1s (no HMDS)
- Softbake: 90°C, 5min
- Expose: 16s (without filter)
- Develop: 300K: ~1min
- Feature size: 4um: ~4um, 12um: ~12um, 75um: ~75um
- Descum 150W, 60sec
- HCL dip
- Ebeam: 120nm Ni
- Liftoff Sonicated Acetone, and IPA rinse
- Descum 100W, 60sec
- Features look good, perfect alignment

Ridge Etch

- Sap Oxide, 1860 sec

- Descum Between 100W, 60sec @ 600s
- TC1 10 min and Descum 100W, 60sec @ 1200sec
- Ni etch 7 min
- TC1 (H2O2:RS-6=1:10, 55C) 10min
- Descum: 100W, 60sec
- Dehybake
- Height Etched: ~3.2um
- Etch Rate: 1.67nm/sec
- Oxide where etched looks bad features look good

Core Expose

- Pattern MMI/Splitter Core Expose mask using AZP4620
- Spin AZP4620 1500 rpm, 60s
- Soft bake 80C, 10min
- Expose 30s, Filtered Aligner
- Develop (AZ400K:H2O = 1:4) ~3min
- Hard bake 150C, 30 min
- Descum: 150W, 60sec
- BHF etch 490sec

SU-8 Core Etching

- 60mL H2O2 + 40mL Sulfuric Acid (Piranha)
- Placed in acid until 5/13/16

7.6 Appendix F MMI Spot Pattern Analyzer Software

The following program allows users to easily load, analyze and save the MMI Patterns that are taken by the compound microscope camera.

The image file name should contain the wavelength information. The position of the liquid-core among selected dark images should be same.

Step 1: Load Illuminated Image

Load the illuminated image to roughly get the idea of where the liquid core waveguide is. If all the images are dark, a dark image can be loaded to select the rough position of the core.

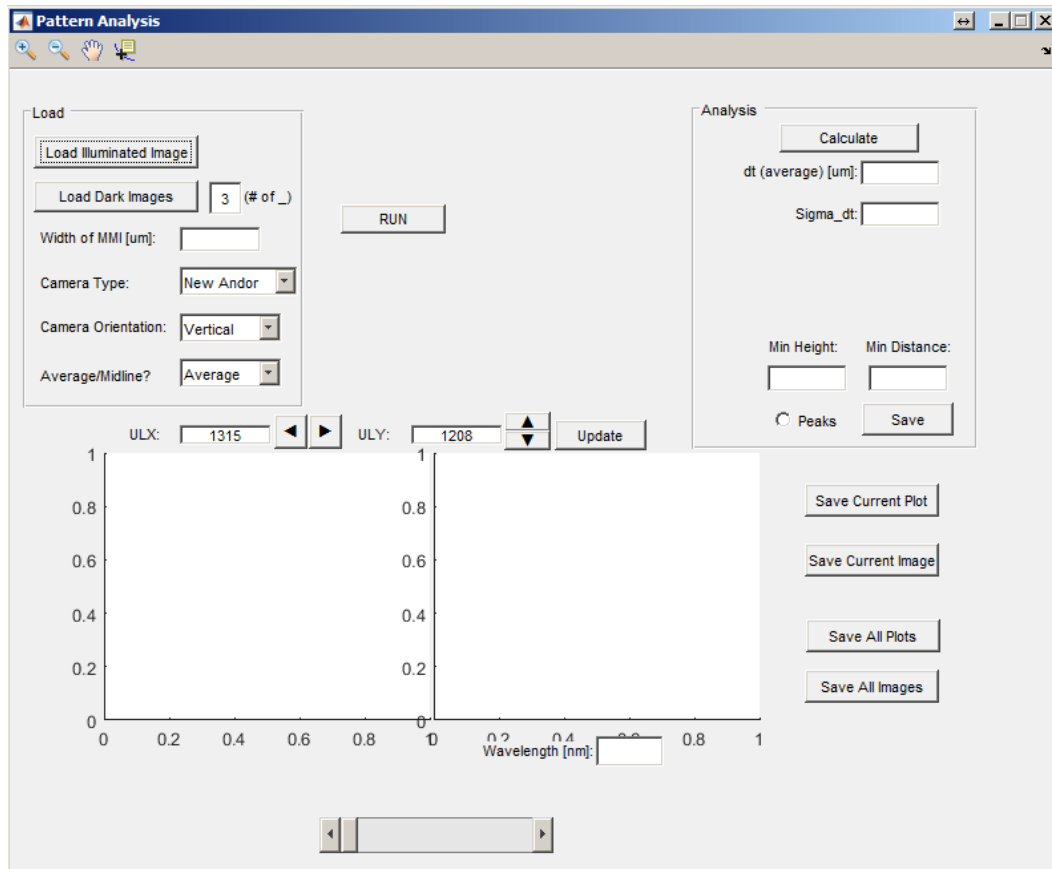


Fig. F. 1 Load Illuminated Image

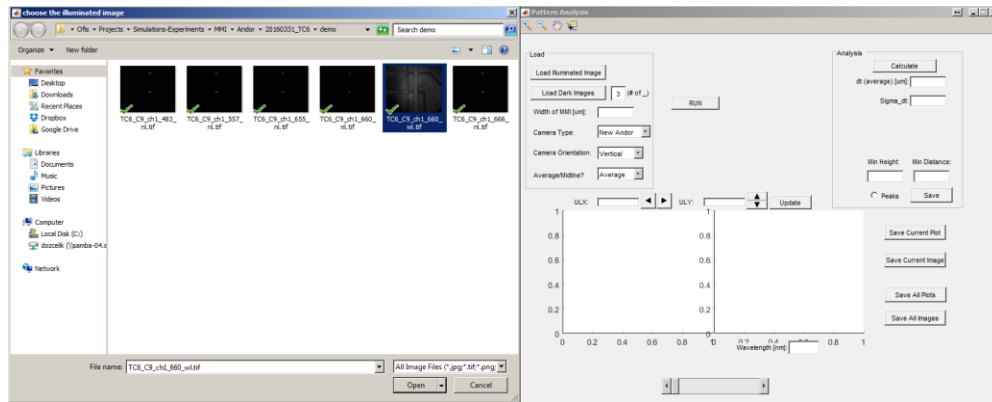


Fig. F. 2 Choose Illuminated Image

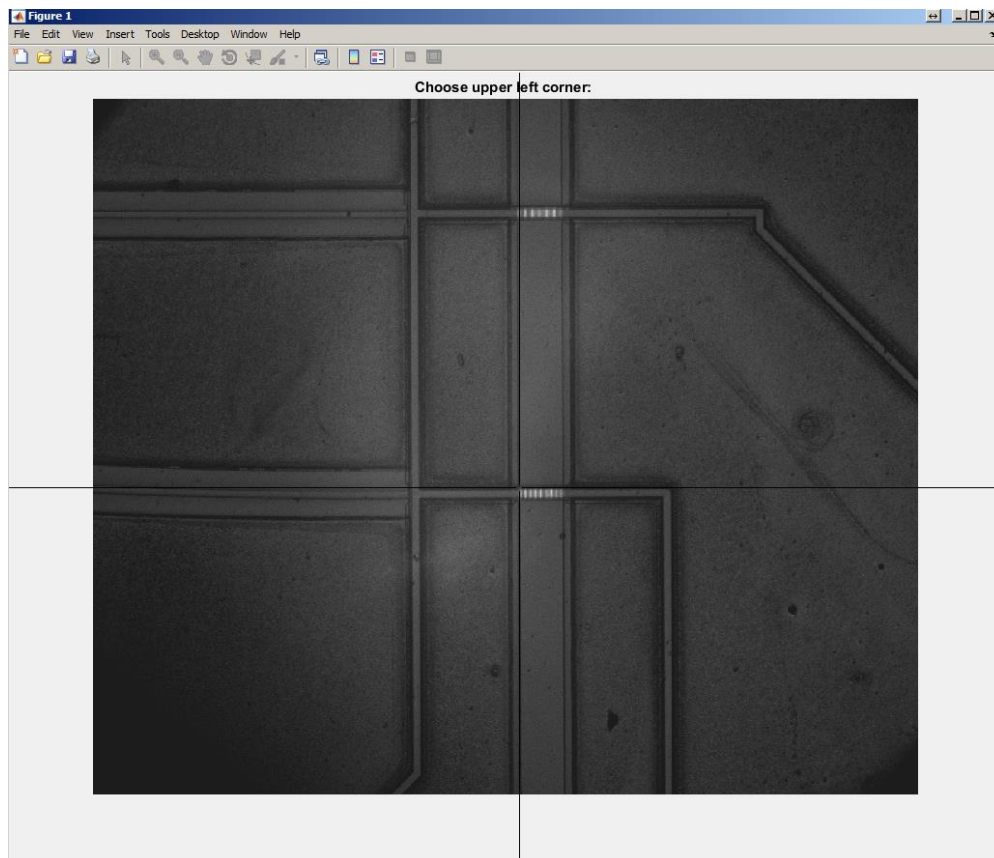


Fig. F. 3 Choose upper left corner

Upper left corner of the core is selected.

Step 2: Load Dark Images

In this step, multiple images can be loaded. The liquid-core positions should be same for all of them.

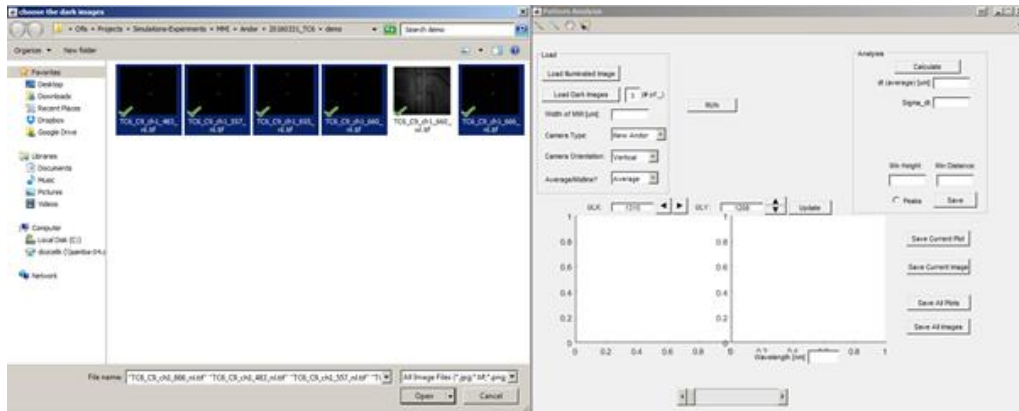


Fig. F. 4 Load Dark Images

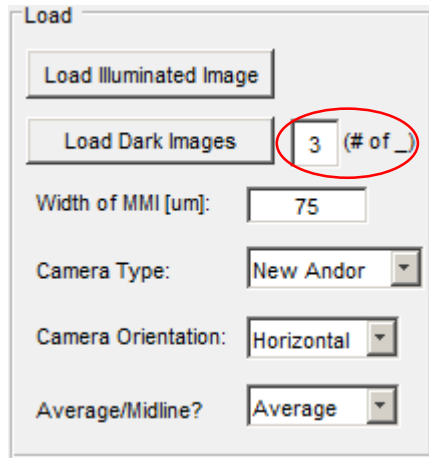


Fig. F. 5 Locate the wavelength information in the file name

The files also need to have the wavelength information in nanometers. The delimiter is underscore as default. The number “3” is the number of underscores in the file name before the wavelength information. The delimiter can be changed and the position of the wavelength can be changed based on the position. For example, in the file name

“TC6_C9_ch1_557_nl.tif”, there are 3 underscores before the wavelength. Also, note that there is an underscore after the wavelength, if there is more text. The delimiter is underscore in this case.

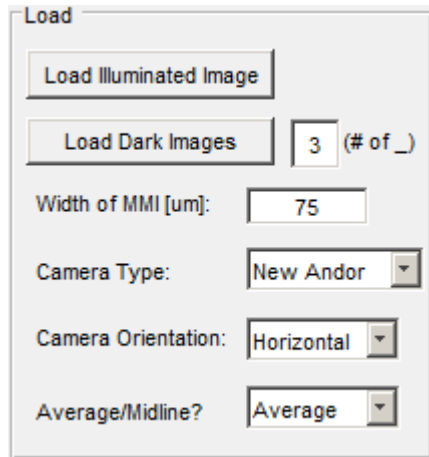
Examples:

TC6_557.tif Delimiter is underscore, the number should be “1”.

557.tif the number should be “0”.

TC6_557 nm Not a valid format

TC6_557nm Not a valid format



The image shows a software dialog box titled "Load". It contains several controls: a "Load Illuminated Image" button, a "Load Dark Images" button followed by a text input field containing "3" and a label "(# of _)", a "Width of MMI [um]" label with a text input field containing "75", a "Camera Type:" label with a dropdown menu showing "New Andor", a "Camera Orientation:" label with a dropdown menu showing "Horizontal", and an "Average/Midline?" label with a dropdown menu showing "Average".

Fig. F. 6 Entry for MMI Width, camera type and orientation.

Enter width of the MMI.

Select camera type (Old Andor (Andor Luca S) vs New Andor (Andor Zyla 5.5)) since they have different pixel to um ratios.

The liquid core can be horizontal or vertical depending on the chip orientation.

The analysis can be done on the middle line of the liquid core, or the average of the spot lines.

Step 3: RUN

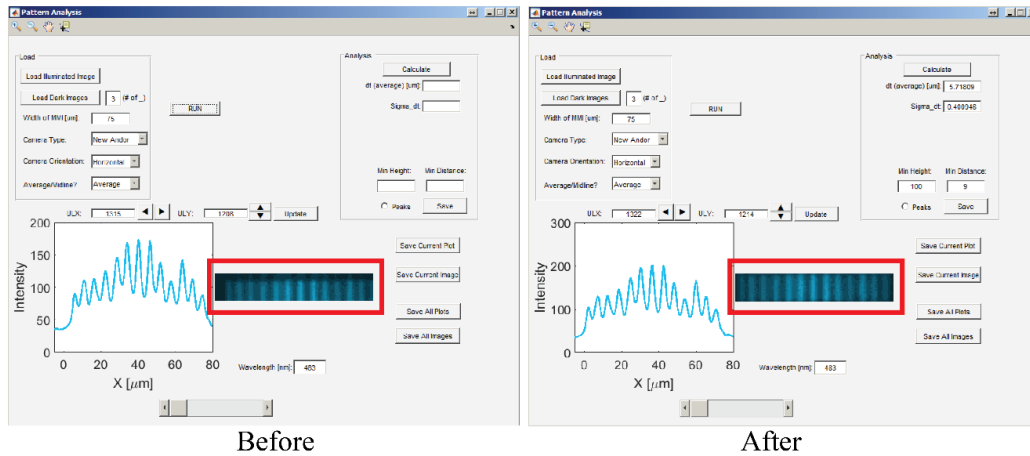


Fig. F. 7 Running the program and positioning the liquid-core.

Hit the RUN button to plot the pattern. Notice that the patterns are not perfectly in the analysis area because our previous selection was not perfectly on the corner. Use the arrows to position the pattern in the analysis area.

Navigate through the different wavelengths by using the slider. The wavelength of the current image is shown in the “Wavelength” box.

Step 4: Analysis

The peaks of the pattern can be shown on the plot by clicking peaks on the Analysis Panel. The minimum height and minimum distance between the peaks can be configured as well.

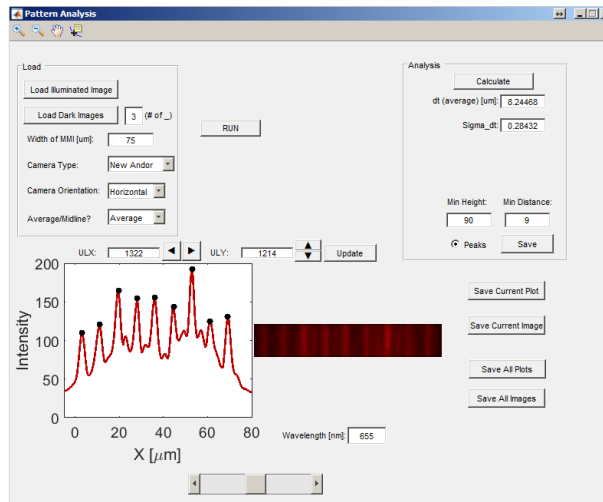
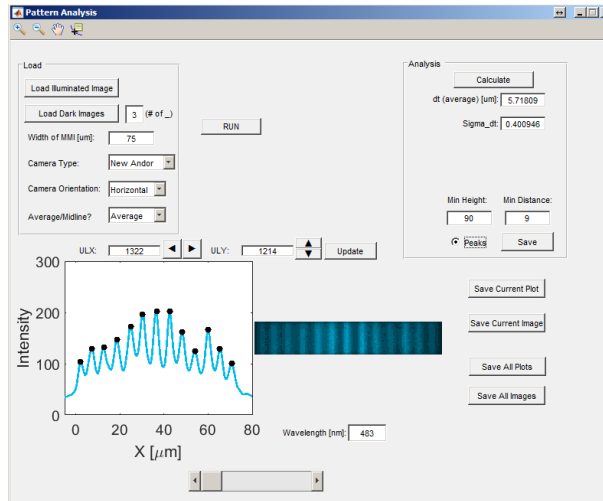


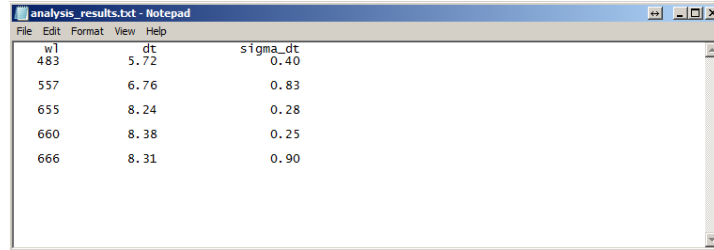
Fig. F. 8 Spot Pattern Analysis

The average distance between the peaks can be found in “dt (average)” box. Their standard deviation is found in “sigma_dt” box.

Note: Make sure to go through the plots to see if the right peaks are picked, and change the min height and distance accordingly.

The analysis results can be saved using “Save” button in the analysis panel.

The output file is called “analysis_results” in txt format. It contains the wavelength, average dt and standard deviation information.



w1	dt	sigma_dt
483	5.72	0.40
557	6.76	0.83
655	8.24	0.28
660	8.38	0.25
666	8.31	0.90

Fig. F. 9 Analysis Output

Step 5: Save Plots and Images

All the plots and images can be exported to separate MATLAB figure files and *.tif image files. In order to only save the current figure and image, select the upper 2 buttons. To save all the images, select lower 2 buttons.

The plots can be saved with or without the peaks. You could select/deselect to adjust that.

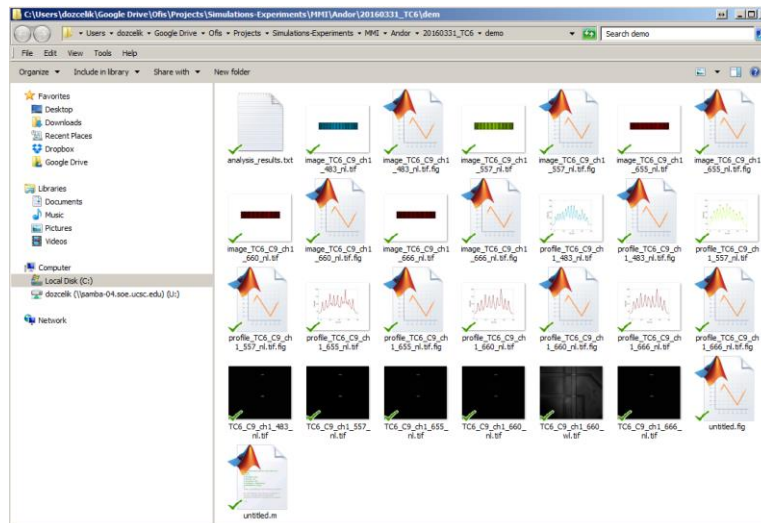


Fig. F. 10 Saving the data

7.7 Appendix G Multiple-peak Identification Software

The following program allows for analyzing the multiple peaks in the collected data. It automatically finds the multiple peaks in each particle signal, based on the given specifications. It also allows for manual verification, and correction for the identification of the peaks. It also calculates the error in the automatic identification by comparing it to the manual corrections.

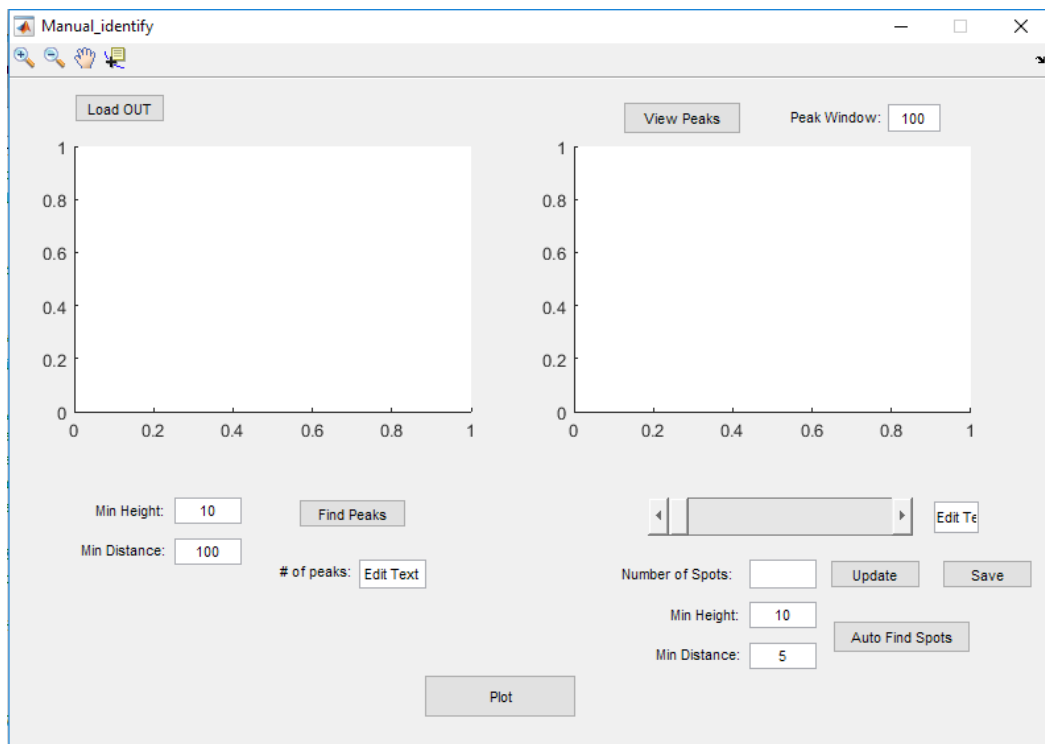


Fig. G. 1 The application window of the program.

The guidelines for analyzing a signal collected from a TC detection of different kinds of targets with different number of peaks.

Step 1: Loading the data

The data should be in the format of MATLAB data file and the first column should be for the time axis, and second column should be the corresponding intensity values.

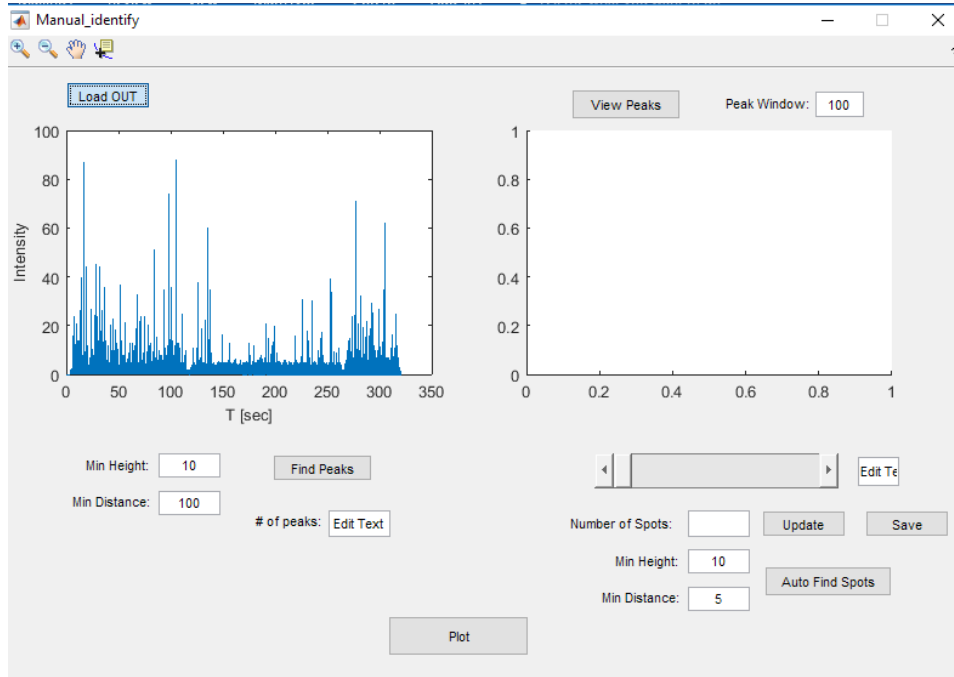


Fig. G. 2 Loading the data.

Once the data is loaded, the program will plot it on the left side of the application window, shown in Fig. G. 2.

Step 2: Determining the threshold for particle signal.

The threshold values for detected particles should be entered in the “Min Height” and “Min Distance” boxes. The units for the distance is each data point, depending on the binning time, and the units for the height is the photon count per binning time. These parameters should be chosen carefully to result in single selection per single particle, not counting the multiple peaks within each particle. After this step, “Find Peaks” button will find the peaks based on the parameters entered.

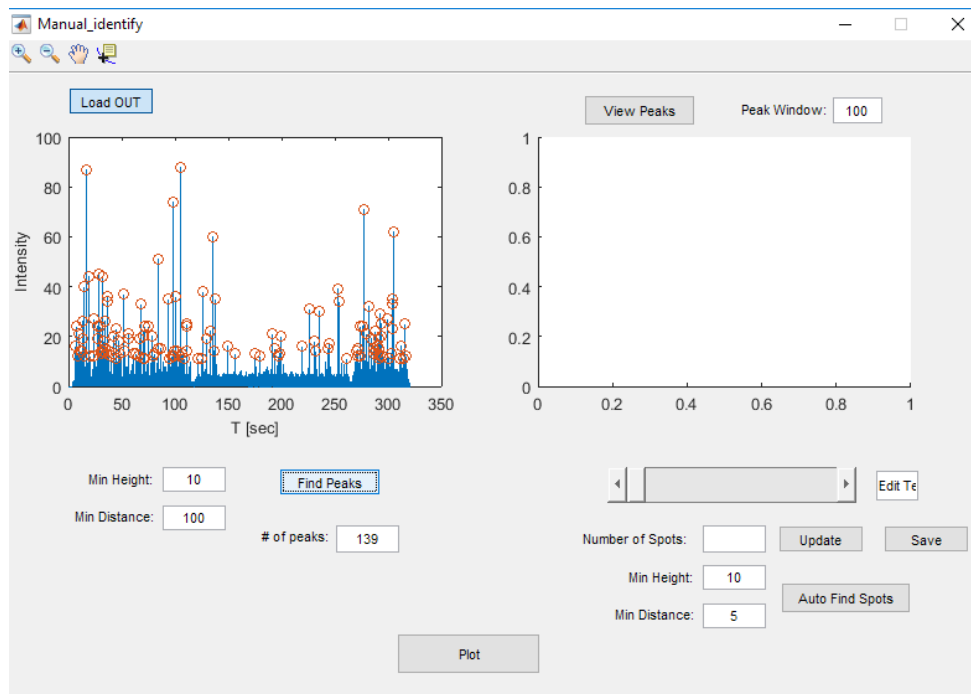


Fig. G. 3 The peaks found based on the threshold parameters entered.

The number of peaks that are found can be seen in the box.

Step 3: Analyzing the multiple peaks, and automatically identifying the number of peaks.

For this step, “View Peaks” button should be clicked in order to show each peak in the window on the right side. Scroll bar allows for going through each peak. Peak window must be chosen to allow the whole peak in the window. This depends on the velocity of the particle and the binning of the data.

Each particle signal shows multiple number of peaks, depending on the type of target.

In order to identify the number of peaks, another peak finding algorithm is run on each peak window, and label them with the number of peaks that are found.

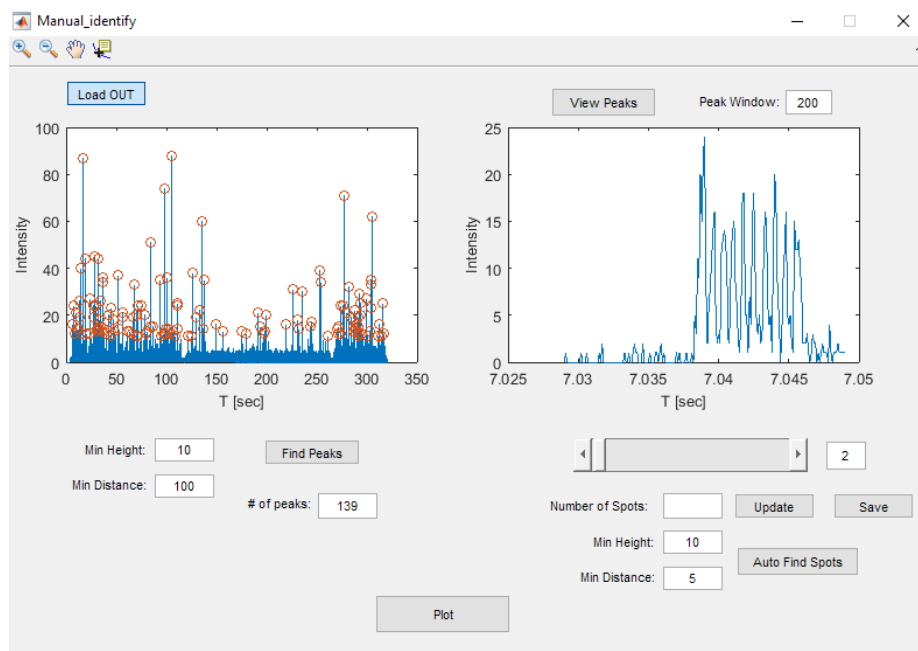


Fig. G. 4 Viewing each particle signal.

Step 4: Identifying the particles based on the number of peaks.

In order to find the peaks, Min Height and Min Distance for that window should be entered. Note that the Min Distance to find the multiple peaks should be smaller than the distance between each peak. Then by clicking the “Auto Find Spots”, the number of spots are found for each particle, and can be visually verified by going through them by using the scroll bar.

The number of spots box shows the number for each particle signal. This data can be saved by using the save button and it can be plotted by using the Plot button.

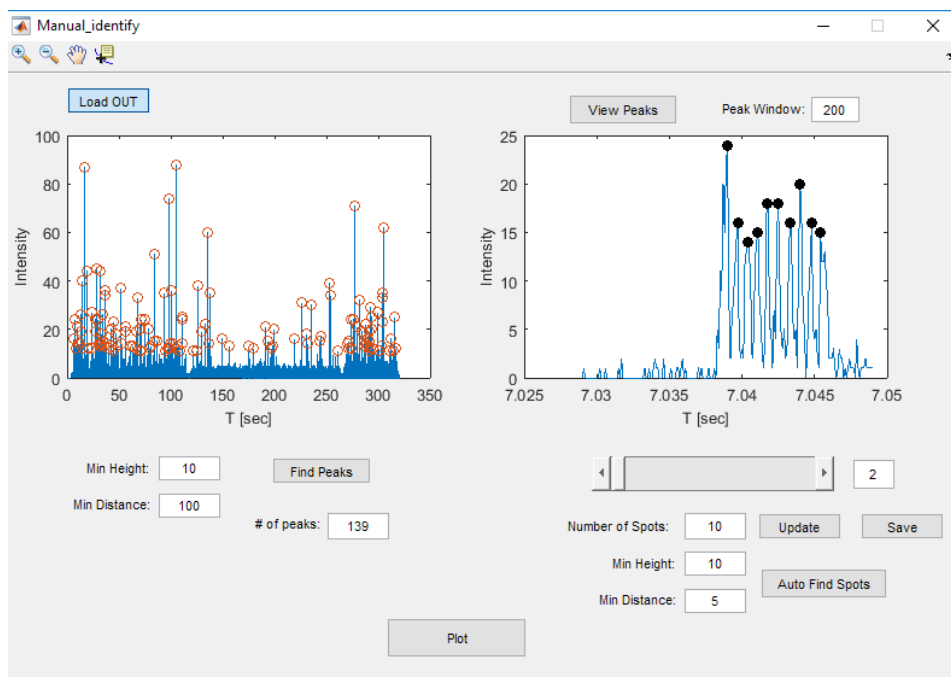


Fig. G. 5 Finding the number of spots

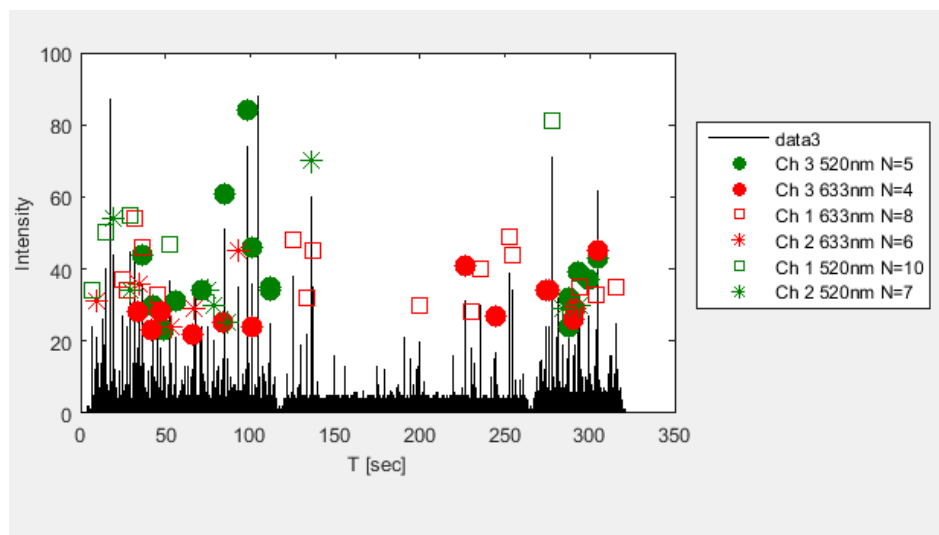


Fig. G. 6 Output plot with the identified peaks

The output plot is shown in Fig. G. 6, showing the different targets in different channels, based on the number of peaks generated previously. The symbols and ranges can be modified in the “plot_Figure_Callback” function.

Step 5: Verification of Identified Peaks

In order to verify the identification carried out by the algorithm, each particle signal can be visually analyzed by using this program. If there is a mismatch found between the algorithm and the visual manual analysis, due to a bad pattern, this information can be updated by changing the number of spots and updating it. After this step, the data can be saved and plotted as in the Step 4. The comparison between the manual verification and the automatic identification gives the error of the algorithm for the data trace.

8 Bibliography

- [1] R. P. Feynman, "There's Plenty of Room at the Bottom," *Eng. Sci.*, vol. 23, no. 5, pp. 22–36, Feb. 1960.
- [2] S. McCartney, *ENIAC: The Triumphs and Tragedies of the World's First Computer*. Walker & Company, 1999.
- [3] A. R. Hawkins and H. Schmidt, Eds., *Handbook of Optofluidics*, 1 edition. Boca Raton: CRC Press, 2010.
- [4] K. E. Petersen, "Silicon as a mechanical material," *Proc. IEEE*, vol. 70, no. 5, pp. 420–457, May 1982.
- [5] L.-S. Fan, Y.-C. Tai, and R. S. Muller, "IC-processed electrostatic micromotors," *Sens. Actuators*, vol. 20, no. 1, pp. 41–47, Nov. 1989.
- [6] D. S. Eddy and D. R. Sparks, "Application of MEMS technology in automotive sensors and actuators," *Proc. IEEE*, vol. 86, no. 8, pp. 1747–1755, Aug. 1998.
- [7] H.-L. Chau and K. D. Wise, "An ultraminiature solid-state pressure sensor for a cardiovascular catheter," *IEEE Trans. Electron Devices*, vol. 35, no. 12, pp. 2355–2362, Dec. 1988.
- [8] E. R. Brown, "RF-MEMS switches for reconfigurable integrated circuits," *IEEE Trans. Microw. Theory Tech.*, vol. 46, no. 11, pp. 1868–1880, Nov. 1998.
- [9] J. W. Judy, "Microelectromechanical systems (MEMS): fabrication, design and applications," *Smart Mater. Struct.*, vol. 10, no. 6, p. 1115, 2001.
- [10] R. Zengerle, J. Ulrich, S. Kluge, M. Richter, and A. Richter, "A bidirectional silicon micropump," *Sens. Actuators Phys.*, vol. 50, no. 1, pp. 81–86, Aug. 1995.
- [11] D. J. Laser and J. G. Santiago, "A review of micropumps," *J. Micromechanics Microengineering*, vol. 14, no. 6, p. R35, 2004.
- [12] W.-H. Chu, R. Chin, T. Huen, and M. Ferrari, "Silicon membrane nanofilters from sacrificial oxide removal," *J. Microelectromechanical Syst.*, vol. 8, no. 1, pp. 34–42, Mar. 1999.
- [13] J. Atencia and D. J. Beebe, "Controlled microfluidic interfaces," *Nature*, vol. 437, no. 7059, pp. 648–655, Sep. 2005.
- [14] K. Perez-Toralla *et al.*, "FISH in chips: turning microfluidic fluorescence in situ hybridization into a quantitative and clinically reliable molecular diagnosis tool," *Lab. Chip*, vol. 15, no. 3, pp. 811–822, Feb. 2015.

- [15] M. E. Piyasena and S. W. Graves, “The intersection of flow cytometry with microfluidics and microfabrication,” *Lab Chip*, vol. 14, no. 6, pp. 1044–1059, Feb. 2014.
- [16] D. Huh, W. Gu, Y. Kamotani, J. B. Grotberg, and S. Takayama, “Microfluidics for flow cytometric analysis of cells and particles,” *Physiol. Meas.*, vol. 26, no. 3, p. R73, 2005.
- [17] A. R. Abate *et al.*, “DNA sequence analysis with droplet-based microfluidics,” *Lab. Chip*, vol. 13, no. 24, pp. 4864–4869, Dec. 2013.
- [18] Z. Nie *et al.*, “Electrochemical sensing in paper-based microfluidic devices,” *Lab Chip*, vol. 10, no. 4, pp. 477–483, Feb. 2010.
- [19] J. Wang, “SURVEY AND SUMMARY From DNA biosensors to gene chips,” *Nucleic Acids Res.*, vol. 28, no. 16, pp. 3011–3016, Aug. 2000.
- [20] P. S. Dittrich and A. Manz, “Lab-on-a-chip: microfluidics in drug discovery,” *Nat. Rev. Drug Discov.*, vol. 5, no. 3, pp. 210–218, Mar. 2006.
- [21] H.A. Stone, A.D. Stroock, and A. Ajdari, “Engineering Flows in Small Devices,” *Annu. Rev. Fluid Mech.*, vol. 36, no. 1, pp. 381–411, 2004.
- [22] S. Haeberle and R. Zengerle, “Microfluidic platforms for lab-on-a-chip applications,” *Lab Chip*, vol. 7, no. 9, pp. 1094–1110, Aug. 2007.
- [23] D. Psaltis, S. R. Quake, and C. Yang, “Developing optofluidic technology through the fusion of microfluidics and optics,” *Nature*, vol. 442, no. 7101, pp. 381–386, Jul. 2006.
- [24] C. Monat, P. Domachuk, and B. J. Eggleton, “Integrated optofluidics: A new river of light,” *Nat Photon*, vol. 1, no. 2, pp. 106–114, Feb. 2007.
- [25] H. Schmidt and A. R. Hawkins, “The photonic integration of non-solid media using optofluidics,” *Nat Photon*, vol. 5, no. 10, pp. 598–604, Oct. 2011.
- [26] D. V. Vezenov *et al.*, “A Low-Threshold, High-Efficiency Microfluidic Waveguide Laser,” *J. Am. Chem. Soc.*, vol. 127, no. 25, pp. 8952–8953, Jun. 2005.
- [27] B. Helbo, S. Kragh, B. G. Kjeldsen, J. L. Reimers, and A. Kristensen, “Investigation of the dye concentration influence on the lasing wavelength and threshold for a micro-fluidic dye laser,” in *Sensors and Actuators A: Physical*, 2003, vol. 111, pp. 21–25.

- [28] Z. Li, Z. Zhang, A. Scherer, and D. Psaltis, “Mechanically tunable optofluidic distributed feedback dye laser,” *Opt. Express*, vol. 14, no. 22, pp. 10494–10499, Oct. 2006.
- [29] W. Song and D. Psaltis, “Pneumatically tunable optofluidic dye laser,” *Appl. Phys. Lett.*, vol. 96, no. 8, p. 081101, Feb. 2010.
- [30] J. P. Barber, E. J. Lunt, Z. A. George, D. Yin, H. Schmidt, and A. R. Hawkins, “Integrated hollow waveguides with arch-shaped cores,” *IEEE Photonics Technol. Lett.*, vol. 18, no. 1, pp. 28–30, Jan. 2006.
- [31] D. Yin, H. Schmidt, J. P. Barber, E. J. Lunt, and A. R. Hawkins, “Optical characterization of arch-shaped ARROW waveguides with liquid cores,” *Opt. Express*, vol. 13, no. 26, pp. 10564–10570, Dec. 2005.
- [32] H. Schmidt and A. R. Hawkins, “Optofluidic waveguides: I. Concepts and implementations,” *Microfluid. Nanofluidics*, vol. 4, no. 1–2, pp. 3–16, Aug. 2007.
- [33] X. Mao, S.-C. S. Lin, M. I. Lapsley, J. Shi, B. K. Juluri, and T. J. Huang, “Tunable Liquid Gradient Refractive Index (L-GRIN) lens with two degrees of freedom,” *Lab. Chip*, vol. 9, no. 14, pp. 2050–2058, Jul. 2009.
- [34] S. K. Y. Tang, C. A. Stan, and G. M. Whitesides, “Dynamically reconfigurable liquid-core liquid-cladding lens in a microfluidic channel,” *Lab Chip*, vol. 8, no. 3, pp. 395–401, Feb. 2008.
- [35] N. Chronis, G. Liu, K.-H. Jeong, and L. Lee, “Tunable liquid-filled microlens array integrated with microfluidic network,” *Opt. Express*, vol. 11, no. 19, pp. 2370–2378, Sep. 2003.
- [36] J. Shi, Z. Stratton, S.-C. S. Lin, H. Huang, and T. J. Huang, “Tunable optofluidic microlens through active pressure control of an air–liquid interface,” *Microfluid. Nanofluidics*, vol. 9, no. 2–3, pp. 313–318, Dec. 2009.
- [37] C. Song, N.-T. Nguyen, Y. F. Yap, T.-D. Luong, and A. K. Asundi, “Multi-functional, optofluidic, in-plane, bi-concave lens: tuning light beam from focused to divergent,” *Microfluid. Nanofluidics*, vol. 10, no. 3, pp. 671–678, Oct. 2010.
- [38] Y. Yang, L. K. Chin, J. M. Tsai, D. P. Tsai, N. I. Zheludev, and A. Q. Liu, “Transformation optofluidics for large-angle light bending and tuning,” *Lab. Chip*, vol. 12, no. 19, pp. 3785–3790, 2012.
- [39] K. Campbell *et al.*, “A microfluidic 2×2 optical switch,” *Appl. Phys. Lett.*, vol. 85, no. 25, pp. 6119–6121, Dec. 2004.

- [40] J.-M. Lim, J. P. Urbanski, T. Thorsen, and S.-M. Yang, “Pneumatic control of a liquid-core/liquid-cladding waveguide as the basis for an optofluidic switch,” *Appl. Phys. Lett.*, vol. 98, no. 4, p. 044101, Jan. 2011.
- [41] G. Testa, Y. Huang, P. M. Sarro, L. Zeni, and R. Bernini, “High-visibility optofluidic Mach-Zehnder interferometer,” *Opt. Lett.*, vol. 35, no. 10, pp. 1584–1586, May 2010.
- [42] S. Lin, E. Schonbrun, and K. Crozier, “Optical Manipulation with Planar Silicon Microring Resonators,” *Nano Lett.*, vol. 10, no. 7, pp. 2408–2411, 2010.
- [43] Y. Huang, P. M. Sarro, L. Zeni, and R. Bernini, “Integrated silicon optofluidic ring resonator,” *Appl. Phys. Lett.*, vol. 97, no. 13, p. 131110, 2010.
- [44] D. Ozcelik *et al.*, “Dual-core optofluidic chip for independent particle detection and tunable spectral filtering,” *Lab. Chip*, vol. 12, no. 19, pp. 3728–3733, Aug. 2012.
- [45] P. Measor, B. S. Phillips, A. Chen, A. R. Hawkins, and H. Schmidt, “Tailorable integrated optofluidic filters for biomolecular detection,” *Lab. Chip*, vol. 11, no. 5, p. 899, 2011.
- [46] J. W. Parks *et al.*, “Hybrid optofluidic integration,” *Lab. Chip*, vol. 13, no. 20, pp. 4118–4123, Sep. 2013.
- [47] J. W. Parks *et al.*, “Integration of programmable microfluidics and on-chip fluorescence detection for biosensing applications,” *Biomicrofluidics*, vol. 8, no. 5, p. 054111, Sep. 2014.
- [48] H. Cai *et al.*, “Optofluidic analysis system for amplification-free, direct detection of Ebola infection,” *Sci. Rep.*, vol. 5, p. 14494, Sep. 2015.
- [49] P. Domachuk, M. Cronin-Golomb, B. J. Eggleton, S. Mutzenich, G. Rosengarten, and A. Mitchell, “Application of optical trapping to beam manipulation in optofluidics,” *Opt. Express*, vol. 13, no. 19, pp. 7265–7275, Sep. 2005.
- [50] M. M. Wang *et al.*, “Microfluidic sorting of mammalian cells by optical force switching,” *Nat. Biotechnol.*, vol. 23, no. 1, pp. 83–87, Jan. 2005.
- [51] B. S. Schmidt, A. H. Yang, D. Erickson, and M. Lipson, “Optofluidic trapping and transport on solid core waveguides within a microfluidic device,” *Opt. Express*, vol. 15, no. 22, pp. 14322–14334, Oct. 2007.
- [52] D. Néel, S. Gétin, P. Ferret, M. Rosina, J. M. Fedeli, and O. G. Hellesø, “Optical transport of semiconductor nanowires on silicon nitride waveguides,” *Appl. Phys. Lett.*, vol. 94, no. 25, p. 253115, Jun. 2009.

- [53] S. Gaugiran *et al.*, “Optical manipulation of microparticles and cells on silicon nitride waveguides,” *Opt. Express*, vol. 13, no. 18, pp. 6956–6963, Sep. 2005.
- [54] S. Lin and K. B. Crozier, “An integrated microparticle sorting system based on near-field optical forces and a structural perturbation,” *Opt. Express*, vol. 20, no. 4, pp. 3367–3374, Feb. 2012.
- [55] L.-C. Hsu *et al.*, “Manipulation of micro-particles through optical interference patterns generated by integrated photonic devices,” *Lab. Chip*, vol. 13, no. 6, pp. 1151–1155, Feb. 2013.
- [56] H. Cai and A. W. Poon, “Optofluidic microparticle splitters using multimode-interference-based power splitters,” in *2012 Conference on Lasers and Electro-Optics (CLEO)*, 2012, pp. 1–2.
- [57] K. Grujic, O. Hellesø, J. Hole, and J. Wilkinson, “Sorting of polystyrene microspheres using a Y-branched optical waveguide,” *Opt. Express*, vol. 13, no. 1, pp. 1–7, Jan. 2005.
- [58] N. Deschermes, U. Perumal Dharanipathy, Z. Diao, M. Tonin, and R. Houdré, “Single particle detection, manipulation and analysis with resonant optical trapping in photonic crystals,” *Lab. Chip*, vol. 13, no. 16, pp. 3268–3274, 2013.
- [59] Y.-F. Chen, X. Serey, R. Sarkar, P. Chen, and D. Erickson, “Controlled Photonic Manipulation of Proteins and Other Nanomaterials,” *Nano Lett.*, vol. 12, no. 3, pp. 1633–1637, Mar. 2012.
- [60] T. van Leest and J. Caro, “Cavity-enhanced optical trapping of bacteria using a silicon photonic crystal,” *Lab. Chip*, vol. 13, no. 22, pp. 4358–4365, Nov. 2013.
- [61] S. Mandal, X. Serey, and D. Erickson, “Nanomanipulation Using Silicon Photonic Crystal Resonators,” *Nano Lett.*, vol. 10, no. 1, pp. 99–104, Jan. 2010.
- [62] H. Cai and A. W. Poon, “Optical manipulation of microparticles using whispering-gallery modes in a silicon nitride microdisk resonator,” *Opt. Lett.*, vol. 36, no. 21, pp. 4257–4259, Nov. 2011.
- [63] S. Lin and K. B. Crozier, “Planar silicon microrings as wavelength-multiplexed optical traps for storing and sensing particles,” *Lab. Chip*, vol. 11, no. 23, pp. 4047–4051, Nov. 2011.
- [64] H. Cai and A. W. Poon, “Optical manipulation and transport of microparticles on silicon nitride microring-resonator-based add-drop devices,” *Opt. Lett.*, vol. 35, no. 17, pp. 2855–2857, 2010.

- [65] P. Measor, S. Kühn, E. J. Lunt, B. S. Phillips, A. R. Hawkins, and H. Schmidt, “Hollow-core waveguide characterization by optically induced particle transport,” *Opt. Lett.*, vol. 33, no. 7, pp. 672–674, Apr. 2008.
- [66] S. Kühn *et al.*, “Loss-based optical trap for on-chip particle analysis,” *Lab. Chip*, vol. 9, no. 15, pp. 2212–2216, Aug. 2009.
- [67] S. Kühn, E. J. Lunt, B. S. Phillips, A. R. Hawkins, and H. Schmidt, “Optofluidic particle concentration by a long-range dual-beam trap,” *Opt. Lett.*, vol. 34, no. 15, pp. 2306–2308, Aug. 2009.
- [68] S. Kühn, B. S. Phillips, E. J. Lunt, A. R. Hawkins, and H. Schmidt, “Ultralow power trapping and fluorescence detection of single particles on an optofluidic chip,” *Lab. Chip*, vol. 10, no. 2, pp. 189–194, Dec. 2009.
- [69] K. D. Leake, M. A. B. Olson, D. Ozcelik, A. R. Hawkins, and H. Schmidt, “Spectrally reconfigurable integrated multi-spot particle trap,” *Opt. Lett.*, vol. 40, no. 23, pp. 5435–5438, Dec. 2015.
- [70] K. D. Leake, B. S. Phillips, T. D. Yuzvinsky, A. R. Hawkins, and H. Schmidt, “Optical particle sorting on an optofluidic chip,” *Opt. Express*, vol. 21, no. 26, pp. 32605–32610, Dec. 2013.
- [71] “WHO | The top 10 causes of death,” *WHO*. [Online]. Available: <http://www.who.int/mediacentre/factsheets/fs310/en/>. [Accessed: 30-Jun-2016].
- [72] M. M. Alsan, M. Westerhaus, M. Herce, K. Nakashima, and P. E. Farmer, “Poverty, Global Health and Infectious Disease: Lessons from Haiti and Rwanda,” *Infect. Dis. Clin. North Am.*, vol. 25, no. 3, pp. 611–622, Sep. 2011.
- [73] “Migration and health: key issues,” 29-Oct-2016. [Online]. Available: <http://www.euro.who.int/en/health-topics/health-determinants/migration-and-health/migrant-health-in-the-european-region/migration-and-health-key-issues>. [Accessed: 29-Oct-2016].
- [74] S. Banoo *et al.*, “Evaluation of diagnostic tests for infectious diseases: general principles,” *Nat. Rev. Microbiol.*, vol. 8, pp. S16–S28, Nov. 2008.
- [75] A. R. Trombley *et al.*, “Comprehensive Panel of Real-Time TaqMan™ Polymerase Chain Reaction Assays for Detection and Absolute Quantification of Filoviruses, Arenaviruses, and New World Hantaviruses,” *Am. J. Trop. Med. Hyg.*, vol. 82, no. 5, pp. 954–960, May 2010.
- [76] J. S. Towner *et al.*, “Rapid Diagnosis of Ebola Hemorrhagic Fever by Reverse Transcription-PCR in an Outbreak Setting and Assessment of Patient Viral Load as a Predictor of Outcome,” *J. Virol.*, vol. 78, no. 8, pp. 4330–4341, Apr. 2004.

- [77] F. Watzinger, K. Ebner, and T. Lion, "Detection and monitoring of virus infections by real-time PCR," *Mol. Aspects Med.*, vol. 27, no. 2–3, pp. 254–298, Jun. 2006.
- [78] P. Measor *et al.*, "On-chip surface-enhanced Raman scattering detection using integrated liquid-core waveguides," *Appl. Phys. Lett.*, vol. 90, no. 21, p. 211107, May 2007.
- [79] M. Wang, N. Jing, I.-H. Chou, G. L. Cote, and J. Kameoka, "An optofluidic device for surface enhanced Raman spectroscopy," *Lab Chip*, vol. 7, no. 5, pp. 630–632, May 2007.
- [80] I. M. White, S. H. Yazdi, and W. W. Yu, "Optofluidic SERS: synergizing photonics and microfluidics for chemical and biological analysis," *Microfluid. Nanofluidics*, vol. 13, no. 2, pp. 205–216, Mar. 2012.
- [81] H.-Y. Wu and B. T. Cunningham, "Point-of-care detection and real-time monitoring of intravenously delivered drugs via tubing with an integrated SERS sensor," *Nanoscale*, vol. 6, no. 10, pp. 5162–5171, Apr. 2014.
- [82] S. Arnold, V. R. Dantham, C. Barbre, B. A. Garetz, and X. Fan, "Periodic plasmonic enhancing epitopes on a whispering gallery mode biosensor," *Opt. Express*, vol. 20, no. 24, pp. 26147–26159, Nov. 2012.
- [83] T.-Y. Chang *et al.*, "Large-scale plasmonic microarrays for label-free high-throughput screening," *Lab. Chip*, vol. 11, no. 21, pp. 3596–3602, Oct. 2011.
- [84] K. Kumar, A. B. Dahlin, T. Sannomiya, S. Kaufmann, L. Isa, and E. Reimhult, "Embedded Plasmonic Nanomenhirs as Location-Specific Biosensors," *Nano Lett.*, vol. 13, no. 12, pp. 6122–6129, Dec. 2013.
- [85] R. Adato and H. Altug, "In-situ ultra-sensitive infrared absorption spectroscopy of biomolecule interactions in real time with plasmonic nanoantennas," *Nat. Commun.*, vol. 4, p. 2154, Jul. 2013.
- [86] D. Yin, D. W. Deamer, H. Schmidt, J. P. Barber, and A. R. Hawkins, "Single-molecule detection sensitivity using planar integrated optics on a chip," *Opt. Lett.*, vol. 31, no. 14, pp. 2136–2138, Jul. 2006.
- [87] D. Yin, E. J. Lunt, M. I. Rudenko, D. W. Deamer, A. R. Hawkins, and H. Schmidt, "Planar optofluidic chip for single particle detection, manipulation, and analysis," *Lab. Chip*, vol. 7, no. 9, pp. 1171–1175, Aug. 2007.
- [88] M. I. Rudenko, S. Kühn, E. J. Lunt, D. W. Deamer, A. R. Hawkins, and H. Schmidt, "Ultrasensitive Q β phage analysis using fluorescence correlation spectroscopy on an optofluidic chip," *Biosens. Bioelectron.*, vol. 24, no. 11, pp. 3258–3263, Jul. 2009.

- [89] D. Yin, E. J. Lunt, A. Barman, A. R. Hawkins, and H. Schmidt, "Microphotonic control of single molecule fluorescence correlation spectroscopy using planar optofluidics," *Opt. Express*, vol. 15, no. 12, pp. 7290–7295, Jun. 2007.
- [90] M. I. Rudenko *et al.*, "Fluorescence correlation spectroscopy of single molecules on an optofluidic chip," *ResearchGate*, vol. 6898, Feb. 2008.
- [91] G. Testa, G. Persichetti, and R. Bernini, "Optofluidic approaches for enhanced microsensor performances," *Sensors*, vol. 15, no. 1, pp. 465–484, Dec. 2014.
- [92] "Respiratory Virus PCR Panel I." [Online]. Available: http://www.questdiagnostics.com/testcenter/testguide.action?dc=TS_RespVirusPanel. [Accessed: 01-Jul-2016].
- [93] C. Zander, J. Enderlein, and R. A. Keller, *Single molecule detection in solution: methods and applications*. Wiley-VCH, 2002.
- [94] P. Holzmeister, G. P. Acuna, D. Grohmann, and P. Tinnefeld, "Breaking the concentration limit of optical single-molecule detection," *Chem. Soc. Rev.*, vol. 43, no. 4, pp. 1014–1028, Jan. 2014.
- [95] S. Hohng, C. Joo, and T. Ha, "Single-Molecule Three-Color FRET," *Biophys. J.*, vol. 87, no. 2, pp. 1328–1337, Aug. 2004.
- [96] E. A. Abbondanzieri, W. J. Greenleaf, J. W. Shaevitz, R. Landick, and S. M. Block, "Direct observation of base-pair stepping by RNA polymerase," *Nature*, vol. 438, no. 7067, pp. 460–465, Nov. 2005.
- [97] A. Muschielok, J. Andrecka, A. Jawhari, F. Brückner, P. Cramer, and J. Michaelis, "A nano-positioning system for macromolecular structural analysis," *Nat. Methods*, vol. 5, no. 11, pp. 965–971, Nov. 2008.
- [98] A. A. Hoskins *et al.*, "Ordered and Dynamic Assembly of Single Spliceosomes," *Science*, vol. 331, no. 6022, pp. 1289–1295, Mar. 2011.
- [99] S. Kalinin *et al.*, "A toolkit and benchmark study for FRET-restrained high-precision structural modeling," *Nat. Methods*, vol. 9, no. 12, pp. 1218–1225, Dec. 2012.
- [100] T. Ha, "Single-molecule methods leap ahead," *Nat. Methods*, vol. 11, no. 10, pp. 1015–1018, Oct. 2014.
- [101] J.-L. Archambault, R. J. Black, S. Lacroix, and J. Bures, "Loss calculations for antiresonant waveguides," *Light. Technol. J. Of*, vol. 11, no. 3, pp. 416–423, Mar. 1993.

- [102] H. Schmidt and A. R. Hawkins, "Single Molecule Analysis with Planar Optofluidics," in *Advanced Photonic Structures for Biological and Chemical Detection*, X. Fan, Ed. Springer New York, 2009, pp. 487–512.
- [103] H. Schmidt, D. Yin, J. P. Barber, and A. R. Hawkins, "Hollow-core waveguides and 2-D waveguide arrays for integrated optics of gases and liquids," *IEEE J. Sel. Top. Quantum Electron.*, vol. 11, no. 2, pp. 519–527, Mar. 2005.
- [104] D. Yin *et al.*, "Planar single-molecule sensors based on hollow-core ARROW waveguides," 2006, vol. 6125, p. 61250Q–61250Q–13.
- [105] E. J. Lunt, P. Measor, B. S. Phillips, S. Kuhn, H. Schmidt, and A. R. Hawkins, "Improving solid to hollow core transmission for integrated ARROW waveguides," *Opt. Express*, vol. 16, no. 25, pp. 20981–20986, Dec. 2008.
- [106] E. J. Lunt, B. Wu, J. M. Keeley, P. Measor, H. Schmidt, and A. R. Hawkins, "Hollow ARROW Waveguides on Self-Aligned Pedestals for Improved Geometry and Transmission," *Photonics Technol. Lett. IEEE*, vol. 22, no. 15, pp. 1147–1149, Aug. 2010.
- [107] Y. Zhao *et al.*, "Optimization of Interface Transmission Between Integrated Solid Core and Optofluidic Waveguides," *IEEE Photonics Technol. Lett.*, vol. 24, no. 1, pp. 46–48, Jan. 2012.
- [108] D. Yin, H. Schmidt, J. P. Barber, and A. R. Hawkins, "Integrated ARROW waveguides with hollow cores," *Opt. Express*, vol. 12, no. 12, pp. 2710–2715, Jun. 2004.
- [109] Y. Zhao *et al.*, "Hollow waveguides with low intrinsic photoluminescence fabricated with Ta₂O₅ and SiO₂ films," *Appl. Phys. Lett.*, vol. 98, no. 9, p. 091104, Feb. 2011.
- [110] M. Stott *et al.*, "Silicate Spin-on-Glass as an Overcoat Layer for SiO₂ Ridge Waveguides," in *CLEO: 2015 (2015)*, paper JTh2A.29, 2015, p. JTh2A.29.
- [111] T. A. Wall, R. P. Chu, J. W. Parks, D. Ozcelik, H. Schmidt, and A. R. Hawkins, "Improved environmental stability for plasma enhanced chemical vapor deposition SiO₂ waveguides using buried channel designs," *Opt. Eng.*, vol. 55, no. 4, pp. 040501–040501, Apr. 2016.
- [112] T. A. Wall, J. Parks, K. D. Leake, H. Schmidt, and A. R. Hawkins, "Optofluidic Waveguiding for Biomedical Sensing," in *Symposium D – Materials and Concepts for Biomedical Sensing*, 2015, vol. 1720, p. mrsf14–1720–d06–01 (10 pages).

- [113] M. Holmes, J. Keeley, K. Hurd, H. Schmidt, and A. Hawkins, “Optimized piranha etching process for SU8-based MEMS and MOEMS construction,” *J. Micromechanics Microengineering*, vol. 20, no. 11, p. 115008, 2010.
- [114] J. W. Parks, T. A. Wall, H. Cai, A. R. Hawkins, and H. Schmidt, “Enhancement of ARROW Photonic Device Performance via Thermal Annealing of PECVD-based SiO₂ Waveguides,” *IEEE J. Sel. Top. Quantum Electron.*, vol. PP, no. 99, pp. 1–1, 2016.
- [115] D. Yin, J. P. Barber, A. R. Hawkins, and H. Schmidt, “Highly efficient fluorescence detection in picoliter volume liquid-core waveguides,” *Appl. Phys. Lett.*, vol. 87, no. 21, p. 211111, Nov. 2005.
- [116] A. Chen *et al.*, “Dual-color fluorescence cross-correlation spectroscopy on a planar optofluidic chip,” *Lab. Chip*, vol. 11, no. 8, pp. 1502–1506, Apr. 2011.
- [117] F. B. Myers and L. P. Lee, “Innovations in optical microfluidic technologies for point-of-care diagnostics,” *Lab. Chip*, vol. 8, no. 12, p. 2015, 2008.
- [118] J. R. Lakowicz, *Principles of Fluorescence Spectroscopy*, 3rd edition. Springer, 2006.
- [119] “Streptavidin, Alexa Fluor 633 conjugate - Thermo Fisher Scientific.” [Online]. Available: <https://www.thermofisher.com/order/catalog/product/S21375>. [Accessed: 18-Aug-2016].
- [120] H. A. MacLeod, *Thin-Film Optical Filters, Third Edition*. CRC Press, 2001.
- [121] M. Dandin, P. Abshire, and E. Smela, “Optical filtering technologies for integrated fluorescence sensors,” *Lab. Chip*, vol. 7, no. 8, p. 955, 2007.
- [122] M. Adams, M. Enzelberger, S. R. Quake, and A. Scherer, “Microfluidic Integration on Detector Arrays for Absorption and Fluorescence Micro-Spectrometers,” *Sens. Actuators A*, vol. 104, no. 1, pp. 25–31, 2003.
- [123] M. A. Burns, “An Integrated Nanoliter DNA Analysis Device,” *Science*, vol. 282, no. 5388, pp. 484–487, Oct. 1998.
- [124] E. Thrush, O. Levi, W. Ha, K. Wang, S. J. Smith, and J. S. Harris Jr., “Integrated bio-fluorescence sensor,” *J. Chromatogr. A*, vol. 1013, no. 1–2, pp. 103–110, Sep. 2003.
- [125] G. Lammel, S. Schweizer, and P. Renaud, “Microspectrometer based on a tunable optical filter of porous silicon,” *Sens. Actuators Phys.*, vol. 92, no. 1–3, pp. 52–59, Aug. 2001.

- [126] E. Lorenzo *et al.*, “Porous silicon-based rugate filters,” *Appl. Opt.*, vol. 44, no. 26, pp. 5415–5421, Sep. 2005.
- [127] S. A. M. Martins *et al.*, “Monitoring intracellular calcium in response to GPCR activation using thin-film silicon photodiodes with integrated fluorescence filters,” *Biosens. Bioelectron.*, vol. 52, pp. 232–238, Feb. 2014.
- [128] A. Llobera, S. Demming, H. N. Joensson, J. Vila-Planas, H. Andersson-Svahn, and S. Büttgenbach, “Monolithic PDMS passband filters for fluorescence detection,” *Lab. Chip*, vol. 10, no. 15, pp. 1987–1992, 2010.
- [129] C. L. Bliss, J. N. McMullin, and C. J. Backhouse, “Integrated wavelength-selective optical waveguides for microfluidic-based laser-induced fluorescence detection,” *Lab. Chip*, vol. 8, no. 1, pp. 143–151, Dec. 2007.
- [130] J. A. Chediak, Z. Luo, J. Seo, N. Cheung, L. P. Lee, and T. D. Sands, “Heterogeneous integration of CdS filters with GaN LEDs for fluorescence detection microsystems,” *Sens. Actuators Phys.*, vol. 111, no. 1, pp. 1–7, Mar. 2004.
- [131] V. P. Iordanov, J. Bastemeijer, R. Ishihara, P. M. Sarro, A. Bossche, and M. J. Vellekoop, “Filter-Protected Photodiodes for High-Throughput Enzymatic Analysis,” *IEEE Sens. J.*, vol. 4, no. 5, pp. 584–588, Oct. 2004.
- [132] O. Hofmann *et al.*, “Monolithically integrated dye-doped PDMS long-pass filters for disposable on-chip fluorescence detection,” *Lab Chip*, vol. 6, no. 8, pp. 981–987, Jun. 2006.
- [133] B. S. Phillips, P. Measor, Y. Zhao, H. Schmidt, and A. R. Hawkins, “Optofluidic notch filter integration by lift-off of thin films,” *Opt. Express*, vol. 18, no. 5, p. 4790, Mar. 2010.
- [134] P. Yeh, *Optical Waves in Layered Media*, 2nd ed. Wiley-Interscience, 2005.
- [135] P. Yeh, A. Yariv, and C.-S. Hong, “Electromagnetic propagation in periodic stratified media. I. General theory*,” *JOSA*, vol. 67, no. 4, pp. 423–438, Apr. 1977.
- [136] Y. Zhao *et al.*, “Tailoring the spectral response of liquid waveguide diagnostic platforms,” *J. Biophotonics*, vol. 5, no. 8–9, pp. 703–711, Aug. 2012.
- [137] D. Erickson, T. Rockwood, T. Emery, A. Scherer, and D. Psaltis, “Nanofluidic tuning of photonic crystal circuits,” *Opt. Lett.*, vol. 31, no. 1, pp. 59–61, Jan. 2006.

- [138] D. Ozcelik, B. Phillips, P. Measor, A. Hawkins, and H. Schmidt, "Independent Particle Detection and Tunable Spectral Filtering on Optofluidic Chip," in *CLEO: Science and Innovations*, 2012, p. CW1G.5.
- [139] S. Liu, T. A. Wall, D. Ozcelik, J. W. Parks, A. R. Hawkins, and H. Schmidt, "Electro-optical detection of single λ -DNA," *Chem. Commun.*, vol. 51, no. 11, pp. 2084–2087, Jan. 2015.
- [140] P. B. Kelter, M. D. Mosher, and A. Scott, *Chemistry: The Practical Science*. Cengage Learning, 2007.
- [141] H. Schmidt and A. R. Hawkins, "Single-virus analysis through chip-based optical detection," *Bioanalysis*, vol. 8, no. 9, pp. 867–870, May 2016.
- [142] C. Luan, Z. Yang, and B. Chen, "Signal Improvement Strategies for Fluorescence Detection of Biomacromolecules," *J. Fluoresc.*, vol. 26, no. 3, pp. 1131–1139, May 2016.
- [143] C. C. Chang, Y. M. Hsu, T. C. Chen, C. C. Ho, C. Te Chen, and P. T. Chen, "A study on the biological detection chip through the use of PDMS lens for the reinforcement of fluorescence receiving signal," *Opt. - Int. J. Light Electron Opt.*, vol. 125, no. 7, pp. 1846–1852, Apr. 2014.
- [144] Y.-C. Tung, M. Zhang, C.-T. Lin, K. Kurabayashi, and S. J. Skerlos, "PDMS-based opto-fluidic micro flow cytometer with two-color, multi-angle fluorescence detection capability using PIN photodiodes," *Sens. Actuators B Chem.*, vol. 98, no. 2–3, pp. 356–367, Mar. 2004.
- [145] K. Aslan, M. Wu, J. R. Lakowicz, and C. D. Geddes, "Fluorescent Core–Shell Ag@SiO₂ Nanocomposites for Metal-Enhanced Fluorescence and Single Nanoparticle Sensing Platforms," *J. Am. Chem. Soc.*, vol. 129, no. 6, pp. 1524–1525, Feb. 2007.
- [146] O. Stranik, R. Nooney, C. McDonagh, and B. D. MacCraith, "Optimization of Nanoparticle Size for Plasmonic Enhancement of Fluorescence," *Plasmonics*, vol. 2, no. 1, pp. 15–22, Dec. 2006.
- [147] P. Zijlstra, P. M. R. Paulo, and M. Orrit, "Optical detection of single non-absorbing molecules using the surface plasmon resonance of a gold nanorod," *Nat. Nanotechnol.*, vol. 7, no. 6, pp. 379–382, Jun. 2012.
- [148] L. Zhou, F. Ding, H. Chen, W. Ding, W. Zhang, and S. Y. Chou, "Enhancement of Immunoassay's Fluorescence and Detection Sensitivity Using Three-Dimensional Plasmonic Nano-Antenna-Dots Array," *Anal. Chem.*, vol. 84, no. 10, pp. 4489–4495, May 2012.

- [149] K. Kneipp *et al.*, “Surface-Enhanced Raman Spectroscopy in Single Living Cells Using Gold Nanoparticles,” *Appl. Spectrosc.*, vol. 56, no. 2, pp. 150–154, Feb. 2002.
- [150] W. Xu *et al.*, “Surface enhanced Raman spectroscopy on a flat graphene surface,” *Proc. Natl. Acad. Sci.*, vol. 109, no. 24, pp. 9281–9286, Jun. 2012.
- [151] S. S. Gorthi, D. Schaak, and E. Schonbrun, “Fluorescence imaging of flowing cells using a temporally coded excitation,” *Opt. Express*, vol. 21, no. 4, pp. 5164–5170, Feb. 2013.
- [152] P. Kiesel, M. Bassler, M. Beck, and N. Johnson, “Spatially modulated fluorescence emission from moving particles,” *Appl. Phys. Lett.*, vol. 94, no. 4, pp. 041107-041107-3, Jan. 2009.
- [153] S. Chu, S. Wang, Y. Deng, and Q. Gong, “Optimizing two-photon fluorescence of Coumarin dye by combined temporal–spatial pulse shaping,” *Opt. Commun.*, vol. 284, no. 16–17, pp. 4070–4072, Aug. 2011.
- [154] Z. Mei *et al.*, “Applying an optical space-time coding method to enhance light scattering signals in microfluidic devices,” *Biomicrofluidics*, vol. 5, no. 3, p. 034116, Aug. 2011.
- [155] J. Martini, M. I. Recht, M. Huck, M. W. Bern, N. M. Johnson, and P. Kiesel, “Time encoded multicolor fluorescence detection in a microfluidic flow cytometer,” *Lab. Chip*, vol. 12, no. 23, pp. 5057–5062, Oct. 2012.
- [156] S. W. Kettlitz, C. Moosmann, S. Valouch, and U. Lemmer, “Particle detection from spatially modulated fluorescence signals,” 2014, vol. 9129, p. 91291B–91291B–10.
- [157] S. W. Kettlitz, C. Moosmann, S. Valouch, and U. Lemmer, “Sensitivity improvement in fluorescence-based particle detection,” *Cytometry A*, vol. 85, no. 9, pp. 746–755, Sep. 2014.
- [158] M. Muluneh, B. Kim, G. Buchsbaum, and D. Issadore, “Miniaturized, multiplexed readout of droplet-based microfluidic assays using time-domain modulation,” *Lab. Chip*, vol. 14, no. 24, pp. 4638–4646, 2014.
- [159] V. Lien, Kai Zhao, Y. Berdichevsky, and Yu-Hwa Lo, “High-sensitivity cytometric detection using fluidic-photonic integrated circuits with array waveguides,” *Sel. Top. Quantum Electron. IEEE J. Of*, vol. 11, no. 4, pp. 827–834, 2005.
- [160] C. H. Chen, F. Tsai, V. Lien, N. Justis, and Y. H. Lo, “Scattering-Based Cytometric Detection Using Integrated Arrayed Waveguides With

- Microfluidics,” *IEEE Photonics Technol. Lett.*, vol. 19, no. 6, pp. 441–443, Mar. 2007.
- [161] J. D. Ingle and S. R. Crouch, “Signal-to-noise ratio comparison of photomultipliers and phototubes,” *Anal. Chem.*, vol. 43, no. 10, pp. 1331–1334, Aug. 1971.
- [162] R. W. Hamming, *The Art of Probability: For Scientists and Engineers*. Westview Press, 1991.
- [163] M. Munowitz and D. J. Vezzetti, “Numerical modeling of coherent coupling and radiation fields in planar Y-branch interferometers,” *J. Light. Technol.*, vol. 10, no. 11, pp. 1570–1574, Nov. 1992.
- [164] S. O. Kasap, *Optoelectronics and Photonics: Principles and Practices*. Prentice Hall, 2001.
- [165] D. Ozcelik *et al.*, “Signal-to-Noise Enhancement in Optical Detection of Single Viruses With Multispot Excitation,” *IEEE J. Sel. Top. Quantum Electron.*, vol. 22, no. 4, pp. 6–11, Jul. 2016.
- [166] J. Pfitzner, “Poiseuille and his law,” *Anaesthesia*, vol. 31, no. 2, pp. 273–275, Mar. 1976.
- [167] K. K. W. To *et al.*, “Viral load in patients infected with pandemic H1N1 2009 influenza A virus,” *J. Med. Virol.*, vol. 82, no. 1, pp. 1–7, Jan. 2010.
- [168] S. I. Stoeva, J.-S. Lee, J. E. Smith, S. T. Rosen, and C. A. Mirkin, “Multiplexed Detection of Protein Cancer Markers with Biobarcode Nanoparticle Probes,” *J. Am. Chem. Soc.*, vol. 128, no. 26, pp. 8378–8379, Jul. 2006.
- [169] D. C. Pregibon, M. Toner, and P. S. Doyle, “Multifunctional Encoded Particles for High-Throughput Biomolecule Analysis,” *Science*, vol. 315, no. 5817, pp. 1393–1396, Mar. 2007.
- [170] C. Lin, Y. Liu, and H. Yan, “Self-Assembled Combinatorial Encoding Nanoarrays for Multiplexed Biosensing,” *Nano Lett.*, vol. 7, no. 2, pp. 507–512, Feb. 2007.
- [171] D. Zhang, Y. Peng, H. Qi, Q. Gao, and C. Zhang, “Label-free electrochemical DNA biosensor array for simultaneous detection of the HIV-1 and HIV-2 oligonucleotides incorporating different hairpin-DNA probes and redox indicator,” *Biosens. Bioelectron.*, vol. 25, no. 5, pp. 1088–1094, Jan. 2010.
- [172] D. Gershon, “Microarray technology: An array of opportunities,” *Nature*, vol. 416, no. 6883, pp. 885–891, Apr. 2002.

- [173] G. MacBeath and S. L. Schreiber, "Printing Proteins as Microarrays for High-Throughput Function Determination," *Science*, vol. 289, no. 5485, pp. 1760–1763, Sep. 2000.
- [174] S. P. A. Fodor, R. P. Rava, X. C. Huang, A. C. Pease, C. P. Holmes, and C. L. Adams, "Multiplexed biochemical assays with biological chips," *Nature*, vol. 364, no. 6437, pp. 555–556, Aug. 1993.
- [175] T. M. McHugh, R. C. Miner, L. H. Logan, and D. P. Stites, "Simultaneous detection of antibodies to cytomegalovirus and herpes simplex virus by using flow cytometry and a microsphere-based fluorescence immunoassay," *J. Clin. Microbiol.*, vol. 26, no. 10, pp. 1957–1961, Oct. 1988.
- [176] B. Liu, D. Du, X. Hua, X.-Y. Yu, and Y. Lin, "Paper-Based Electrochemical Biosensors: From Test Strips to Paper-Based Microfluidics," *ResearchGate*, vol. 26, no. 6, Jun. 2014.
- [177] J. W. Lim, D. Ha, J. Lee, S. K. Lee, and T. Kim, "Review of Micro/Nanotechnologies for Microbial Biosensors," *Front. Bioeng. Biotechnol.*, vol. 3, May 2015.
- [178] Y. Zhao *et al.*, "Rapid multiplex detection of 10 foodborne pathogens with an up-converting phosphor technology-based 10-channel lateral flow assay," *Sci. Rep.*, vol. 6, p. 21342, Feb. 2016.
- [179] S. R. Nicewarner-Peña *et al.*, "Submicrometer Metallic Barcodes," *Science*, vol. 294, no. 5540, pp. 137–141, Oct. 2001.
- [180] Y. Li, Y. T. H. Cu, and D. Luo, "Multiplexed detection of pathogen DNA with DNA-based fluorescence nanobarcodes," *Nat. Biotechnol.*, vol. 23, no. 7, pp. 885–889, Jul. 2005.
- [181] J.-M. Nam, C. S. Thaxton, and C. A. Mirkin, "Nanoparticle-Based Bio-Bar Codes for the Ultrasensitive Detection of Proteins," *Science*, vol. 301, no. 5641, pp. 1884–1886, Sep. 2003.
- [182] J. J. Storhoff, A. D. Lucas, V. Garimella, Y. P. Bao, and U. R. Müller, "Homogeneous detection of unamplified genomic DNA sequences based on colorimetric scatter of gold nanoparticle probes," *Nat. Biotechnol.*, vol. 22, no. 7, pp. 883–887, Jul. 2004.
- [183] H. Li, Z. Sun, W. Zhong, N. Hao, D. Xu, and H.-Y. Chen, "Ultrasensitive Electrochemical Detection For DNA Arrays Based on Silver Nanoparticle Aggregates," *Anal. Chem.*, vol. 82, no. 13, pp. 5477–5483, Jul. 2010.

- [184] G. Liu, J. Wang, J. Kim, M. R. Jan, and G. E. Collins, "Electrochemical Coding for Multiplexed Immunoassays of Proteins," *Anal. Chem.*, vol. 76, no. 23, pp. 7126–7130, Dec. 2004.
- [185] J. Wang, G. Liu, and A. Merkoçi, "Electrochemical Coding Technology for Simultaneous Detection of Multiple DNA Targets," *J. Am. Chem. Soc.*, vol. 125, no. 11, pp. 3214–3215, Mar. 2003.
- [186] J. Wang, "Electrochemical biosensors: Towards point-of-care cancer diagnostics," *Biosens. Bioelectron.*, vol. 21, no. 10, pp. 1887–1892, Apr. 2006.
- [187] J. B. Haun, T.-J. Yoon, H. Lee, and R. Weissleder, "Magnetic nanoparticle biosensors," *Wiley Interdiscip. Rev. Nanomed. Nanobiotechnol.*, vol. 2, no. 3, pp. 291–304, May 2010.
- [188] C. Sideris and A. Hajimiri, "Design and Implementation of an Integrated Magnetic Spectrometer for Multiplexed Biosensing," *IEEE Trans. Biomed. Circuits Syst.*, vol. 7, no. 6, pp. 773–784, Dec. 2013.
- [189] C. A. Brackett, "Dense wavelength division multiplexing networks: principles and applications," *IEEE J. Sel. Areas Commun.*, vol. 8, no. 6, pp. 948–964, Aug. 1990.
- [190] R. Petry, M. Schmitt, and J. Popp, "Raman Spectroscopy—A Prospective Tool in the Life Sciences," *ChemPhysChem*, vol. 4, no. 1, pp. 14–30, Jan. 2003.
- [191] Y. C. Cao, R. Jin, and C. A. Mirkin, "Nanoparticles with Raman Spectroscopic Fingerprints for DNA and RNA Detection," *Science*, vol. 297, no. 5586, pp. 1536–1540, Aug. 2002.
- [192] C. Yu and J. Irudayaraj, "Multiplex Biosensor Using Gold Nanorods," *Anal. Chem.*, vol. 79, no. 2, pp. 572–579, Jan. 2007.
- [193] J. Homola, H. B. Lu, and S. S. Yee, "Dual-channel surface plasmon resonance sensor with spectral discrimination of sensing channels using dielectric overlayer," *Electron. Lett.*, vol. 35, no. 13, pp. 1105–1106, Jun. 1999.
- [194] J. Homola, H. B. Lu, G. G. Nenninger, J. Dostálek, and S. S. Yee, "A novel multichannel surface plasmon resonance biosensor," *Sens. Actuators B Chem.*, vol. 76, no. 1–3, pp. 403–410, Jun. 2001.
- [195] J. Dostálek, H. Vaisocherová, and J. Homola, "Multichannel surface plasmon resonance biosensor with wavelength division multiplexing," *Sens. Actuators B Chem.*, vol. 108, no. 1–2, pp. 758–764, Jul. 2005.
- [196] J. Homola, "Surface Plasmon Resonance Sensors for Detection of Chemical and Biological Species," *Chem. Rev.*, vol. 108, no. 2, pp. 462–493, Feb. 2008.

- [197] M.-C. Estevez, M. A. Otte, B. Sepulveda, and L. M. Lechuga, “Trends and challenges of refractometric nanoplasmonic biosensors: A review,” *Anal. Chim. Acta*, vol. 806, pp. 55–73, Jan. 2014.
- [198] J. N. Anker, W. P. Hall, O. Lyandres, N. C. Shah, J. Zhao, and R. P. Van Duyne, “Biosensing with plasmonic nanosensors,” *Nat. Mater.*, vol. 7, no. 6, pp. 442–453, Jun. 2008.
- [199] M. Iqbal *et al.*, “Label-Free Biosensor Arrays Based on Silicon Ring Resonators and High-Speed Optical Scanning Instrumentation,” *IEEE J. Sel. Top. Quantum Electron.*, vol. 16, no. 3, pp. 654–661, May 2010.
- [200] C. F. Carlborg *et al.*, “A packaged optical slot-waveguide ring resonator sensor array for multiplex label-free assays in labs-on-chips,” *Lab. Chip*, vol. 10, no. 3, pp. 281–290, 2010.
- [201] D.-X. Xu *et al.*, “Label-free biosensor array based on silicon-on-insulator ring resonators addressed using a WDM approach,” *Opt. Lett.*, vol. 35, no. 16, pp. 2771–2773, Aug. 2010.
- [202] M. Han, X. Gao, J. Z. Su, and S. Nie, “Quantum-dot-tagged microbeads for multiplexed optical coding of biomolecules,” *Nat. Biotechnol.*, vol. 19, no. 7, pp. 631–635, Jul. 2001.
- [203] W. C. W. Chan, D. J. Maxwell, X. Gao, R. E. Bailey, M. Han, and S. Nie, “Luminescent quantum dots for multiplexed biological detection and imaging,” *Curr. Opin. Biotechnol.*, vol. 13, no. 1, pp. 40–46, Feb. 2002.
- [204] E. R. Goldman *et al.*, “Multiplexed Toxin Analysis Using Four Colors of Quantum Dot Fluororeagents,” *Anal. Chem.*, vol. 76, no. 3, pp. 684–688, Feb. 2004.
- [205] A. M. Smith, S. Dave, S. Nie, L. True, and X. Gao, “Multicolor quantum dots for molecular diagnostics of cancer,” *Expert Rev. Mol. Diagn.*, vol. 6, no. 2, pp. 231–244, Mar. 2006.
- [206] R. H. Cole, N. de Lange, Z. J. Gartner, and A. R. Abate, “Compact and modular multicolour fluorescence detector for droplet microfluidics,” *Lab Chip*, vol. 15, no. 13, pp. 2754–2758, Jun. 2015.
- [207] L. B. Soldano and E. C. M. Pennings, “Optical multi-mode interference devices based on self-imaging: principles and applications,” *Light. Technol. J. Of*, vol. 13, no. 4, pp. 615–627, 1995.
- [208] C. Yao *et al.*, “An ultracompact multimode interference wavelength splitter employing asymmetrical multi-section structures,” *Opt. Express*, vol. 20, no. 16, pp. 18248–18253, Jul. 2012.

- [209] R. M. Jenkins, R. W. J. Devereux, and J. M. Heaton, “Waveguide beam splitters and recombiners based on multimode propagation phenomena,” *Opt. Lett.*, vol. 17, no. 14, pp. 991–993, Jul. 1992.
- [210] I. Johnson, *The Molecular Probes Handbook: A Guide to Fluorescent Probes and Labeling Technologies, 11th Edition*. Life Technologies Corporation, 2010.
- [211] R. Adar, C. H. Henry, M. A. Milbrodt, and R. C. Kistler, “Phase coherence of optical waveguides,” *J. Light. Technol.*, vol. 12, no. 4, pp. 603–606, Apr. 1994.
- [212] D. Ozcelik *et al.*, “Optofluidic wavelength division multiplexing for single-virus detection,” *Proc. Natl. Acad. Sci.*, p. 201511921, Oct. 2015.
- [213] R. Rigler and E. S. Elson, *Fluorescence Correlation Spectroscopy*, vol. 65. Berlin, Heidelberg: Springer Berlin Heidelberg, 2001.
- [214] R. M. Ratcliff, G. Chang, T. Kok, and T. P. Sloots, “Molecular diagnosis of medical viruses,” *Curr. Issues Mol. Biol.*, vol. 9, no. 2, pp. 87–102, Jul. 2007.
- [215] P. Baccam, C. Beauchemin, C. A. Macken, F. G. Hayden, and A. S. Perelson, “Kinetics of Influenza A Virus Infection in Humans,” *J. Virol.*, vol. 80, no. 15, pp. 7590–7599, Aug. 2006.
- [216] T. Suess *et al.*, “Comparison of Shedding Characteristics of Seasonal Influenza Virus (Sub)Types and Influenza A(H1N1)pdm09; Germany, 2007–2011,” *PLoS ONE*, vol. 7, no. 12, Dec. 2012.
- [217] D. Ozcelik *et al.*, “High Sensitivity Fluorescence Detection with Multi-spot Excitation Using Y-splitters,” in *CLEO: 2013 (2013), paper CTh3J.5*, 2013, p. CTh3J.5.
- [218] D. Ozcelik, M. A. Stott, H. Cai, A. Hawkins, and H. Schmidt, “Spatially Multiplexed Bioparticle Detection Using Multi-mode Interference,” in *Conference on Lasers and Electro-Optics (2016), paper SF2H.7*, 2016, p. SF2H.7.
- [219] J. W. Parks and H. Schmidt, “Flexible optofluidic waveguide platform with multi-dimensional reconfigurability,” *Sci. Rep.*, vol. 6, p. 33008, Sep. 2016.
- [220] N.-T. Nguyen and S. T. Wereley, *Fundamentals and Applications of Microfluidics*. Artech House, 2002.
- [221] T. Laurell and A. Lenshof, *Microscale Acoustofluidics*. Royal Society of Chemistry, 2014.

- [222] J. B. Knight, A. Vishwanath, J. P. Brody, and R. H. Austin, “Hydrodynamic Focusing on a Silicon Chip: Mixing Nanoliters in Microseconds,” *Phys. Rev. Lett.*, vol. 80, no. 17, pp. 3863–3866, Apr. 1998.
- [223] J. K. Ranka, R. S. Windeler, and A. J. Stentz, “Visible continuum generation in air-silica microstructure optical fibers with anomalous dispersion at 800 nm,” *Opt. Lett.*, vol. 25, no. 1, pp. 25–27, Jan. 2000.